Fabrication of porous calcium phosphate bioceramics

Hsu, Yu-Hsiu

Award date:
2005

Awarding institution:
University of Bath

FABRICATION OF POROUS CALCIUM PHOSPHATE BIOCERAMICS

Submitted by **Yu-Hsiu Hsu**

For the degree of PhD of the University of Bath
2005

Yu-Hsiu HSU

ProQuest LLC
789 East Eisenhower Parkway
P.O. Box 1346
Ann Arbor, MI 48106-1346

To my parents.

ACKNOWLEDGEMENTS

I am delighted to have the opportunity to present my tremendous appreciation to my supervisors Dr. Irene Turner and Professor Tony Miles. I am greatly thankful for the constant guidance, practical suggestions and friendly help that were a great source of motivation for the project. It was a great pleasure for me working with them.

I also want to express thanks to Stryker Howmedica Osteonics as represented by Dr. Gerard Insley for their materials and financial support.

I am deeply grateful to Professor Ronald Stevens for numerous suggestions especially on the preparation of the relevant specimens for the mechanical testing and to Dr. Brain Casey who imparted lots of laboratory experience in the early stages of this project. Thanks should also go to Dr. Chris Bowen and Dr. Martin Ansell for providing many useful suggestions. I would also like to thank Dr Bernd Grimm who helped with the die-plunger testing, Dr. Sung Quek for data processing and Dr. Sabina Gheduzzi for compressive testing. I am also eternally grateful to my colleagues at the University of Bath, specifically Jonathan Gittings, Andrew Dent, William Wang, Arnold Towo and Sam Blackmore for their technical support and good humour throughout the study.

I would also like to give special thanks to all the technical and administrative staff at the former Department of Engineering & Applied Science and the Department of Mechanical Engineering for their daily assistance, without which, this work would not have been possible. In this context I would like to thank Mr. Peter Taylor, Mr. Frank Hammett, Mr. Ian Trussler, Mr. Christopher Arnold and Mr. Richard Weston.

I would like to extend my thanks to my good friends, Vanessa Lin who helps in solving many non-academic problems and Shanru Ying, Helen Tsai, Frank Kao, Jimmy Zhang who help me in various ways during the study.

Last but not least I would like to give my gratitude to my parents Han-Pang and Chu-Chen for their invariable financial and moral support, sympathetic understanding and motivation throughout the long years of my education. Particularly, I am indebted to a weekly home letter, which is constant throughout the study.

ABSTRACT

Bioceramics are currently used in a range of applications including reconstructive, orthopaedic, otologic, maxillofacial, craniofacial and dental procedures. However, up until now the hydroxyapatite (HA) and tricalcium phosphate (TCP) bioceramics developed have had isolated porosity which constrains potential for bone ingrowth and have had poor mechanical properties so that they could not be used for heavy load-bearing applications.

The aim of this study was to fabricate porous HA/TCP bioceramics with interconnected porosity combined with good mechanical properties. Porous HA/TCP bioceramics with interconnected porosity and the controlled pore sizes necessary to allow bone ingrowth were fabricated by a novel technique of vacuum impregnation of reticulated polymeric foams with ceramic slip.

By varying the characteristics of the slips and using PU foams of different pores per inch (ppi), samples of porous HA/TCP, blocks and granules, with a wide range of pore sizes were successfully manufactured. The porous HA/TCP granules were in the size range of 2 – 8 mm with interconnected porosity and controlled size and shape – hitherto not possible using existing manufacturing techniques. Functional gradient materials (FGM) with porosity gradients close to the bimodal structure of cortical and cancellous bone were also made and no weakness was found at the interface. The macropore size of the HA/TCP bioceramics was in the range of 197 – 254 μm (for 20 ppi foam), 143 – 182 μm (for 30 ppi foam) and 105 – 135 μm (for 45 ppi foam). The macroporosities made from three different porosity PU foams were similar and in the range of 5.24 to 9.67 %. The average apparent density of the HA/TCP samples was 2.48 g/cm^3 (range: 2.32 to 2.59 g/cm^3), four-point bending strength was 16.98 MPa (range: 13.03 to 22.03 MPa), work of fracture was 15.46 J/m^2 (range: 12.23 to 17.98 J/m^2) and compressive strength was 105.56 MPa (range: 58.46 to 138.72 MPa). The wide ranges of mechanical properties resulted from various combinations of different grades of PU foam and the solid loading of slips. These results indicate that it is possible to manufacture open pore HA/TCP bioceramics with compressive strengths comparable to human bone which could be of significant clinical interest.

TABLE OF CONTENTS

LIST OF FIGURES

LIST OF TABLES

CHAPTER 1

INTRODUCTION AND AIMS OF STUDY

The chapter gives an introduction to the project and includes background, aims and layout of the thesis

1. Introduction and Aims of Study

Bone stock loss represents a major challenge in orthopaedic surgery. As surgical techniques and medical knowledge continue to advance, there is an increasing demand for the development of synthetic bone substitute materials, resulting from the limited supply of autograft material and the knowledge that allografting introduces the risk of disease and infection[1].

Porous calcium phosphate based ceramics are attractive for use as synthetic bone graft substitutes allowing successful tissue ingrowth, which further enhances the implant-tissue attachment. The two calcium phosphate ceramics (CaP ceramics) widely used in clinical applications are tricalcium phosphate (TCP) and hydroxyapatite (HA). HA has proved to be one of the most biocompatible materials as a result of the compositional similarities with the mineral found in hard tissues of the body such as bones and teeth[2]. Tricalcium phosphate (TCP) is a resorbable temporary bone space filler material. Development of synthetic porous HA/TCP bone replacement materials for the filling of both load-bearing and non-load-bearing osseous defects has become of increasing interest. The degree of interconnectivity and the pore size are the critical factors that determine the success of the implants. Numerous authors have reported the optimum pore sizes for bone ingrowth. A minimum pore size of approximately 100 to 150 μm has been generally accepted[3-4] due to cell size, migration requirements and transport[5]. Research has suggested that the degree of interconnectivity is more critical than the pore size[6-7]. However, it is well known that the mechanical strength of a material generally decreases as its porosity increases. Conflicting interests exist between biological and mechanical requirements, thus the design of porous implant materials with a sufficient degree of interconnected porosity combined with optimal mechanical properties is the most important challenge. A balance must be reached depending on the repair, rate of remodelling and rate of degradation of the scaffold materials[5].

Many methods have been developed to fabricate porous ceramics, such as organic particle embedding techniques, production of gas bubbles in slips and the replication of reticulated porous structures. However, these methods are regarded to be unsatisfactory as they may fail to meet either or both of the two main demands which are: an adequate degree of interconnected porosity and optimal mechanical properties.

This research project was based on the development of the replication of reticulated porous structures as a method to manufacture porous calcium phosphate bioceramics. The main aims of this research work are summarised as follows:

- Fabrication of porous calcium phosphate bioceramics with completely interconnected porosity.
- Improvement of the mechanical strength of porous calcium phosphate bioceramics to enable their use in heavy load-bearing applications.
- Manufacture of porous granules which could be useful for impaction grafting and space filling.
- Development of a functional gradient material (FGM) with graded pore structures similar to the bimodal structure of cortical and cancellous bone.

The layout of thesis is described as follows:

- **Chapter 1. Introduction:** introduces the project and includes background, aims and layout of the thesis.
- **Chapter 2. Literature Review:** covers the clinical utilization of materials and the associated problems, physical, chemical and mechanical properties of the hard tissues and calcium phosphate bioceramics. Common methods of fabrication of porous ceramics, fundamentals of mechanical testing and Functional Gradient Materials (FGM) will be discussed.
- **Chapter 3. Experimental Procedure:** details manufacturing processes for porous blocks, granules, solid calcium phosphate, Functional Gradient Materials (FGM) and macro- and microscopic analysis and measurement of physical and mechanical properties.
- **Chapter 4. Results and Discussion:** covers the macro- and micrographs of porous blocks, granular forms and solid calcium phosphate and Functional Gradient Materials (FGM) and results of physical and mechanical testing of properties.
- **Chapter 5. General Discussion and Conclusions**
- **Chapter 6. Suggestions for Future Work**

CHAPTER 2

LITERATURE REVIEW

The literature review covers the clinical utilization of materials and the problems associated with their use, the physical, chemical and mechanical properties of the hard tissues and calcium phosphate bioceramics. Common methods used to fabricate porous ceramics, fundamentals of mechanical testing and Functional Gradient Materials (FGM) will be discussed.

2. Literature Review

2.1 Hard Tissue Replacement Implants

Bone is particularly prone to fracture in older people because of a loss of bone density and strength with age[8-10]. This is a particular problem for women as a result of the hormonal changes associated with the onset of the menopause. Bone density decreases due to an imbalance between bone resorption and formation[11]. Bone-growing cells (osteoblasts) become gradually less productive in making new bone and repairing microfractures with age.

In normal conditions, osteoclasts and osteoblasts ensure a balanced control of bone resorption and formation, resulting in bone repair, renewal and growth[12]. The self-healing capacity of bone is widely used for the repair of small fractures. Any changes in this equilibration by uncoupling of the balance of bone resorption by osteoclasts and bone formation by osteoblasts causes an absolute reduction in the amount bone which can result in osteoporosis[13].

Historically, when tissues become diseased or injured, physicians had little option but to remove the offending part. In some cases, removal of joints, part of the spinal column, teeth, or organs led to only a slightly improved quality of life. However, human survivability rarely exceeded the progressive decrease in quality of tissues (strength and density) as shown in Figure 2.1[14]. Therefore, the requirement for replacement parts was small. Since the last century, the situation has changed greatly. Life expectancy is now in the range of 80+ years. This increase in survivability[12] means that many people outlive the quality of their connective tissue. In addition, there is a necessity for replacing bone substances that are fractured, diseased, worn or damaged as a result of sports- and traffic-related injuries.

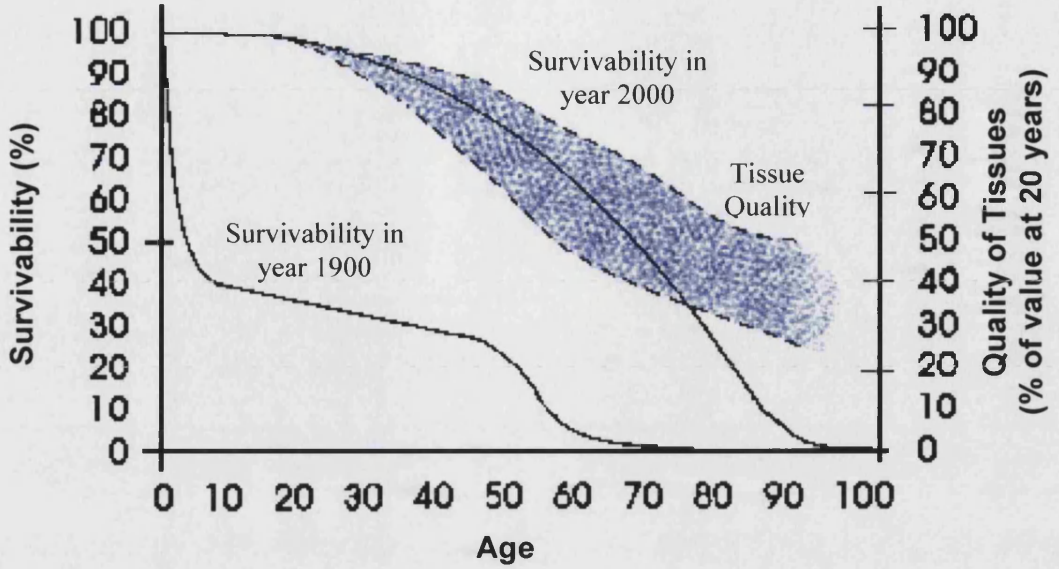

Figure 2.1 Contrast of human survivability in year 1900 versus 2000 with effects of age on the quality of connective tissue[14].

Bone grafts can be utilised as part of a number of surgical procedures[12,15-17] such as filling of voids left after removal of disease tissue following trauma, infection, tumour and in spinal fusion, reconstructive, maxillofacial, craniofacial, oral and plastic surgery procedures.

The treatment of large bone defects requires the use of cortical and cancellous bone grafts[18]. Bone grafts are needed to provide support, fill defects and enhance biological repair when the skeletal defect reaches a crucial size[12].

The graft materials of choice are autograft, allograft or xenograft[1,19-20] Although autograft is certainly the biological gold standard[12], shortcomings are encountered with its usage. The drawbacks to its use include: (1) harvesting of this material increases surgery time and causes additional trauma, (2) postoperative pain (this is permament in some cases), (3) available autologous bone quantity is frequently not sufficient in quantity, (4) inadequate size and shape and (5) difficulties in shaping the bone graft to fill the defect[11-12,19,21].

Allograft, which provides most of the desirable tissue characteristics of autograft, is increasingly unpopular due to: (1) the risk of disease transmission such as HIV (Human Immunodeficiency Virus), hepatitis and acquired immunological deficiency syndrome (AIDS), (2) the difficulty of procurement and processing, (3) it may be rejected by the human body and (4) premature resorption[11,15,18,22-24].

Xenograft, typically bovine in origin (e.g. Kiel bone), is similarly considered problematic owing to the unfavourable immune response[23].

For these reasons synthetic materials are being widely developed as bone graft substitutes. There are also many clinical reasons to develop bone tissue-engineering alternatives, including the need for better biomaterials that can be used in the reconstruction of large orthopaedic defects and the need for orthopaedic implants that are mechanically more suited to their biological environment. An important advantage of synthetic materials is that they can be produced in unlimited quantities[16] as no biological source is needed.

The materials suitable for service in the skeletal system must be biocompatible which means that the tissue of the patient that comes into contact with the materials does not suffer from any toxic, irritating, inflammatory, allergic, mutagenic or carcinogenetic reaction[25-28]. In addition they must have the required bending, compressive, tensile strengths combined with wear and fatigue resistance to sustain the loads applied during bone growth and remodelling. They should also be sufficiently unreactive in body fluids so as not to suffer severe degradation, which would weaken their mechanical performance.

The selection and application of an ideal synthetic material for surgical implants has been shown to directly depend upon the following characteristics[13, 29-34]:

(1) It should be biocompatible and biodegradable with a controllable degradation and resorption rate to match cell/tissue growth.

(2) It should have an optimum porosity with an interconnected pore network to facilitate vascular regeneration along with bone regrowth.

(3) It should have suitable mechanical properties to match those of the tissues at the site of implantation and be strong enough to fulfil required load-bearing functions at least during the early post-implantation period (i.e. before significant bone ingrowth and replacement has occurred).

(4) It should degrade and be resorbed so there will be no long-term foreign bodies remaining. The ultimate goal is to return full biological and mechanical functionality to a damaged tissue or organ.

(5) It should be made from versatile processing techniques that can produce irregular, usually complex, shapes to match those of the defect in the tissue of the patient.

(6) It should have suitable surface chemistry for cell attachment, proliferation and differentiation.

Potential materials include natural polymers, synthetic polymers, ceramics, metals and combinations of these materials. Polymers are attractive as materials for reconstruction because of their great versatility. However, polymeric materials generally have a limited used in orthopaedic and dental applications, mainly because of strength constraints.

Metals and ceramics have contributed to major advances in orthopaedic tissue replacements. Metals are tough but have high stiffness[35]. Engineering alloys such as stainless steel, cobalt-chromium alloys and titanium alloy have been used in orthopaedic surgery as replacements for bone. The implants made from these metallic materials have the strength and toughness properties that are required in heavy load-bearing parts of the body and due to these advantages, metals will continue to play an important role as orthopaedic biomaterials in the future, even though there are various problems related to metallic materials in the human body due to corrosion, wear or adverse tissue reaction[36]. When the implant is a metal, the surface can provide a focus for corrosion of the implant and loss of metal ions into the tissue, which can cause a variety of medical problems.

Ceramics are inorganic, nonmetallic materials. Ceramics used for the repair and reconstruction of diseased or damaged parts of the human body are termed bioceramics. They offer many advantages compared to other materials. The obvious advantage of ceramics is that they are relatively inert in body fluids and thus release negligible amounts of toxic degradation products into body tissues[37]. They are harder and stiffer than steel and more heat and corrosion resistant than metals or polymers while at the same time being less dense than most metals. The main concern with the use of ceramics is the fact that they are brittle and may not have the mechanical properties required for the high load-bearing applications characteristic of many orthopaedic and dental implants.

Until the 1960s the inherent limitations of the mechanical properties of traditional structural ceramics restricted their applications in medicine. However, ceramics are more similar to natural skeletal materials than the more widely used metallic implants.

Applications[38] of bioceramics include replacements for hip, knees, teeth and repair for periodontal disease, maxillofacial reconstruction, augmentation and stabilization of the jawbone, spinal fusion and bone fillers after tumour surgery. The clinical uses of bioceramics are summarised in Table 2.1[8,38].

Initially, attention was focused on ceramics which would elicit very little tissue reaction, so called bioinert ceramics. Alumina (Al_2O_3) and zirconia (ZrO_2) soon emerged as materials of great potential, owing to their high mechanical strength. However, a series of studies revealed that alumina and zirconia do not bond directly to bone or conduct bone ingrowth into pore channels.

One highly successful area of for bioceramics as implant materials over the last two decades is the emergence and medical use of bioactive ceramics. These include calcium phosphates, Bioglass®, Alumina-wollastonite glass ceramic (AW-GC) and other bioactive glasses and glass-ceramics that elicit a specific biological response at the interface of the material resulting in the formation of a strong bond between the tissue and the biomaterial[39].

Hydroxyapatite (HA) is the major component of the skeletal tissue of vertebrates. Studies have shown that synthetic HA is totally biocompatible, non-toxic and osteoconductive[2,40-41]. Calcium phosphate based bioceramics have received considerable attention as bone graft substitute, primarily because of their excellent biocompatibility, bioactivity and osteoconduction characteristics[39]. Recently, attention has been particularly focused on using porous HA, either in block or granular form as the porous network promotes tissue ingrowth, which further enhances the implant-tissue attachment[42]. However, the low mechanical properties of these bioactive ceramics limit their clinical application to areas where major load bearing does not occur[43-44].

In summary, none of the materials currently available for clinical implantation have properties that mimic all of those of natural bone. This has limited their use in clinical applications and hence more research needs to be conducted to improve their properties. The focus of this research is on fabrication of porous calcium phosphate based ceramics. These will be reviewed in detail in sections 2.3 and 2.4.

Application	**Materials**
Orthopaedic	Al_2O_3 Stabilized ZrO_2 HA powders Bioactive glass powders
Coatings for bioactive bonding	HA Bioactive glass ceramics
Bone space fillers	Tricalcium phosphate Calcium phosphate salts Bioactive glass granules Bioactive glass – ceramic granules
Dental implants	Al_2O_3 HA Bioactive glasses
Artificial tendon and ligament	PLA – carbon - fibre composite
Periodontal pocket obliteration	HA HA - PLA composite Tricalcium phosphate Calcium phosphate salts Bioactive glasses
Alveolar ridge augmentations	Al_2O_3 HA HA - autogenenous bone composite HA - PLA composite Bioactive glasses
Maxillofacial reconstruction	Al_2O_3 HA PE - HA composite Bioactive glasses
Spinal surgery	Bioactive glasses-ceramic HA
Therapeutic treatment of tumours	Rare – earth - doped aluminosilicate glasses
Artificial heart valves	Pyrolytic carbon coatings
Otolaryngological	Al_2O_3 HA Bioactive glasses Bioactive glass ceramics PE - HA composite
Cranial repair	Bioactive glasses
Percutaneous access devices	Bioactive glass – ceramics Bioactive glasses HA
Orthopaedic load-bearing applications	Al_2O_3 ZrO_2 PE - HA composite HA coating on metal Bioactive glass- ceramic coating on metal
HA: Hydroxyapatite, PE: Polyethylene and PLA: Poly lactic acid	

Table 2.1 Clinical uses of bioceramics[8,38].

2.2 Composition and Properties of Hard Tissues

It is of great importance to know the physical, chemical and mechanical properties of the hard tissues because they provide quantitative parameters necessary for fabrication of synthetic bone replacement implants. Bone is an extremely complex tissue that performs many essential functions in the body and is complex to analyse because it has so many levels of organization. Bone and teeth are mineralised tissues whose primary function is "load-carrying." Teeth are exposed to more extreme physiological circumstances as their function is carried out in direct contact with *ex vivo* substances, while the functions of bone are carried out inside the body in conjunction with muscles and tendons. Bone has numerous primary functions in the body as a system, such as;[45-46] (1) protection of vital organs, e.g. the rib cage protects the heart and lungs, (2) providing support and site of muscle attachment for locomotion, (3) generation of red and white blood cells for immunoprotection and oxygenation of other tissues and (4) retaining reserve stores of calcium, phosphate and other important ions. Bone is a self-repairing structural material, able to adapt its mass, shape and properties to change in mechanical requirements and endure voluntary physical activity for life without breaking or causing pain.

2.2.1 Structure of Bone

Mature bone exists in two main forms: compact (cortical) and spongy (cancellous) as shown in Figure 2.2[47-48]. Compact bone forms the outer wall of all bone and is largely responsible for the supportive and protective function of the skeleton (Figure 2.3)[46]. Compact bone has a denser structure and is made of Haversian systems (in honour of Clopton Havers, a seventeenth-century English anatomist who first described them); cylinders of bone matrix with osteocytes in concentric rings around central Haversian canals. In the Haversian canals are blood vessels; the osteocytes are in contact with these blood vessels and with one another through microscopic channels (canaliculi) in the matrix[46,48].

Spongy bone is much more porous and found in the inner parts of bone. Spongy bone has a sponge-like morphology. Osteocytes, matrix and blood vessels are present but are not arranged in complete Haversian systems. The cavities in spongy bone often contain red bone marrow, which produces red blood cells, platelets and white blood cells[46].

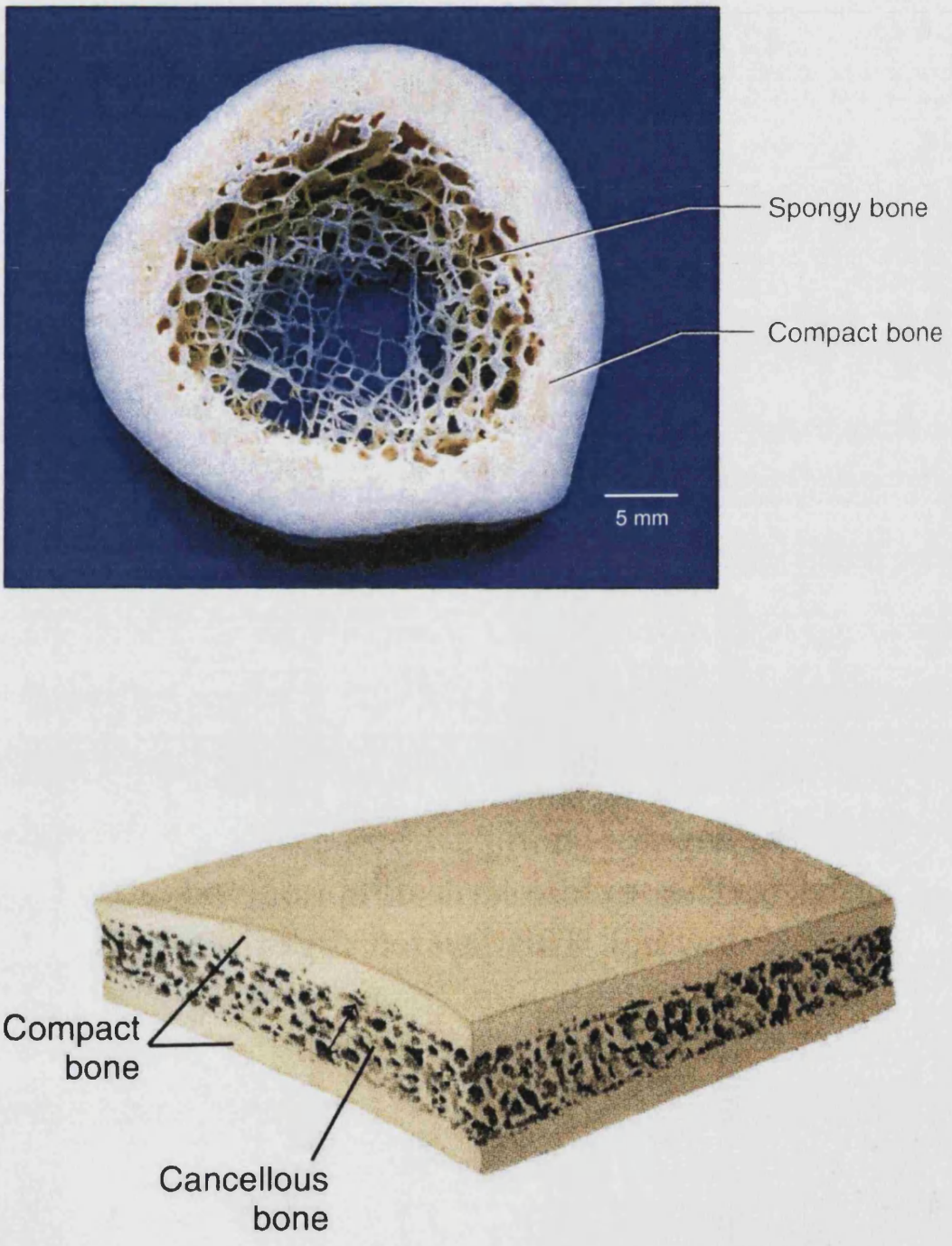

Figure 2.2 Compact bone and spongy bone (a) cross section of a long bone. (b) flat bone[47-48].

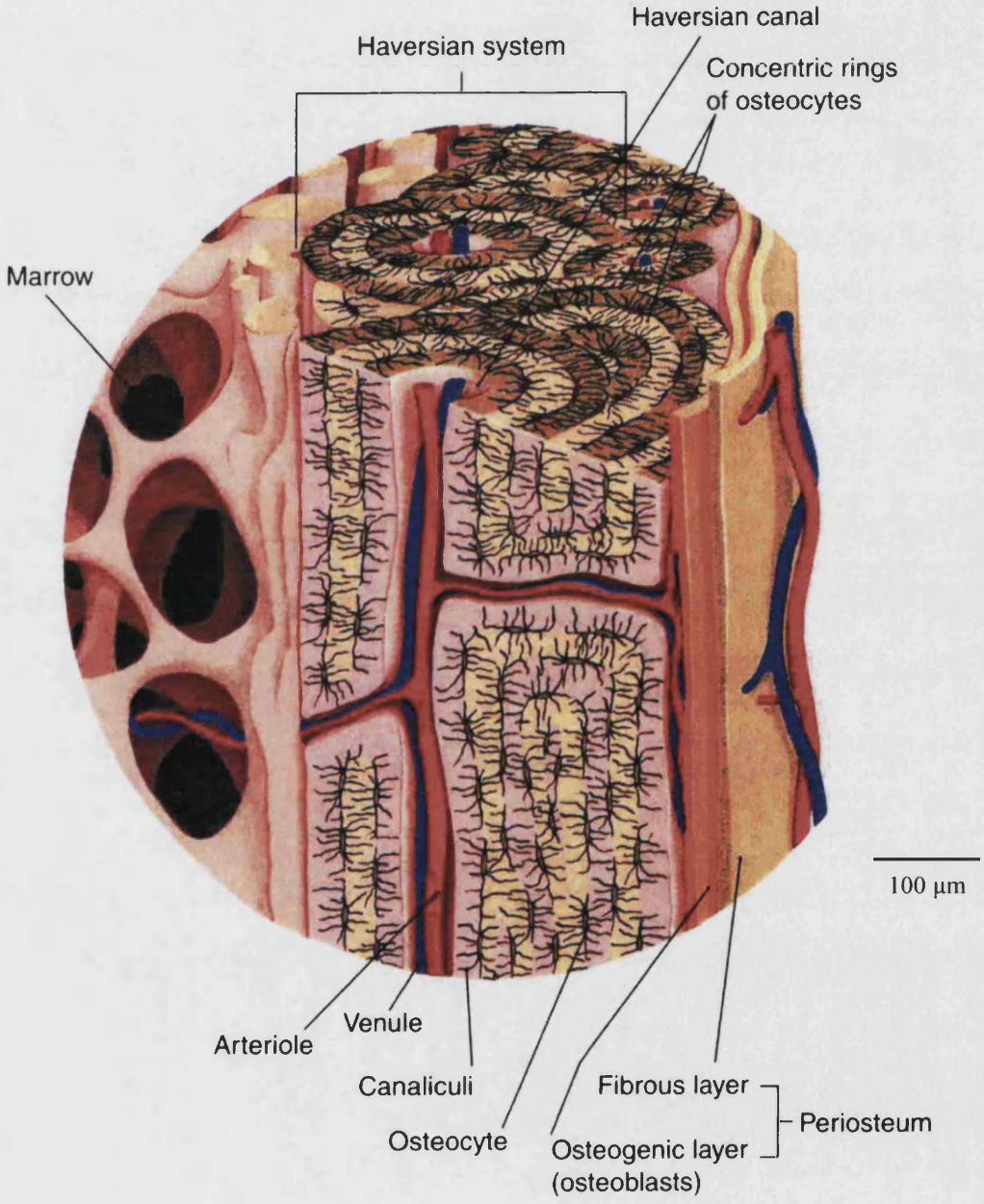

Figure 2.3 Haversian systems in compact bone[46].

Approximately 80 % of the skeletal mass in the adult human skeleton is cortical bone and the remaining 20 % of the bone mass is cancellous bone. The distribution of cortical and spongy bone varies greatly between individual bones[45]. Table 2.2 shows an example of how the proportions of compact and spongy bone differ at various locations in the skeleton. The ulna consists of 92 % cortical and only 8 % spongy bone, while a typical vertebra consists of 62 % cortical and 38 % spongy bone[49].

	Cortical bone	Spongy bone
Skeletal mass	80 %	20 %
Ulna	92 %	8 %
Vertebra	62 %	38 %

Table 2.2 The variation in the distribution of cortical and cancellous bone between individual bones[49].

The porosity and density of cortical and cancellous bone are given in Table 2.3. The porosity of human compact bone is less than 30 % and from 50 to 90 % in cancellous bone[45]. The densities of human compact bone and spongy bone are in the range of 1.7 to 2.0 g/cm^3 and 0.15 to 1 g/cm^3, respectively[50].

	Cortical bone	Spongy bone
Porosity	< 30 %	50 to 90 %
Density	1.7 to 2.0 g/cm^3	0.15 to 1 g/cm^3

Table 2.3 The porosity and density of cortical and cancellous bone[45, 50].

2.2.2 Composition of Bone

Bones are composite materials composed of highly interconnected inorganic hard tissues (calcium phosphates) and organic soft components (collagen fibres). The main components of wet cortical bone are 69 wt% mineral; 22 wt% organic matrix of which 90 – 96 wt% is collagen; and 9 wt% water as given in Table 2.4[51].

Components	Amount (wt %)
Mineral (apatite)	**69**
Organic matrix	**22**
Collagen	(90 – 96 % of organic matrix)
Others (such as proteins, polysaccharides and lipids)	(4 – 10 % of organic matrix)
Water	**9**

Table 2.4 Composition of bone[51].

Bone mineral is composed of nano-crystalline platelets, originally described as hydroxyapatite (HA). The HA crystals, present in the form of plates or needles, are about 40 – 60 nm long, 20 nm wide and 1.5 – 5 nm thick. However, most synthetic apatites differ from bone mineral, which is the main component of hard tissues such as bone and teeth. The mineral phase of hard tissue is a so-called biological apatite. Table 2.5[52] shows the three primary differences between synthetic apatites and biological apatites.

Synthetic apatites	Biological apatites
Hydroxyapatite (HA)	Carbonated hydroxyapatite (CHA)
High crystallinity	Low crystallinity (disordered crystals through inclusion of hetero-ions such as Mg^{2+}, F^- and CO_3^{2-})
Larger agglomerates (Micron-size range)	Nanocrystal (size ca. 40 – 60 × 20 × 1.5 – 5 nm^3)

Table 2.5 The differences between synthetic apatites and biological apatites[52].

Biological apatites differ from theoretical hydroxyapatite $Ca_{10}(PO_4)_6(OH)_2$ and contain carbonate ion (about 3 – 5 wt%) and other trace elements such as Mg^{2+}, Fe^{2+}, Na^+, HPO_4^{2-}, F^- and Cl^-[53-55]. It is now agreed that bone apatite can be better described as carbonate hydroxyapatite (CHA)[53,56-61] and approximated by the formula: $(Ca,Mg,Na)_{10}(PO_4,CO_3)_6(OH)_2$[62].

Furthermore, all biologically formed apatites in bone, dentin and mineralised tendons are nanocrystalline (with enamel being the only exception)[59]. This results in a much lower biodegradation rate of sintered HA compared to nanocrystalline bone mineral[53, 63] as nanocrystalline bone mineral has more grain boundaries and biodegradation will be more active in disordered crystals.

Organic materials, such as proteins, polysaccharides and lipids are also present in small quantities. Collagen, which can be considered as the matrix, is in the form of small microfibres. It is difficult to observe distinct collagen fibres because of their net-like mass appearance. The diameter of the collagen microfibres varies from 100 to 2000 nm.

2.2.3 Mechanical Properties of Bone

The *in vitro* properties of bone can vary significantly from the *in vivo* properties depending on the freshness of the tissue and the means by which the tissue was preserved. Elastic properties, density, bone mineral content and strength have all been shown to vary significantly with aging, activity and disease[50]. Any treatment of bone which changes the nature or relative composition of these components can change the properties. Drying, freezing, storage in solutions of certain salinities and embalming have all been shown to affect the properties of bone[49]. The mechanical properties of bone depend largely on the humidity, mode of applied load (compressive or tensile), rate of loading, the kind of bone and direction of the applied load with respect to the orientation of the microstructure[2]. Tables 2.6 and 2.7 give some general idea of the mechanical properties of different bones. The major bones of the skeleton are shown in Figure 2.4[46]. The mechanical properties of bone in Table 2.6 show most of bones have higher compressive strengths than tensile strengths. However, fibula, radius and ulnar bones have higher tensile strengths than compressive. The reason might be most bones often suffer compressive stress but fibula, radius and ulnar bones often endure in tensile stresses.

Tissue	Direction of test	Modulus of elasticity (GPa)	Tensile strength (MPa)	Compressive strength (MPa)
Leg bones				
Femur	Longitudinal	17.2	121	167
Tibia	Longitudinal	18.1	140	159
Fibula	Longitudinal	18.6	146	123
Arm bones				
Humerus	Longitudinal	17.2	130	132
Radius	Longitudinal	18.6	149	114
Ulna	Longitudinal	18.0	148	117
Vertebrae				
Cervical	Longitudinal	0.23	3.1	10
Lumbar	Longitudinal	0.16	3.7	5
Spongy bone	Longitudinal	0.09	1.2	1.9
Skull	Tangential	-	25	-
	Radial	-	-	97

Table 2.6 Properties of bone[64].

	Test direction related to bone axis	
	Parallel	Normal
Tensile strength (MPa)	124 – 174	49
Compressive strength (MPa)	170 – 193	133
Bending strength (MPa)	160	
Shear strength (MPa)	54	
Young's modulus (GPa)	17.0 – 18.9 20 – 27 (random)	11.5
Work of fracture (J/m^2)	6000 (low strain rate) 98 (high strain rate)	
K_{IC} ($MPa \cdot m^{1/2}$)	2 – 12[a]	
Ultimate tensile strain	0.014 – 0.031	0.007
Ultimate compressive strain	0.0185 – 0.026	0.028
Yield tensile strain	0.007	0.004
Yield compressive strain	0.010	0.011

[a]Direction of measurement not specified.

Table 2.7 Mechanical properties of human compact bone[2].

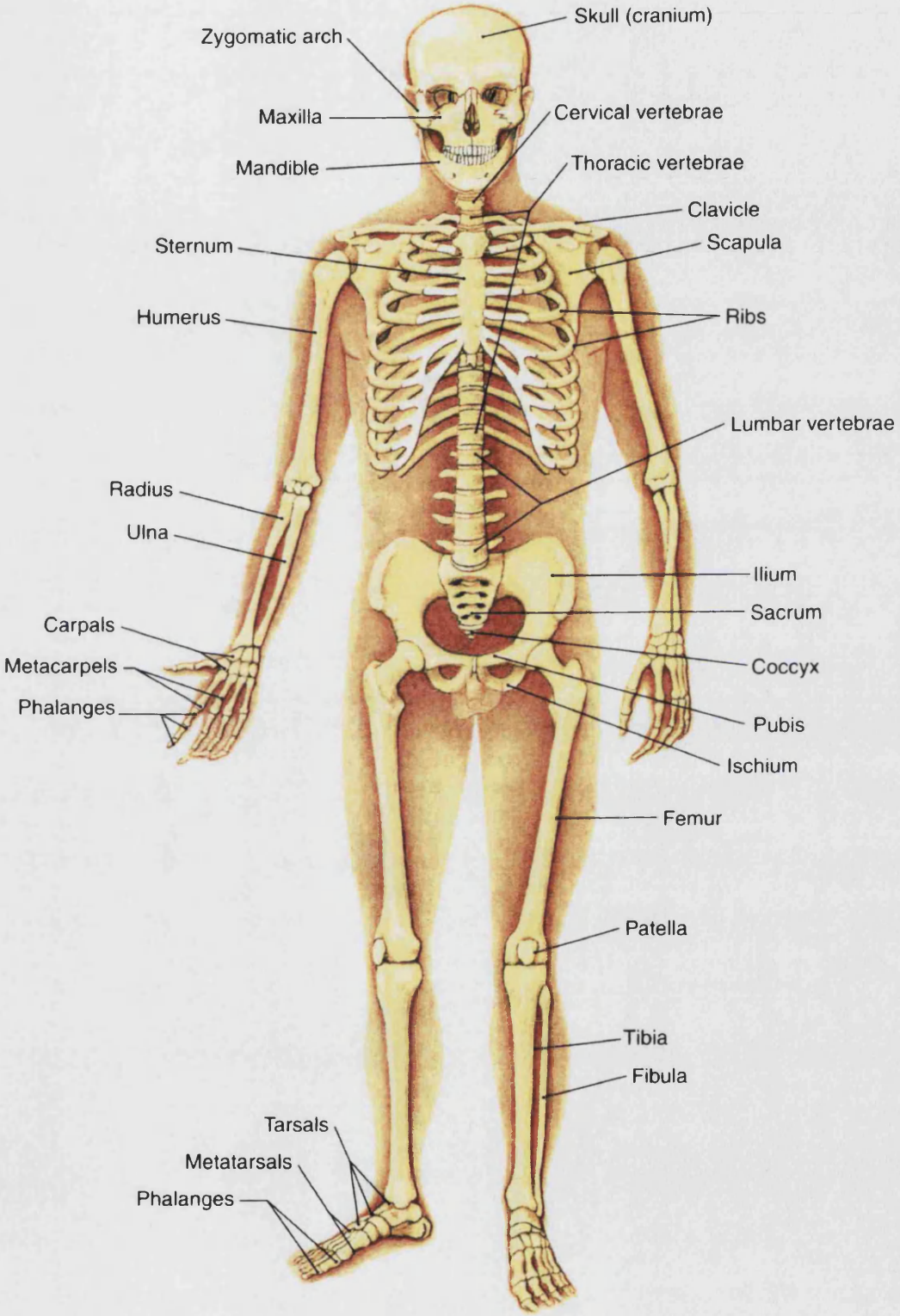

Figure 2.4 Major bones of the skeleton[46].

Bone comprises mainly apatite, collagen and water. The collagen gives the bone its strength and resilience[65]. The Young's modulus of apatite in bone is about 80 GPa and that of collagen 1.5 GPa, these combine in bone to give a material with a Young's modulus less than 80 GPa[66] due to the composite nature of bone where is determined by the volume proportion and Young's modulus of individual materials. Table 2.8 gives the general ranges of mechanical properties of human tissues.

	Tensile strength (MPa)	Compressive strength (MPa)	Young's modulus (GPa)
Cancellous bone	N/a	4 – 12	0.02 – 0.5
Compact bone	60 – 150	130 – 180	3 – 30
Cartilage	3.7 – 10.5	N/a	0.7 – 15.3 (MPa)
Ligament	13 – 16	N/a	0.065 – 0.541
Tendon	24 – 112	N/a	0.143 – 2.31

Table 2.8 Mechanical properties of human tissues[67].

In summary, bone is a complex material whose structure and properties are unique. It is not possible to reproduce the properties of bone in a man-made material. This has limited the use of current biomaterials in clinical applications and hence more research needs to be conducted to improve their properties. Calcium phosphate based materials have been increasingly studied and used in implants for orthopaedic and dental applications. This will be introduced in the following section.

2.3 Calcium Phosphate Bioceramics

2.3.1 Introduction to Calcium Phosphate Bioceramics

A bone implant requires biocompatibility, mechanical strength and porosity to promote the interactions between the biomaterials and the host tissue without causing undesirable biological responses. The scaffolds should also degrade and be resorbed after they have been implanted so there will be no long-term foreign bodies remaining.

Since Levitt et al[68] described a method, hot pressing, of preparing an apatite ceramic from mineral fluorapatite ($Ca_{10}(PO_4)_6F_2$) and recommended the possible use of this apatite ceramic in clinical applications in 1969, calcium phosphate based materials, such as apatites, have been increasingly studied and used in implants for orthopaedic and dental applications.

Hydroxyapatite (HA, chemical formula $Ca_{10}(PO_4)_6(OH)_2$, Ca/P = 1.67) is one of the most biocompatible materials due to similarities with the mineral constituents of teeth and bones[2,69] and HA material is the major component of the skeletal tissue of vertebrates[70]. HA and other related calcium phosphate ceramics (CP) such as β-tricalcium phosphate (β-TCP; $Ca_3(PO_4)_2$) and mixtures of both (the so-called biphasic calcium phosphates; BCP) do not exhibit any cytoxic effects, have a similarity of composition and good biocompatibility with natural bone[71-73]. As such they have become essential research subjects of many medical as well as materials scientists[2,72,74-89].

Hydroxyapatite (HA) and tricalcium phosphate (TCP, Ca/P = 1.50) are highly biocompatible, bioactive, biodegrabable, non-toxic, cause no immunological or irritating response, have excellent osteoconductive ability[90] and have been shown to promote bone ingrowth[21,91-95]. Due to these merits, calcium phosphates are being increasingly used as fillers, coatings on orthopaedic and dental implants, alveolar ridge augmentation, oral and maxillo–facial surgery, spine fusion, otolaryngology, and scaffolds for bone growth, bone substitutes in orthopaedic surgery and as granules in total hip and knee surgery[38, 62, 65, 96].

Such bioactive implant materials are commonly used as[23,97] blocks[83,98-101], cements [102-109], pastes, powders, coating[110-113] or granules[98, 114-116]. Furthermore, porous HA has begun to gain attention as a potential water filter due to its ability to remove heavy metal ions by ion exchange due to its crystal structure and chemical composition[117-119]. For this application there is a need for high-porosity ceramics.

2.3.2 Porous Calcium Phosphate Bioceramics

2.3.2.1 Introduction of Porous Calcium Phosphate Bioceramics

Porous ceramics can be grouped as open or closed cell depending on whether interconnected channels are present or not between the hollow cells[120]. Although

porosity is the main cause of the reduction in mechanical properties in brittle solids, the development of porous materials is needed for some industries. The increase in the use of porous materials has been related mainly to their specific properties[119,121-125], such as high surface area, high specific stiffness, high thermal shock resistance, good insulating characteristics, low mass, low specific heat and low thermal conductivity.

These porous ceramics, commercially available or the subject of current study, are made of various materials[119,124,126] such as alumina[125,127-130], cordierite, mullite ($3Al_2O_3 \cdot 2SiO_2$)[123], silica[121], silicon carbide[131], silicon nitride[132,133], partially stabilized zirconia, TiO_2[134], calcium phosphate and composite materials[135,136].

Porosity has been found to be essential for technological applications that can include[122,125,131,137-140] thermal insulating materials for furnaces and also for aerospace applications (tiles for space shuttles), thermal and acoustic insulation, humidity sensors, catalyst support, filters for molten metals and diesel engine exhaust and industrial hot gases, gas detectors and heat exchangers. Expanding applications are now also being found for porous implants in the area of biomaterials.

A ceramic with open porosity is a material whose structure can closely resemble that of bone and porous HA/TCP exhibits strong bonding to the bone. The medical applications [2] include synthetic bone graft[32, 52,141-143], filling bone defects, drug delivery system[33, 144,145] and alveolar ridge augmentation[62].

Since the early 1970's it has been well known that if a biocompatible ceramic prosthesis with appropriate interconnected pores is used, growth of hard and soft tissue into the surface pores will be observed[146]. A strong attachment and hence a resultant mechanical and chemical bond to the existing surrounding tissue will be formed. In recent years attention has particularly focussed on the fabrication of calcium phosphate ceramics with a porous configuration as synthetic bone grafts because the porous network promotes tissue ingrowth, which further enhances the implant-tissue attachment[6,21,42,147-152]. The advantage of using ceramics is that they are mechanically anchored by the physical growth of natural bone into the pores. The strength of porous HA is lower than that of dense bodied HA but the bone tissue ingrowth can increase the strength of the HA implants, enhancing their potential for use as bone substitutes[60,153].

Numerous researchers have reported that porous HA was fragile and had poor mechanical properties[4,69,108], especially in wet environments (decrease of 25%)[154], so

the HA ceramics cannot currently be used for heavy load-bearing applications, such as artificial teeth or bones. Their applications are limited to small implants, powders, coatings and low-loaded porous implants[38].

Baer et al[21] used HA to fill bone defects in the hands of 22 patients and supported the use of HA ceramic as an alternative to autologous cancellous bone graft but it is not suitable for bridging osseous defects. Vuola et al[100,155] implanted porous HA into an intramuscular site of a rat and reported that HA is not a suitable material for repairing weight-bearing cortical defects because bone ingrowth strengthens the materials but they will still never be as strong as compact bone.

In contrast to this, several medical scientists implanted porous HA in heavy load-bearing bone and concluded that the result was acceptable. Huec et al[156] tested 150 cylindrical hydroxyapatite samples with open porosity and indicated that it is possible to obtain ceramics with open porosity whose resistance under compressive stress is comparable to that of human bone. Holmes et al[157] reported that the weak mechanical properties of porous HA might be eliminated once incorporation and bone ingrowth into the pores were achieved. Tamai et al[158] revealed that compression testing of implanted calcium hydroxyapatite ceramics at nine weeks showed a steady increase in strength to more than double the value measured in the initial test. Koshino et al[101] inserted a porous HA wedge into the tibia in ten knees of seven patients with osteoarthritis of the knee who underwent high tibial osteotomy and suggested that HA could be applied in human adults, even in heavy load-bearing bone. Piecuch et al[152] inserted porous HA on the mandibular ridges of three dogs and reported that porous HA is quite weak when compared to bone, but when its pores are penetrated by connective tissue and bone, the resulting tissue-implant combination gains a significant amount of strength. This level of strength is thought to be sufficient for withstanding the masticatory forces exerted by complete dentures. Martin et al[98] noted that when coralline HA was implanted in cancellous bone, it became stronger than the surrounding bone but when implanted in cortical bone for 16 weeks, it achieved only a small percentage of the bending strength of cortical bone.

However, for bone ingrowth and attachment to the body tissue, pore characteristics are an essential feature for the bone-graft materials. The level of porosity, pore size distribution, pore morphology and the degree of pore interconnectivity in such grafts significantly influences the extent of bone ingrowth[93,153,159].

Table 2.9 shows the classification of micro-, meso- and macro-porosity[93,161]. The classification is of interest for both mechanical properties and behaviour in terms of biodegradation. Micropores can be described as pores having a diameter < 5 – 10 μm and the macropores as pores with a diameter > 100 μm[93,161]. Pore sizes between 10 and 100 μm are defined as mesopores[161]. Dense hydroxyapatite has been described as having a maximum porosity of 5 % by volume with the micropores measuring about 1 μm in diameter[160].

Micropores: diameter < 5 – 10 μm
Mesopores: diameter between 10 and 100 μm
Macropores: diameter > 100 μm
Dense: total volume of porosity < 5 %[160]

Table 2.9 The classification of porosity[93,161].

The degree of interconnectivity and the nominal pore size are the critical factors that determine the success of the implants. The large interfacial area required for the porosity is due to the need to provide a blood supply to the ingrowing connective tissues. White and Shors[162] reported that there is a relationship between pore size and the tissue elements that favours good bone ingrowth shown in Table 2.10. A pore size of less than 10 μm would prevent ingrowth of cells; a pore size of 15 to 50 μm would encourage the fibrous tissue ingrowth; a pore size of 50 to 150 μm would result in osteoid formation; and a pore size of greater than 150 μm would favour new bone formation.

Pore size	**Tissue elements**
< 10 μm	No tissue ingrowth
15 to 50 μm	No bone ingrowth, fibrous tissue ingrowth
50 to 150 μm	Osteoid and fibrous tissue ingrowth
> 150 μm	New bone formation

Table 2.10 The effect of implant pore size on tissue regeneration[162].

However, the pore size for new bone formation varies between reports and the optimal pore diameter may depend on the location of the defect to be filled[17]. Hulbert et al[163] particularly emphasized the importance of pore size and claimed that a minimum pore size of 100 μm is necessary for the porous implant materials to function well and a pore size greater than 200 μm was an essential requirement for osteo-conduction. Tsuruga[164] and co-workers have demonstrated that for sufficiently rapid growth of cells, a pore size of 300 – 400 μm is required. Holmes[165] similarly suggested that the optimal pore range is 200 – 400 μm with the average human osteon size of approximately 223 μm. Additionally, the porosity should be high enough to lower the Young's modulus to values comparable with those of bone[166]. If the porosity fails to match that in the host bone, then not only may larger vessels fail to penetrate the graft but also the finer vessels. Without blood and nutrition the tissue dies[39], inflammation ensues and the interfacial stability can be destroyed[8].

Although there are wide discrepancies regarding the optimal pore size for bone in-growth, a minimum pore size of 100 μm is extensively accepted[3,4] due to cell size, migration requirements and transport[5].

A number of groups[3,6,7,167] have suggested that the degree of interconnectivity is more essential than the pore size for bone formation. Tamai et al[158] proposed that the size of the interpore connections rather than the diameter of pores themselves might be the major limiting factor with respect to osteoconduction into the central area of implant materials. This is because interpore connections < 2 – 3 μm in diameter do not allow cell migration or vascularization into the pore, these events being essential for new bone formation. Additionally, Flautre et al[151] indicated that the ceramics with 130 μm mean interconnection sizes, which are the pathways between the pores and 175 – 260 μm mean pore sizes had the best osteoconduction results. Lu et al[6] detailed that in resorbable materials, porosity and the degree of interconnection are more important than their pore size, contrary to unresorbable materials in which the pore sizes and the porosities are equally important.

Although macroporosity has a strong impact on osteogenic outcomes, microporosity (pore size < 10 μm) and pore wall roughness play an important roll as well. Hydroxyapatite ceramic rods with average pore size of 200 μm and smooth and dense pore walls failed to induce ectopic bone formation in dogs, in contrast to rods made from the same materials with average pore size 400 μm but with rough and porous pore

walls[42]. Microporosity results in a larger surface area that is believed to contribute to higher bone-inducing protein adsorption as well as to ion exchange and bone-like apatite formation by dissolution and reprecipitation[42].

2.3.2.2 Mechanical Properties of Porous Calcium Phosphate Bioceramics

Although increased porosity and pore size facilitate bone ingrowth, the result is a reduction in mechanical properties. The mechanical properties of synthetic HA/TCP and all engineering ceramics are greatly dependent on the processing route as a consequence of the effects of processing on the microstructure of the final product. This dependency results from mechanical sensitivity to parameters, such as variations in the grain size, micropore size and micropore distribution[76]. However, the macroporosity appears to be the dominating factor in influencing the mechanical properties, particularly if the microstructure was uniform for all specimens. Bulk ceramics of calcium phosphate are strong in compression, weak in tension and not resistant to fatigue failure[160].

The strength of a material significantly depends on the portion of the total volume of the material occupied by the various pores. An equation relating the porosity to the strength of calcium phosphate was established by Ryshkewitch[168] in 1953:

$$\sigma = \sigma_0 e^{-BP}$$

in which:

σ = the strength of the porous material (Pa)

σ_0 = the strength of the dense material (Pa)

B = a constant

P = the porosity expressed as a fraction

The decrease in mechanical strength correlated with the increase in porosity. However, Duckworth[169] indicated that this relationship no longer held at high porosity in the order of 50 %.

In addition, Huec et al[156] designated that not only total porosity but also pore size could influence compressive strength. A large number of small pores were less likely to initiate failure than a small number of large pores. In materials with the same porosity,

those with the larger pore size may have lower mechanical strength. This relationship is expressed by the Griffith equation as below[170]:

$$\sigma = \left[\frac{2E\gamma}{\pi c}\right]^{1/2}$$

where

σ = Fracture stress (MPa)

E = Young's modulus

γ = Specific surface energy

c = Radius the crack length

2.3.3 Dissolution Rates of Calcium Phosphate Bioceramics

No material implanted in living tissue is inert. All materials induce a response from living tissue. Table 2.11[8] shows the four types of response which result in different means of achieving attachment of prostheses to the musculo-skeletal system.

Characters of the material	Response
Toxic	The surrounding tissue dies
Non-toxic and biologically inactive (almost inert)	A fibrous tissue of variable thickness forms
Non-toxic and biologically active (bioactive)	An interfacial bone forms
Non-toxic and dissolves	The surrounding tissue replaces it

Table 2.11 Four types of implant-tissue response[8].

Bioceramics can be divided into the following three categories by biodegradation rate: (Table 2.12)[67,171]

	Categories	**Example**
1	Nearly Inert	Alumina, zirconia
2	Surface bioactive	Sintered HA (s-HA) Bioglass Alumina-wollastonite glass ceramic (AW-GC)
3	Bioresorbable	Unsintered HA (u-HA) α- or β-tricalcium phosphate (α-TCP, β-TCP) Tetracalcium phosphate (TTCP) Octocalcium phosphate (OCP)

Table 2.12 Classification of bioceramics by biodegradation rate[67,171].

The concept of bioactivity was defined as: 'A bioactive material is one that elicits a specific biological response at the interface of the material which results in the formation of a bond between the tissues and the material'[172]. It is intermediate between resorbable and bioinert. Resorbable implants are designed to degrade gradually with time and be replaced with natural host tissues.

When degradation proceeds in bioresorbable materials, ions are released from the material, especially Ca and P. These released ions can diffuse into the surrounding tissues and stimulate osteogenesis[173]. For biodegradation purposes, the choice of bioceramics should be from category 3 (in Table 2.12). However, a very soluble ceramic might not be suitable for active resorption by osteoclasts since a large number of released calcium ions could inhibit osteoclast activity[174].

Thus, choices should be based on the different biodegradation rate of the materials for different tissue applications. The rate of biodegradation is in the following order: OCP > α-TCP > β-TCP > u-HA >> s-HA (OCP: Octocalcium phosphate; u-HA: Unsintered

HA; s-HA: Sintered HA). It is also affected by many other factors as shown in Table 2.13[67,175]. Sintered HA (s-HA) has a well-crystallized structure, which has little or no activity in terms of bioresorption[176]. Material aspects include the method of preparation, the resultant crystallinity and density and the extent of ionic substitutions into the apatite lattice. Some ionic substitutions such as carbonate have been shown to increase the solubility of apatite, while fluoride substitution into the apatite lattice decreases solubility. The degree of crystallinity affects the solubility behaviour of apatites. Poorly crystalline apatites have higher relative solubilities, while highly crystalline apatites tend to be very insoluble.

Increase biodegradation	**Decrease biodegradation**
Surface area increase	Fluorine ion (F^-) substitution in HA
Crystallinity decreases	Mg^{2+} substitution in β-TCP
Crystal perfection decreases	Decreasing β-TCP/HA ratios in biphasic calcium phosphate
Crystal or grain size decreases	
Ionic substitutions of carbonate ion (CO_3^{2-}), Mg^{2+}, Sr^{2+} in HA take place	

Table 2.13 The factors affect the rate of biodegradation[67,175].

Bioceramics of calcium phosphate can be produced either as permanent implants meaning that such implants will remain intact for at least five to ten years or as degradable implants, disappearing within a few months[160]. Degradable implants can be used for repair only, whereas permanent implants are suitable for both repair of bone and permanent augmentation.

The most widely studied[43,177] calcium phosphate bioceramics are HA and TCP. The clinical application of HA may be limited[147] because HA has been considered bioactive but non-biodegradable. The use of a rigid non-resorbable HA for skeletal reconstructions is associated with potential long-term interference with mechanical stress and strain in heavy load-bearing area.

Gatti et al[173] implanted HA granules (size: 0.9 – 1.2 mm) and TCP granules (size: 0.7 – 1.4 mm) in separate holes drilled in the mandibular bone of sheep and found TCP granules induce total repair of the hole after four months but HA granules crumbled and no new bone induction occurred even after 12 months. The authors declared the failure of the HA granules in the experiment was due to the low resorption rate and inadequate cohesive strength among the granules. Using another HA with a more suitable size and shape might give better results. A similar examination was made by Kurashina who implanted porous HA rods with or without the periosteum in rabbits and reported no formation of bone and calcified tissue in any of the specimens with HA alone[178].

β-TCP exhibits rapid degradation and weak mechanical properties, which have limited its application as a bone graft substitute, though it has good biocompatibility and osteoconductivity[179]. While some reports on biodegradable porous TCP alone implanted at extraskeletal sites suggest that degradation occurred quickly with no formation of bone[180,181], at least one study on implanted porous TCP found that the bone which formed during the initial stages was resorbed later on, so that bone repair after one year was not significantly enhanced[182].

An ideal bone grafting material should be replaced by the host bone. Resorption of the scaffold should ideally parallel bone ingrowth[12]. Hydroxyapatite (HA) ceramics are too stable[183] and tricalcium phosphate (TCP, Ca/P = 1.50) ceramics have low mechanical properties and biodegrade too fast for optimum bonding to bone *in vivo*[184].

Therefore, biphasic calcium phosphate ceramics combining the long-term stability of the HA and the high reactivity of the TCP have been recently developed and have shown better performance in living body than pure HA or pure TCP alone[3,82,90,174,185,186].

A recent *in vivo* study[174,184] indicates that the biodegradation rate of biphasic calcium phosphate (BCP) ceramics depends on the ratio of TCP to HA in the compound. The calcium phosphate ceramics containing a greater amount of TCP phase showed greater biodegradation. Other calcium phosphates such as α-TCP, tetracalcium phosphate (TTCP) and β-calcium pyrophosphate (β-CPP), though bioactive, have proven less useful as bone replacement materials due to excessively high resorption rates[187].

However, it has also been mentioned that osteogenesis also depends on the species of animal used[42,180,188]. Yang et al[180] implanted porous calcium phosphate ceramics in

several kinds of animals for up to 120 days and found an extensive amount of bone formed in dogs and pigs, but not in goats, rabbits and rats. This showed that osteogenic response varies among kinds of animals therefore these results might also be different to human. However, this might result from different loading and implant site.

Several studies[18,90] reported that mixing 60 % HA with 40 % β-TCP, combining the high reactivity of the β-TCP and the long-term stability of the HA, resulted in a material suitable for clinical application, i.e. a compromise between solubility and mechanical strength.

2.3.4 Granular Form of Calcium Phosphate Bioceramics

The attention of some groupe of researchers has focussed on porous calcium phosphate ceramic granulates. Various granules are widely used as filler or packing materials[70,116, 189]. The different forms of granular calcium phosphate include irregular multifaceted granules and round smooth granules, with solid or porous structures. However, the behaviour of granules in the body depends on their morphology and microstructure. Irregular morphology causes non-desirable inflammatory reactions from the body tissues or the bone formation may be slower, so the granules with a smooth geometry are superior[70].

TCP, HA and biphasic TCP/HA granules have been used as bone defect fillers with complete healing of the defects[96,114,116,173,190-192], especially when mixed with human bone or marrow[190-192]. Calcium phosphate granules can also be impregnated with a drug, e.g. antibiotics, antimicrobial agent, growth factor etc. and used as a system for targeted and drug delivery[115].

A number of studies have reported the development of calcium phosphate granules by various techniques such as crushing sintered blocks[193], hydrothermal conversion of natural corals[194,195], dripping[189], drip casting[196], gelcasting[197] and stirring mixtures of immiscible liquids[70,115,198]. Table 2.14 summarises the characterisation of granules developed by the various methods as reported in the literature. Granules made by crushing sintered blocks have irregular shape ands sizes. Further sieving and milling procedure are needed to obtain suitable sizes and a more regular shape. This increases the complexity of the process and wastes much of the material. Granules made by dripping, drip casting, gelcasting and stirring mixtures of immiscible liquids methods

have good shapes which are spherical or near-spherical in form. Most of these granules exhibited a controllable porosity and porous character. However, the porous network of these granules is not highly interconnected. Although, some authors stated the porous network of these granules is highly interconnected, this may only appear in samples with high porosity and the mechanical strengths may be insufficient.

No.	Materials	Forming methods	Pore-creating medium	Pore size / Porosity	Granular size / shape	Ref.
1	Dense HA	Crushing sintered blocks	–	–	105 – 150 μm / irregular	193
2	Calcium phosphate	Dripping in liquid nitrogen	Stirring with organic binder	30 – 230 μm / 71 – 57%	1600 – 3000 μm / spherical	189
3	HA	Drip casting	PVB	95 – 400 μm / 24 – 76%	700 – 4000 μm / spherical or near-spherical	196
4	HA	Gelcasting into a spherical-shaped mould	PVC	10 – 40 μm / –	2200 μm / spherical	197
5	HA	Stirring mixtures of immiscible liquids (vegetable oil)	Bovine gelatin	3 – 6 μm / 30 – 45%	50 – 2000 μm / spherical	115
6	Hydroxyapatite and fluorhydroxyapatite	Stirring mixtures of immiscible liquids (vegetable oil)	Bovine gelatin	1 – 6 μm / 43 – 62%	50 – 200 μm / spherical	198
7	HA	Stirring mixtures of immiscible liquids (paraffin)	Chitosan (a deacetylated product of chitin)	1 – 30 μm / –	212 – 1000 μm / spherical	70
8	HA	–	–	300 – 500 μm / –	900 – 1200 μm / –	173
9	Tricalcium phosphate	–	–	200 – 400 μm / 60%	700 – 1400 μm / –	173

Table 2.14 Granules made by various methods.

In summary, there is an increasing interest in the development of synthetic bone substitute materials. Calcium phosphate based ceramics with a porous configuration are attractive for use as synthetic bone grafts as the porous network allows tissue ingrowth, which further enhances the implant-tissue attachment. The degree of interconnectivity

and the nominal pore size are the critical factors that determine the success of the implants. The aim of this study was to produce open pore HA/TCP blocks and granules with connected porosity combined with good mechanical properties. The characterisation of granules developed by the various methods as reported in the literature has been reviewed earlier in this section. The development of porous blocks will be reviewed in the following section.

2.4 Fabrication Methods for Porous Calcium Phosphate Bioceramics

The creation of a porous structure relating the pore size, shape and distribution, and their relative orientation, is one of the most important problems of biomaterial engineering. A number of papers have reported methods for the preparation of porous ceramics. The three main methods are discussed in the following sections.

2.4.1 Organic Particle Embedding Technique

The first method is an organic particle embedding technique, which is based on admixing foreign combustible organic materials that are sacrificed during firing, leaving free spaces and void in the resulting body. These embedded organic particles must have lower burn-out temperatures than the ceramic sintering temperature. Polymers such as polyvinyl chloride[199], polyvinyl butyral (PVB)[141,196,197,200-202], polyvinyl polyacrylate (PVC)[203], naphthalene[82], polyethylene glycol (PEG)[204,205], polymethylmethacrylate (PMMA)[17,151,206], polybutylmethacrylate (PBMA)[207], acrylic beads and carbon fibre[208] have been used. Table 2.15 summarises the forms of porous ceramic made by the organic particle embedding method as reported in the literature.

No.	Materials	Pore-creating medium	Forming methods	Macro pore size/ Porosity	Mechanical strength	Ref.
1	HA	Polyvinyl butyral (PVB): 0.188 mm (24 – 62 vol%)	Slip casting	160 – 200 μm / 32 – 78%	10 – 40 MPa (3-point bending)	202
2	HA	Polyvinyl butyral (PVB): 0.093 mm, 0.188 mm and 0.42 mm (42 – 61 vol%)	Die-press: 27 MPa	45 – 78%	2 – 36 MPa (Compressive strength)	201
3	HA	Polyvinyl butyral (PVB)	Gelcasting	10 – 40 μm	–	197
4	HA	PVC: > 100 μm: 20 wt%	Slip casting	100 μm / 40%	–	203
5	HA	Polymethylmethacrylate PMMA	Not-specified	175 – 435 μm / 61 - 66%	–	151
6	HA	Flour	Isostatic pressing	> 100 μm / 28 - 46%	–	209
7	Calcium phosphate	Naphthalene	Isostatic pressing	–	10.9 MPa (Compressive strength)	82
8	Tricalcium phosphate	PMMA 210 – 250 μm	Slip casting	190 μm 65, 75 and 85 %	–	17
9	Calcium silicate ($CaSiO_3$)	Polyethylene glycol (PEG)	Die-press: 14 MPa	125 – 500 μm / 41.28-73.6%	4.92 – 65.21 MPa (Compressive strength)	204

Table 2.15 Porous ceramics made by the organic particle embedding method.

HA, calcium phosphate, tricalcium phosphate and calcium silicate materials are presented in this table. The organic particle embedding method allows control over the size and shape of the pores[141,200,201,203] and porosities by changing the size, shape and volume fraction of the embedding organic particles. Most of the macropore sizes give in Table 2.15 are larger than 100 μm which is the suitable size for bone ingrowth. Only sample No. 3 has a smaller pore size. However, this method was not regarded as satisfactory because it does not ensure a uniform distribution of pores in the ceramic body, especially when organic powders reside in the discrete pockets after mixing with the ceramic powders and do not provide any control over the interconnectivity[210]. Undesirable isolated pores and blind ends are common in implants manufactured with the organic particle embedding technique[39,148].

Furthermore, this method commonly utilizes uniaxial or isostatic compaction in samples No. 2, 6, 7 and 9. This forming method limited the resulting sample to simple geometric forms[17, 202].

Many of these studies do not provide information concerning mechanical strength or do not have details of poresize and porosity so it is difficult to analyze the mechanical characteristics of samples made by this method.

2.4.2 Foam Generation in a Slip

This method was patented by Sundermann and Viedt[211] in 1973 and involves introducing gas bubbles into a slip. The bubbles can be formed either by chemical reaction (water and carbon dioxide[108,212-214]), mechanical frothing[117,125,215], stirring with H_2O_2 solution[180,216] or adding Freon (CCl_3F)[121,123] as the foaming agent. The boiling point (23.8°C) of Freon is less than that of water and it is relatively insoluble in water. Thus, it can be dispersed in water as liquid droplets and later heated above its boiling temperature to induce foaming by its vaporization. In most cases the addition of a surfactant is required to stabilise the presence of bubbles. Table 2.16 lists the range of porous ceramics that can be made by the method of foam generation in a slip.

No.	Materials	Pore-creating medium	Macro pore size / Porosity	Mechanical strength	Ref.
1	HA	Chemical reaction CO_2 and H_2O	– / up to 62%	–	214
2	HA	Chemical reaction CO_2 and H_2O	– / 5 – 60%	–	212
3	HA	Mechanical frothing Stirred at 1200 rpm	– / < 85%	–	215
4	Calcium phosphate	Chemical reaction CO_2	100 μm / 39 – 56%	1.2 – 15 MPa (Compressive strength)	108
5	Calcium phosphate	Stirred with H_2O_2	402 μm / 61%	–	180
6	Apatite	Stirred with H_2O_2	–	–	216
7	Alumina	Mechanical frothing Foaming agents (Triton X114 and Tween 80)	30 – 600 μm / 70 – 92%	2 – 26 MPa (3 point bending)	125
8	Silica	Adding freon (CCl_3F)	90 – 400 μm / 50 – 86%	0.4 MPa (porosity: 86%) 9 MPa (porosity: 67%) (3 point bending)	121
9	Silica and mullite	Adding freon (CCl_3F)	~ 1000 μm / 83%		123

Table 2.16 Porous ceramics made by the foam generation into a slip method.

Specific information on pore size achieved in HA made by this method is not available but the pore size in other ceramics seems to be quite large. Only sample No. 2 has a low and wide range of porosity. Although high levels of porosity can be obtained by this foam generation method, the distribution of macroporosity is not homogeneous and the average pore volume is not well controlled as some bubbles may shrink and disappear whilst others may coalesce to form larger bubbles. Furthermore, connectivity obtained with such structures is poor when compared to the volume of the pores[82]. The mechanical strength of calcium phosphate made by this method is not comparable with those of samples made by other methods as there is no data on mechanical strength of HA and only one piece of datum on calcium phosphate.

2.4.3 The Replication of Reticulated Porous Structures

An early patent by Schwartzwalder and Somers[217] described the polymeric-sponge method. This technique has been known for more than 40 years and seems to be the most popular method employed to produce open-cell porous ceramics.

The technique involves coating reticulated polymeric foams or natural sponges of desired cellular structure by ceramic slip. The ceramic impregnated foam is dried to remove the slip liquids. After drying, the foam is heated slowly to sinter the ceramic material. During the thermal treatment, the polymeric skeleton burns out, leaving a porous ceramic. The method is via the replication of reticulated porous structures, which act as polymeric substrates[20,97,120,131,136,137,150,218-229] or coral exoskeleton[147, 230].

The starting point of the coral replamine process is to choose a suitable coral. The dimensions of pores vary from species to species. The natural coral structure can be shaped to into the desired final ceramic geometry. The coral structure is then filled with wax and the wax allowed to harden. Hydrochloric acid is used to leach out the coral phase, which is usually calcium carbonate ($CaCO_3$), before the structure is re-impregnated with the desired ceramic slip. The advantage of this method is that the coral is mechanically strong and quite easy to machine to the desired shape before the wax impregnation process begins. However, the coral replamine process requires natural coral from the ocean as the starting replica material and the processes are complex, making this method industrially and environmentally unfavourable[206].

Tancred et al[159] used a similar method to replicate the macrostructure of cancellous bone. This involved a multistage process requiring the manipulation of positive and negative forms of the inorganic matrix. By infiltration of a wax negative mould of cancellous bone with a ceramic slip, followed by burn out of the wax leaving porous ceramics, a bioceramic, which was a positive replica of the original cancellous macrostructure, was produced.

Reinforced calcium phosphates have also been manufactured by coating the calcium phosphate ceramics onto alumina[224] and zirconia[97] foams, which were fabricated by the polymeric sponge method. Table 2.17 shows porous ceramics made by the replication of reticulated porous structures method as reported in the literature.

No.	Materials	Foam	Macro pore size / Porosity	Mechanical strength	Ref.
1	HA	Polyurethane	150 – 400 μm / 36 – 80 %	0.2 – 18 MPa (Compressive strength)	150
2	HA	Polyurethane	200 – 400 μm / ~ 71%	~5 MPa (Compressive strength)	228
3	HA	Polymer foam	190 – 230 μm / 70 – 80%	1 MPa (Flexural strength) 2 MPa (Compressive strength)	220
4	β-TCP/HA	Polyurethane	300 – 400 μm / 73%	9.8 ± 0.3 MPa (Compressive strength)	218
5	Calcium phosphate	Polyurethane	500 ~ 600 μm / 65 – 90%	0.3 ~ 3.3 MPa (Compressive strength)	223
6	Calcium metaphosphate	Polyurethane	200 μm	–	20
7	Calcium phosphate	Polyurethane	1000 μm / ~ 70%	2 – 12 MPa (Compressive strength)	219
8	TCP	Polyurethane foams	300 – 800 μm / 70%	6 ± 3 MPa (Flexural strength) 11 ± 3 MPa (Compressive strength)	208
9	Carbonate hydroxyapatite	Natural cellulose sponges	> 100 – 200 μm / 45%	6.0 ± 0.5 MPa (Compressive strength)	56
10	Calcium phosphate (10 – 20 μm) coating on porous alumina	Polyurethane	~ 800 μm / 80%	~ 6 MPa (Compressive strength)	224
11	Calcium phosphate (30 μm thickness) coating on porous zirconia	Polyurethane	~ 600 μm / 74 – 92%	1.6 – 35 MPa (Compressive strength)	97
12	Alumina	Polymeric foam and PVA	1000 – 2000 mm / 86%	1.3 MPa (Compressive strength)	227
13	SiC	Polyurethane	–	2.33 MPa (3 point bending strength)	131

Table 2.17 Porous ceramics made by the replication of reticulated porous structures method.

A variety of polymer foams materials are suited to this method. These reticulated porous substrates should volatilise at a temperature below that required for sintering the final ceramic and not leave any toxic products. Some of the polymer materials, which can satisfy the requirement, are polyurethane, cellulose, polyvinyl chloride, polystyrene and latex[124,139]. The low softening temperature of polyurethane makes it particularly attractive as a reticulated porous material[139]. The polyurethane foam readily softens and burns off while it is heated to volatilise, thereby relieving any thermal stress, which might disrupt the unsintered ceramics[231].

The replication of reticulated porous structures method is the most common approach for producing ceramics with interconnected pores. The porous ceramics obtained from reticulated polymer substrates potentially have a range of unique properties such as controllable pore size, uniform pore structure and the ability to produce complex ceramic shapes for different applications[150].

In addition, slip methods enable the attainment of higher packing density values and thereby the development of reliable green ceramics with optimal properties[232-238]. Toriyama et al[239] reported that the flexural strength of the sintered body formed by the slip casting method is about 50% higher than that of die-pressed sample. However, most researchers have made porous ceramics using this method by coating only the walls of the polymer foams. The resulting porous ceramics would be a positive image of the polymeric foam material and have a high level of porosity. The space occupied by the foam remains as an internal defect in the ceramic body thus the ceramic parts of the structure would be hollow[122] and the strengths were reduced significantly[228,240].

Furthermore, several researchers[120,122,222,225,241-243] mentioned the presence of cracks in the cellular struts or even collapse during the sintering stage. These cracks are expected to decrease the mechanical properties drastically. Brown and Green[222] identified that the primary cause of the cracking is thermal expansion differences between the ceramic coating and the polymer substrate at temperatures slightly below the melting point of the polymer. Han et al[225] reported that the sudden removal of the polymeric foams and the impact of large volumes of gas produce cracks and this could be avoided by increasing the viscosity of slurry and decreasing heating rate.

The advantages and disadvantages of the three methods for the preparation of porous ceramic are summarized in Table 2.18. Generally, the deficiencies of these methods are described as follows: Methods 1 and 2 cannot produce samples with interconnected

porosity especially for samples with low porosity. Method 3 can only produce samples with high porosity and low mechanical properties.

Method	Advantage	Disadvantage
1. Organic particle embedding technique	Control over the size and the shape of the pores Control over the macroporosity	Do not ensure a uniform distribution of pores in the ceramic body Do not provide any control over the interconnectivity Limited to simple geometric forms
2. The production of gas bubbles	High levels of macroporosity can be obtained Controlled geometry	The distribution of macroporosity is not homogeneous Do not provide any control over the interconnectivity Do not allow a precise control of pore size shape and porosity
3. The replication of porous structures	Control over the interconnectivity Controllable pore size The ability to produce complex ceramic shapes for different applications	Most porous ceramics manufactured using this method, coat only the walls of the polymer foams resulting of number of cracks and hollow struts. Poorer mechanical properties are a typical characteristic of this method and this may restrict possible heavy load-bearing clinical applications.

Table 2.18 Advantages and disadvantages of the three main methods for the preparation of porous ceramics.

Recently, porous HA with a designed connection pattern and controlled channel size was developed by Chu et al[148,149]. The method involved casting a HA suspension onto a negative epoxy mould which was built by stereo lithography technique. The mould was removed by pyrolysis. The channels created in the sintered HA ceramics were between 366 μm and 968 μm in diameter and the porosity was between 26 % and 52 %. A similar method was used by Charriere et al[244]. More details of polymers and ceramics scaffolds with designed 3D architecture are published by a number of authors [245-247]. This method seems to have advantages. However, the procedures are quite complex.

As can be seen from the review of this literature, many authors have been striving to make porous calcium phosphate. Two major kinds of porous calcium phosphate have been produced. The first is produced by organic particle embedding or the production of gas bubbles methods. The main authors are Liu[141,196,200-202], Arita[212-214], Wilkinson[212-214], Castano[212-214] and Binner[117,125,215] etc. Controllable size, shape or macroporosity of pores are the advantages of these samples. However, the difficulty of controlling the interconnectivity is the fatal drawback of these samples. This will be unfavorable for bone ingrowth. The other type of porous calcium phosphate is produced by the replication of porous structure method which is used by Ramay[218,228], Zhang[218, 228], Hong[223,224], Jun[223,224] and Celotti[56,220] etc. The main advantage of the resulting samples is that they have highly interconnected porosity which is beneficial for bone ingrowth. However, poor mechanical properties are the typical deficiency of this method.

It would appear from reviewing the literature that porous calcium phosphate which combines interconnected porosity and high mechanical properties which can be used in the heavy load-bearing applications has not been reported. A range of calcium phosphate ceramics have been produced using a diversity of methods but they all still have deficiencies.

The main aim of this research project is therefore to develop a novel method, based on the replication of porous structure method to produce porous calcium phosphate with interconnected porosity and improved mechanical properties. The details will be given in the following chapter.

2.5 Experimental Background of Mechanical Testing as Applied to Ceramics

Each newly developed biomaterial needs to be mechanically tested to ensure its functionality and reliability. For ceramics, their mechanical properties are more variable than metals, as mechanical properties depend heavily on the microstructural defects associated with the manufacturing process[109]. The conventional methods of mechanical characterization for bioceramics including flexural stregth testing, work of fracture (Tattersall-Tappin testing), compressive testing and die-plunger testing will be described in the following sections.

2.5.1 Flexural Strength Testing

Tensile testing can be one of the most accurate methods for measuring mechanical properties, provided that force is applied without inducing a coupled bending moment. However, tensile tests for brittle materials are very complicated in practice due, in particular, to the difficulty of preparing tensile testing specimens. Researchers have resorted to the use of the well know flexure test as it is a low-cost, simple, versatile method of measuring the tensile strength of an engineering ceramic[248].

Flexural testing is one of the most traditional and common methods to measure the strength of a brittle ceramics[249], as it requires only a simple specimen and loading jigs are readily available[250].

Flexure causes tensile stresses on one side of the sample and compressive stresses on the other, so in a bending test, failure usually occurs on the tensile side of the specimen and the test accentuates the influence of surface flaws on strength. The samples cross sections is usually rectangular, square or circular but sometimes, trapezoidal or triangular[248].

Flexural testing can be applied using either three-point or four-point loading (Figure 2.5) [248].

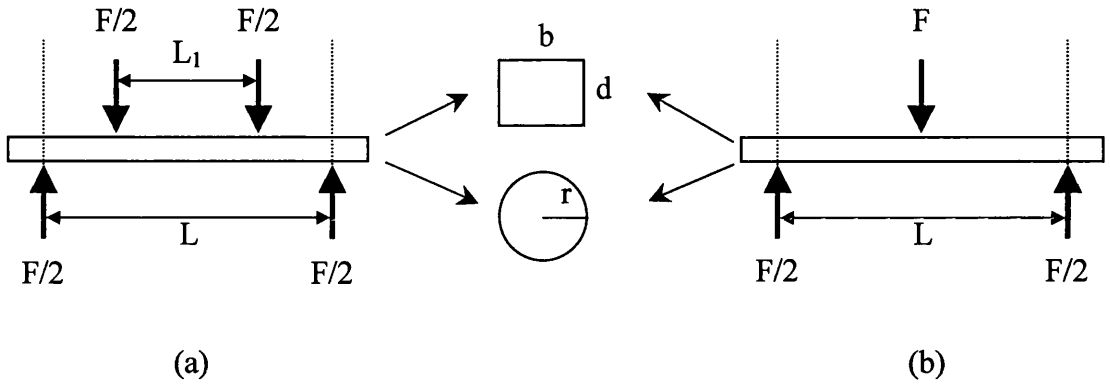

Figure 2.5 Schematic of (a) four-point bend (b) three point bend apparatus.

The advantage of three-point bending is its simplicity but it has the disadvantage of creating high shear stresses near the midsection of the sample. The maximum flexural stress is at the point of load application but linearly decreases to zero at the outer supports. The result is from a relatively small region of samples[251].

Four-point bending is often preferable to three-point bending since it tests a large region of sample between the inner supports that is a result of that material being exposed to the maximum flexural stress and produces pure bending between the two upper loading points, which ensures that transverse shear stresses are zero and gives a better characterisation of the material's strength[248]. However, four-point bending requires that force at each loading point be equal so requires some care in specimen preparation and the test execution to obtain results with low errors. The results of three-point and four-point bending testing for the same materials are usually different due to nature of the test.

The separation of the roller supports is dependent on the size of the samples being tested. Ideally, the supports should be as far apart as possible. According to ASTM standard D 790M-82, the span of the specimen (L) must be long enough to guarantee an accurate test. Such samples should have a length to thickness ratio (L/d) of at least 16. If L is very short, much of the displacement induced by loading will be due to shear stresses and not bending. This causes the measured displacement to be greater than the flexural displacement, resulting in an overestimation of strain and an underestimation of Young's modulus. However, the samples also needed to be thick enough to avoid

having pores which cover a significant fraction of their cross section. In addition, the relatively fragile nature of the porous ceramics make cutting them risky. Based on these reasons, Martin et al[92] suggested the samples could be thicker in proportion to their length than the ASTM standard which is the most pertinent variable. A summary of existing standards for flexure tests is shown in the Appendix A.

The strength of three or four point-bending test with rectangular or circular bars can be determined from the equations in Table 2.19.

		M	y	I	$\sigma = My/I$
3 point bending	Rectangular	FL/4	d/2	$bd^3/12$	$3FL/2bd^2$
	Circular	FL/4	r	$\pi r^4/4$	$FL/\pi r^3$
4 point bending	Rectangular	$F(L-L_1)/4$	d/2	$bd^3/12$	$3F(L-L_1)/2bd^2$
	Circular	$F(L-L_1)/4$	r	$\pi r^4/4$	$F(L-L_1)/\pi r^3$

M = maximum bending moment
F = applied force
L = the span of the support loaders
L1= the separation of the loading span
y = distance from the neutral axis of specimen to outer fibers
b = specimen width
d = specimen thickness
r = specimen radius
I = moment of inertia of cross section
σ = bending stress

Table 2.19 Parameters for three- and four- point bending tests.

Table 2.20 gives an overview of the bending strengths measured by a number of groups for calcium phosphate ceramics. The high variation of these bending strengths might result from the different forming methods of various authors. The pore sizes of these porous calcium phosphate ceramics are quite large and the porosities are high but the bending strengths are low. Almost all of the bending strengths of porous calcium phosphate ceramics are below 11 MPa. The highest bending strength of porous samples is ~ 40 MPa but the pore size is not clear.

Material	Bending strength (MPa)	Test conditions	Ref.
HA Dense	25 – 65 MPa	4 point bending	81
HA Dense	96.4 – 152.7 MPa	4 point bending	239
HA Dense	16.5 MPa	4 point bending 48 mm	252
HA Dense	43 MPa	4 point bending Span: 30 ×10 CS: 0.5 mm/min	253
HA Dense	40 – 60 MPa	3 point bending SD: 30 × 6× 5mm Span: 26 mm CS: 0.5 mm/min	254
HA Dense	69 ± 5 MPa 84 ± 5 GPa (Young's modulus)	4 point bending SD: 50 × 8 ×5 mm Span: 25 × 11mm CS: 0.5 mm/min	236
HA Dense	61 – 113 MPa	3 point bending 2 × 4 mm (cross-section) Span: 15 mm CS: 0.5 mm/min	255
HA Dense	28 ± 7 MPa	4 point bending Span: 20 × 10 mm CS: 5 mm/min	256
Calcium phosphate Dense	115 MPa	3 point bending SD: 15 × 3 × 1 mm Span: 12 mm CS: 0.105 mm/min	154
HA (reinforced with Ti particles)	78.59 MPa	3 point bending	257
Calcium phosphate (reinforced with fibers)	12 – 25 MPa	3 point bending Span: 20 mm CS: 1 mm/min	107
HA Porosity: 32 - 78%	10 – 40 MPa	3 point bend SD: 5 × 8× 50 mm CS: 0.5 mm/min	202
TCP Pore size: 300 – 700 µm Porosity: 55 ± 6%	11 ± 3 MPa	3 point bending Span: 30 mm SD: 50 × 5 × 5 mm CS: 0.5 mm/min	208
HA Pore size: 190 – 230 µm Porosity: 70 – 80%	1 MPa	–	220
HA Pore size: 100 – 250 µm Porosity: 60 – 90%	5 – 10 Mpa	3 point bending	210

TCP Pore size: 300 – 800 μm Porosity: 70 ± 4%	6 ± 3 MPa	3 point bending SD: 50 × 5 × 5 mm Span: 30 mm CS: 0.5 mm/min	208
HA Pore size: 200 – 400 μm Porosity: 95%	3.5 ± 0.15 MPa	3 point bending	258
β-TCP Pore size: 100 – 300 μm Porosity: 75%	5 ± 0.15 MPa	3 point bending	258
SD: Specimen dimensions, CS: Crosshead speed			

Table 2.20 The bending strengths for dense and porous calcium phosphate.

2.5.2 Work of Fracture (Tattersall-Tappin Testing)

Research in fracture mechanics has long been of major interest to the materials scientist and structural engineer. It is also of interest to those in the field of medicine and bioengineering. In 1966 Tattersall and Tappin[259] proposed to use the quantity defined as "the work of fracture" from the testing of notch bend specimens for estimating the fracture toughness of various materials. This method is a modification of the work by Nakayama in 1965[260] and required loading Chevron-notched specimens in three-point bending at a constant deformation rate. Work of fracture, which quantifies the ability of materials to resist fracture, is a property of fundamental importance in brittle materials and has been suggested as a possible comparator.

Most brittle materials fracture catastrophically when deformed in three-point bending. However, when a sufficiently sharp notch is present the specimen is so much weakened that the total stored energy becomes small compared with the surface energy required to break the specimen.

The specimen shape most commonly used in this series of experiments is shown in Figure 2.6. It is a square bar containing two cuts to reduce the square cross-section to an isosceles triangular cross-section in the centre of the test piece. This shape allows the more ductile materials to be tested because a sharp crack grows from A, the apex of the triangular cross-section, before very much plastic flow take place.

The apex A of the triangular cross-section is placed in tension, thus causing a crack to initiate due to the extremely high stress concentration. A crack initiates from the apex A before sufficient elastic energy is available to break the specimen completely. The increasing cross sectional area through the thickness of sample prevents rapid catastrophic fracture and the crack is slowed down thereby and travels at controlled speed, at a rate governed by the cross-head speed of the testing machine.

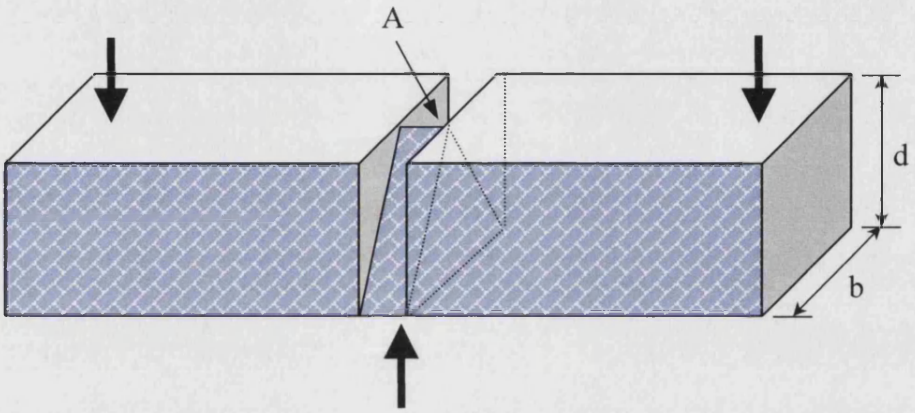

Figure 2.6 Schematic diagram showing the shape of sample used to measure the work of fracture and the method of loading.

A classic load-displacement curve for the Tattersall-Tappin test is in Figure 2.7. It can be seen that as the load increases, the specimen and testing machine store elastic energy which is equal to the area under the load-displacement curve (AB). When a crack is generated the load falls, the specimen and machine begin to lose their stored strain energy (BC). The region BC corresponds to rapid crack extension, as the stored energy is lost. This is because initially the rate of strain energy release is greater than the energy require to generate the new fracture surface[261]. After a crack has been generated, it continues to grow in a controlled manner (CD). There is insufficient stored elastic energy in the specimen-machine system to totally fracture the specimen, so the crack propagation is then controlled by the strain rate (or cross-head speed) of the machine.

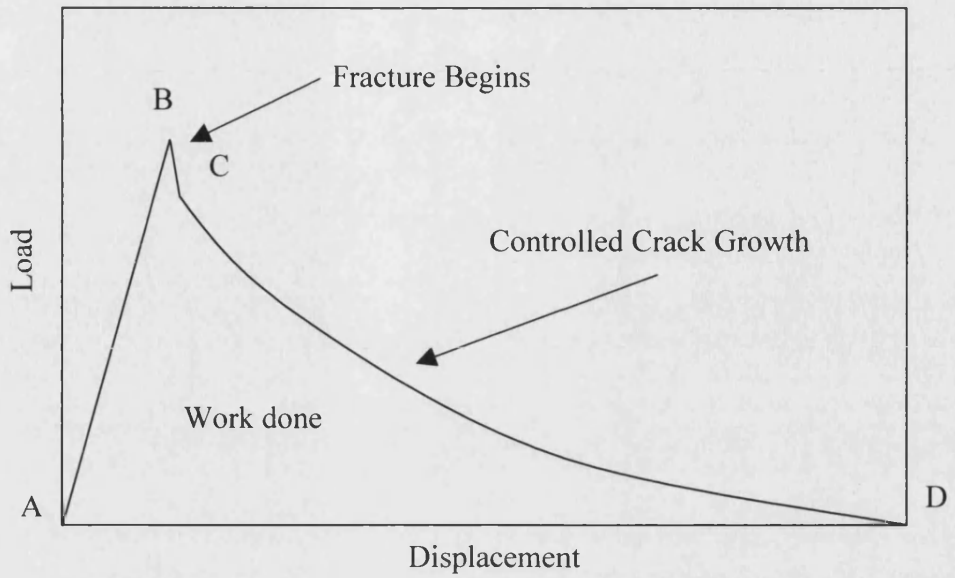

Figure 2.7 Load-displacement curve for a Tattersall-Tappin test.

Work of fracture (γ_{wof}) is calculated by the equation:

γ_{wof} (J/m^2) = W/2A (Nm/m^2)

where

W(work done) is the area under the load-displacement curve,

A is the area of the crack face (projected cross-section area of the fracture surface)

Although the test procedure is simple, many different test conditions and suggestions have been reported. According to these results, not only specimen sizes but also the depths of notch might affect the values of work of fracture.

Tattersall and Tappin[259] investigated the effects of specimen size and discovered that doubling the specimen size caused a 6 % increase in work of fracture. Rogers and Moyle[262] used the Tattersall and Tappin test method to determine the work of fracture for different specimen sizes of Plexiglas, bovine tibial bone and aluminium and found work of fracture was dependent on specimen area for bone but independent of specimen area for aluminium and Plexiglas®.

Davidge and Tappin[263] determined the work-of fracture for various brittle materials, using a notched beam fractured in three-point bending as shown in Figure 2.8. In this study, they reported that the work of fracture values decrease with increasing notch depth ratio(c/d).

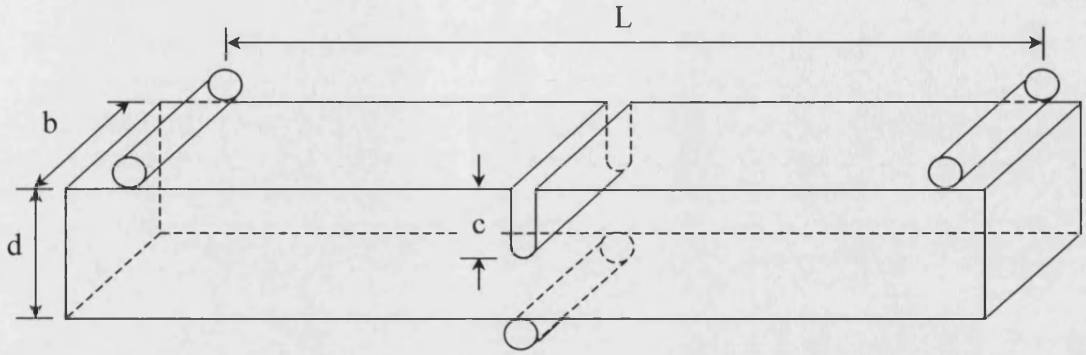

Figure 2.8 Schematic diagram showing the notched sample used by Davidge and Tappin[263].

A similar observation was made by Simpson[264] testing alumina specimens with altered notch geometry in the Tattersall and Tappin configuration. Figure 2.9 displays the effect of varying the notch geometry on load-deflection curves. As deeper notches were used, the proportion of stable propagation increased. The apparent fracture energy decreases until a minimum value, which corresponds to completely stable fracture, is reached. The author affirmed that to obtain meaningful results from a Tattersall-Tappin test, completely stable crack propagation is required. If this theory is tenable, that means the aspect ratio of the base to the height (h/w) of specimens had to be extremely low and most research groups have not followed the theory in the Tattersall-Tappin test.

Although some variable parameters may affect the results of the Tattersall and Tappin test, this method has been accepted as a means to estimate the fracture toughness of various materials especially brittle materials. There are not many available results for work of fracture for calcium phosphate in the literature. Table 2.21 shows the work of fracture for various materials. The only data on calcium phosphate based ceramics are HA reinforced with Ti particle and calcium phosphate reinforced with fibres. However, their values of work of fracture are significantly different, probably due to the different types of reinforcment.

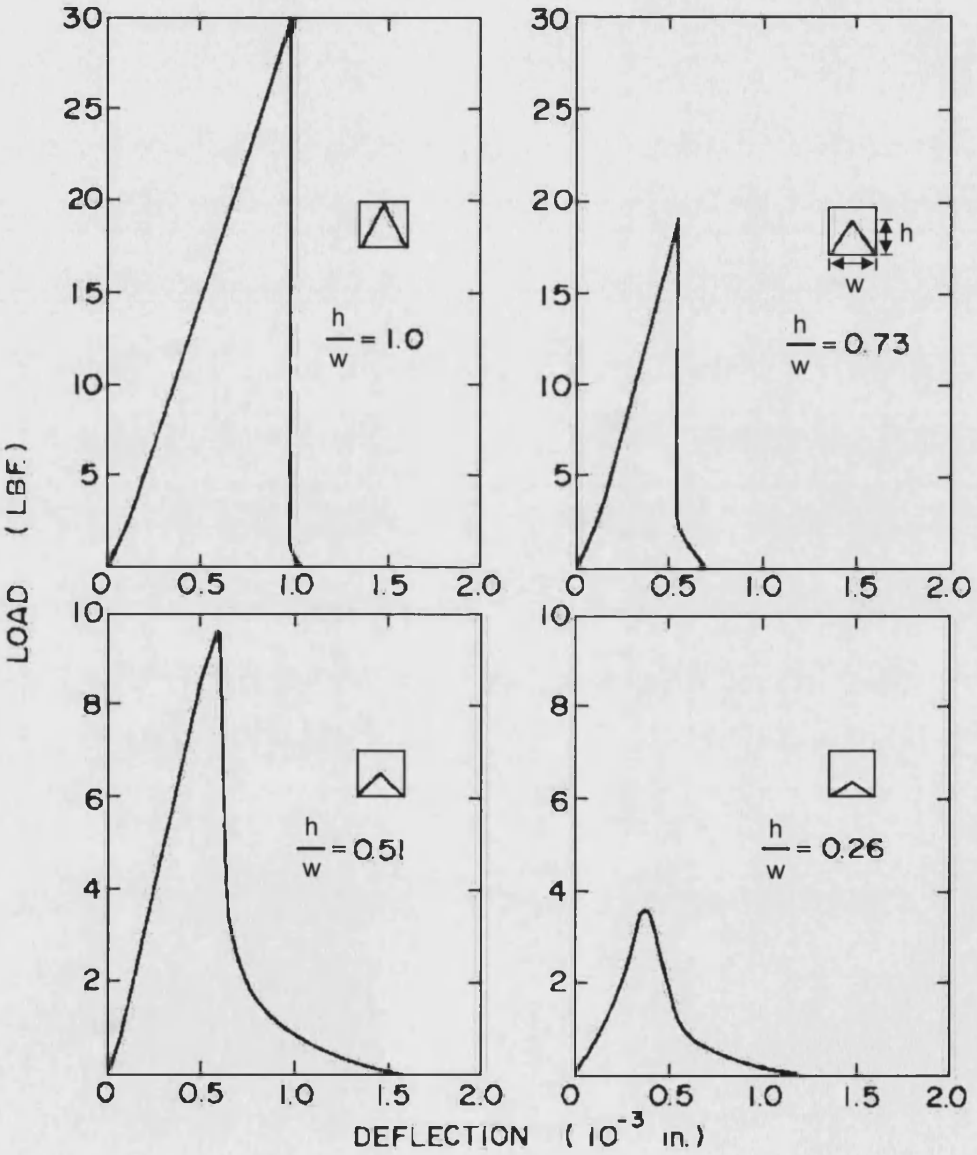

Figure 2.9 Typical load-displacement curves as a function of notch configuration for alumina specimens in the Tattersall-Tappin tests completed by Simpson[264].

Material	Work of fracture	Test conditions	Ref.
Bovine femur	$5.9 - 6.25 \times 10^4$ J/m^2	Slow strain rate	265
	9.6×10^2 J/m^2	High strain rate	265
Bovine tibiae	$9.72 \pm 1.93 \times 10^3$ J/m^2	Area 5.89 – 11.7 mm^2	262
	$5.48 \pm 1.79 \times 10^3$ J/m^2	Area 3.48 ± 0.68 mm^2	262
HA (reinforced with Ti particles)	12.8 J/m^2	Un notch	257
Calcium phosphate (reinforced with fibers)	$1.5 - 3.5 \times 10^3$ J/m^2	Un notch	107
Alumina	11.5 – 36.2 J/m^2		264
Alumina	40 J/m^2		259
Silicon nitride Dense	70.2 J/m^2	Span: 30 mm 0.01 mm/min	132
Silicon nitride Porosity: 24%	492.7 J/m^2	Span: 30 mm 0.01 mm/min	132
Firebrick	20 – 70 J/m^2		259
Beryllia	20 J/m^2		
Magnesia	10 J/m^2		
Reactor graphite	1×10^2 J/m^2		
Cellulose	2×10^3 J/m^2		
Deal wood	2×10^3 J/m^2		
Teak wood	6×10^3 J/m^2		
Polystyrene	1×10^3 J/m^2		
Toughened polystyrene	4×10^3 J/m^2		
Plexiglas	$6.20 \pm 0.074 \times 10^2$ J/m^2		262
Cast iron	4×10^3 J/m		259
Brass	3×10^4 J/m^2		
Key steel	5×10^4 J/m^2		
Copper	5×10^4 J/m^2		
Aluminium	$5.98 \pm 13.7 \times 10^4$ J/m^2		262
Dural	1.4×10^5 J/m^2		259

Table 2.21 The work of fracture values for various materials.

2.5.3 Compressive Testing

The conventional methods of mechanical characterization such as tensile and impact testing cannot usually be applied to porous brittle materials due to the difficulty of machining and gripping samples. Instead, the compression test has been widely accepted and used successfully for characterization of porous ceramics.

Some factors could affect the results for compressive testing. The most important factor is the specimen should be aligned with the loading platen. However, it is hard to achieve this goal due to the difficulty for preparing the specimen with two perfectly flat and parallel faces. Samples are often misaligned with the loading platen. This produces a large stress concentration at one edge of the sample causing an underestimation of both Young's modulus and strength. A device shown in Figure 2.10[266] can be employed during the compressive testing to reduce this problem. The placement of a pivoting platen in the load train can reduce misalignment errors[49].

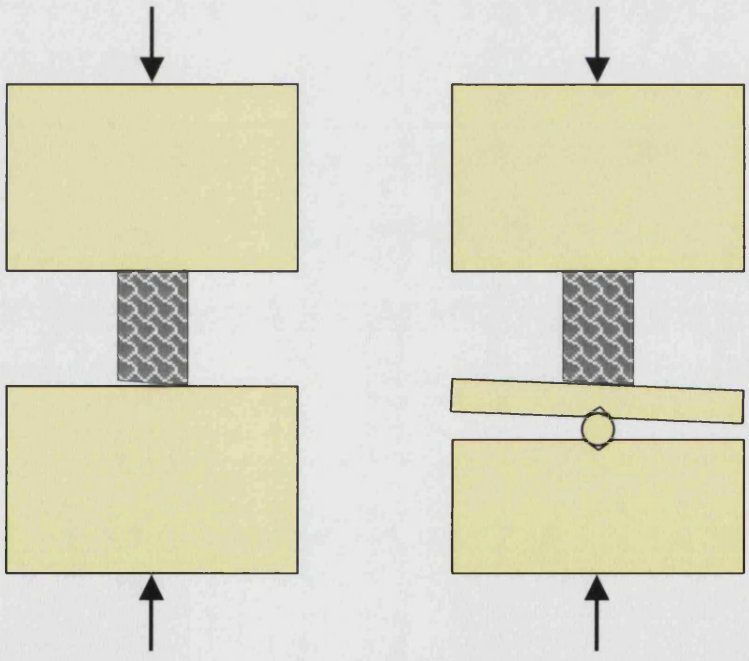

Figure 2.10 Compressive test of a specimen. (a) the loading platens are slightly misaligned with sample. (b) a pivoting platen is incorporated into the load train to correct for the misalignment[25].

The size and geometry of a sample can have a significant influence on the outcome of mechanical testing. The most common sample geometry is a cube or a cylinder. One important concept in the production of these samples is the length to diameter (L/D) ration of the samples. Various ratios have been reported in the literature ranging from 2 to 0.25 with diameters between 5 and 20 mm. Longer samples (L/D ratio > 5) have a tendency to "buckle" during testing and should be avoided. On the other hand, shorter samples (L/D < 1) will exhibit a significant friction effect between the samples and the platens leading to overestimation of stiffness. Consequently, most investigators have recommended an L/D ratio of between 1 and 2 for typical compression testing[267]. Besides, friction between the specimen and compression platen can also contribute to measurement error.

Although compressive tests tend to be less accurate than tensile tests due to the above-mentioned effects imposed on the specimen during the test, compressive tests have several advantages[49]: (1) the compressive specimens allows the use of relatively small specimens. This is a major advantage when testing bone and bone substitute materials, (2) fabrication of compressive specimens may not be as difficult as with tensile test specimens and (3) in some regions of the skeleton, compressive tests closely simulate the *in vivo* loading conditions to which the bone is exposed. Compressive tests can provide useful biomechanical data.

Compressive strength is calculated by the equation:

σ (Pa) = F/A (N/m^2)

where σ is stress,

F is force

A is the specimen cross-sectional area

Table 2.22 shows the compressive strength for calcium phosphate as reported in the literature. The compressive strengths for both dense and porous calcium phosphate cover a wide range. This might resulte from different forming methods. Dense calcium phosphate has much higher compressive strength compares to porous samples and is in the order of 308 – 917 MPa. The compressive strengths for porous calcium phosphate

are quite low. Most of them are around 0.2 to 18 MPa and the highest is about 36 MPa. This shows these porous samples are not useful for heavy load-bearing applications.

Material	Compressive strength	Test conditions	Ref.
HA Dense	308 – 509 MPa Elastic modulus: 42 – 81 GPa	SD: 10 × 5 × 5 mm CS: 2 mm/min	255
HA Dense	917 MPa	SD: 2 × 4.6 mm (height × diameter) cylinder	268
Calcium phosphate Dense	800 MPa Elastic modulus: 112 GPa	SD: 15 × 5 mm (height × diameter) cylinder	154
HA Pore size: 17 – 122 μm Porosity: 72 – 90%	1.6 – 5.8 MPa Elastic modulus: 3.6 – 21 GPa	–	118
HA Pore size: 150 – 400 μm Porosity: 36 – 80%	0.2 – 18 MPa	SD: 20 × 20 × 20 mm^3 CS: 1 mm/min	150
HA Porous	~ 5 MPa Elastic modulus: ~ 8 GPa	CS: 0.4 mm/min	228
HA Pore size: 190 – 230 μm Porosity: 70 – 80%	2 MPa	–	220
HA Pore size: 20 – 200 μm Porosity: porosity: 76 – 80%	4.4 – 7.4 MPa	SD: 11 – 13 mm (height × diameter) cylinder CS: 0.5 mm/min	73
HA Porosity: 45 – 78%	2 – 36 MPa	SD: 18 × 18 × 5 mm	201
HA Density: 0.38 – 1.25 g/cm^3	1 – 11 MPa Elastic modulus: 0.2 to 3.1 GPa	SD: 8.76 × 4.58 mm (height × diameter) cylinder CS: 0.1 mm/min	76
Calcium phosphate Pore size: 100 μm Porosity: 39 – 56%	1.2 – 15 MPa	CS: 1 mm/min	108
Calcium phosphate Porous	10.9 MPa	SD: 5 × 5 mm cylinder CS: 0.1mm/min	82
Calcium phosphate Porosity: 75%	10 MPa	SD: 10 × 10 mm (height × diameter) cylinder	158
Calcium phosphate Pore size: 400 – 600 μm Porosity: 50%	2.6 ± 0.3 MPa	SD: 6 × 6 mm (height × diameter) cylinder	18
Calcium phosphate Pore size: 500 – 600 μm Porosity: 65 – 90%	0.3 – 3.3 MPa	SD: 10 × 5× 5 mm CS: 0.5 mm/min	223

β-TCP/HA Pore size: 300 – 400 μm Porosity: 73%	9.8 ± 0.3 MPa	SD: 2 × 1 mm (height × diameter) cylinder CS: 0.4 mm/min	218
TCP Pore size: 300 – 800 μm Porosity: 70 ± 4%	11 ± 3 MPa Elastic modulus: 2.1 ± 0.3 GPa	SD: 10 × 15 mm (height × diameter) cylinder CS: 0.5 mm/min	208
TCP Pore size: 300 – 700 μm Porosity: 55 ± 6%	22.5 ± 4 MPa Elastic modulus: 5 ± 0.3 GPa	SD: 10 × 15 mm (height × diameter) cylinder CS: 0.5 mm/min	208
β-TCP Porosity: 62 – 82%	0.2 – 2.5 MPa	CS: 0.5 mm/min	1
Calcium phosphate (30 μm thickness) coating on porous zirconia Pore size: ~ 600 μm Porosity: 74 – 92%	1.6 – 35 MPa	SD: 5 × 5 × 10 mm CS: 0.05 mm/min	97
Calcium phosphate (10 – 20 μm) coating on porous alumina Pore size: 800 μm Porosity: 80%	~ 6 MPa	SD: 10 × 10 × 25 mm CS: 0.5 mm/min	224
Carbonate hydroxyapatite Pore size: > 100 – 200 μm Porosity: 45%	6.0 ± 0.5 MPa	SD: 10 × 7 mm (height × diameter) cylinder CS: 0.5 mm/min	56
SD: Specimen dimensions, CS: Crosshead speed			

Table 2.22 The compressive strengths reported for calcium phosphate ceramics.

2.5.4 Die-Plunger Testing

A die-plunger device is normally used to press ceramic powder tablets prior to sintering and is commonly used in ceramic testing laboratories. A die-plunger test can be used to measure basic properties like compression stiffness, relaxation and elastic recoil of granular forms of ceramic materials.

The protocol adopted in the current study was based on that of Grimm[269] to analyse the performance of graft materials in terms of initial mechanical stability for the use in impaction grafting. These properties influence mechanical stability against subsidence in impaction grafting, the compaction properties and the sensory feedback experienced by a surgeon during impaction. There is a complex loading situation for the graft materials in impaction grafting but the die-plunger test is a simple easily reproducible experiment to determine the fundamental mechanical properties of graft materials. A schematic drawing of the die-plunger set-up is shown in Figure 2.11.

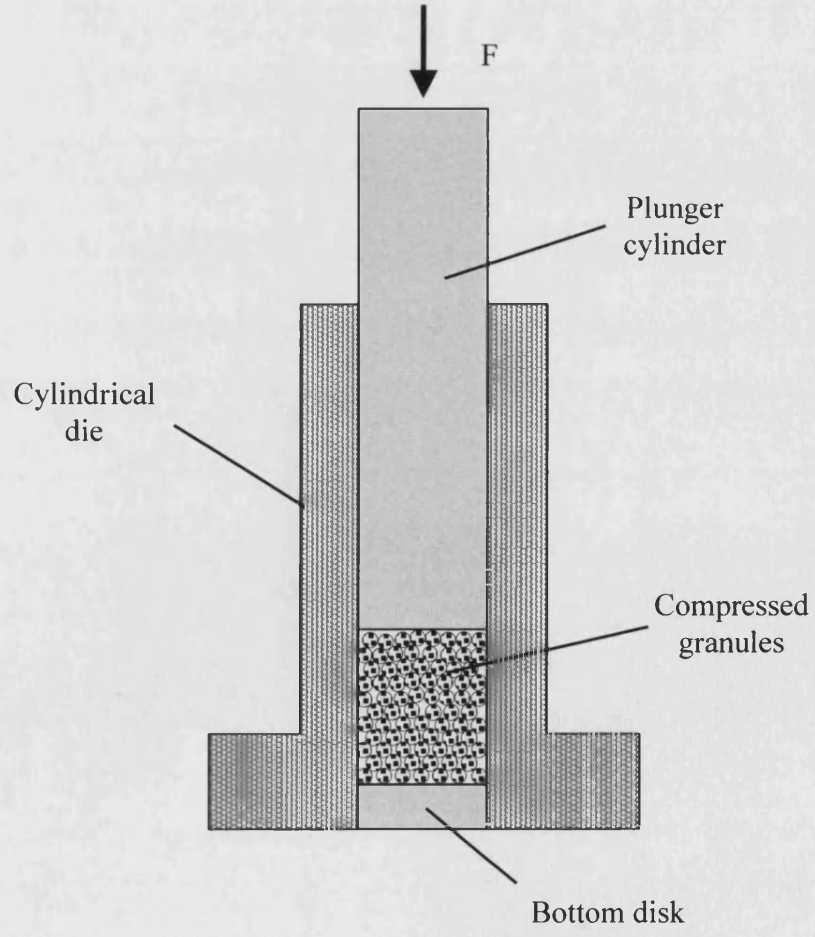

Figure 2.11 Schematic drawing of the die-plunger device.

2.6 Functional Gradient Materials (FGM)

Functional gradient materials (FGM) are defined as materials which have a gradient of properties (microstructure and/or composition) which change with position[270,271]. In recent times, FGM have been developed for use in engineering fields. The materials exhibiting graded or layered porous structures are a special case of functionally graded materials and are interesting for several applications.

In biological systems, bamboo has a typical functional gradient structure, i.e. a negative density gradient of fibres in the thickness direction[272]. Figure 2.12 shows that bone also has a functionally graded structure from the surface of cortical compact bone toward the inner cancellous bone. Therefore, the design of porous implant materials with a porosity gradient mimicking as closely as possible the biomodal structure of bone (compact and spongy) and with a sufficient degree of interconnectivity is the most important challenge[76, 273].

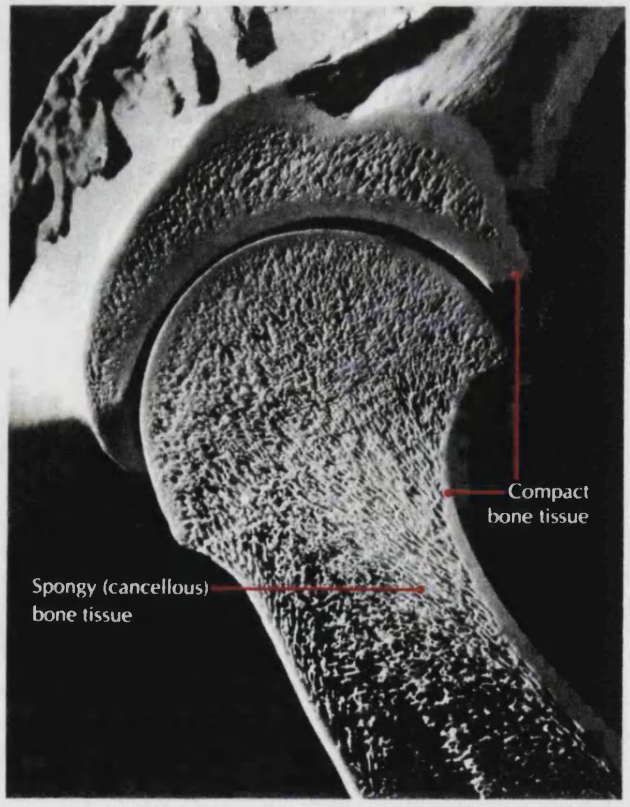

Figure 2.12 The structures of spongy and compact bone in a section through a human hip joint[274].

The wide variety of methods used to process FGM have been reviewed[270,271]. Graded porosity ceramics were manufactured by compacting ceramic powders with varying amounts of porosity generating additives such as polymers or carbon[275], using 3D printing techniques[276], using centrifugal force[277], stacking of tapes with different porosity[207, 278,279], by foaming a silicone resin[280], or using in situ foaming process and the porosity gradient was generated by variation of the foaming temperatures[281]. Cichocki et al[282] developed a technique for producing ceramic preforms with graded porosity via colloidal infiltration of moulded polymer foams. The method of making porous ceramics was based on the replication of reticulated polymer foams method. However, the polymer foams were compression moulded into various shapes with continuous and/or stepwise gradients in porosity.

FGM have also attracted much attention in the field of biomaterials[203,207,214,273,278,283,284] where two main types of gradients are used. One is a gradient in chemical composition and the other one is porosity or pore size gradients.

For gradients in chemical composition, Wang et al[284] used a plasma spray system to form a functionally graded coating, which had a compositional gradient from the surface to the interior of the material. Kon et al[285] developed a dense sintered α-TCP/HA sample where α-TCP gradually decreased from the surface to the interior.

Pore gradient ceramics offer interesting potential for use as biocompatible implants. Tampieri et al[273] produced porous HA with a porosity gradient in order to simulate bone tissue morphology. HA has a high-porosity portion (representing spongy bone) which allows good and fast bone ingrowth and a low-porosity side (similar to compact bone) which can withstand early physiologic mechanical stress. Cylindrical specimens exhibiting a porosity gradient showed promising behaviour after implantation in the femurs of rabbits. Newly formed bone grew in tight contact with the ceramic in a very short time[273].

Arita et al[214] used a tape casting method to produce a thin hydroxyapatite layer 150 – 200 μm thick and the HA layer obtained allowed them to produce laminates with desired porosity gradients, up to several millimetres thick but the pore size was limited to only several micrometres which might be inadequate for bone ingrowth.

Vaz et al[203] used a multiple slip-casting technique, in order to obtain dual-layer samples with different sized porosities. It was proposed that the external layer, because

of its porosity (40 %), controlled by the addition of organic compounds (PVC), should promote bone ingrowth. It was also proposed that the internal denser layer (porosity: 10 %), due to the addition of lithium phosphate (Li_3PO_4) as sintering additive, should give mechanical resistance to the implant.

Werner et al[207] developed functionally pore-graded materials with the aim of improving the mechanical strength of hydroxyapatite (HA) ceramics used as bone implants and to enhance cellular penetration. The macropores in the outer layers provide access for cell, blood vessels and enhance new bone formation whereas the inner dense ceramic structure improves the mechanical stability of the implants. The results showed that the bending strength of the pore-graded ceramics was approximately 50% higher compared to HA of the same pore volume fraction but without the gradient structure. The bending strength for pore-graded structure was in the range of 6 – 9 MPa and one single pore size sample was in the range of 4 – 5 MPa. Similar work was carried out by G. Carotenuto et al[4]. They obtained dense/porous hydroxyapatite laminates by slip casting technology. Their results showed the first layer consisted of macroporous hydroxyapatite with high osteoconductive properties and the second layer was a dense hydroxyapatite substrate able to improve the laminate with good mechanical properties.

Although a large number of papers have reported on fabrication of pore gradient bioceramics, many of them have layer fractures and nearly all of them can only be used to manufacture simple shapes with flat layered porous gradient structures which are not representation of the normally circular shape of long bone.

2.7 Aims and Objectives of the Current Study

From reviewing the literature it can be concluded that the properties of currently available porous calcium phosphates are insufficient for current clinical applications and need to be improved. The main aims and objectives of this research work are to fabricate porous calcium phosphate blocks and granules with completely interconnected porosity and to improve the mechanical strength of porous calcium phosphate bioceramics to enable their use in heavy load-bearing applications. Furthermore, the aim is to develop of a functional gradient material (FGM) with graded pore structures similar to the bimodal structure of compact and spongy bone. The details of manufacturing processes for porous blocks, granules, solid calcium phosphate and functional gradient materials (FGM) will be described in Chapter 3.

CHAPTER 3

EXPERIMENTAL PROCEDURE

This chapter gives the details of:

- *Manufacturing processes for porous blocks, granules, solid calcium phosphate and Functional Gradient Materials (FGM)*
- *Macro- and microscopic analysis and measurement of physical and mechanical properties*

3. Experimental Procedure

3.1 Raw Materials

3.1.1 Powders

Two grades of calcium phosphate powder, TCP 118 and TCP 130 (Stryker Howmedica Osteonics), were used in this study. The TCP 118 powder, Ca/P ratio 1.5, is a low crystallinity (i.e. imperfect and unstable) hydroxyapatite, that contains the phase calcium phosphate hydrate (CPH) which allows the final sintered products to comprise β-tricalcium phosphate (β-TCP) and α-tricalcium phosphate (α-TCP) as well as some hydroxyapatite (HA) depending on the sintering temperature. TCP 130, Ca/P ratio 1.67, is a stable, highly crystalline form of HA and almost does not undergo phase transition on subsequent firing. XRD traces of the TCP 118 and TCP 130 powders as received are shown in Appendix B[286]. TCP 130 will remain predominantly as HA on sintering at up to 1280°C and TCP 118 is readily transformed to TCP above 1100 °C. Varying the blend ratios of TCP 118 and TCP 130 and sintering temperature, changes the ratios of HA and TCP in the sintered samples. This allows a trade off between long-term stability associated with HA and high bioactivity and solubility associated with TCP. The blend ratio of TCP 118 and TCP 130 powders used in this study was 1:1 and the sintering temperature was 1280 °C as described in earlier published work[286]. The sintered samples will be 75 % HA and 25 % TCP.

3.1.2 Polyurethane (PU) foams

The organic reticulated foams, which were completely burnt out during sintering were made of polyurethane (PU) that had one of three different porosities – 20 ppi, 30 ppi and 45 ppi (Sydney Heath and Sons Ltd.). The PU foams were sectioned by scalpel and scissors to the desired shape and dimensions, then soaked in water for 24 hours. This stage of the process removed dust and impurities from the foams. The standard foams dimensions used in this research were 30 × 30 × 25 mm; these were the most appropriate size for experimental purposes. The manufacturing method developed can be used on PU foams in a full range of sizes, encompassing a range of geometries from small granules up to large blocks. Table 3.1 shows the main foam dimensions and their utilisation. These foams are shown in Figure 3.1.

Foam dimensions (mm)	Utilisation
30 × 30 × 25	The standard samples in this research project
70 × 70 × 25	Sectioned to smaller bars for mechanical tests
3.1, 6.3, 8.3 and 12.5(cubes)	Granules (regular cubes)

Table 3.1 Foam dimensions and the purposes.

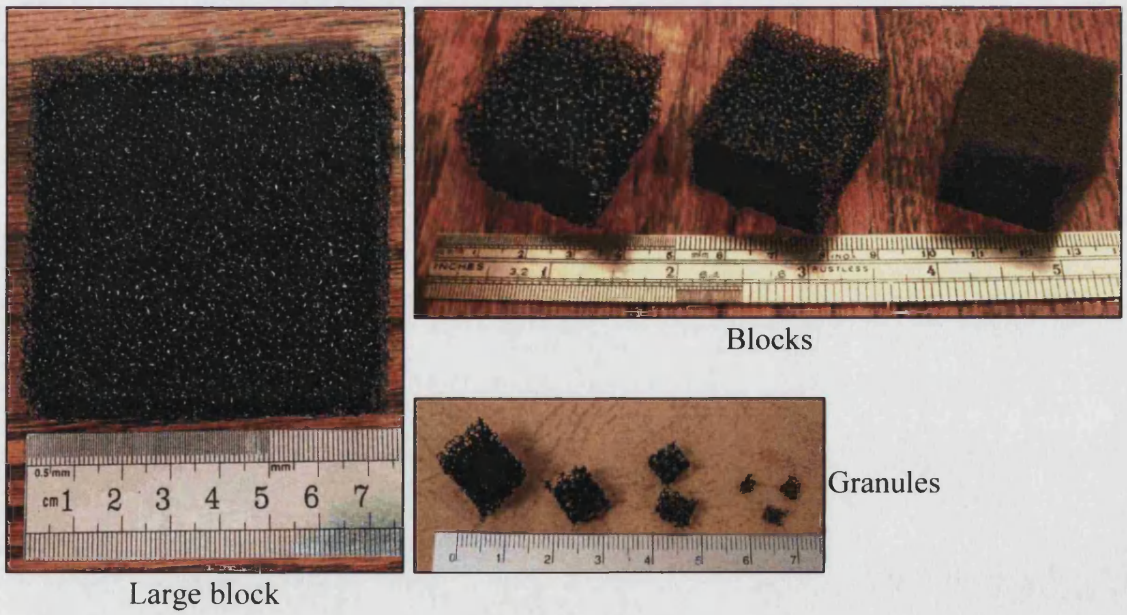

Figure 3.1 Macrographs of the foams after sectioning and before impregnation.

3.2 Manufacturing Process

3.2.1 Production of Ceramic Slips

The steps in the experimental procedure are shown schematically in Figure 3.2. The ceramic suspensions were prepared by first adding the dispersing agent, Dispex A40, (Ammonium polyacrylate, Ciba, England) to distilled water. This decreases the slip viscosity and improves the flow properties without decreasing the solid loading. For slips with higher solids loading large amounts of dispersant were added, otherwise the slips were too thick to mill. While stirring, TCP 118 and TCP 130 powders (1:1) were gradually added in different proportions to distilled water in order to achieve various solid loading levels in the slips. After adding the required amounts of powder, the mixtures were ball milled in polyethylene jars, using ZrO_2 balls as the milling media, for 24 hours. This process improves the rheological properties of the suspensions and the packing ability during consolidation.

To investigate the effect of solids loading on the viscosity of the slip, physical and mechanical properties of the resulting samples, slips of 450 – 1,800 g of powder per litre (45 – 180 wt%) were prepared. A high solid loading is required for greater density, improved mechanical properties, and minimal shrinkage in the final sintered product. However, the slip with a high solid loading has a high viscosity causing difficulty with impregnation and thus requires more dispersant. After ball milling, more dispersant was added to adjust the slip to an exact viscosity. The viscosity characteristics of the slip were measured using a Brookfield viscometer via a constant spindle speed of 10 rpm using a No. 5 spindle as shown in Figure 3.3. A conversion factor of 400 was employed to convert the reading from the viscometer into a centipoises (cps) viscosity reading. Table 3.2 shows the components and viscosities of the range of slips produced. The viscosity of the slip must be sufficiently low to enter and fill the foams, however, it should also be high enough to avoid the ceramic slip draining from the foam. Hence, the slip was vacuumed for ten minutes before impregnation to remove any entrapped air bubbles which could decrease the density and compromise the mechanical strength of the bioceramics.

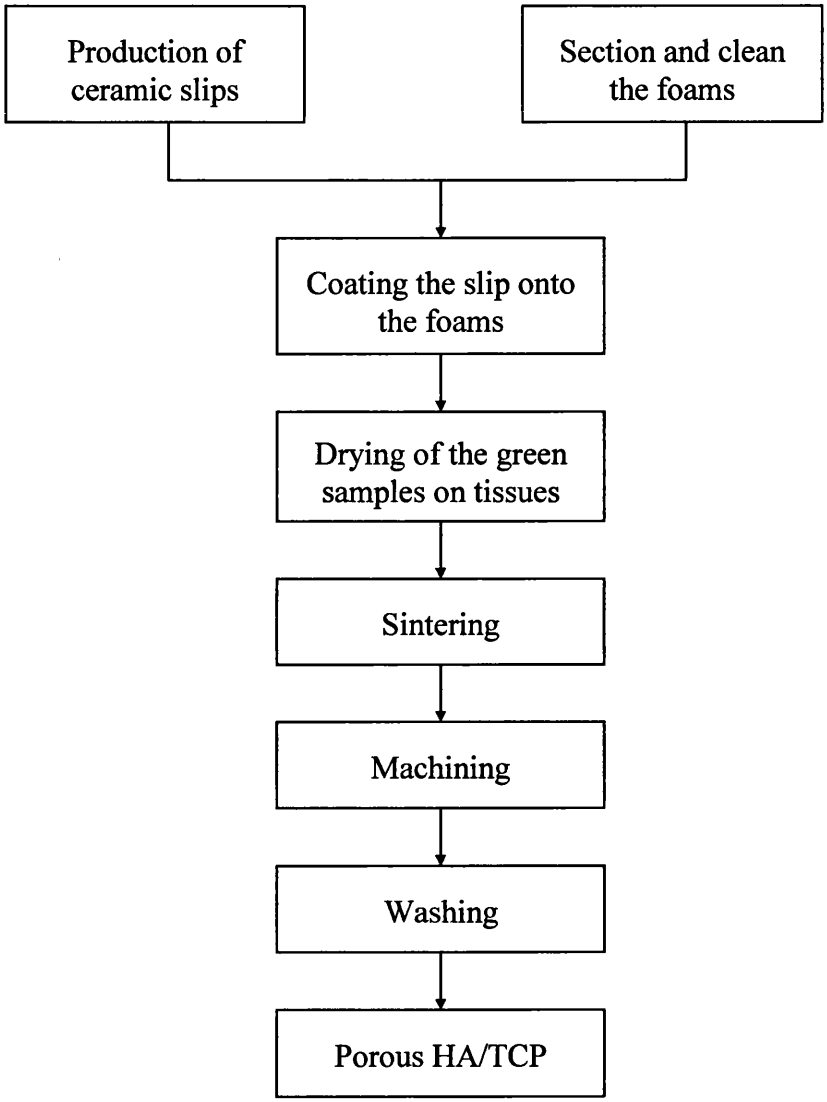

Figure 3.2 Fabrication procedure for porous HA/TCP.

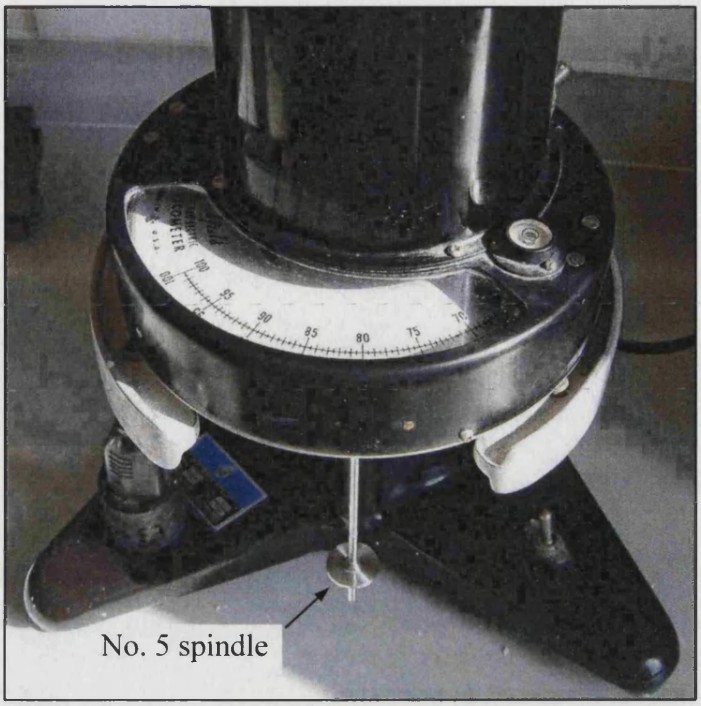

Figure 3.3 Brookfield viscometer used to measure the viscosity characteristics of the slip via a constant spindle speed of 10 rpm using a No. 5 spindle.

First vacuum impregnation method (Vacuum before and during impregnation)				
	Constituents			Viscosity (cps)
Solid loading	Powder (g)	Distilled Water (ml)	Dispex A40 (ml)	
60 wt%	600	1,000	4.5	8,800
80 wt%	800	1,000	15	8,000
100 wt%	500	500	7	8,400
120 wt%	600	500	12.3	8,000
140 wt%	700	500	18	8,000
160 wt%	800	500	19	6,800
Second vacuum impregnation method (Vacuum after impregnation)				
60 wt%	600	1,000	3.5	13,600
80 wt%	800	1,000	10.5	9,800
100 wt%	750	750	13	7,800
120 wt%	600	500	14.5	8,800
140 wt%	700	500	16.8	9,600
180 wt%	900	500	22.8	9,200

Table 3.2 Ranges of slip loadings and viscosities.

3.2.2 Impregnating the Foams with Slip

An important feature of the method developed is that the slip substantially fills the foams as opposed to only coating the walls. In the latter case, the resulting product would be a replica of the reticulated foam material and the ceramic parts of the structure would be hollow and therefore less strong. These differences are illustrated in Figure 3.4. Where (a) represents the structure of the foam before impregnation, (b) shows the foam structures coated in ceramic and (c) shows the foam substantially filled with ceramic slip.

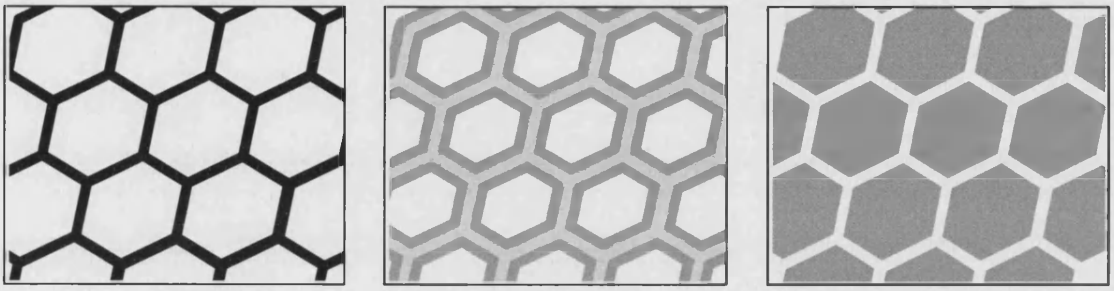

(a) (b) (c)

Figure 3.4 (a) The reticulated structure of the polymer foam (b) result of coating just the walls of the polymer foam (c) result of substantially filling the foams with slips.

The foams were substantially impregnated with ceramic slip by vacuum impregnation. Two main methods were developed for this procedure; both used a vacuum technique. A diagram of the procedure used in the first vacuum impregnation method is shown in Figure 3.5. The system comprised a vacuum pump and a vacuum vessel, connected to a length of plastic tubing, the end of which was immersed in the ceramic slip. Inside the vacuum vessel was a container in the bottom of which sections of PU foam were held between a pair of meshes. In the central section of the plastic tubing there was an adjuster, which could be used to control the flow capacity of the slip.

Initially, the adjuster was closed and the foams were held in an unstressed state between two meshes in the container. The vessel was then placed under vacuum for 5 minutes in order to remove the gas from the vessel and the foams. As the pressure in the vessel reduced, the adjuster was opened to allow the ceramic slip to enter the container until the foam was fully submerged in the slip. The impregnated foams were then taken out and allowed to dry on tissue. The difficulty encountered during the impregnation was the tendency of the slip to drain from parts of the foam structure. Using a slip with a higher viscosity and repeating the impregnation process solved the problem.

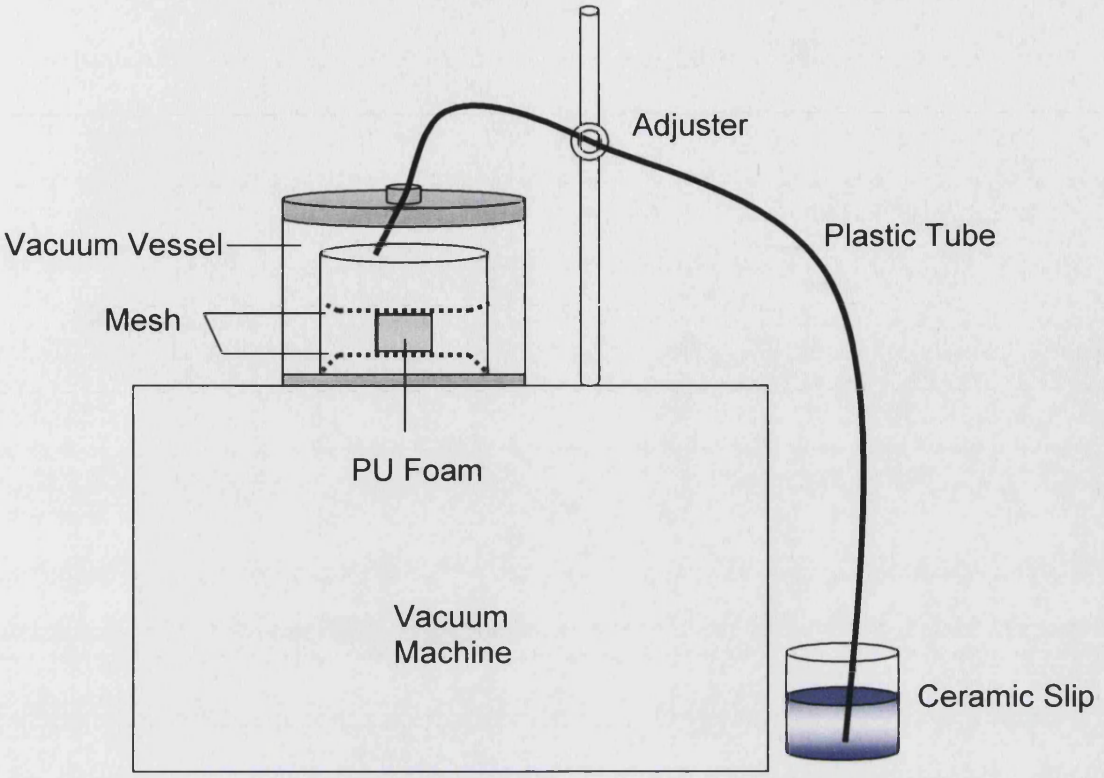

Figure 3.5 Schematic representation of the deposition technique using vacuum equipment.

The second vacuum impregnation method was to introduce the slip into the foam before vacuum treatment. An outline of this procedure is shown in Figure 3.6. The slip was placed in a small beaker. The PU foam was compressed to remove air, immersed in the slip, then allowed to expand. The compression and expansion procedures were repeated in order to fill all the pores while the samples were submerged. The beaker was then subject to a vacuum for five minutes to remove the air in the foam and the slip. Using this method the samples could be impregnated twice. However, no pressure was applied to the foams during the second impregnation. Because the slip no longer needed to flow through the tube, slips with higher solid loading and viscosity could be used in the second method.

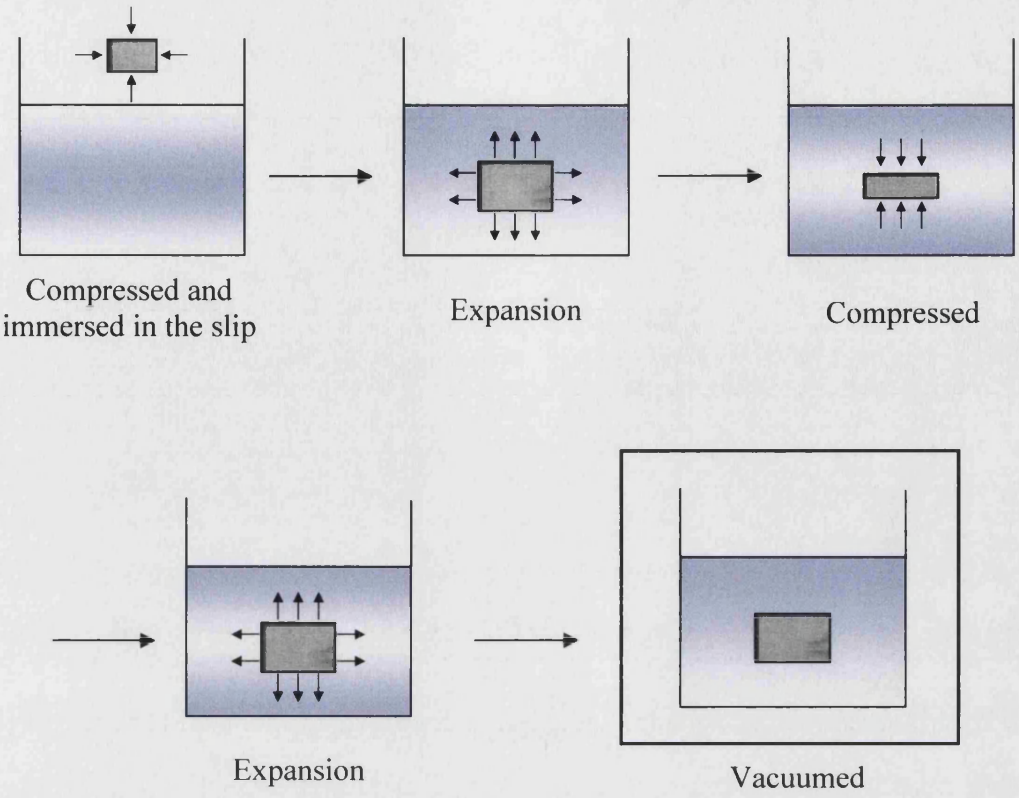

Figure 3.6 Schematic representation of the second vacuum impregnation technique.

3.2.3 Manufacturing Process for Porous Granular Forms of Calcium Phosphate

As described before, the method of vacuum impregnation could be applied to make a broad size range of porous materials. Based on the same technique, it was possible to produce porous HA/TCP granules. Each PU foam was sectioned to the shape of a cube whose sides were of a length in the range of 3 to 12.5 mm and the resulting porous ceramics were in the range of 2 to 8 mm. When making granules many pieces of PU foam could be placed together in the container, rather than treating each piece individually. After impregnation the foam was separated from the slip by sieving. Before the drying process, it was necessary to ensure the small pieces of impregnated granular foam did not stick together. Otherwise, the granules would be difficult to separate without incurring damage after drying.

3.2.4 Manufacturing Process for Solid Calcium Phosphate

In order to compare the mechanical properties and failure modes of porous and solid samples, solid HA/TCP blocks with no porosity were made. The method of slip casting was employed to produce the solid blocks. The ceramic slip was prepared in the same way as for vacuum impregnation. Different containers, which are shown in Figure 3.7, such as plastic and ceramic moulds, paper flowerpots and egg boxes were used. Ceramic slips were poured into the moulds and dried for several days. The surface of the mould was coated with a layer of petroleum jelly or covered with a layer of tissue to ensure the sample could be removed from the porous moulds without damage when sufficiently dry.

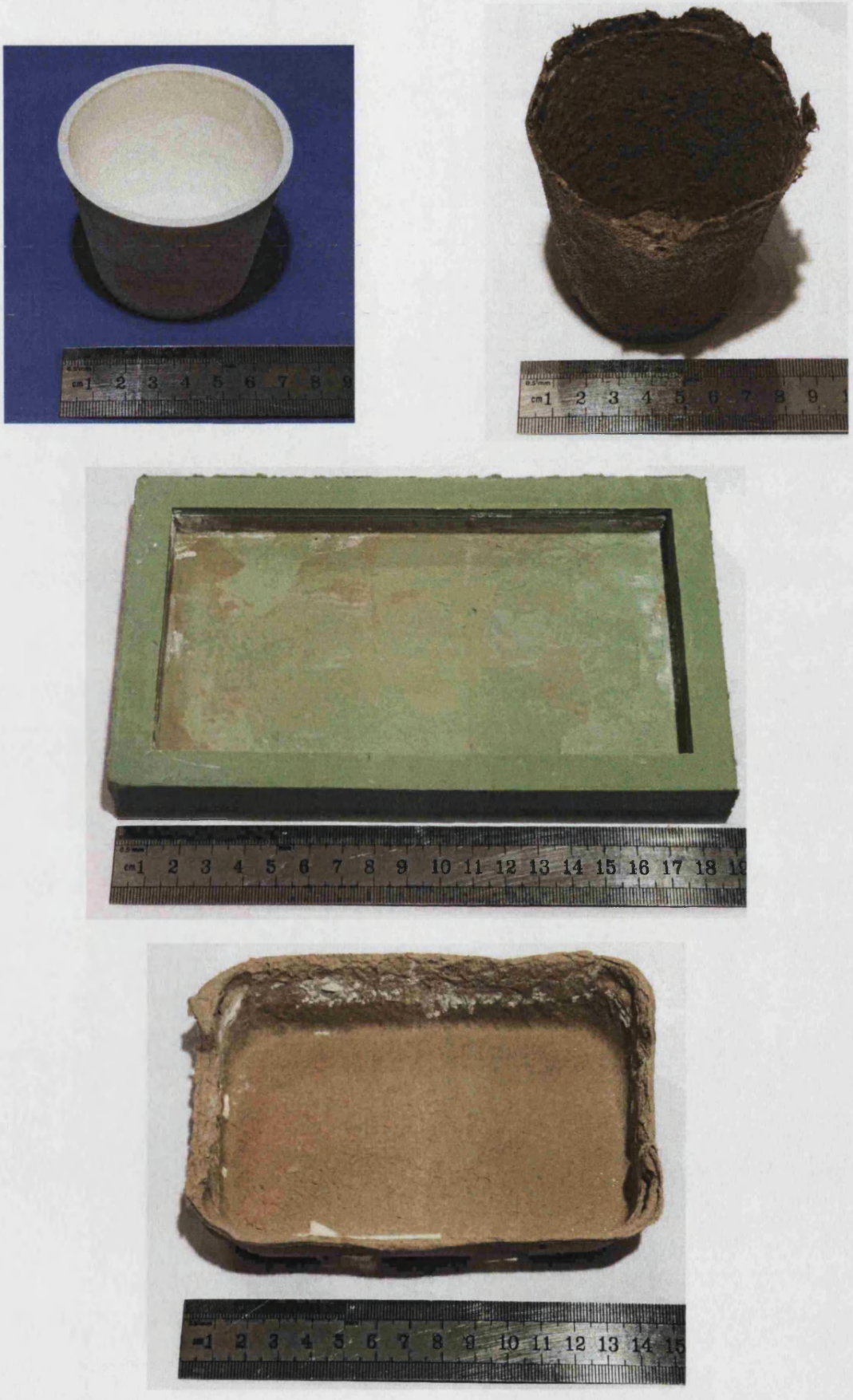

Figure 3.7 Plastic and ceramic moulds, paper flowerpots and egg boxes are used as the moulds for slip-casting method.

3.2.5 Drying and Sintering

Two drying processes were used. The impregnated foams were removed from the slip and allowed to dry on tissue at room temperature. For the first 30 minutes of the initial drying step, the impregnated foams were turned every 5 – 10 minutes in order to avoid specific porous orientation effects occurring in the sintered samples. The time taken for this first drying step was at least 24 hours, followed by the second drying step in an oven at 40°C for another 24 hours. When the samples were made from the slips with higher solid loading, or had large dimensions, the duration of drying was increased. In extreme conditions, the first drying step duration could be more than one week in order to obtain samples without any cracks. Pyrolysis of polymer foams is essential during the next stage of sintering. Sufficient time should be allowed for the polymer to completely burn out before the sintering of ceramic starts, in order to avoid cracks forming in the samples.

The green samples were sintering in a programmable furnace in two stages (as shown in Figure 3.8). In the first stage the samples were heated at a rate of 60°C/h from room temperature to 600°C with a holding time of 1 hour to burn out the polyurethane foam support without the ceramic structure collapsing. In this step, slow and controlled heating to the desired temperature is critical. Rapid heating may result in thermal stresses causing destruction of the ceramic structure. During this first step, all of the PU foam decomposed and a green porous material was left. In the second stage, the heating rate was further increased to 120°C/h and the final sintering temperature was 1280°C with a holding time of 4 hours for small blocks and 5 hours for large blocks of ceramic. The cooling rate was kept to 200°C/h until room temperature was reached. At the end of the second stage of heating the sintered porous material had been formed.

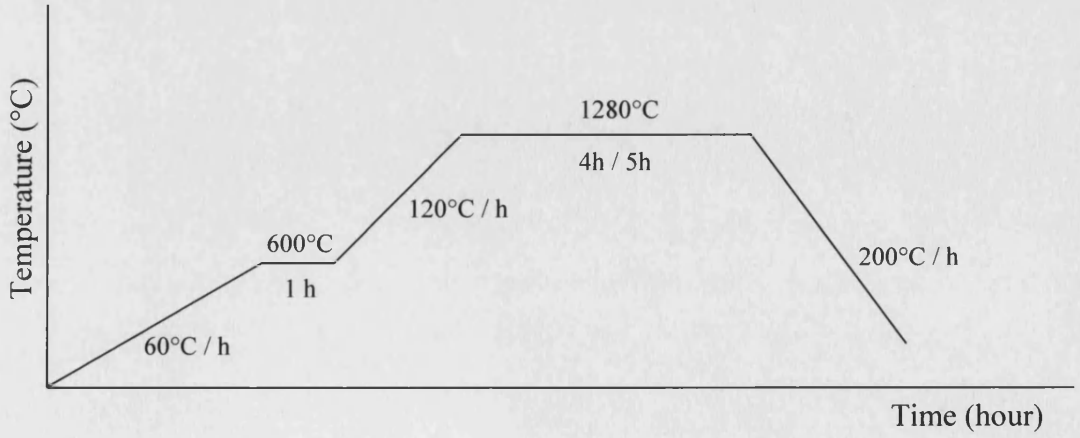

Figure 3.8 Stages in sintering of the green porous HA / TCP.

3.2.6 Machining and Washing

The sintered porous HA/TCP could be cut to the desired shape and size using a slow diamond saw followed by grinding by machine to give a smooth surface and more accurate dimensions and shape. The samples were cleaned in an ultrasonic bath after machining to remove any dust that may have collected in the sample pores.

3.3 Macro- and Microscopic Analysis

3.3.1 Macroscopic Analysis

There are many ways to observe and record macroscopic features of the samples such as Optical Microscopy (OM) and Scanning Electron Microscopy (SEM). The samples for OM need to be extremely flat as the depth of field is quite short for OM. It is time-consuming to prepare observable samples. Using a scanner had some advantages over using microscopy (SEM or OM). A scanner could deal with the sintered samples without any further procedure. The images of the samples could be recorded quickly and easily. The other advantage is that a large area of the sample can be observed in one scan. A Hewlett Packard® (HP ScanJet 5300C) scanner was used in this research. The resolution was set for 900 dots per inch (dpi) to obtain a clear picture, which could be scaled for different applications.

3.3.2 Scanning Electron Microscopy (SEM)

The pore size and distribution and the grain size of the sintered HA/TCP samples was investigated using a Scanning Electron Microscope (SEM, Jeol, T-330) with an accelerating voltage of 15 kV. Samples were first vacuum mounted in resin. The resin used should have low viscosity to fill the pores of the sample. The mounted samples were placed in an oven at 50°C for 24 hours for hardening. After hardening, the samples were ground using SiC 240 to 1,200 paper and Polymet cloth with a 3 μm water-based diamond suspension. The samples were then polished with Texmet cloth with 0.5 μm water-based diamond suspension for five minutes followed by a Chemomet cloth using Masterprep 0.05 μm polishing suspension for three minutes. Finally, they were polished on a Microcloth cloth with Masterprep 0.05 μm polishing suspension for three minutes. The samples were washed, dried and then coated with a thin layer of gold to avoid the

build up of static electrical charge during the microscopy session. The mounted samples, before coating in gold, are shown in Figure 3.9. SEM photos taken at magnifications of x 20, x 100, x 1000 and x 3,000 were used for analysis of macroporosity and microporosity in a range of samples.

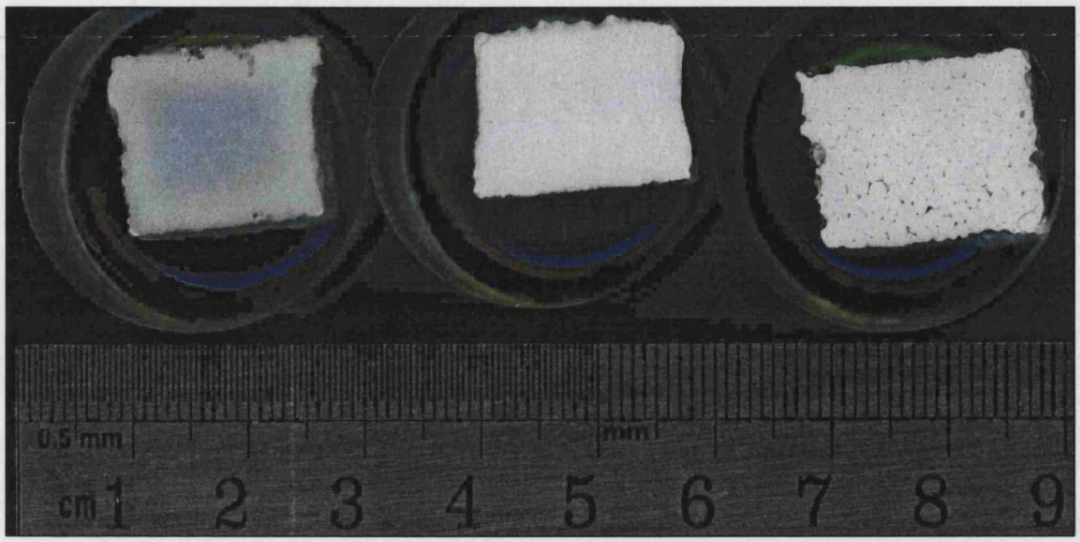

Figure 3.9 Samples mounted in resin.

3.3.3 Pore Size and Porosity

The Optimas 6.1 computer software was used for image analysis to quantitatively assess the scale and structure of the macro- and micro-porosity and the macro- and micro-pore sizes of the material. The area equivalent diameters were taken as pore sizes and were calculated from the measured feature areas. The average pore size and porosity for each condition were measured from eight regions on two surfaces (20 × 20 mm). The pore size was calculated using the equation:

The area equivalent diameter (pore diameter) = $(\text{Feature area}/\pi)^{1/2} \times 2$

This was an automatic calculation carried out by Optimas 6.1 computer software.

3.4 Measurement of Physical and Mechanical Properties

3.4.1 Density

The apparent densities of the samples were determined by a geometric wt/vol method. The dimensions of the sample were measured using a micrometer. The mass of the samples were also measured, thus simple density measurements could be made by the formula density (g/cm^3) = mass (g) / volume (cm^3). Six to eight specimens were used to determine the average density, for each sample group.

3.4.2 Mechanical Testing

Samples for the mechanical tests were prepared as shown in Figure 3.10. Large blocks of dimensions 45 × 45 × 17 mm were made, then sectioned to give smaller bars of 45 × 5 × 4 mm for four-point bending tests. After the bending test, the remains of the samples were prepared for Tattersall-Tappin fracture toughness testing and compressive testing. Five to eight samples from each group were tested to obtain an average value for the mechanical strength.

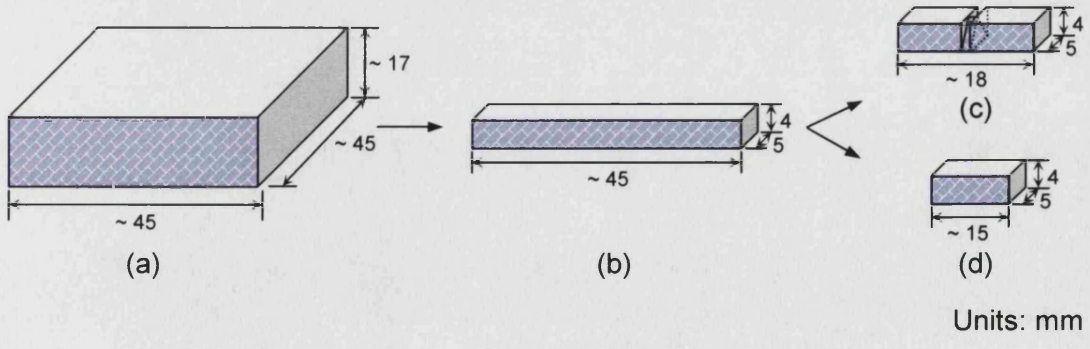

Figure 3.10 Samples for mechanical testing (a) original block sample (b) four-point bend testing sample (c) Tattersall-Tappin testing sample (d) compressive testing sample.

Four-point bending tests, work of fracture (Tattersall-Tappin testing), compressive tests and die-plunger tests were carried out using an Instron 1122 testing machine which is shown in Figure 3.11. The load versus displacement was recorded via an x-y-plotter on paper and stored on a PC using "Marandy" software.

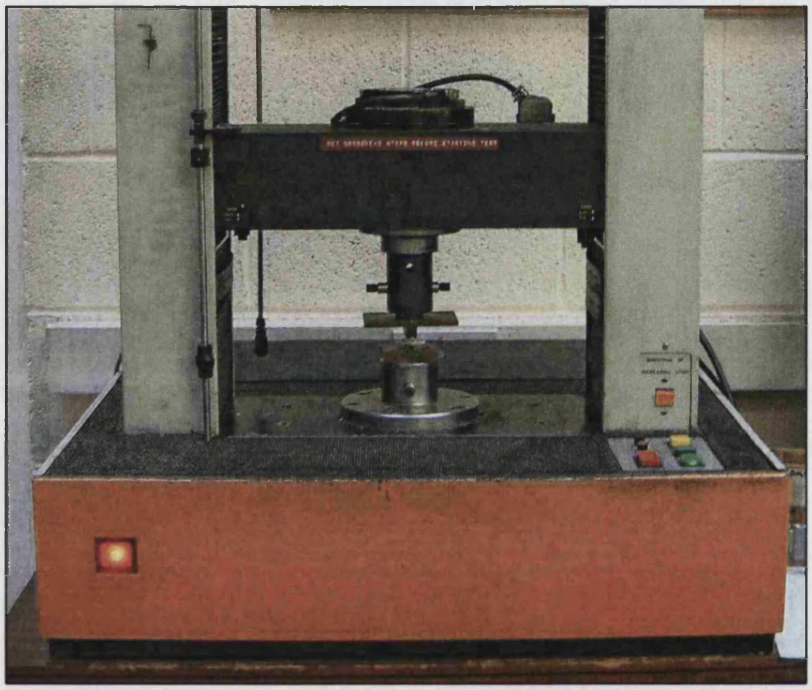

(a)

(b)

Figure 3.11 (a) The Instron 1122 testing machine (b) a chart recorder and a computer were connected to the Instron machine to record the load versus displacement.

3.4.2.1 Four-Point Bend Testing

The testing was carried out using rectangular bars with dimension of 45 × 5 × 4 mm which were sectioned from large block samples using a Buehler Isomet™ 2000 Prelision saw. The load and the rotational speed of the saw were 100 - 120 g and 3600 rpm, respectively. Rough and chipped edges were ground off with silicon carbide paper. An example of the bars used for the test is shown in Figure 3.12. A detailed picture of the test set-up is given in Figure 3.13. The samples were tested using an Instron 1122 testing machine with a crosshead speed of 0.5 mm/min and the span was 20 × 40 mm (Figure 3.14). The four-point bend strengths (σ) were calculated using the equation:

σ (Pa) = $3F(L-L_1) / 2bd^2$ (N/m^2)

where

F = applied force

L = the span of the support loaders

L_1= the separation of the loading span

b = sample width

d = sample thickness

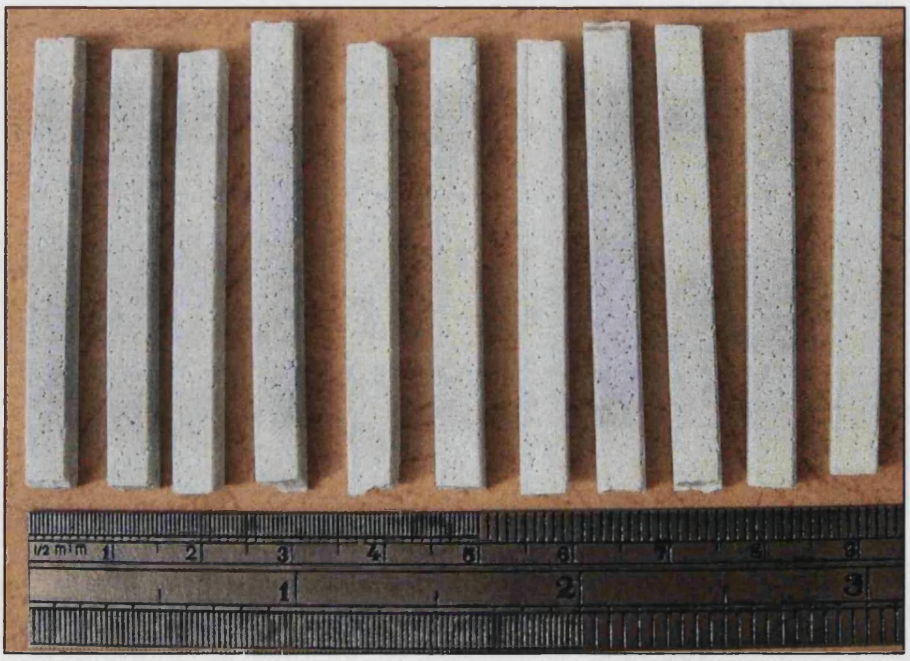

Figure 3.12 The bars for four-point bend test, which were sectioned from a large block.

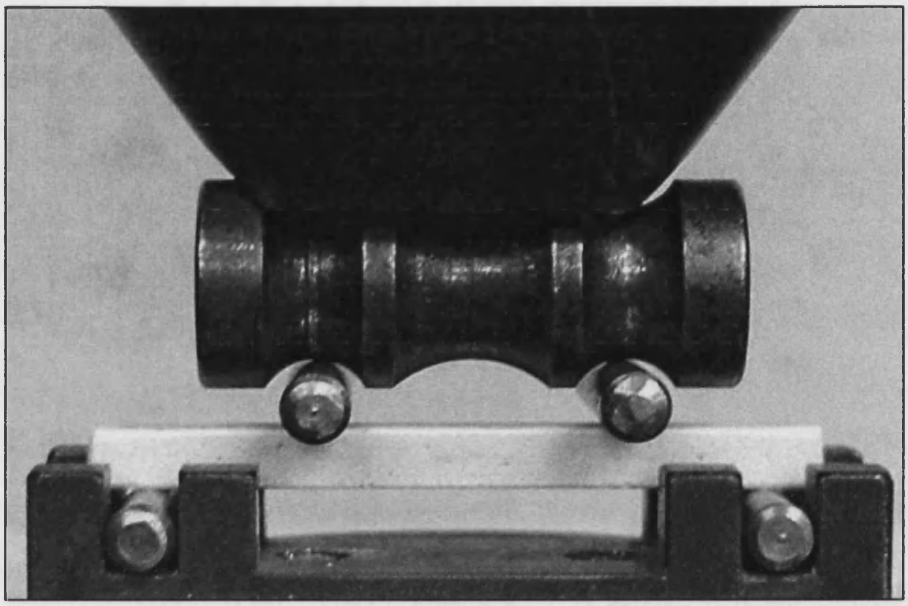

Figure 3.13 The set-up for four-point bend testing.

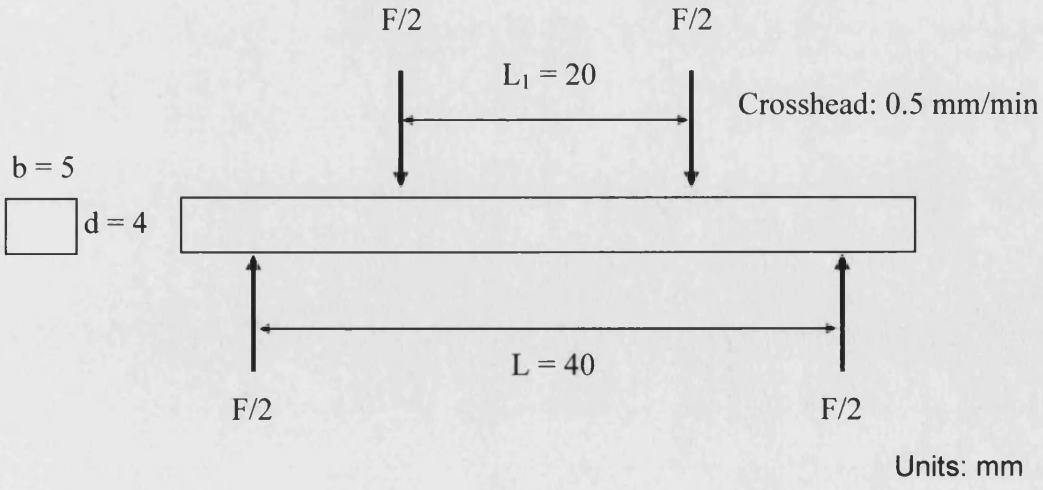

Figure 3.14 Schematic drawing of the four-point bend testing.

3.4.2.2 Work of Fracture (Tattersall-Tappin Test)

Rectangular bar samples approximately 18 mm long were cut from the remains of the samples used for four-point bending testing. Two cuts, to reduce the square cross-section to an isosceles triangular cross-section in the centre of the test piece, were made using a diamond-wafering saw. The chevron-shaped notched samples and the method of loading are shown in Figure 3.15. This test required loading the notched specimen in three-point bending. Figure 3.16 shows a picture of the test set-up. The samples with dimensions: 18 × 5 × 4 mm were loaded in the Instron 1122 test rig set on its most sensitive range, using a constant cross-head speed of 0.05 mm/min; the span was 15 mm (Figure 3.17). The apex of the triangular cross-section was placed in tension, thus causing a crack to initiate due to the extremely high stress concentration. This stress concentration meant that the crack was initiated at a load much less than that required for complete catastrophic failure.

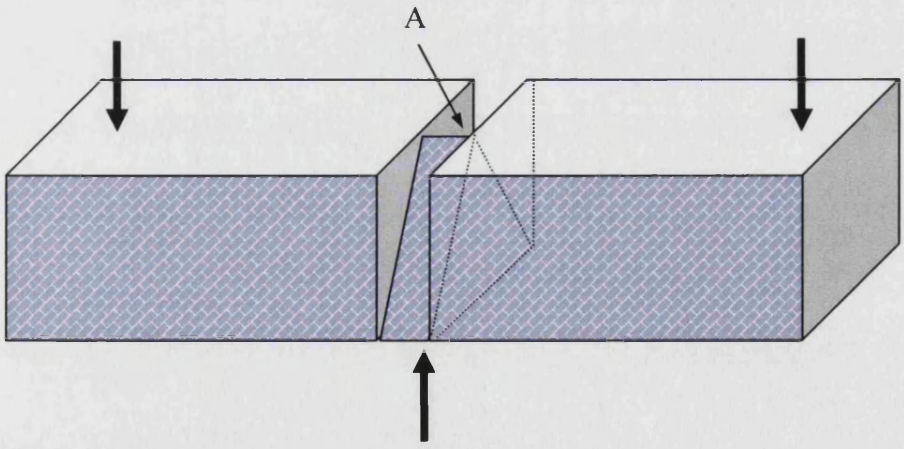

Figure 3.15 Schematic diagram showing the shape of sample used to measure the work of fracture and the method of loading.

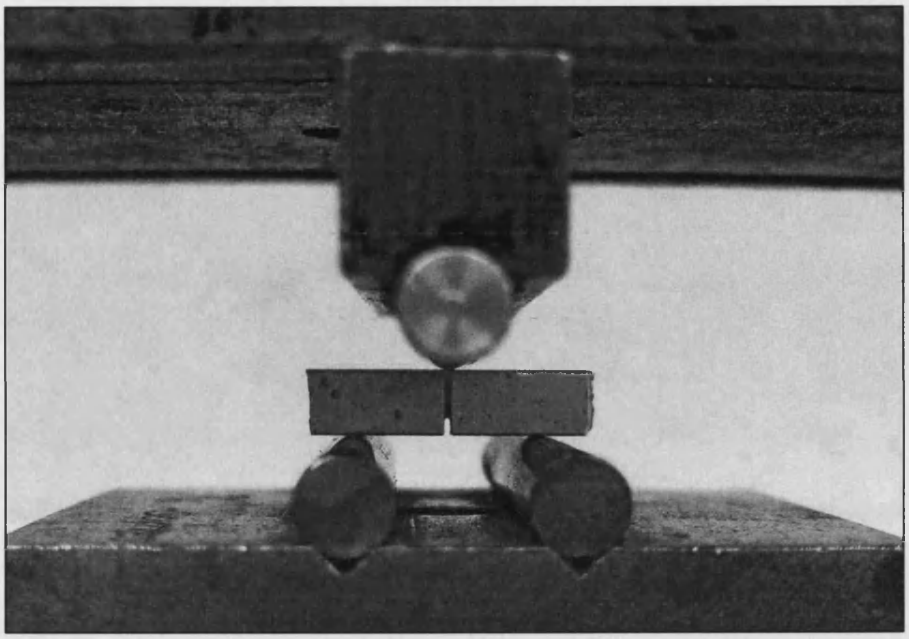

Figure 3.16 The set-up for Tattersall-Tappin test.

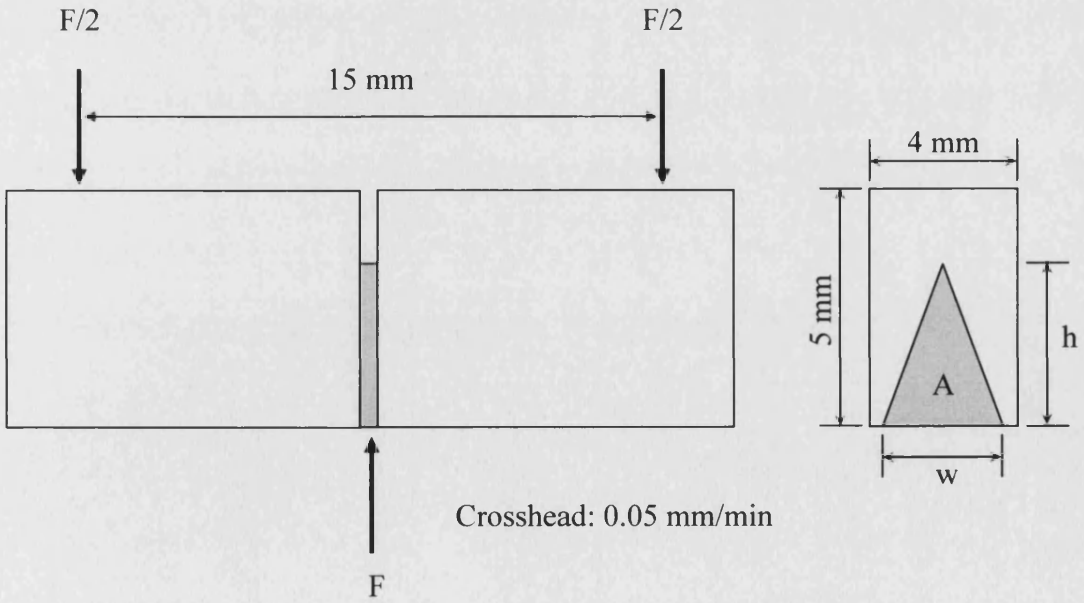

Figure 3.17 Schematic drawing for Tattersall-Tappin test.

Compression force and time were recorded on an x-y-plotter on paper and stored on a PC using "Marandy" software. The recorded data were converted into force (N) and displacement (m) measurements and used to calculate the work done (Nm). A typical compression force versus displacement curve for the test is shown in Figure 3.18.

The total work done, which represents the energy necessary to cause fracture in the sample, was the area under the compression force and displacement curve. This was calculated from the data, recorded via Marandy, using "TableCurve 2D v5.01" software.

A HP ScanJet 5300C scanner was used to obtain qualitative information about the fracture surface of the test sample. Figure 3.19 shows the two triangular fracture surfaces of the sample after the testing. The area of the triangular shape was measured by computer software Image Tool 3.0.

The work of fracture (J/m^2) was calculated by dividing the total work done (Nm) by the sum of the two areas of the triangular fracture surface (m^2). The equation is shown as follow:

Work of fracture (J/m^2) = $W/2A$ (Nm/m^2)

where W (work done) is the area under the load-displacement curve (Figure 3.18)

A is the area of the triangular crack face = wh/2 (Figures 3.17 and 3.19)

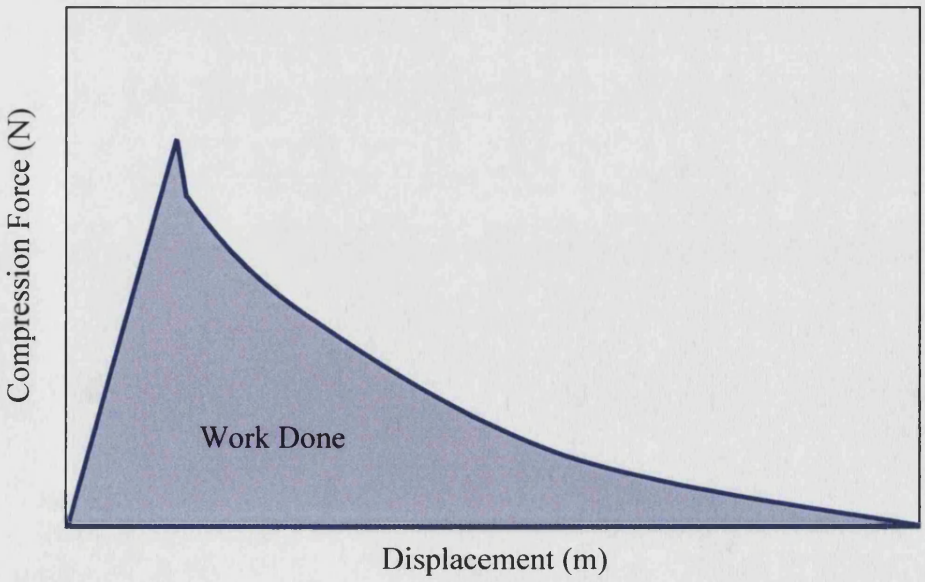

Figure 3.18 Typical compression force versus displacement curve for a Tattersall-Tappin test.

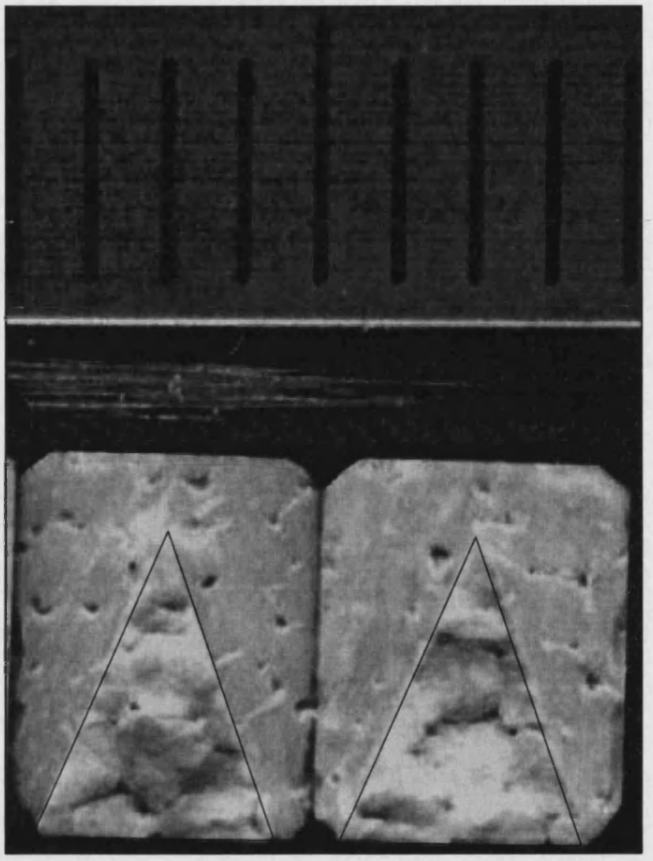

Figure 3.19 The triangular fracture surface of the sample after Tattersall-Tappin testing.

3.4.2.3 Compressive Testing

Compression testing samples were made from the remains of the samples used for the four-point bend tests. Rectangular sections with an aspect ratio of in the order of 3:1, 15 × 5 × 4 mm, were produced. This test required the top and the bottom of the samples to be flat and parallel so that the pressure was uniform on the surfaces and the force was applied parallel to the axis of the sample. Therefore, a device as shown in Figure 3.20 was developed to help grind the samples as flat as possible. Samples were fastened in the recess of the device by a screw. By adjusting the screw, various sizes of samples can be prepared. First, the top of the sample was ground flat; the sample was then reversed to allow the opposite surface to be similarly prepared. The holding jig allowed samples of different heights to be prepared by the use of a range of plastic pads employed to support the sample during grinding. Using the device, more accurate dimensions could be obtained.

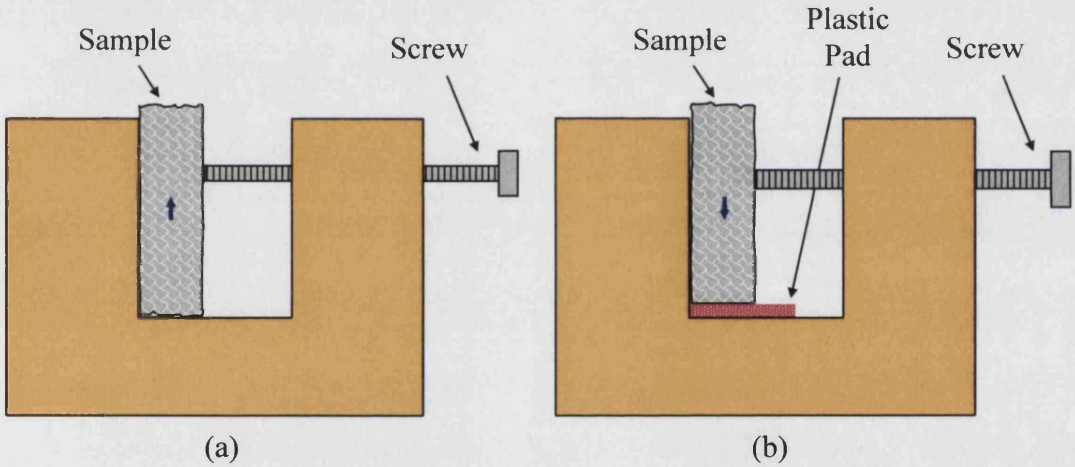

Figure 3.20 A device for grinding samples for compressive testing (a) the sample is fastened in the gap by a screw and the top surface is ready to be ground (b) reversing the samples and inserting plastic pads under the sample allowed the opposite surface to be ground.

Compressive tests were performed using an Instron 1122 materials testing machine with polished steel compression cylinders. Compressive testing was carried out both with and without inserting rubber supports. This is illustrated in Figure 3.21. For the test with inserted rubber supports, a thin layer of rubber was placed between each end of the sample and the loading plates of the machine. The aim was to reduce shear stress concentration. The samples were loaded up to fracture with a constant crosshead speed

of 2 mm/min. Compressive strength was calculated from the load-deformation curve, by the ratio of ultimate applied force and cross-sectional area of the specimen.

Compressive strength is calculated by the equation:

σ (Pa) = F/A (N/m^2)

where

σ is compressive stress

F = applied force

A = the specimen cross-sectional area

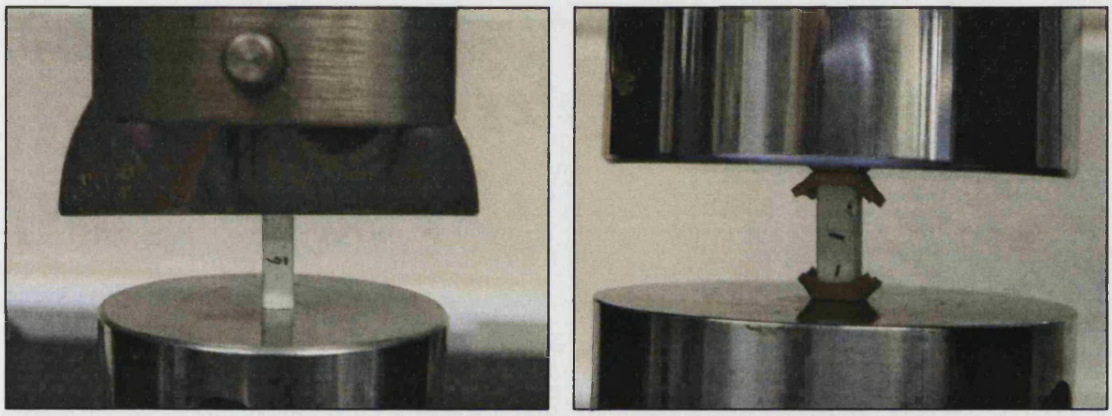

(a) (b)

Figure 3.21 (a) Compressive testing without inserting rubbers. (b) compressive testing with inserted rubber supports.

3.4.2.4 Die-Plunger Testing

Die-plunger testing was employed to measure the compressive modulus, relaxation and energy absorption properties of granules. A die-plunger normally used to press ceramic powder tablets for sintering was utilized to compress the granules under controlled parameters in a screw driven Instron 1122.

An illustration of the die-plunger is shown in Figure 3.22. It consists of a plunger cylinder of 20 mm diameter and 150 mm length which is pushed into a hole of equivalent diameter in the 100 mm long outer cylindrical die. The bottom of the hole is closed with a 20 mm diameter disc which can be easily removed after the compression experiment to retrieve the granules.

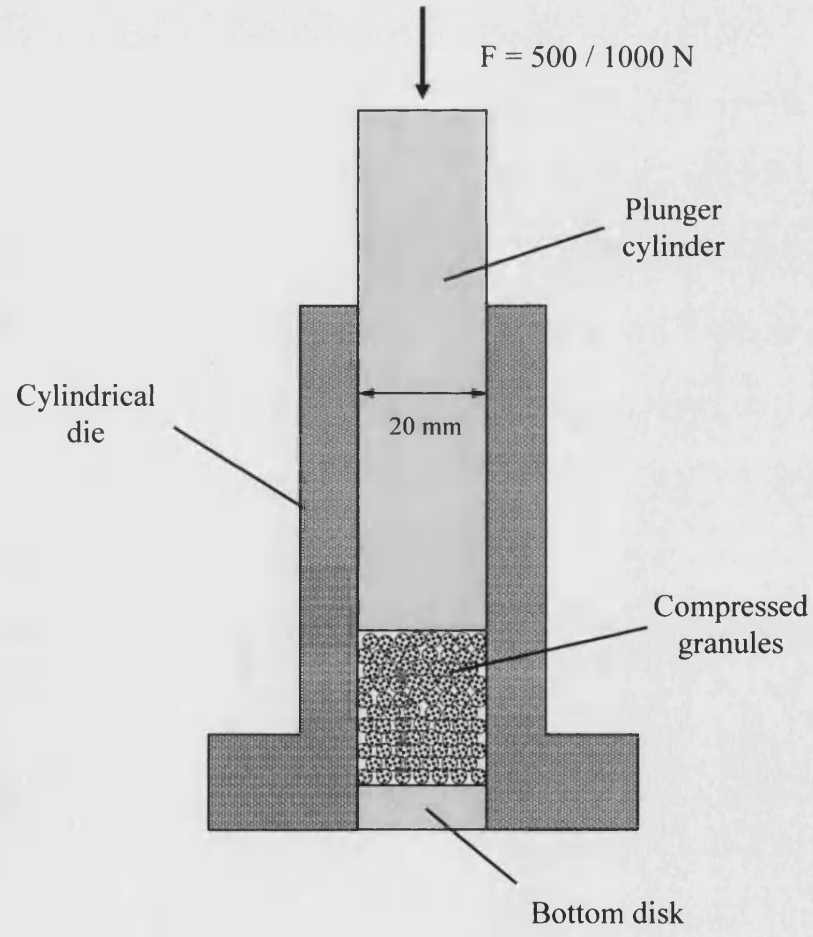

Figure 3.22 Schematic representation of the die-plunger equipment.

The experimental procedure for the die-plunger testing can be described as follows. A measuring glass was used to measure a constant volume of 10 cm^3 of loose and uncompressed granules. The granules were manually inserted into the die and pushed down slightly by the steel plunger cylinder's own weight. A volume of 10 cm^3 of granules converts to a theoretically filling height of 31.8 mm. However, for accuracy in converting absolute deformation into strain, the real height of the 10 cm^3 granules in the cylindrical die should be recorded by measuring the starting position of the plunger cylinder. The cross-head speed of the Instron device was set to 2 mm/min. For each test, the following cycle as shown in Figure 3.23 was applied.

1. Loading to 500 N
2. Position kept constant for a relaxation period of 120 seconds
3. Releasing load to 0 N
4. Loading to 1000 N
5. Position kept constant for a relaxation period of 120 seconds
6. Releasing load to 0 N and retrieving the granules

The force and displacement values were recorded via an x-y-plotter on paper and stored on a PC using "Marandy" software. The recorded data were converted into force (N) and strain (displacement/initial height) measurements and used to calculate compression elasticity modulus and relaxation.

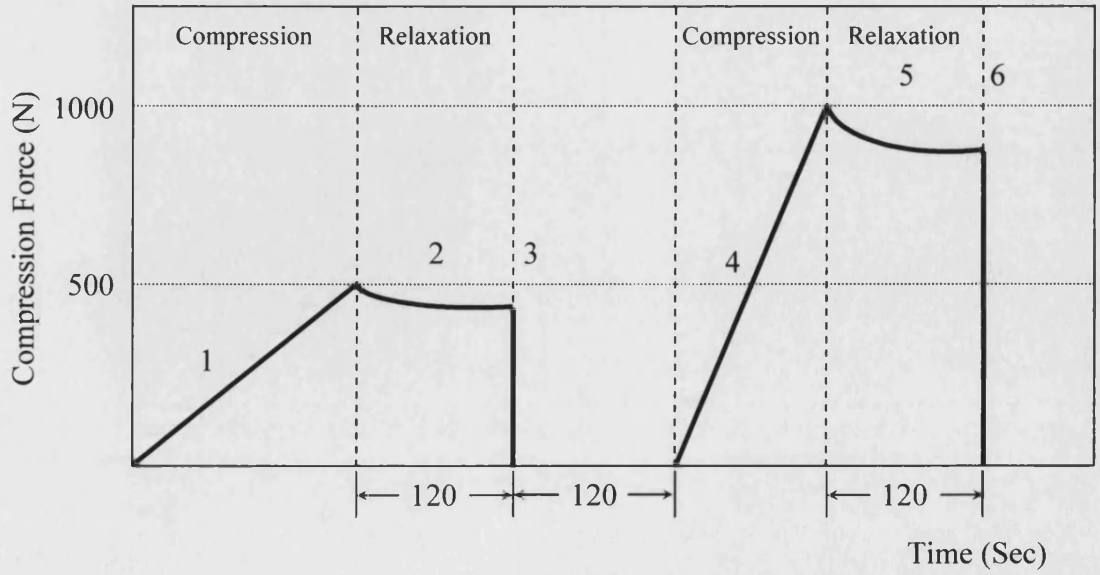

Figure 3.23 Stages in the die-plunger testing.

3.5 Functional Gradient Materials (FGM)

3.5.1 Fabrication Techniques for Functional Gradient Materials (FGM)

In order to make a functional gradient material (FGM) with porosity gradients similar to the bimodal structure of cortical and cancellous bone, two different foams were joined together either by stitching or pressfitting. Figure 3.24 shows two foams which were joined by stitching. A hot cut method was applied to make cylindrical foam templates by using stainless steel cylinders of different dimensions as shown in Figure 3.25. Figure 3.26 shows a cylindrical foam and a hollow foam produced by the hot cut method and Figure 3.27 shows these two foams joined together by pressfitting. Foams with different ppi could be used as the cylindrical foams and the hollow foams. The relative ratio of the diameter of the insert foam and the diameter of the hole can be changed. In Figure 3.26, the cylindrical foam is a little bit larger than the hole to give a more porous structure in the centre of the sample. After the cylindrical foam was pressfitted into the hole, it was slightly compressed and became a more dense structure as shown in Figure 3.27.

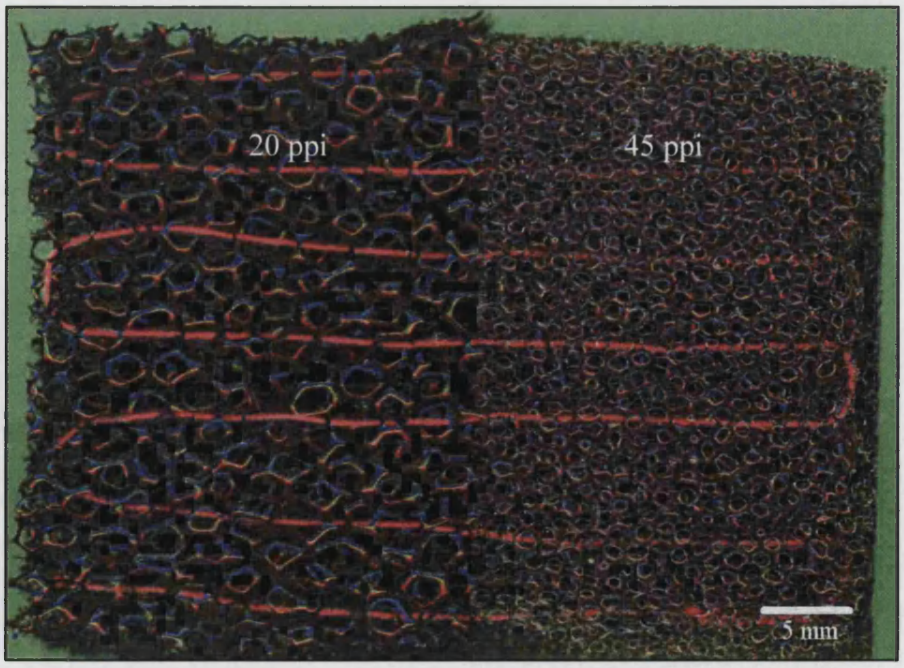

Figure 3.24 Two different ppi foams joined together by stitching.

Figure 3.25 Stainless steels cylinders used in a hot cutting method.

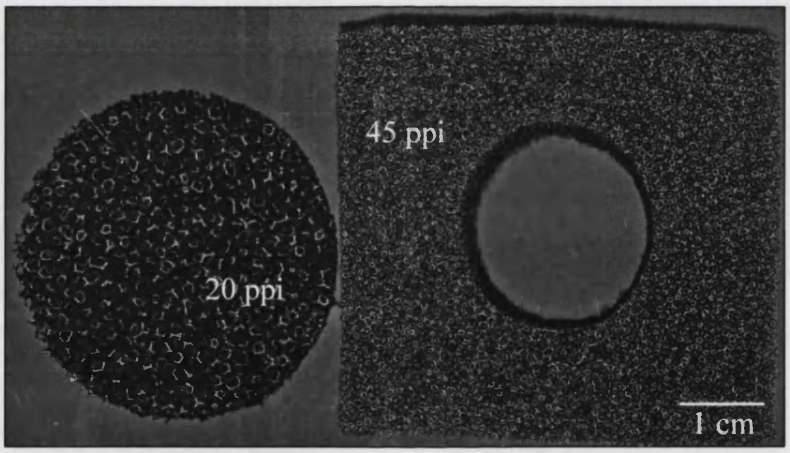

Figure 3.26 The foams were made by the hot cutting method.

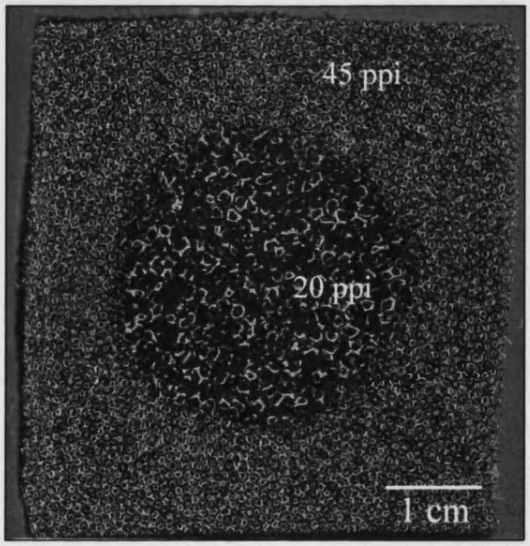

Figure 3.27 Two different ppi foams joined together by pressfitting.

In order to obtain samples with graded pore structures the following approach was employed:

a. A method of dipping foams into a slip of lower viscosity (less than 6,000 cps) was used to make a porous HA/TCP with higher porosity.

b. A low porosity green state sample from the vacuum impregnation (Figure 3.28 (b)) and the high porosity green state samples, obtained from work (a) (Figure 3.28 (a)), could also be combined together by pressfitting as shown in Figure 3.28 (c). It was possible to make a FGM with much greater porosity gradient.

The relative ratio of the diameter of the insert foam and the diameter of the hole can be changed.

(a) High porosity sample from dipping method.
(b) Low porosity sample from vacuum impregnation method.
(c) Sample (a) and (b) joined together by pressfitting.

Figure 3.28 The method to obtain samples with two extremely different graded pore structures as close as possible to human bone morphology.

3.5.2 Four-Point Bending Testing for FGM

In order to estimate the strength of the interface between the two different structures of the FGM, four-point bend testing was employed. Four samples were tested in four-point bending testing. The samples for the testing were prepared in the similar way to those samples described before. The FGM were joined together by stitching as shown in Figure 3.29.

A slip of 100 wt% solid loading was used. The sintered large block of FGM was sectioned into small bars, which have two different porous structures, for four-point bending testing. The aim of the testing was to compare the strength of the FGM and homogeneous materials and to investigate if the interface of the FGM a source of weakness. The samples were tested using an Instron 1122 testing machine with a crosshead speed of 0.5 mm/min and the span was 20 × 40 mm. The conditions for four-point bending testing were the same as described before in section 3.4.2.1. Four-point bend testing was used rather than three-point bending to maintain consistency with the previous testing. Three-point bend testing has limitations in that the maximum flexural stress is at the point of load application, but linearly decreases to zero at the outer supports. The sample should be damaged near the point of load application. In four-point bending, there is a large region of maximum flexural stress between the inner supports so this test should be able to explore the source of weakness more accurately.

The four-point bend strengths (σ) were calculated by the equation:

σ (Pa) = $3F(L-L_1) / 2bd^2$ (N/m^2)

where

F = applied force

L = the span of the support loaders

L_1= the separation of the loading span

b = sample width

d = sample thickness

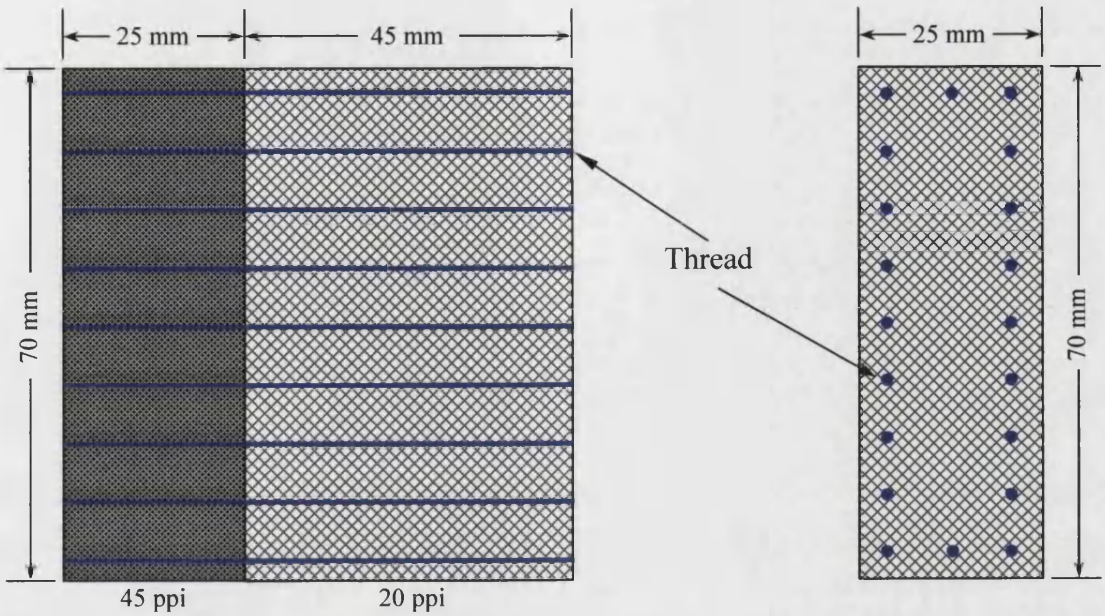

Figure 3.29 Schematic representation of the stitching method used to join two foams together.

CHAPTER 4

RESULTS AND DISCUSSION

This chapter presents the results of macro and microstructural analysis of samples. Mechanical property data on the work of fracture, compressive properties and four point bend strengths are presented. The development of functional gradient materials is also covered.

4. Results and Discussion

4.1 Properties of Slips

Without any dispersant added, the slip was difficult to handle with poor flow properties especially at high solid loadings. After a suitable amount of dispersant (Dispex A40) had been added, the slip was able to flow easily. Sufficient dispersant needed to be added prior to ball milling. An appropriate quantity was important not only at the initial stage but also during the whole process of ball milling, when the viscosity of the slip would increase. If the viscosity was too high, the slip would stick to the wall of the container making the milling process ineffective. Although the slip was made under exactly the same conditions (the same constituents and identical balling conditions), the resulting viscosity could differ from batch to batch. The viscosity was critical to the success of the impregnation so was adjusted to the required value by adding a suitable amount of dispersant before impregnation. The ideal viscosity range for initial impregnation was found to be 6,000 to 8,800 cps as the slip needed to pass through the plastic tube; a broader range was appropriate for the second impregnation method (6,000 to 13,600 cps). However, the ideal viscosity varied between solid loadings.

4.2 Calcium Phosphate Bioceramics

4.2.1 Porous Calcium Phosphate

Figure 4.1 shows the appearance of the sintered porous HA/TCP ceramic blocks before and after grinding. They were made from the foams with standard dimensions, 30 × 30 × 25 mm, but three different ppi. The sintered samples were strong enough to section and grind to any geometry. Figure 4.2 shows different shapes of porous HA/TCP samples made by the vacuum impregnation method. Porous samples with various geometries such as cubic, cylindrical and wedge shapes could be produced by different initial forms of PU foams. The shrinkage of the sintered samples compared to the starting PU foams was about 30 %. Therefore, the dimensions and shapes of the samples can be decided before impregnation. After sintering, samples could be sectioned and ground to a diversity of shapes. This demonstrates that this method can be used to produce porous HA/TCP bioceramics with different shapes or even irregular three-dimensonal shapes.

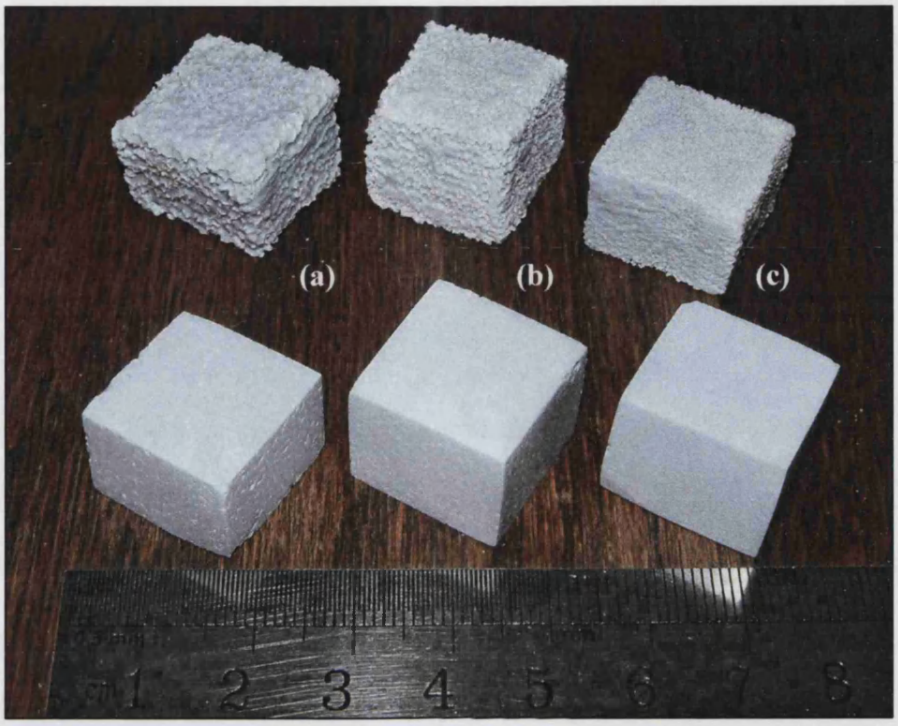

Figure 4.1 Photograph of the sintered porous HA/TCP ceramics before and after grinding. The blocks were generated from the foams (a) 20 ppi (b) 30 ppi (c) 45 ppi.

Figure 4.2 Photograph of the sintered porous HA/TCP ceramics with different geometries.

Before sintering, all of the samples, including powders and green state blocks were white in colour. After sintering, the HA/TCP samples showed a blue discoloration. Some of them even had gradient colour, which was bluer in the centre of the block samples. The colours seem to be dependent on the sintering temperature and the blend ratios of TCP 118 and TCP 130 powders. The TCP 118 powder allows the final sintered products to comprise β-tricalcium phosphate (β-TCP) and α-tricalcium phosphate (α-TCP) as well as some hydroxyapatite (HA) depending on the sintering temperature. TCP 130 is a stable, highly crystalline form of HA and does not undergo phase transition on sintering. Higher sintering temperature and more TCP 130 powder produced deeper blue samples.

It has been noted by Yubao et al[287] that HA containing manganese shows a blue colour after sintering at high temperature in an oxidizing atmosphere but the TCP samples remained white. When sintering in an argon atmosphere, all HA and TCP samples were white in colour. This phenomenon is related to the oxidation of manganese ions in the crystal structure of hydroxyapatite. The high temperature not only increases the oxidation power of the oxidizing atmosphere but also provides enough energy for the oxidized manganese ions to facilitate their migration within the crystal lattice.

The above discussion may offer a general explanation the blue colouration in samples. However, it does not explain the reason for the deeper blue colour observed in the centre of the block samples produced for this project. During the sintering process, the highest temperature and most oxidizing atmosphere are unlikely to be at the centre of the sample. Further investigation is needed to determine the colour change in the samples and whether such a change depends only on the oxidation of manganese ions or also on other factors, such as impurities other than manganese.

4.2.2 Porous Granular Form of Calcium Phosphate

Figure 4.3 shows porous HA/TCP bioceramics with various dimensions fabricated by the vacuum impregnation method. The largest sample (left) in this figure was made from the standard foam dimensions, 30 × 30 × 25 mm. Figure 4.4 shows 4 mm granules, which were made from different ppi foams, having a regular size and shape. A cross-section of the porous granules can be seen in Figure 4.5. Granules with the dimensions of 6 mm and 8 mm can be seen in this macrograph. This demonstrates the method could be used to make HA/TCP granules in the size range of 2 to 8 mm with interconnected porosity and controlled size and shape – hitherto not possible using existing manufacturing techniques. The technique developed is efficient when compared to making a large block of material and then breaking up the sintered product into smaller pieces, as is the current practice by one manufacture. Size and shape can be controlled and waste minimised.

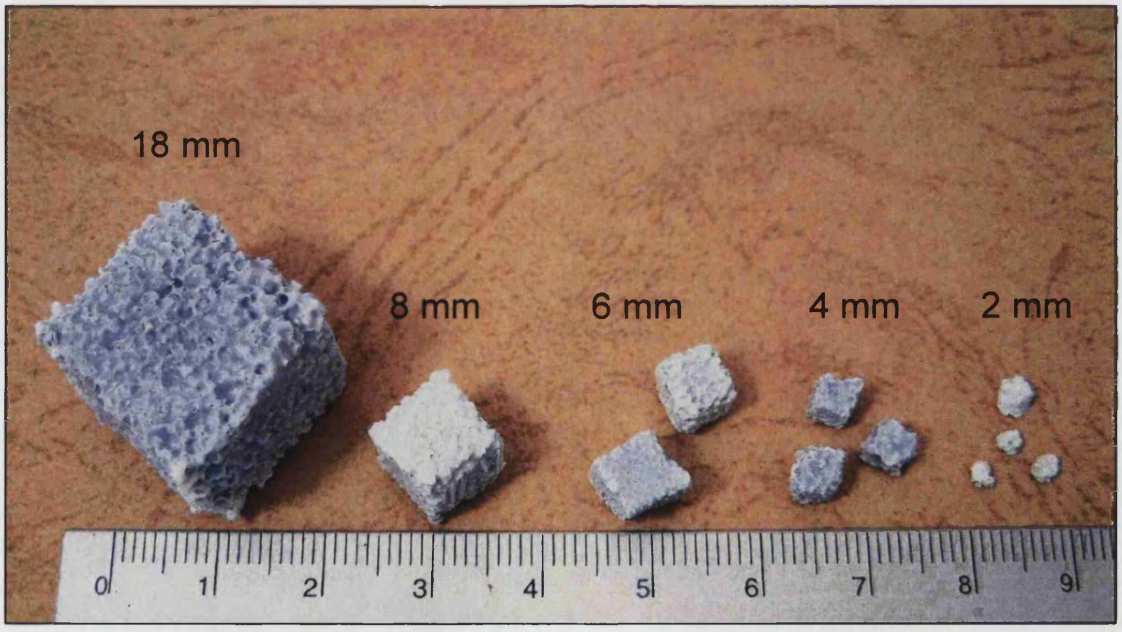

Figure 4.3 Porous HA/TCP bioceramics with different dimensions.

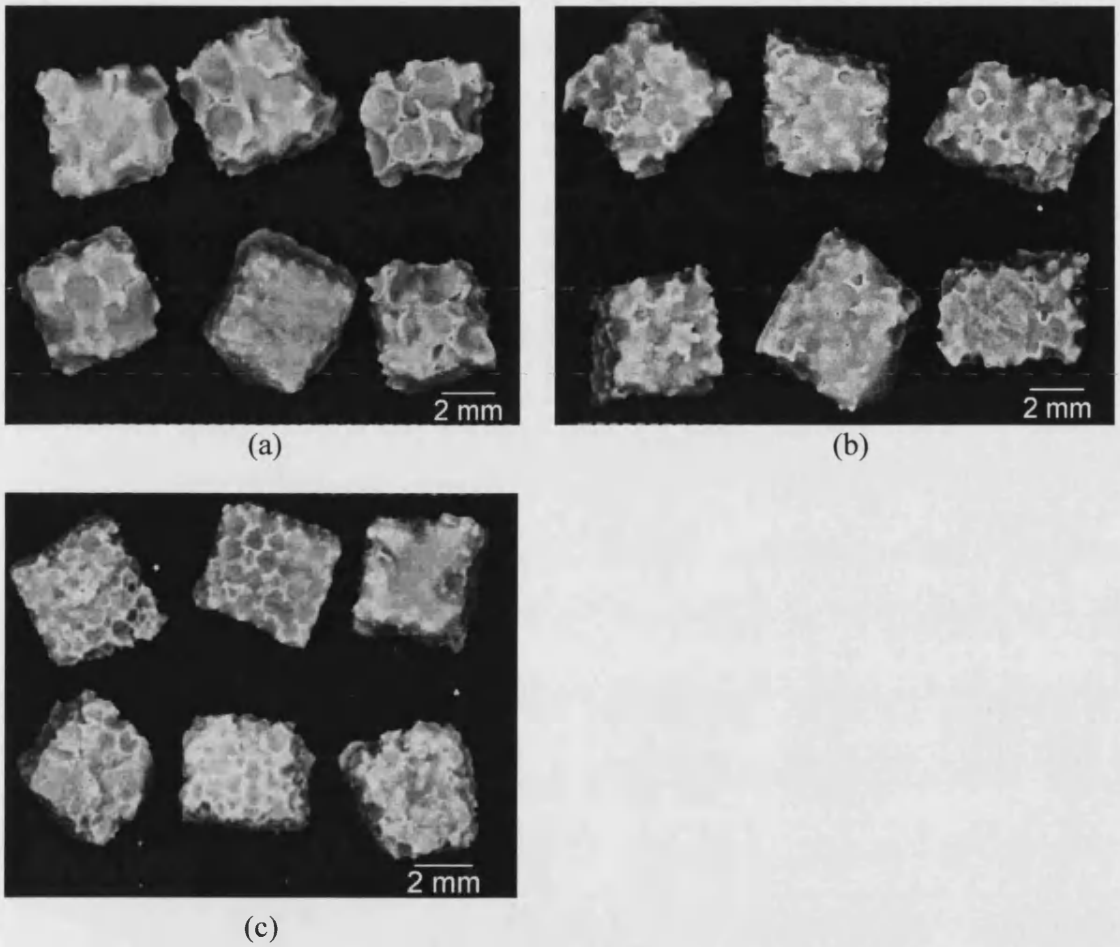

Figure 4.4 Porous HA/TCP granules made from (a) 20 ppi (b) 30 ppi (c) 45ppi foams.

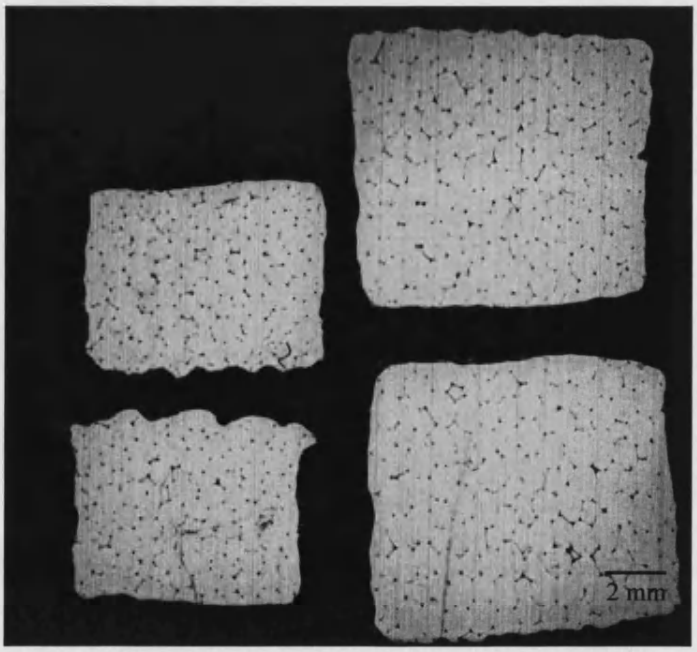

Figure 4.5 A cross-section of porous granules fabricated by the vacuum impregnation method.

4.2.3 Solid Calcium Phosphate

The slip-casting method was used to produce solid calcium phosphates, i.e. a dense material with no porosity. An important feature when making solid calcium phosphates via slip casting was found to be the mould material. The mould should be made of a material that absorbs water, to assist the excess moisture to drain away in order to avoid cracks foaming in the sample during the drying process. Many cracks were generated in samples made using plastic and ceramic moulds. Solid samples without cracks were made successfully by using slip with a higher solid loading and moulds made from paper flowerpots or cardboard egg boxes. Samples from paper flowerpots had limited size and shape for mechanical testing. Using an egg box it was possible to produce two samples in the size of 60 × 40 × 20 mm that were suitable for further mechanical testing. Figure 4.6 shows a solid calcium phosphate sample made using an egg box mould.

Figure 4.6 Solid calcium phosphate made by slip-casting method.

4.2.4 Summary of Results and Key Findings

- Calcium phosphate ceramic slips with very high solid loading (in excess of 100 wt%) and viscosities sufficiently low for impregnation operations could be prepared by adding a suitable amount of Dispex A40 as dispersant and processing using ball milling.
- The vacuum impregnation method can be used to process porous HA/TCP blocks with both regular and irregular three-dimensonal shapes.
- The method can be used to make porous HA/TCP granules in the size range of 2 to 8 mm with interconnected porosity and controlled size and shape – hitherto not possible using existing manufacturing techniques.
- Non-porous solid calcium phosphate samples without cracks were made by the slip-casting method using a mould based on water absorbent materials.

4.3 Macroscopic Analysis

4.3.1 Macroscopic Analysis

This section focuses on analysis of the porous structure of the HA/TCP samples recorded using an optical scanner. Samples were made from slips with 60 to 160 wt% solid loading and the foams of 20, 30 and 45 ppi. The slip viscosities were controlled in the range of 6,800 to 13,600 cps. Two different impregnation methods were used. The first method was to vacuum before and during the impregnation and the second method was to vacuum after the impregnation. Each method involved both single and double impregnation. Single impregnation is on the left and double on the right of the following figures.

Figure 4.7 shows the porous structure of the HA/TCP made using the first vacuum impregnation method. The samples illustrated were made from slips with 60 wt% solid loading combined with 20, 30 and 45 ppi foams, using both single and double impregnation. It can be seen that samples produced using single impregnation have a significant number of large isolated holes internally. This might be because when the samples were dried on tissue, the foams could not retain all of the slip. This problem was overcome by double impregnation. The samples, which can be seen on the right, have an excellent interconnected porous structure without the presence of large isolated holes. Nearly 100% of the macroporosity arises from the PU foam structure. The effect of the second impregnation was probably that when the samples were dried on tissue most of the water would be extracted from the slip and the solid loading of the slip in the foam would increase. The second impregnation would then supplement the first impregnation. Figure 4.8 shows the samples made from the second processing method. These pictures show similar results to the samples made from the first processing method. However, it can be seen that the samples shown in Figure 4.8 (a) and (d) are very similar. This illustrated that for the 20 ppi foam, a single impregnation can sometimes be successful. This may be as a consequence of the larger diameter pores.

Figures 4.9 and 4.10 show the results of the HA/TCP made from both the first and second processing methods with 80 wt% solid loading slip. These pictures show comparable results to the samples from 60 wt% slip. The samples made by double impregnation were of higher quality than those produced by single impregnation. Comparing the samples made both by single impregnation in the first vacuum

impregnation method but different solid loading in Figures 4.9 (a)(b)(c) and Figures 4.7 (a)(b)(c), the samples made from 80 wt% solid loading had less isolated holes. Similar observations were made with respect to the second processing method. The macro-structures in Figures 4.10 (a)(b)(c) look better quality than those illustrated in Figures 4.8 (a)(b)(c). This shows samples made by single impregnation with higher solid loading can be more successful using both the first and second processing method. The samples in Figures 4.10 (a)(d) and 4.10 (b)(e) had similar appearances showing that for the 20 and 30 ppi foams both techniques could be used successfully.

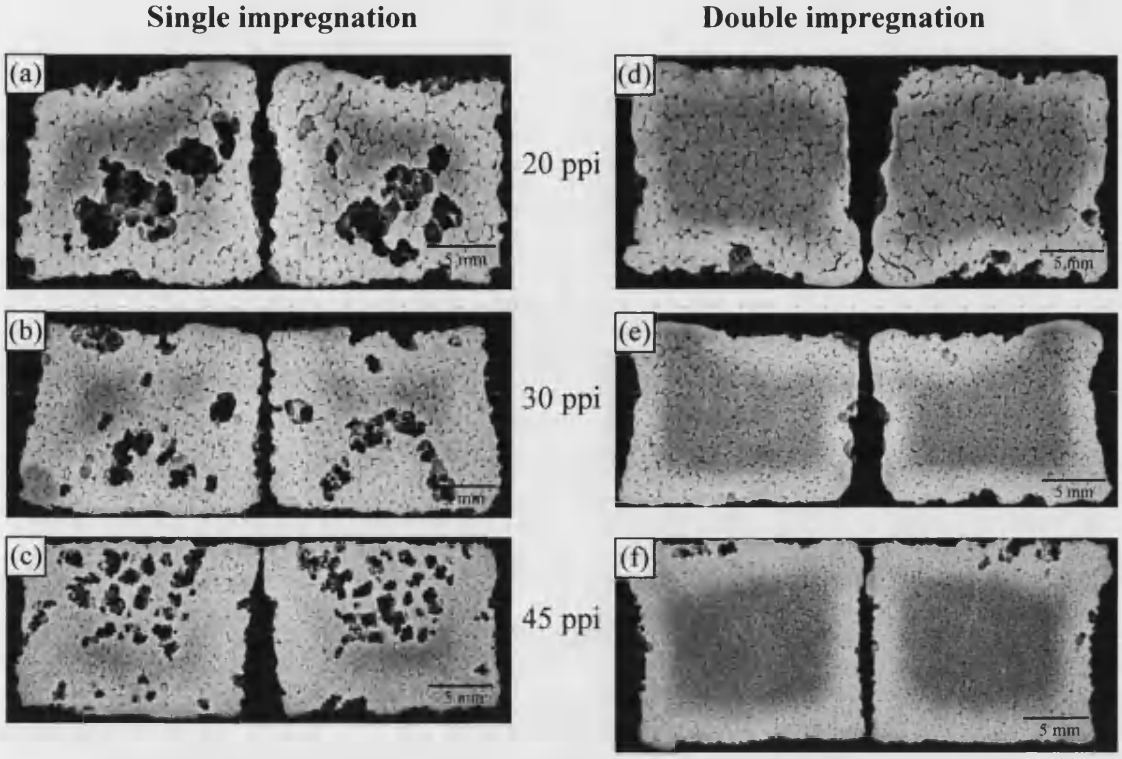

Figure 4.7 A cross-section of porous HA/TCP generated by the first vacuum impregnation method with slip of 60 wt% solid loading. Single impregnation is on the left and double on the right. Foam: (a)(d) 20ppi (b)(e) 30ppi (c)(f) 45ppi.

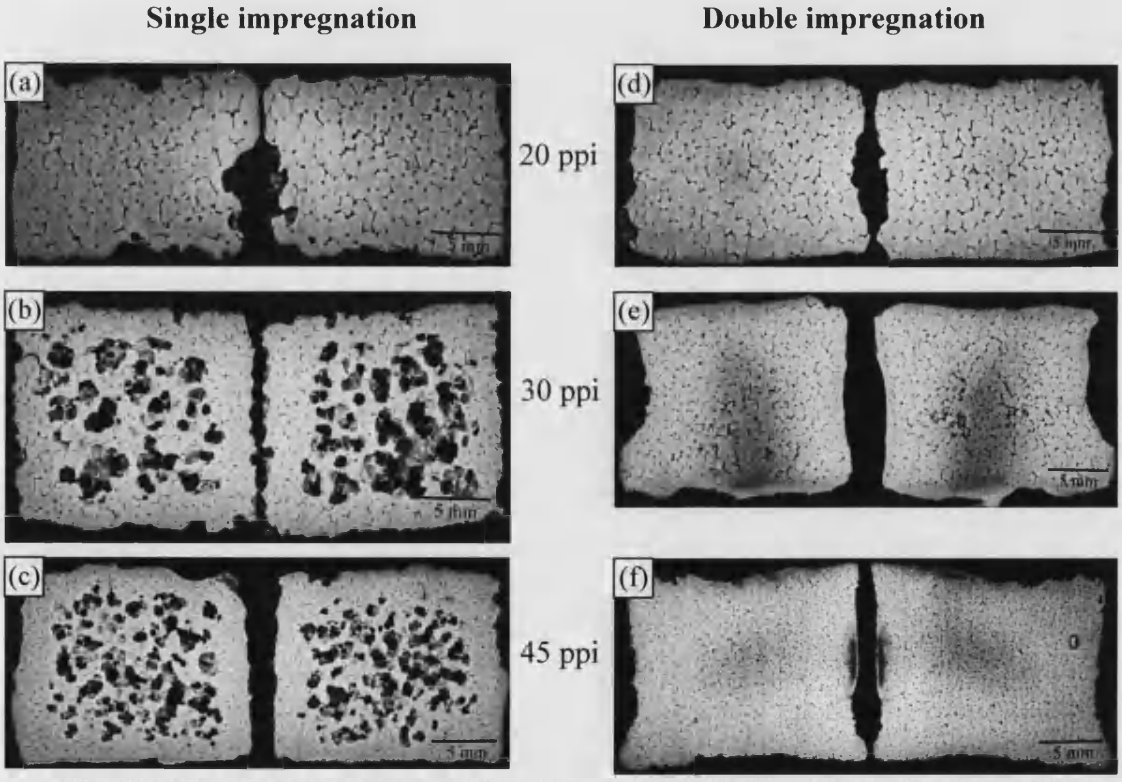

Figure 4.8 A cross-section of porous HA/TCP generated by the second vacuum impregnation method with slip of 60 wt% solid loading. Single impregnation is on the left and double on the right. Foam: (a)(d) 20ppi (b)(e) 30ppi (c)(f) 45ppi.

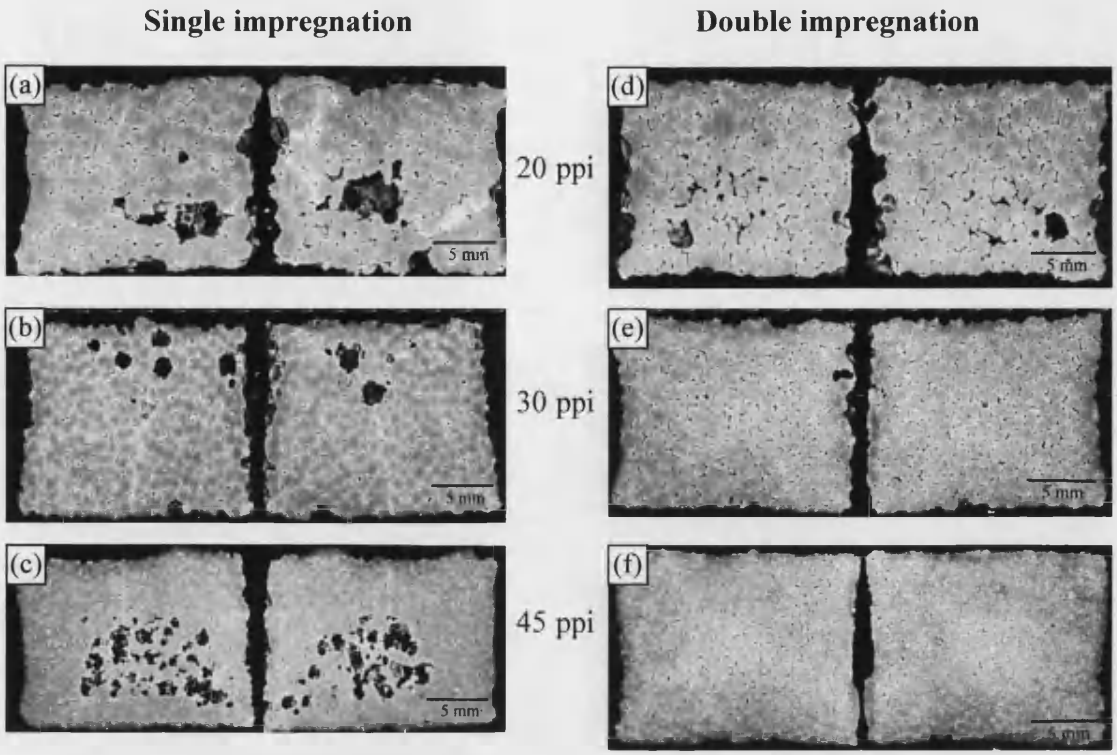

Figure 4.9 A cross-section of porous HA/TCP generated by the first vacuum impregnation method with slip of 80 wt% solid loading. Single impregnation is on the left and double on the right. Foam: (a)(d) 20ppi (b)(e) 30ppi (c)(f) 45ppi.

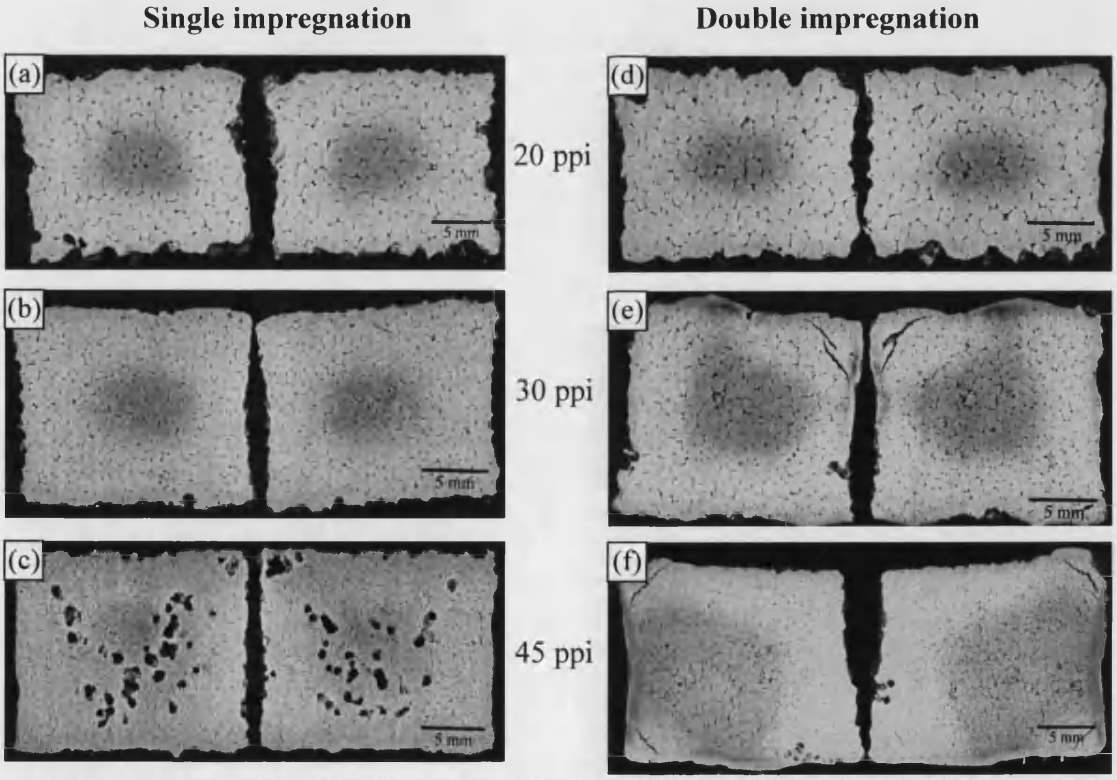

Figure 4.10 A cross-section of porous HA/TCP generated by the second vacuum impregnation method with slip of 80 wt% solid loading. Single impregnation is on the left and double on the right. Foam: (a)(d) 20ppi (b)(e) 30ppi (c)(f) 45ppi.

The samples made from slips with 100 wt% solid loading are shown in Figures 4.11 and 4.12. In the first method, double impregnation was still superior to single impregnation. However, the samples made by single impregnation had fewer large isolated holes in this 100 wt% slip compared to the sample from lower solid loading. This may be as a result of the slip with the higher solid loading drying more quickly enabling more ceramic to stay in the foam after the drying procedure. In the second impregnation method, samples from both single and double impregnation were of a high quality. There was no obvious difference between samples made using both single and double impregnation. If anything, the double impregnation samples seemed to have a greater number of defects relative to the single impregnation samples. Some can be seen clearly at the corners in Figures 4.12 (d) and (f) and holes in Figure 4.12 (e).

Figures 4.13 and 4.14 show the HA/TCP samples made from the slip with 120 wt% solid loading. Surprisingly, as can be seen in Figure 4.13, samples made by the single impregnation method were of better quality than those produced by the double impregnation using the first vacuum impregnation method. The only exception is the samples made from 20 ppi foams seen in Figures 4.13 (a) and (d). There were cracks and holes in the sample made by double impregnation using the first method, particularly in the sample made from 45 ppi foams which can be seen in Figure 4.13 (f). The difference between single and double impregnation using the second method, Figure 4.14, was not as obvious when compared to the first method. The observations in Figure 4.14 were similar to those in the 100 wt% slip as shown in Figure 4.12. Most of the samples produced using the second method had good macro-structures. Some holes appeared in the samples made from 20 ppi foam in Figure 4.14 (d) and small cracks at the corners in Figures 4.14 (a) and (f).

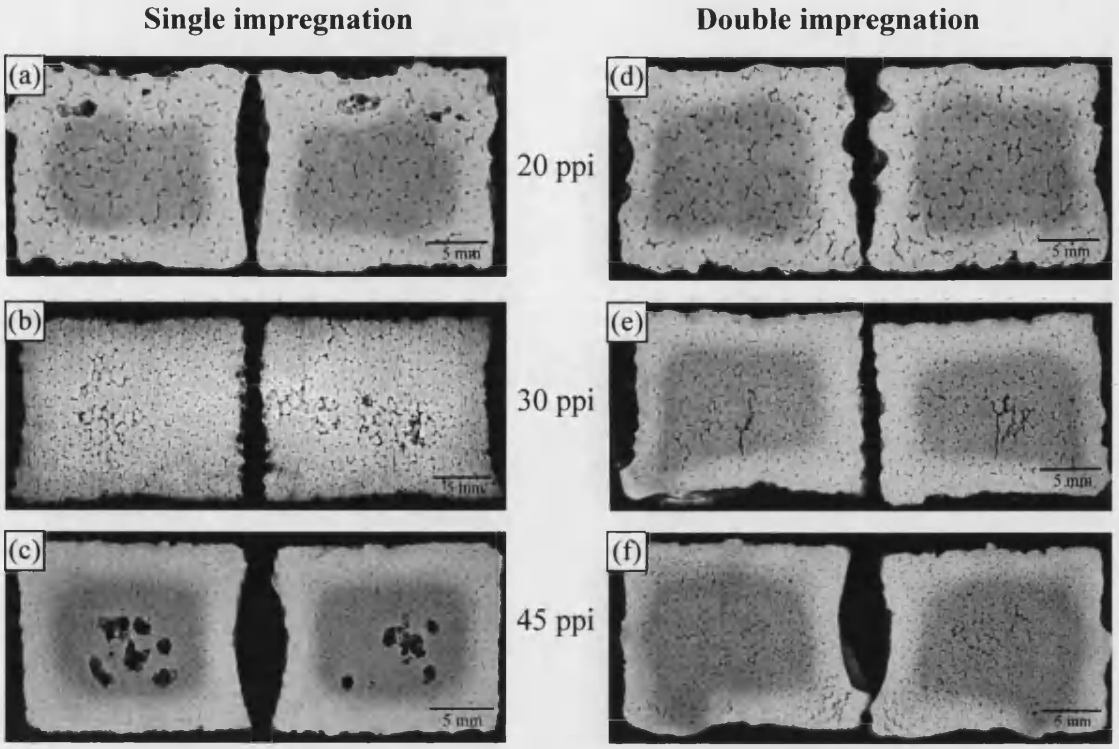

Figure 4.11 A cross-section of porous HA/TCP generated by the first vacuum impregnation method with slip of 100 wt% solid loading. Single impregnation is on the left and double on right. Foam: (a)(d) 20 ppi (b)(e) 30 ppi (c)(f) 45 ppi.

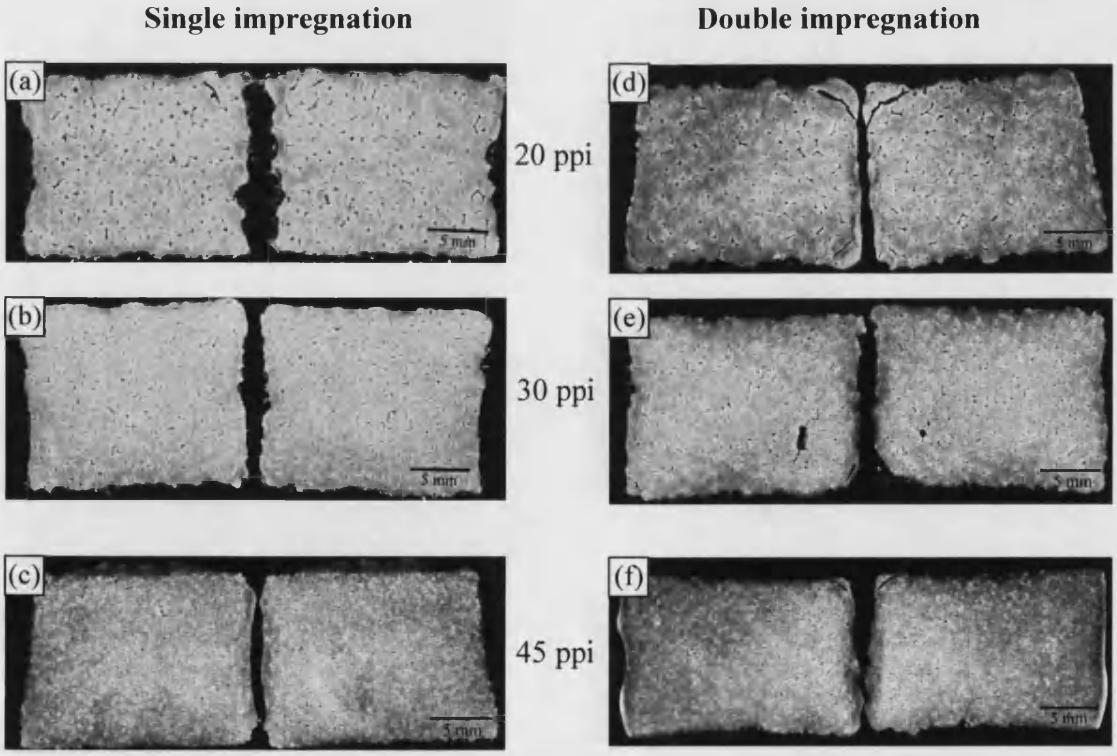

Figure 4.12 A cross-section of porous HA/TCP generated by the second vacuum impregnation method with slip of 100 wt% solid loading. Single impregnation is on the left and double on right. Foam: (a)(d) 20 ppi (b)(e) 30 ppi (c)(f) 45 ppi.

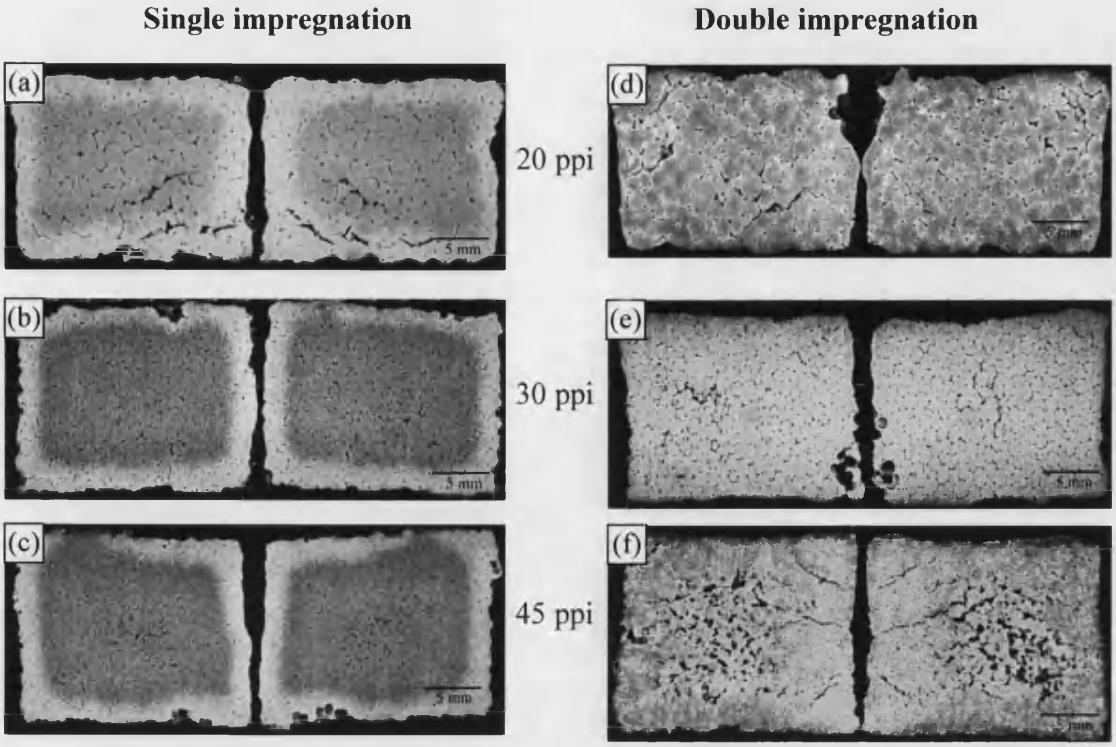

Figure 4.13 A cross-section of porous HA/TCP generated by the first vacuum impregnation method with slip of 120 wt% solid loading. Single impregnation is on the left and double on the right. Foam: (a)(d) 20 ppi (b)(e) 30 ppi (c)(f) 45 ppi.

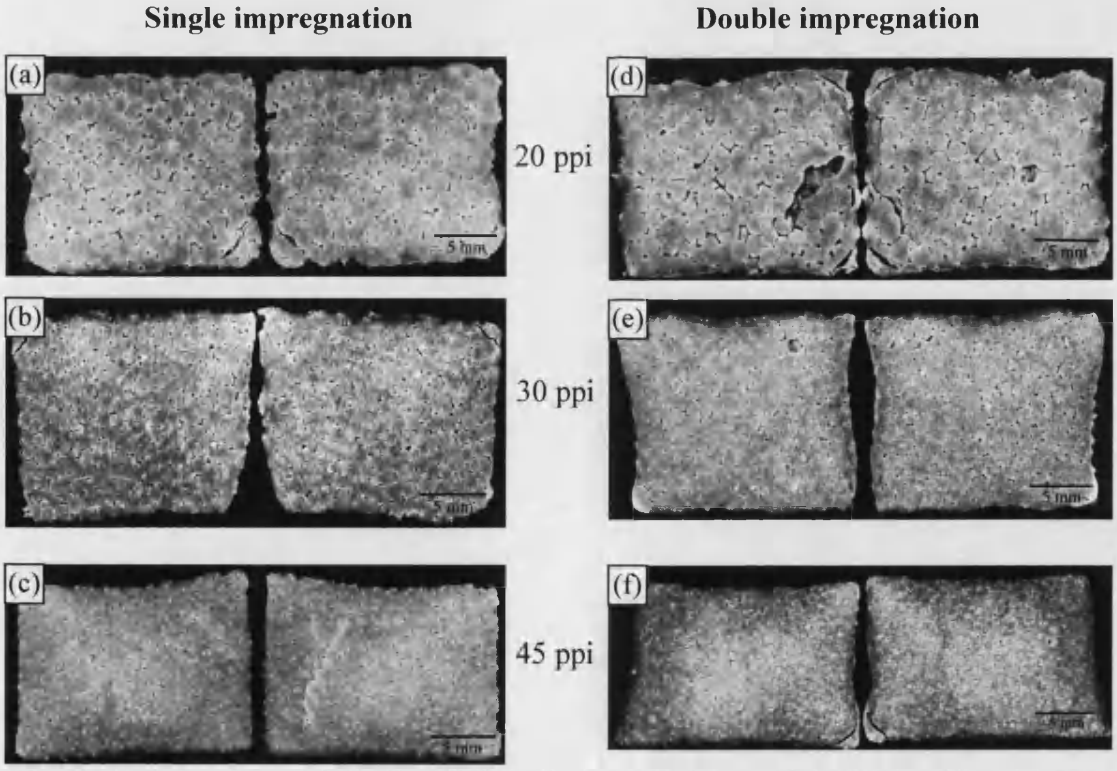

Figure 4.14 A cross-section of porous HA/TCP generated by the second vacuum impregnation method with slip of 120 wt% solid loading. Single impregnation is on the left and double on the right. Foam: (a)(d) 20 ppi (b)(e) 30 ppi (c)(f) 45 ppi.

Figures 4.15 and 4.16 show the samples made from the slip with 140 wt% solid loading. It can be seen clearly from Figure 4.15 that using the first vacuum technique, all of the samples were of poor quality. There are many cracks in these samples and they tended to have large holes in the centre which were also the source of cracks. These cracks may occur due to the difficulty of dispersing the slips which have a very high solid loading. In the most extreme situation, shown in Figure 4.15 (c), the slip did not appear to have impregnated the sample to a significant degree. An outer layer has been produced which has formed a hollow shell as the unimpregnated central PU core has burnt out on sintering. This is the result of the slip having poor flow properties combined with the 45 ppi foam which has the smallest diameter pore structure making it impossible to impregnate. The samples made by second method were much better than those produced by first method. This may be because the second method involved the compression step which could result in more effective impregnation. Using the second method, the samples looked of good quality, although all the samples made by double impregnation had cracks at the corners, as seen in Figures 4.16 (d) (e) and (f). This phenomenon was minimal on samples made by single impregnation. Only the samples made from 20 ppi in Figure 4.16 (a) had small cracks.

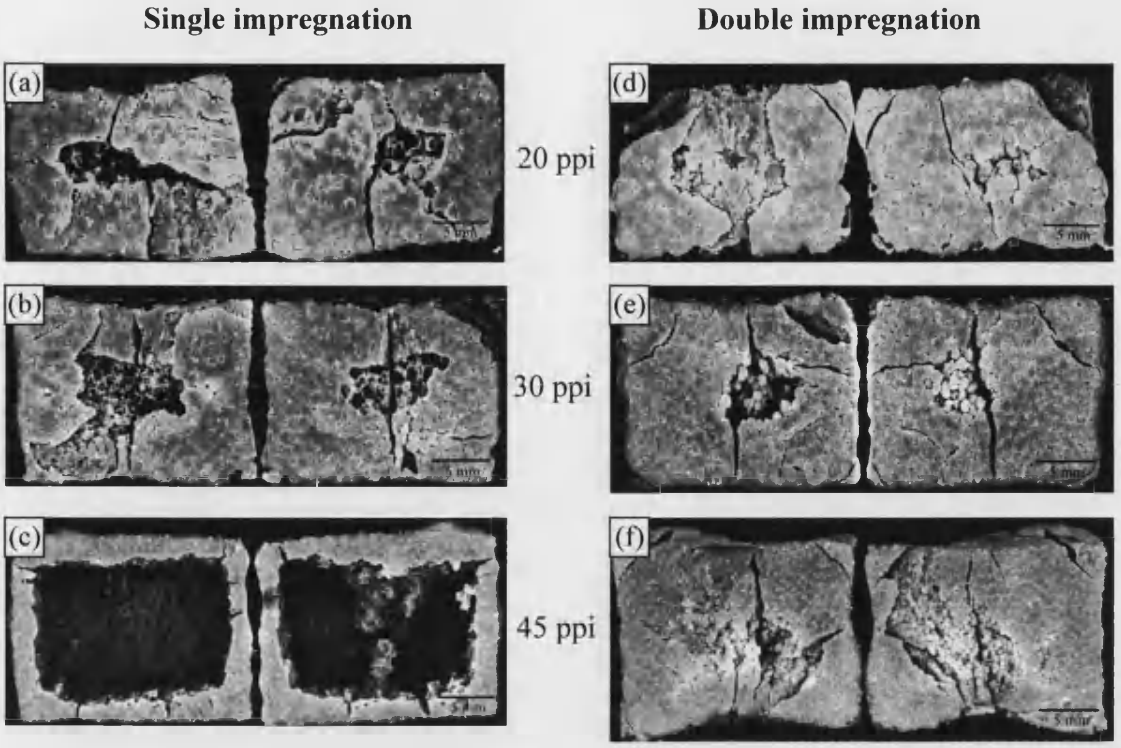

Figure 4.15 A cross-section of porous HA/TCP generated by the first vacuum impregnation method with slip of 140 wt% soild loading. Single impregnation is on the left and double on the right. Foam: (a)(d) 20 ppi (b)(e) 30 ppi (c)(f) 45 ppi.

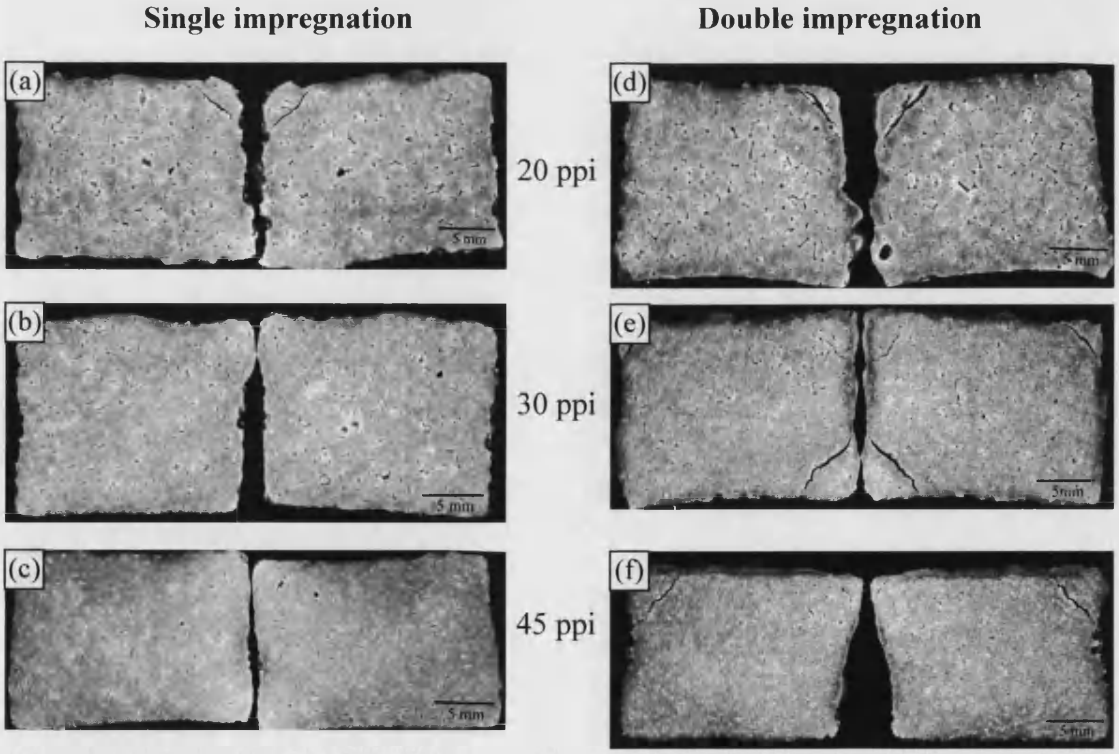

Figure 4.16 A cross-section of porous HA/TCP generated by the second vacuum impregnation method with slip of 140 wt% solid loading. Single impregnation is on the left and double on the right. Foam: (a)(d) 20 ppi (b)(e) 30 ppi (c)(f) 45 ppi.

The samples made from the slip with 160 wt% solid loading are shown in Figures 4.17 and 4.18. There were many cracks in the samples made using the first vacuum impregnation method. These samples in Figure 4.17 were similar to the samples made from the slip with 140 wt% solid loading in Figure 4.15. This showed these slips with high solid loading were not suitable for production using the first vacuum method. The sample in Figure 4.17 (c) had better quality than that in Figure 4.15 (c). This showed the poor impregnation, shown in Figure 4.15 (c), was an extreme case but could sometimes occur. The samples made using the second vacuum method were much better quality than those made by the first method but worse quality than the samples made from the slip with 140 wt% solid loading in Figure 4.16. There were cracks on almost every corner of all the samples shown in Figure 4.18.

The poorer quality of the double vacuum impregnated samples may be the result of the composition of the high loaded slip. The higher the slip loading, the lower the level of moisture present. As a result of this the samples may dry more quickly, particularly on the surface. When the sample is double impregnated, this dry surface may crack, resulting in the features observed in Figures 4.16 and 4.18. The reason why the cracks appear at the corners using single impregnation in Figure 4.18 may be similar. The dry surface may crack when the moisture drains from the centre.

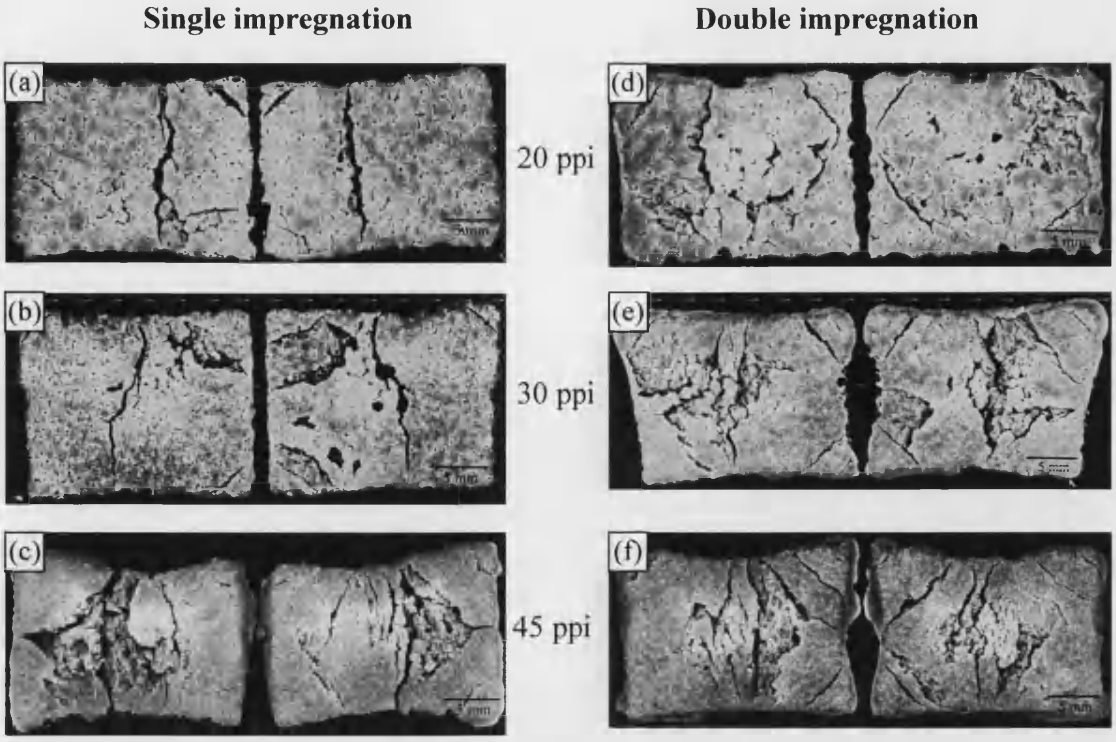

Figure 4.17 A cross-section of porous HA/TCP generated by the first vacuum impregnation method with slip of 160 wt% soild loading. Single impregnation is on the left and double on the right. Foam: (a)(d) 20 ppi (b)(e) 30 ppi (c)(f) 45 ppi.

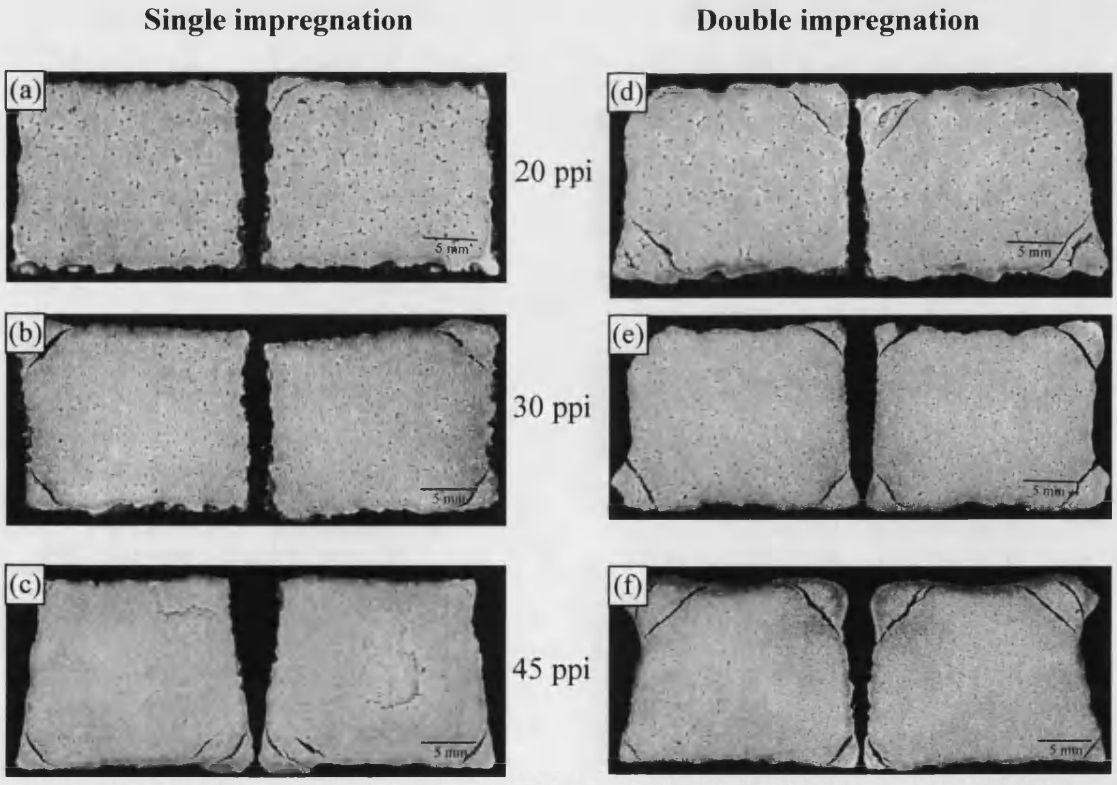

Figure 4.18 A cross-section of porous HA/TCP generated by the second vacuum impregnation method with slip of 160 wt% solid loading. Single impregnation is on the left and double on the right. Foam: (a)(d) 20 ppi (b)(e) 30 ppi (c)(f) 45 ppi.

The observations relating to the impregnation method and solid loading are summarized in Table 4.1. Comparing single and double impregnation in both processing methods, double impregnation was better when the solid loading is below 100 wt%. However, double impregnation was worse than single impregnation when the solid loading was over 100 wt%. Comparing these two main processing methods, the second method was slightly better than the first method with lower solid loadings but much better with higher solid loadings. This shows the compression process had a positive effect on impregnation. In addition, more samples could be produced simultaneously using the second method, as the vacuum vessel was much larger. However, the first vacuum impregnation technique had the advantage that it was possible to make more complex shapes, as using this technique did not involve the compression step. Complex foam structures such as the foams that are joined together to making FGM might be damaged during the compression process in the second vacuum impregnation method.

		First impregnation method		**Second impregnation method**	
Solid loading	Foam	Single impregnation	Double impregnation	Single impregnation	Double impregnation
60%	20 ppi	Poor, large pores	Good, no pores	Good	Excellent
	30 ppi	Poor, medium pores	Good, no pores	Poor, large pores	Good
	45 ppi	Poor, medium pores	Good, no pores	Poor, large pores	Excellent
80%	20 ppi	Poor, medium pores	Poor, small pores	Excellent	Excellent
	30 ppi	Fair, small pores	Good	Excellent	Good, cracks
	45 ppi	Poor, medium pores	Excellent	Poor, medium pores	Good, cracks
100%	20 ppi	Fair, small pores	Excellent	Excellent	Good, cracks
	30 ppi	Fair, small pores	Fair, cracks	Excellent	Fair, small pores
	45 ppi	Poor, medium pores	Good	Excellent	Good, cracks
120%	20 ppi	Fair, medium cracks	Fair, medium cracks	Good	Fair, medium cracks
	30 ppi	Good	Fair, small cracks	Good	Good
	45 ppi	Good	Poor, pores and cracks	Good	Good
140%	20 ppi	Poor, large cracks	Poor, large cracks	Fair	Fair, cracks
	30 ppi	Poor, large cracks	Poor, large cracks	Good	Fair, cracks
	45 ppi	Poor, large hole	Poor, large cracks	Good	Fair, cracks
160%	20 ppi	Poor, large cracks	Poor, large cracks	Good	Fair, cracks
	30 ppi	Poor, large cracks	Poor, large cracks	Fair, cracks	Fair, cracks
	45 ppi	Poor, large cracks	Poor, large cracks	Fair, cracks	Fair, cracks
Grade: excellent, good, fair, poor					

Table 4.1 Summary of the observations relating to the impregnation method and solid loading.

4.3.2 Scanning Electron Microscopy (SEM)

The SEM micrographs gave insight into the ceramic structures with respect to porosity, pore structure and pore size. Figure 4.19 shows the macroporosity generated by the first vacuum impregnation method, vacuumed before and during the impregnation, with 20 ppi foams. These macropores were produced by single or double impregnation with different solid loadings. There is no significant difference between these samples; the pore structures and pore distributions are similar. The main shapes of the macropores were bow tie and triangle shapes, which replicated the original shape of the struts of the PU starting foam. Figure 4.20 shows the macropores generated by the second vacuum impregnation method, vacuumed after the impregnation, with 20 ppi foams. These macropores also appeared bow tie and triangle in shape and the porous samples were the negative shape of the PU foam structures. In Figures 4.19 and 4.20, no obvious difference can be seen between the porous structures made from 20 ppi foams using different impregnation method and solid loading. The measurement of macropore size and porosity are detailed in the next section. The macropore size ranges in samples made from the 20, 30 and 45 ppi foams are shown in Table 4.2. The average macropore size in samples made from the 20 ppi foams was in the range of 197 to 254 μm. Figures 4.21 and 4.22 show the pore structure in 30 and 45 ppi foams. The shape and distribution of the macropores was similar to these made from 20 ppi foams. However, the relative sizes of the macropore were significantly different. This is not entirely surprising given that the foam structures are different. The macropore size in 30 ppi samples was in the range of 143 to 182 μm. The macropore size in 45 ppi was in the range of 105 to 135 μm, which is the smallest, but is still greater than 100 μm, which is a minimum pore size needed for bone ingrowth. This SEM study demonstrated that the major determinant of the macropore structure was the initial structure of PU foams and the pore sizes produced in this research were appropriate for bone ingrowth.

Foam (ppi)	Macropore size range (μm)
20	197 to 254
30	143 to 182
45	105 to 135

Table 4.2 The macropore size range in samples made from the 20, 30 and 45 ppi foams.

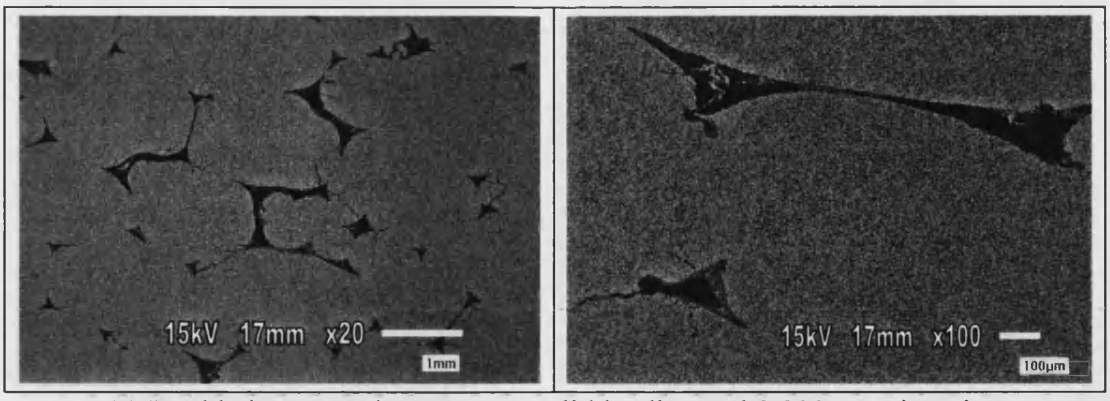

(a) Double impregnation, 60 wt% solid loading and 8,800 cps viscosity.

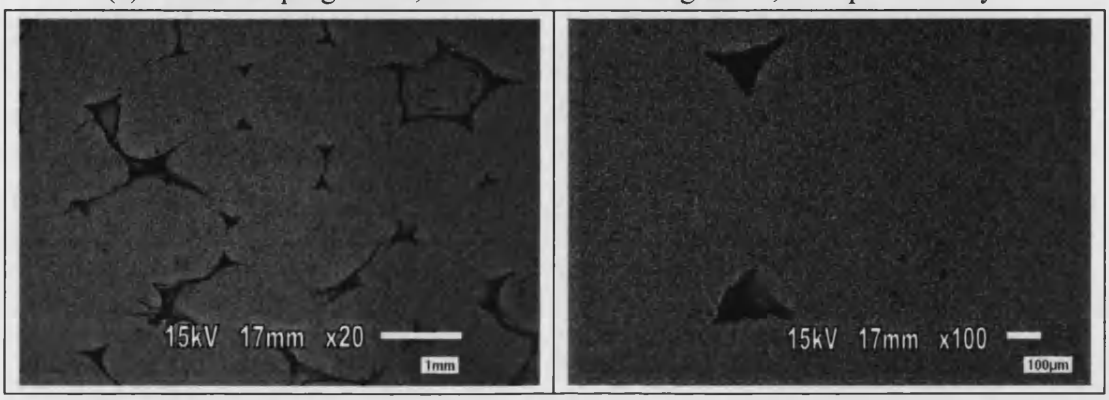

(b) Double impregnation, 80 wt% solid loading and 8,000 cps viscosity.

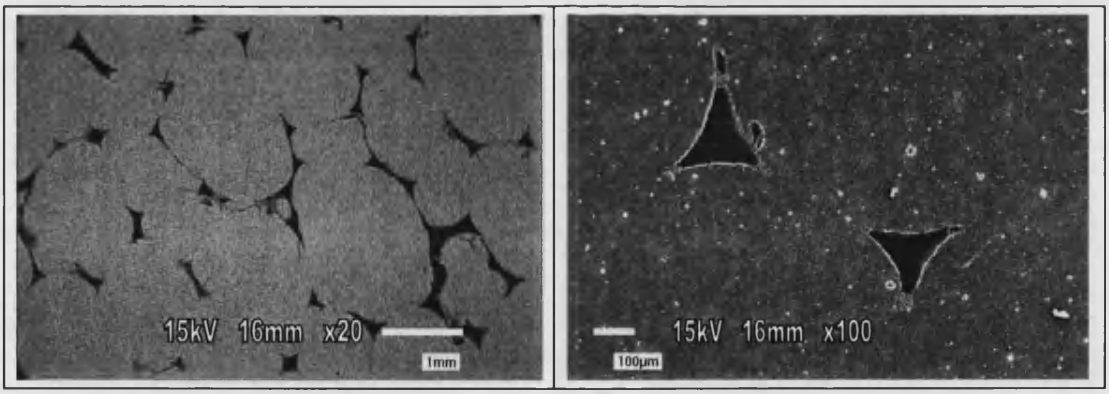

(c) Single impregnation, 100 wt% solid loading and 8,400 cps viscosity.

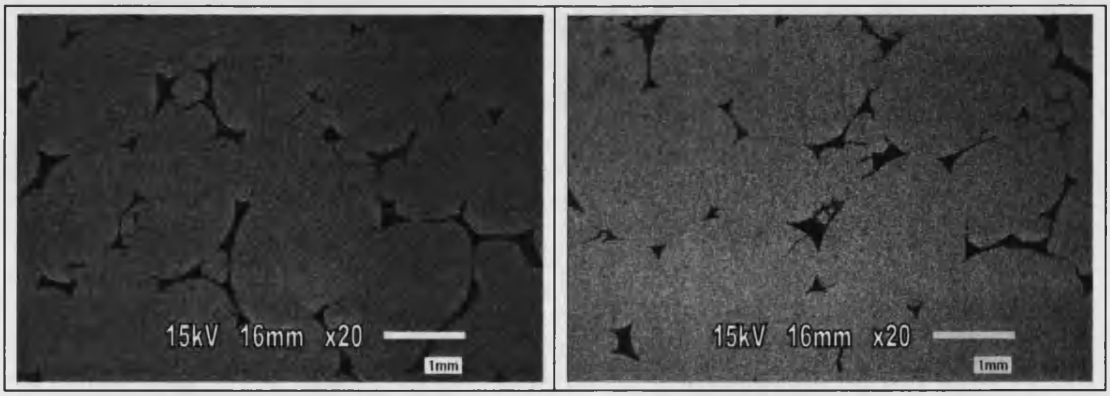

(d) Double impregnation, 100 wt% solid loading and 8,400 cps viscosity.

Figure 4.19 Macropores produced by the first vacuum impregnation method, vacuumed before and during the impregnation, with 20 ppi foams.

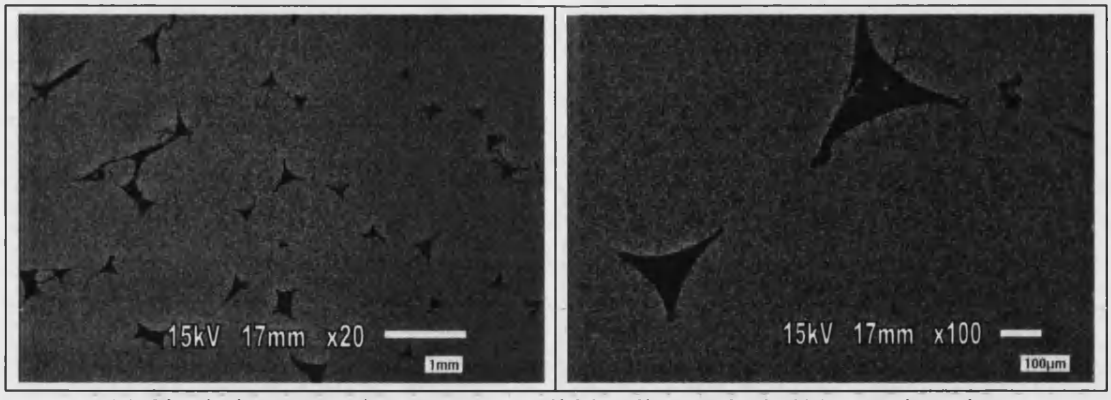

(a) Single impregnation, 60 wt% solid loading and 13,600 cps viscosity.

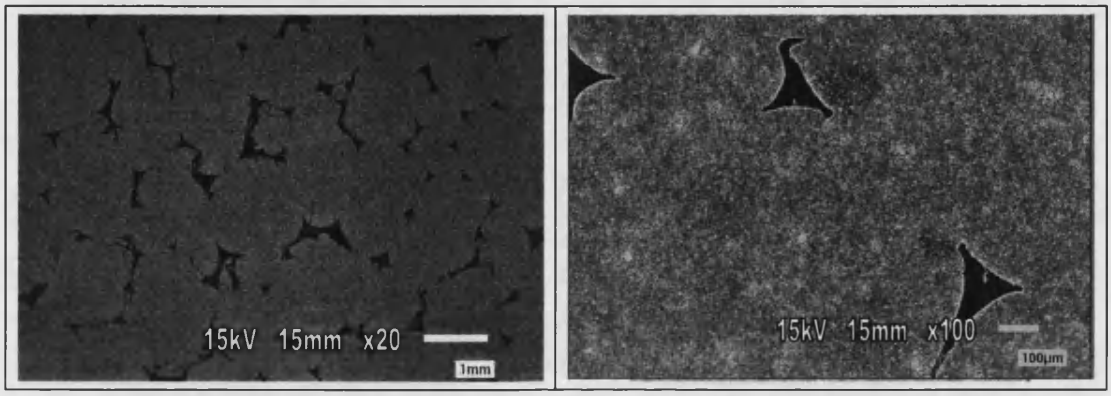

(b) Double impregnation, 60 wt% solid loading and 13,600 cps viscosity.

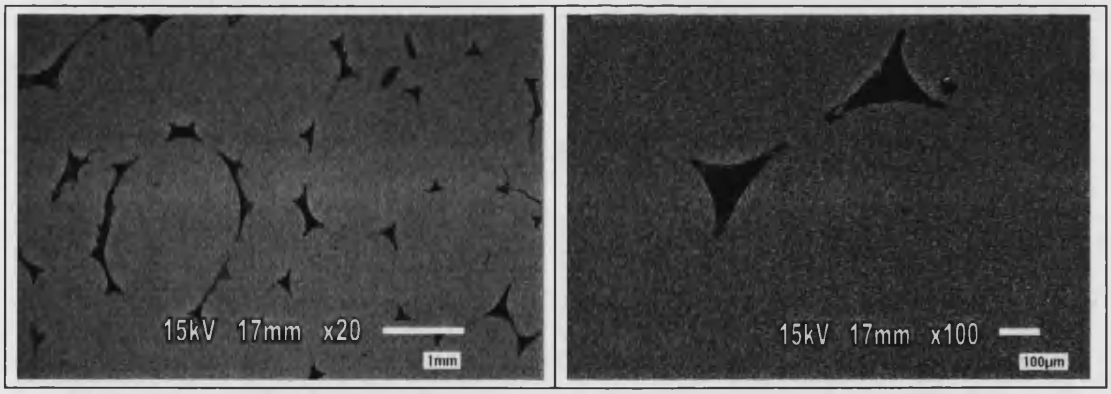

(c) Single impregnation, 120 wt% solid loading and 11,200 cps viscosity.

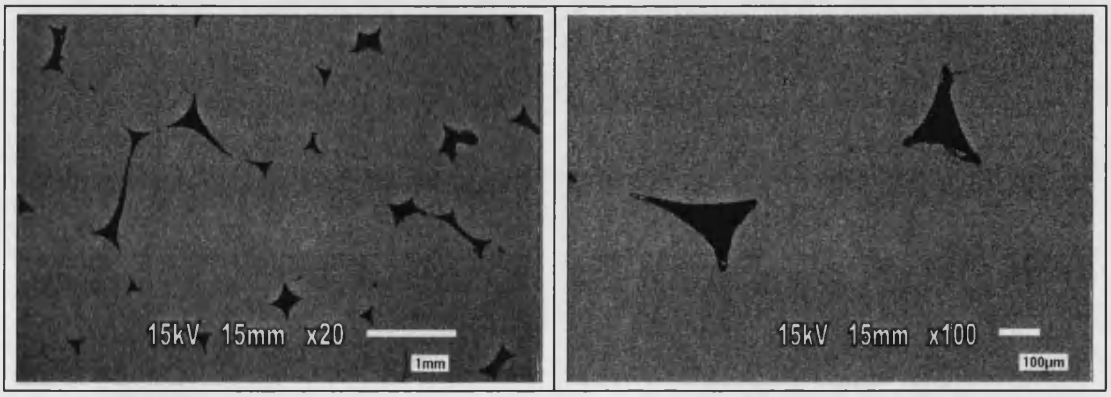

(d) Double impregnation, 120 wt% solid loading and 11,200 cps viscosity.

Figure 4.20 Macropores produced by the second vacuum impregnation method, vacuum after the impregnation, with 20 ppi foams.

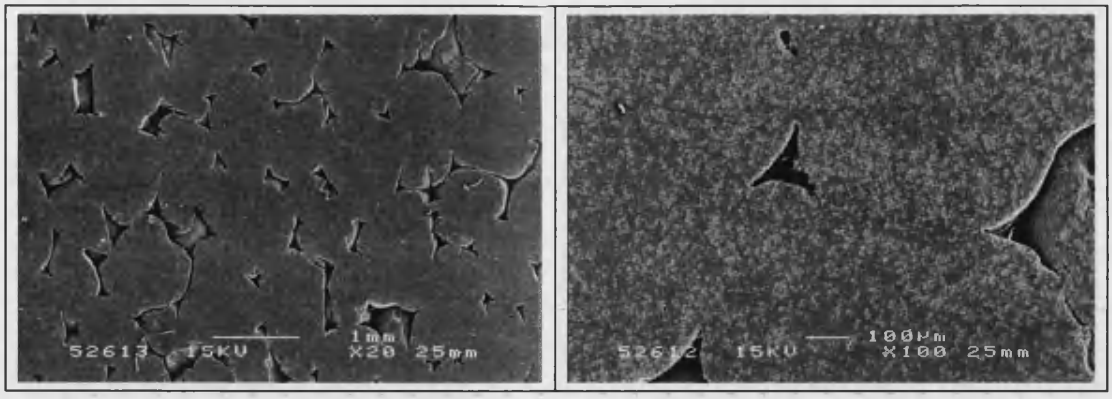

(a) First method, double impregnation, 60 wt% solid loading and 8,800 cps viscosity.

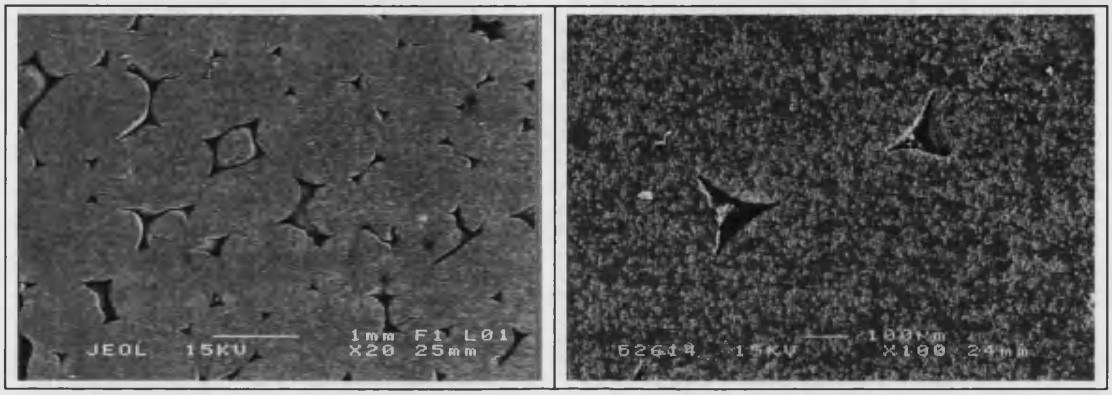

(b) Second method, double impregnation, 80 wt% solid loading and 9,600 cps viscosity.

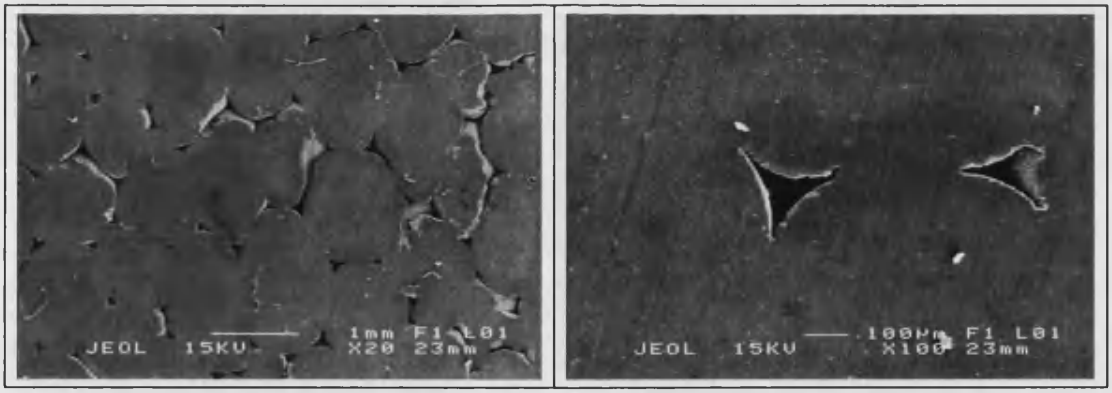

(c) First method, single impregnation, 100 wt% solid loading and 8,400 cps viscosity.

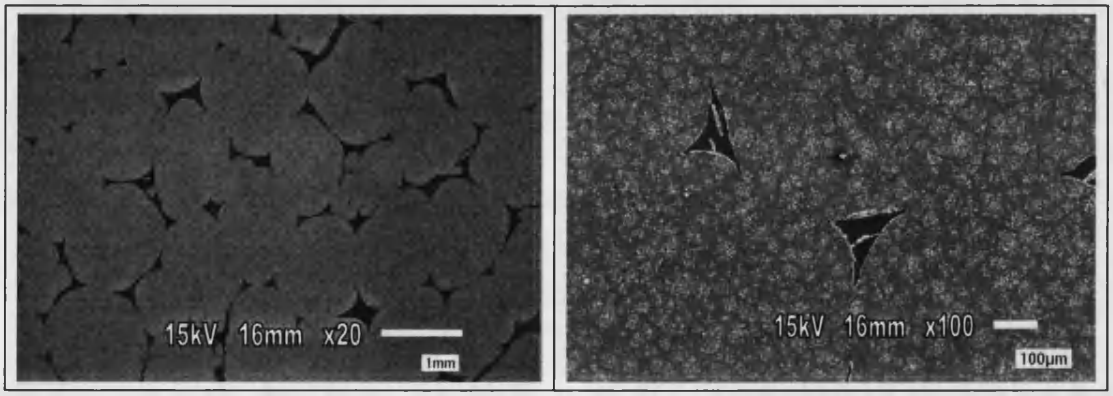

(d) Second method, single impregnation, 120 wt% solid loading and 11,200 cps viscosity.

Figure 4.21 Macropores produced by 30 ppi foams.

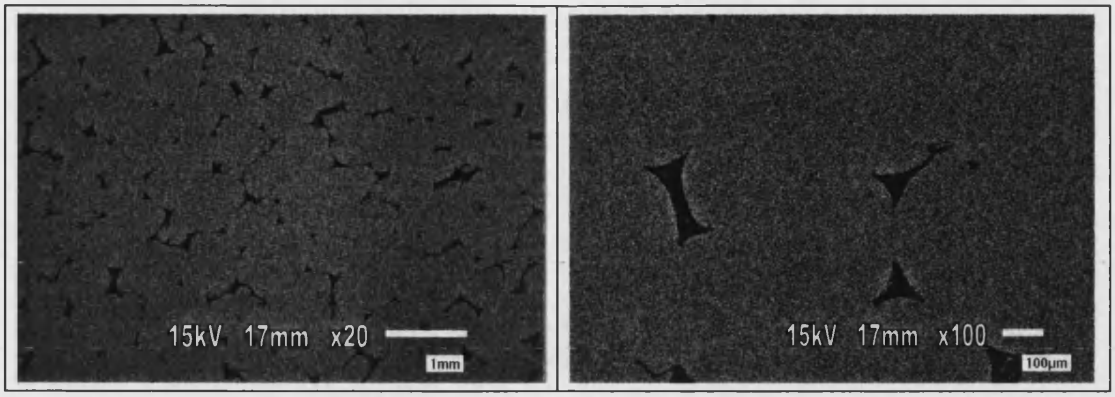

(a) First method, double impregnation, 60 wt% solid loading and 8,800 cps viscosity.

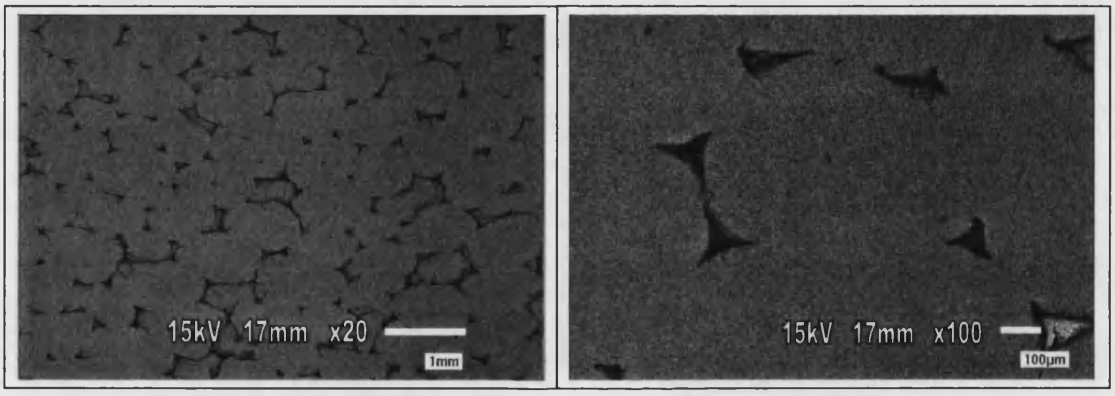

(b) First method, double impregnation, 80 wt% solid loading and 8,000 cps viscosity.

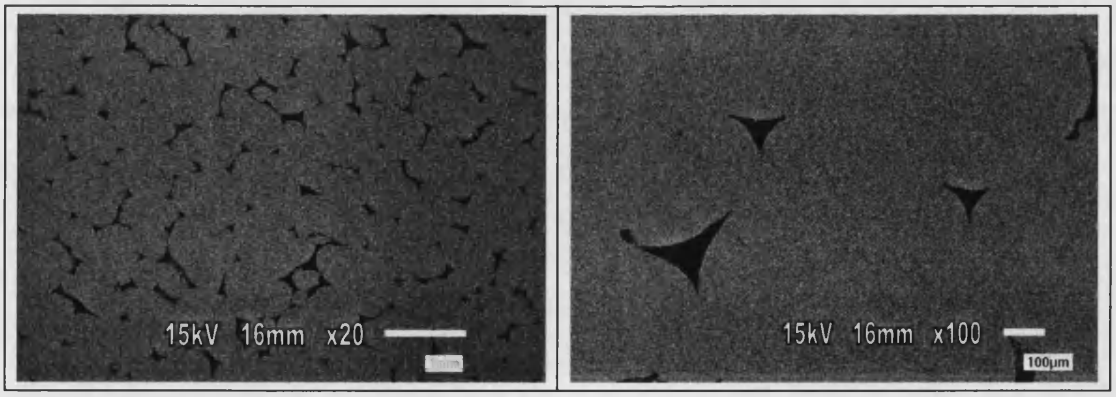

(c) Second method, single impregnation, 120 wt% solid loading and 11,200 cps viscosity.

Figure 4.22 Macropores produced by 45 ppi foams.

4.3.3 Macroporosity and Macropore Size

Macroporosity and macropore size for each sample type were measured from eight regions in two surfaces (20 × 20 mm). Image analysis showed the macroporosities measured for the samples made from three different ppi foams were similar in the range of 5.24 to 9.67%. The porosity measurements are shown in Figure 4.23 and Table 4.3. The porosities of samples made from 20 ppi foams were slightly higher than those made from the other two foams for the 60 to 80 wt% solid loading but lower for the 100 to 120 wt% solid loading. The 45 ppi foam tended to produce slightly higher porosities than 30 ppi foam; the only exception is the 60 wt% solid loading. However, the different ppi foams did not appear to have a large effect on level of macroporosity.

The slip loading did appear to have an effect on the porosity measurements above 80 wt%. For the slips of 60 to 80 wt% solid loading, the porosities were in a similar range of 8.25 to 9.58 %. When the solid loadings were higher than 80 wt%, the porosity decreased significantly. The slips with 100 and 120 wt% solid loadings tended to result in lower porosities than the others and the lowest porosities were produced from the 120 wt% solid loading which was in the range of 5.24 to 5.76 %. Table 4.4 presents the significance test results from a Student T-test for the porosity data from various solid loadings and ppi foams. Comparing the data by the Student T-test, the porosities produced from 100 wt% solid loading were highly significantly or significantly lower than those from the slip loadings less than 80 wt%. The porosities from 120 wt% solid loading were all highly significantly different to those of the 100 wt% solid loading. The reason why the porosity varied with solid loading is not very clear. This might be caused by experimental error and technical limitations. The porosities were all measured using 2–D images which have limitations when estimating the porosity in 3–D bulk materials. However, all the samples were examined using the same technique, so the results should be comparable. The measurements also depended greatly on the character of images such as contrast and quality and it was difficult to obtain images with consistent character in every sample. Comparing the porosity which was measured by the image analysis method and density, there may be inaccuracy in image analysis of samples produced from 120 wt% solid loading. More details will be discussed in section 4.5.1.

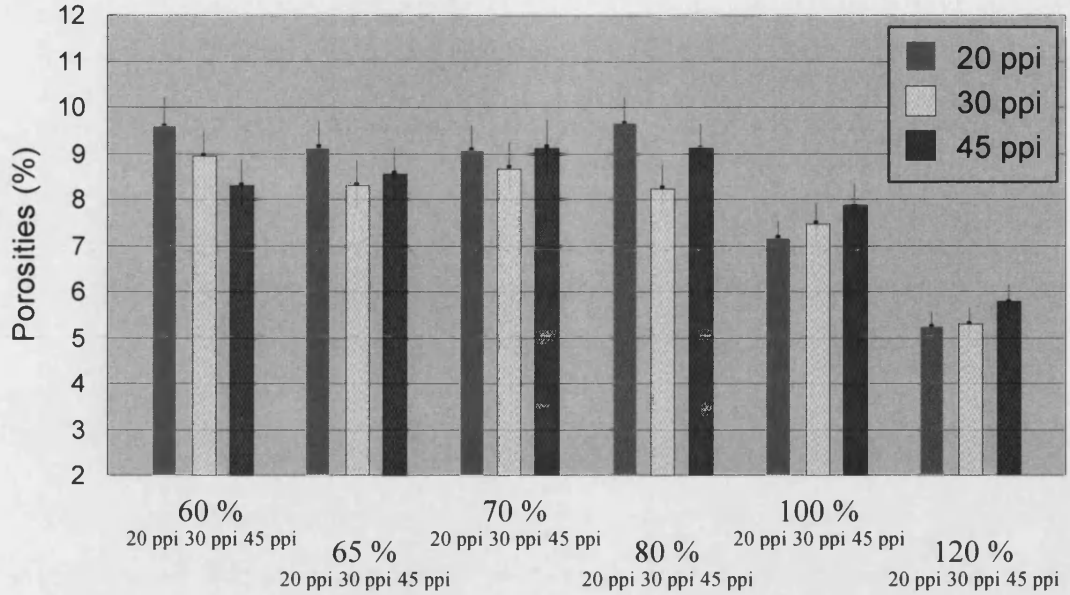

Figure 4.23 The macroporosity measurements of the porous HA/TCP.

	Porosities (%)		
Solid loading	**20 ppi**	**30 ppi**	**45 ppi**
60 wt%	9.58 ± 0.65	8.94 ± 0.56	8.31 ± 0.55
65 wt%	9.15 ± 0.53	8.32 ± 0.54	8.57 ± 0.53
70 wt%	9.07 ± 0.55	8.69 ± 0.55	9.14 ± 0.60
80 wt%	9.67 ± 0.57	8.25 ± 0.51	9.10 ± 0.57
100 wt%	7.16 ± 0.40	7.48 ± 0.46	7.86 ± 0.48
120 wt%	5.24 ± 0.32	5.31 ± 0.33	5.76 ± 0.40

Table 4.3 The porosity measurements of the porous HA/TCP.

Solid loading (wt%)		60			65			70			80			100			120		
	Foam (ppi)	20	30	45	20	30	45	20	30	45	20	30	45	20	30	45	20	30	45
60	20		△	X	O	X	X	O	#	O	O	X	O	XX	XX	XX	XX	XX	XX
	30	△		△	O	△	O	O	O	O	△	#	O	XX	XX	XX	XX	XX	XX
	45	X	△		△	O	O	#	O	#	X	O	#	XX	X	△	XX	XX	XX
65	20	O	O	△		#	△	O	O	O	O	X	O	XX	XX	XX	XX	XX	XX
	30	X	△	O	#		O	#	O	#	X	O	#	XX	X	O	XX	XX	XX
	45	X	O	O	△	O		O	O	△	X	O	O	XX	XX	#	XX	XX	XX
70	20	O	O	#	O	#	O		O	O	O	#	O	XX	XX	XX	XX	XX	XX
	30	#	O	O	O	O	O	O		O	#	O	O	XX	XX	X	XX	XX	XX
	45	O	O	#	O	#	△	O	O		O	#	O	XX	XX	XX	XX	XX	XX
80	20	O	△	X	O	X	X	O	#	O		X	O	XX	XX	XX	XX	XX	XX
	30	X	#	O	X	O	O	#	O	#	X		#	XX	X	O	XX	XX	XX
	45	O	O	#	O	#	O	O	O	O	O	#		XX	XX	XX	XX	XX	XX
100	20	XX	XX	XX	XX	XX	XX	XX	XX	XX	XX	XX	XX		O	X	XX	XX	XX
	30	XX	XX	X	XX	X	XX	XX	XX	XX	XX	X	XX	O		O	XX	XX	XX
	45	XX	XX	△	XX	O	#	XX	X	XX	XX	O	XX	XX	O		XX	XX	XX
120	20	XX	XX	XX	XX	XX	XX	XX	XX	XX	XX	XX	XX	XX	XX	XX		O	#
	30	XX	XX	XX	XX	XX	XX	XX	XX	XX	XX	XX	XX	XX	XX	XX	O		△
	45	XX	XX	XX	XX	XX	XX	XX	XX	XX	XX	XX	XX	XX	XX	XX	#	△	

XX = Highly significant difference
X = Significant difference
# = Probable difference
△ = Possible difference
O = Difference not established

Table 4.4 Student T-test results for the porosity data from various solid loadings and ppi foams.

Most of the pores observed in the porous HA/TCP samples were not circular in shape. The main shapes of macropore in this research were bow tie and triangle shapes, which replicated the initial shape of the struts of the PU foam. In order to indicate the sizes of these pores, the area equivalent diameters were calculated as pore sizes for each set of samples. This involved the translation of the irregular shape to a circular shape which had the same area. The diameter of the circle was deemed to be the area equivalent diameter. The details can be seen in Figure 4.24.

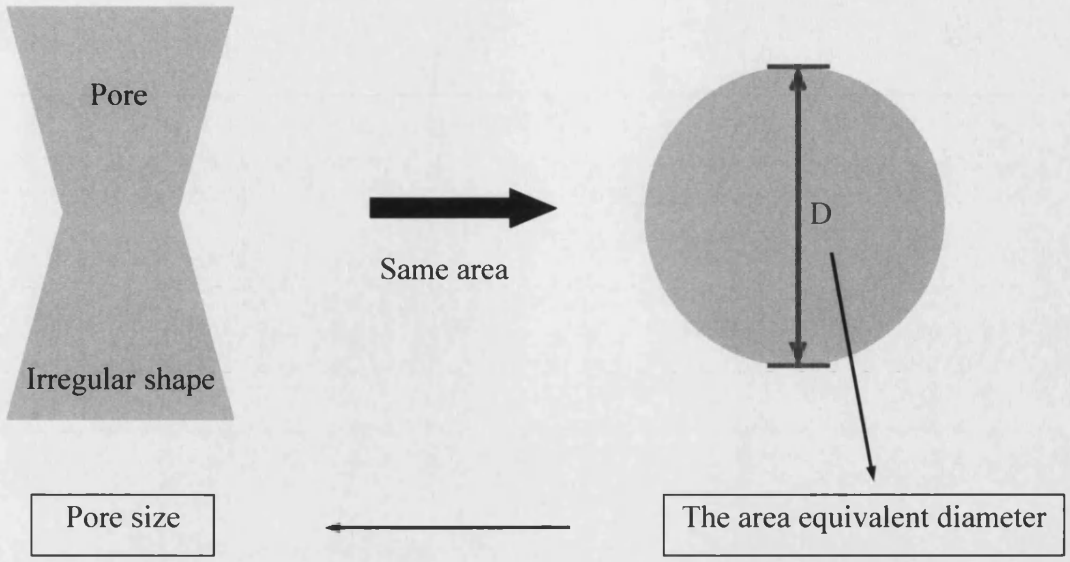

Figure 4.24 The area equivalent diameter is calculated as the pore size.

The area equivalent diameters of the pore structures are shown in Figure 4.25 and Table 4.5. The macropore sizes are highly dependent on the starting foam (ppi). The 20 ppi foam produced a pore size range of 197 μm to 254 μm. The 30 ppi produced a pore size range of 143 μm to 182 μm and the 45 ppi produced 105 μm to 135 μm (Table 4.5). The results showed that the macropore sizes in the porous HA/TCP could be controlled by using different ppi foams. There was no obvious difference between the area equivalent diameters of the HA/TCP samples and the solid loading of slips. The area equivalent diameters tended to decrease slightly when the solid loading was over 100 wt%. Comparing with the macroposity results in Figure 4.23 and Table 4.3, the solid loading had a similar effect on the area equivalent diameters but not as pronounced as on the macroposities. An interesting difference was that the macroposities of samples made from 100 wt% solid loading slip were lower than those of samples made from 60 to 80 wt% solid loading slips but macropore sizes of samples produced from 100 wt% solid loading were relatively high compared to those produced from lower solid loading slips. This might be the result of errors mentioned before and need to be further investigated.

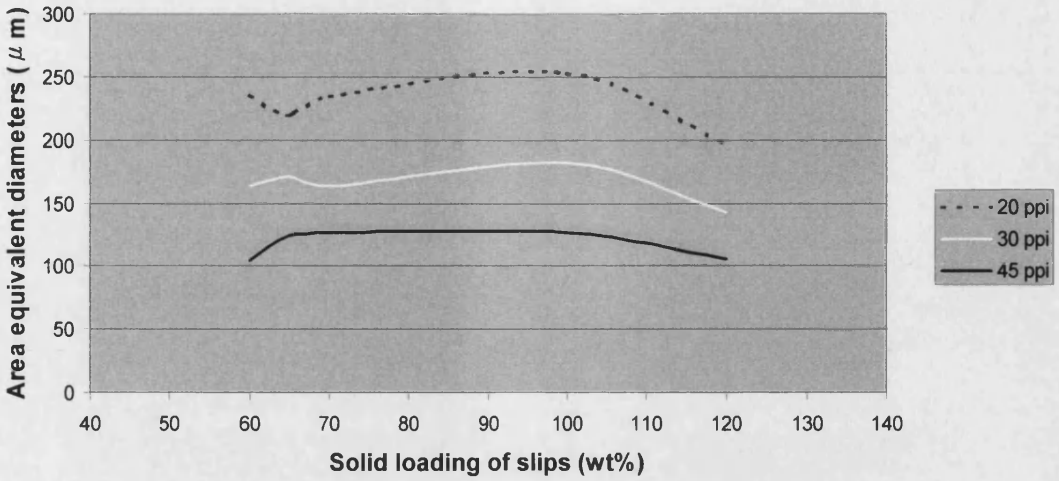

Figure 4.25 The area equivalent diameters of the porous HA/TCP.

	Macropore sizes (μm)		
Solid loading	**20 ppi**	**30 ppi**	**45 ppi**
60 wt%	236	163	105
65 wt%	219	172	124
70 wt%	234	164	127
80 wt%	247	178	135
100 wt%	254	182	126
120 wt%	197	143	106

Table 4.5 The area equivalent diameters of the porous HA/TCP.

The macropore distributions in porous HA/TCP samples generated from 20 ppi foam with 60 wt% slip, 20 ppi foam with 100 wt% slip are shown in Figures 4.26 and 4.27. The average macropore sizes were 236 μm and 254 μm, respectively. The macropores were in the size range of 40 to 500 μm and as such were appropriate for bone ingrowth. Both samples with different slip loadings had similar pore size distributions but the macropore sizes resulting from the 100 wt% solid loading slip are slightly larger than those from the 60 wt% slip. Figure 4.28 shows the samples made from 45 ppi foam had a narrower range of macropore size distribution than samples made from 20 ppi foams. The majority of macropores in the samples made from 45 ppi foam were around 100μm.

The macroporosities measured for the samples made from three different porosity foams were similar in the range of 5.24 to 9.67 %. The 20 ppi foam of resulted in a pore size range of 197 to 254 μm; the 30 ppi a pore size range of 143 to 182 μm and the 45 ppi a pore size range of 105 to 135 μm. According to the measurement of macroporosities and macropore sizes, 20, 30 and 45 ppi foams have different strut sizes which resulted in three different ranges of macropore size, but the relative volume of the polymer is approximately the same, which resulted in a similar range of macroporosities being produced. This demonstrated that the current technology depends on the starting foam density and shape of the struts to achieve the required percentage and shape of macropores. This will be critical to the development of this technology. In order to obtain porous samples with larger channels and higher macroporosities, attempts were made to coat PU foams with either wax or resin before impregnating with ceramic slips. However, the results were disappointing. Many cracks were generated on the impregnated "green" samples. The main reason might be the foam that was coated with either wax or resin had become too stiff to shrink with the ceramic during the drying process. This showed that if the foams could not shrink freely with the ceramic during drying, large cracks were generated. Another reason might be that the wax or resin was not hydrophilic which made it difficult for the ceramic slips to attach to the foams. From these experiments, it can be concluded that it is difficult to alter the foam structure e.g. by increasing the diameters of cellular struts of the foam and obtain acceptable results. Therefore, foams with the required density and strut shape need to be obtained to produce porous samples with the exact pore size, shape and pore volume for various clinical applications.

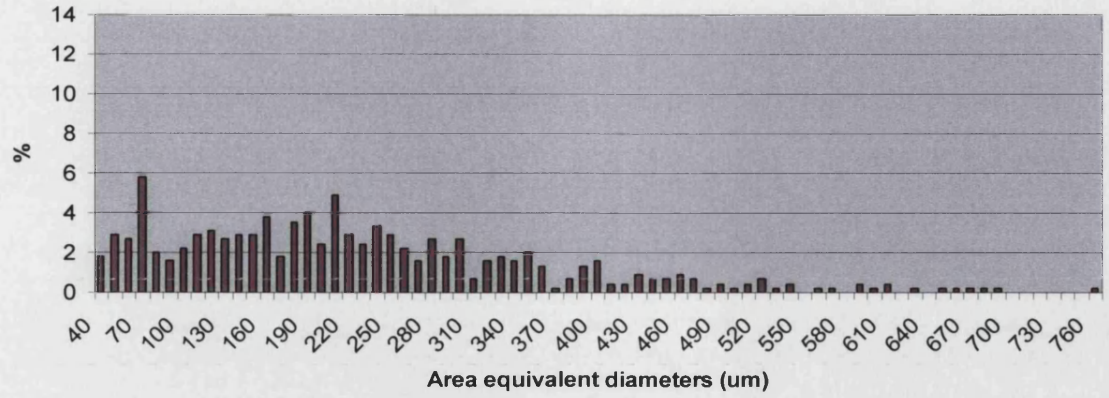

Figure 4.26 The macropore distribution of porous HA/TCP measured in the 20 ppi foam with the 60 wt% concentration slip and 8,800 cps viscosity.

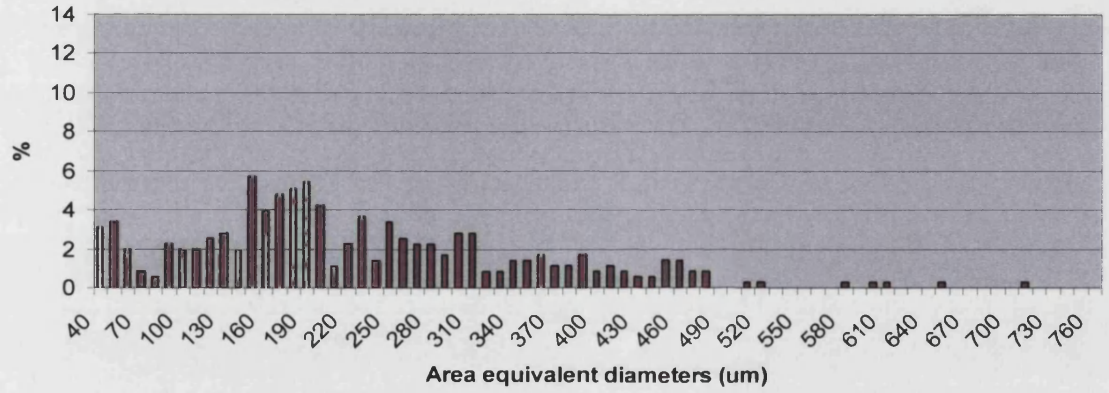

Figure 4.27 The macropore distribution of porous HA/TCP measured in the 20 ppi foam with the 100 wt% concentration slip and 8,400 cps viscosity.

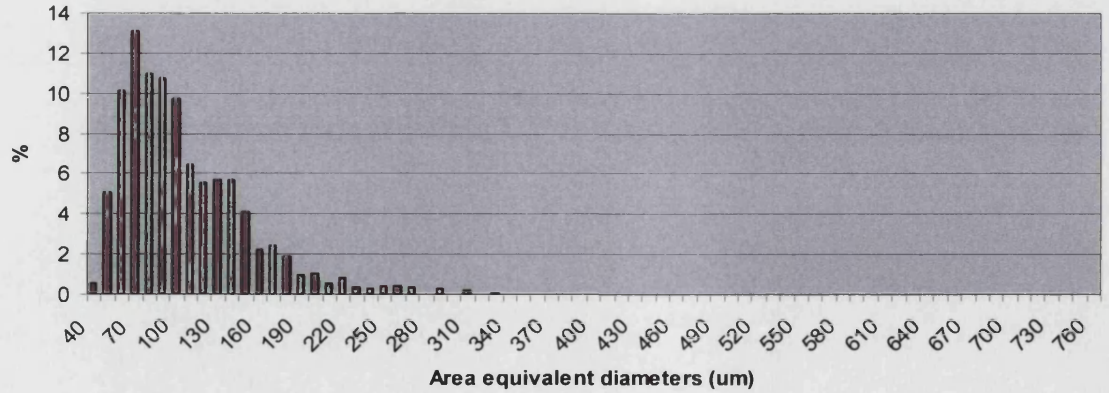

Figure 4.28 The macropore distribution of porous HA/TCP measured in the 45 ppi foam with the 60 wt% concentration slip and 8,800 cps viscosity.

4.3.4 Summary of Results and Key Findings

- Porous HA/TCP bioceramics with interconnecting pores and a range of pore sizes were produced successfully by the two novel vacuum impregnation methods.
- Comparing single and double impregnation, the latter was better when the solid loading was below 100 wt% in the first method and below 80 wt% in the second method. However, double impregnation was less successful than single impregnation when the solid loading was above 100 wt% in both processing methods. The successful samples had an excellent porous structure with interconnecting porosity. Nearly 100% of the macroporosity arose from the PU foam structure.
- Comparing these two main processing methods, the second method was slightly better than the first method in lower solid loading but much better in higher solid loading. However, the first vacuum impregnation technique had the advantage in that it was possible to make more complex shapes, as using this technique did not involve the compression step.
- From the SEM micrographs shown in Figures 4.19 to 4.22, it could be seen that the main shapes of macropores in this research were bow tie and triangular, which replicated the initial shape of the struts of the PU foam. The shapes and distribution of the macropores were similar in the samples made from different ppi foams but the relative sizes of the macropores were significantly different. This demonstrated the current technology depends on the starting foam density and shape of the struts to achieve the required distribution and shape of macropores.
- Image analysis showed, the solid loading does not have an obvious effect on macroporosity when the solid loading was in the range of 60 to 80 wt%. The macroporosities of samples made from 100 to 120 wt% are significantly lower than those from lower slip loadings.
- Image analysis shows the macroporosities measured for the samples made from three different ppi foams were similar in the range of 5.24 to 9.67%. The 20 ppi foam of resulted in a pore size range of 197 to 254 μm; the 30 ppi a pore size range of 143 to 182 μm and the 45 ppi a pore size range of 105 to 135 μm. 20, 30 and 45 ppi foams have different struts sizes resulting in three different ranges of macropore sizes but the relative volume of the polymer is approximately the same,

resulting in a similar range of macroporosities. This demonstrated that the major determinant of the macropore structures is the structure of the PU foams. The macropore sizes produced in this research were larger than 100 μm which is appropriate for bone ingrowth.

4.4 Microscopic Analysis

4.4.1 Scanning Electron Microscopy (SEM)

The microporosities generated from slips of 60 wt%, 100 wt% and 120 wt% solid loadings are shown in Figures 4.29, 4.30 and 4.31, respectively. Figure 4.29 shows the microporosities produced by the slips of 60 wt% with different conditions. Although these samples in Figure 4.29 were made using different ppi foams and slip viscosities, the microstructures all look alike. Most micropores were elongated in shape and only a few of them were circular. This shows the micropore size, shape and distribution were not influenced by the impregnation method and the PU foam structure. Samples in Figures 4.29 (a) and (b) were made with a slip of 8,800 cps viscosity, in Figures 4.29 (c) and (d) were made with 13,600 cps viscosity. This illustrates the viscosity did not have an obvious effect on the microstructure in the range of 8,800 to 13,600 cps. The measurements of microporosity and micropore size are given in next section. The majority of micropores fall in the 0.8 to 2.4 μm size range.

The microporosities generated by the slip of 100 wt% solid loading are shown in Figure 4.30. The shape and distribution of microporosities generated from slips of 100 wt% solid loading are similar to 60 wt% but smaller. The major micropore sizes were in the range of 0.6 to 1.6 μm.

Figure 4.31 shows the microporosity generated by the slips of 120 wt% solid loading. These micropore structures were obviously different to those in samples made from slips with lower solid loading. The micropores sizes from the slip of 120 wt% solid loading were in the similar range to 100 wt% slip but the micropores were less interconnected than in the 100 wt% and 60 wt% slips. The distribution of the micropores was not as regular as those made from the slips with lower solid loading. These micropores were concentrated in some areas and were thus not uniformly distributed. Another difference is that these pore shapes tend to be circular not elongated. The observations relating to the micropore structures and solid loading of slips are summarized in Table 4.6 in the next section. This shows that solid loadings affect micropore size, shape and distribution greatly.

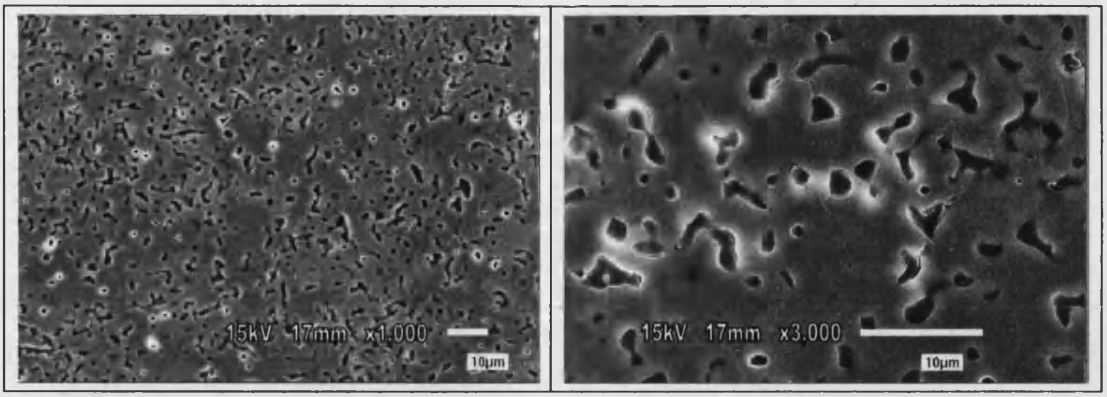

(a) First method, double impregnation, 20 ppi foam, and 8,800 cps viscosity.

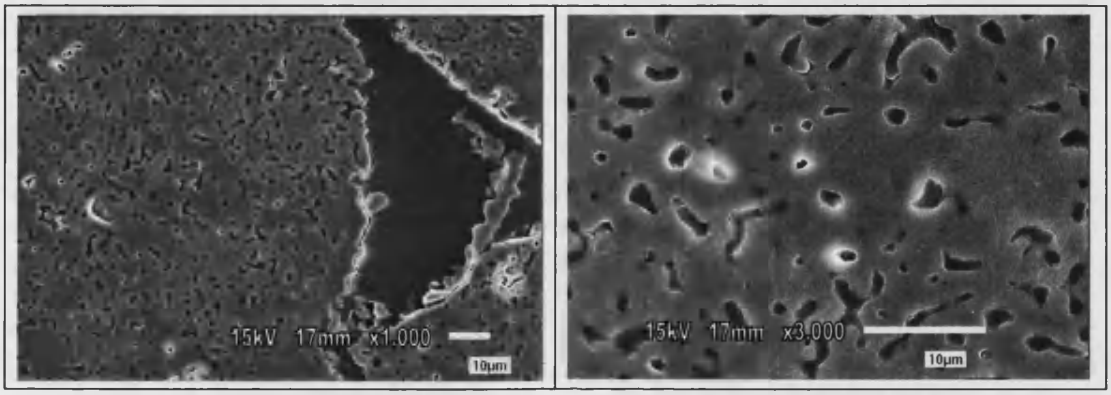

(b) First method, double impregnation, 45 ppi foam, and 8,800 cps viscosity.

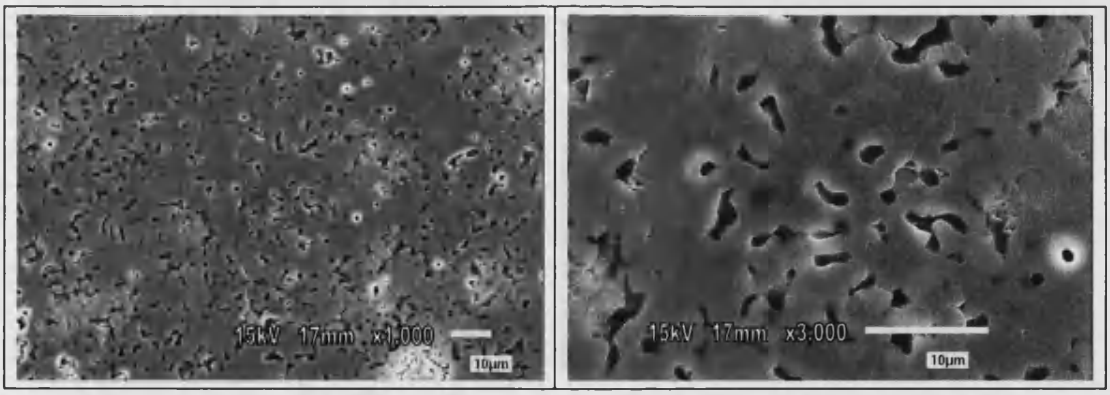

(c) Second method, single impregnation, 20 ppi foam, and 13,600 cps viscosity.

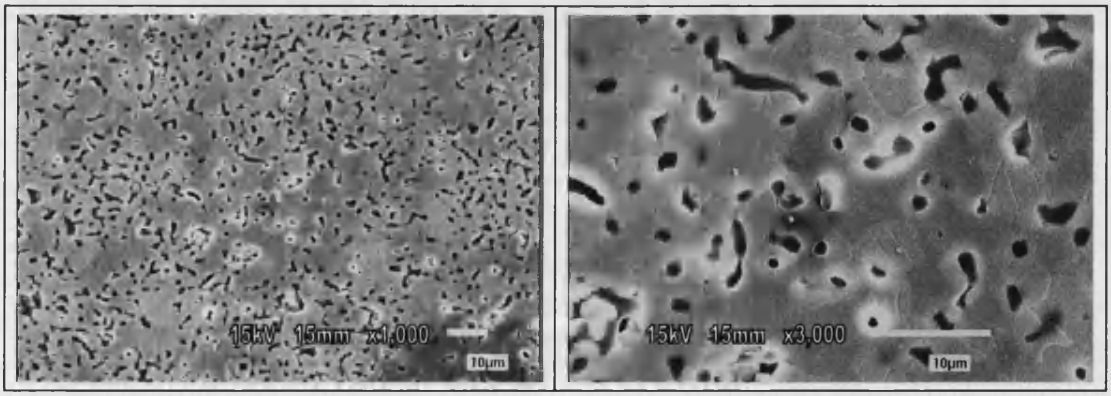

(d) Second method, double impregnation, 20 ppi foam, and 13,600 cps viscosity.

Figure 4.29 Micropores produced by the slips of 60 wt% solid loading.

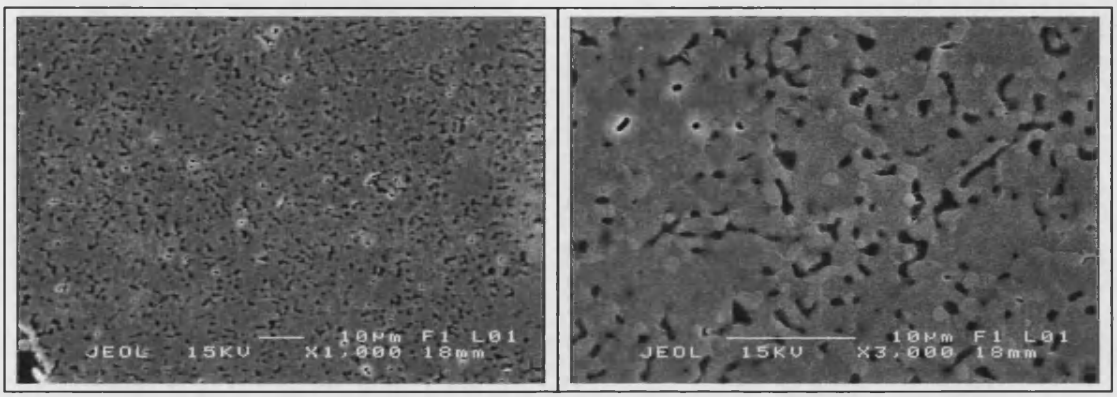

(a) First method, single impregnation, 20 ppi foam, and 8,400 cps viscosity.

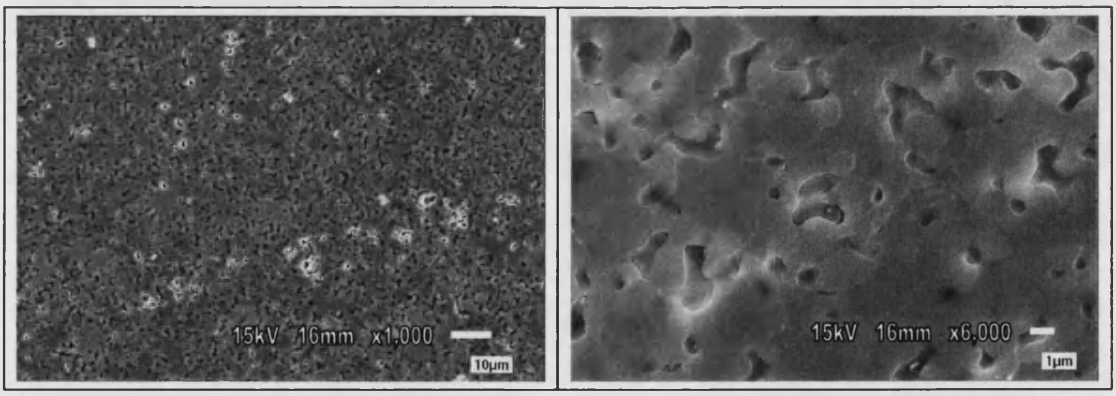

(b) First method, double impregnation, 20 ppi foam, and 8,400 cps viscosity.

Figure 4.30 Micropores produced by the slips of 100 wt% solid loading.

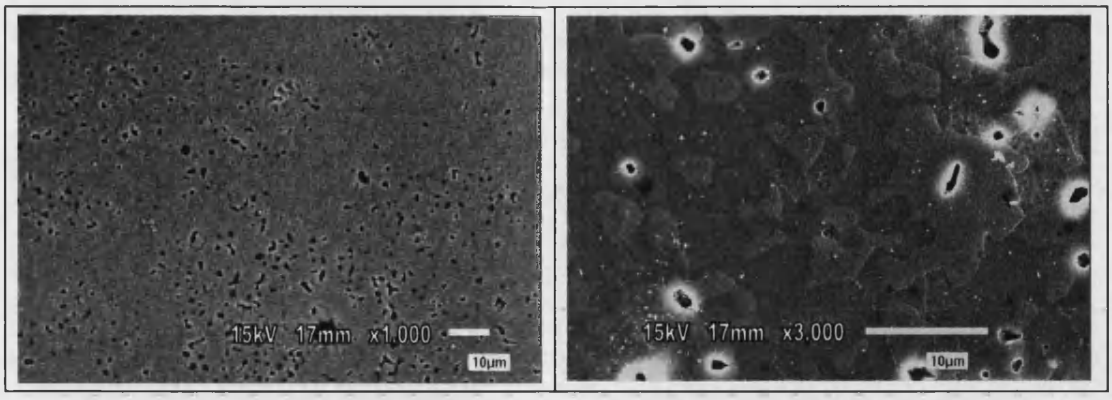

(a) Second method, single impregnation, 20 ppi foam and 11,200 cps viscosity.

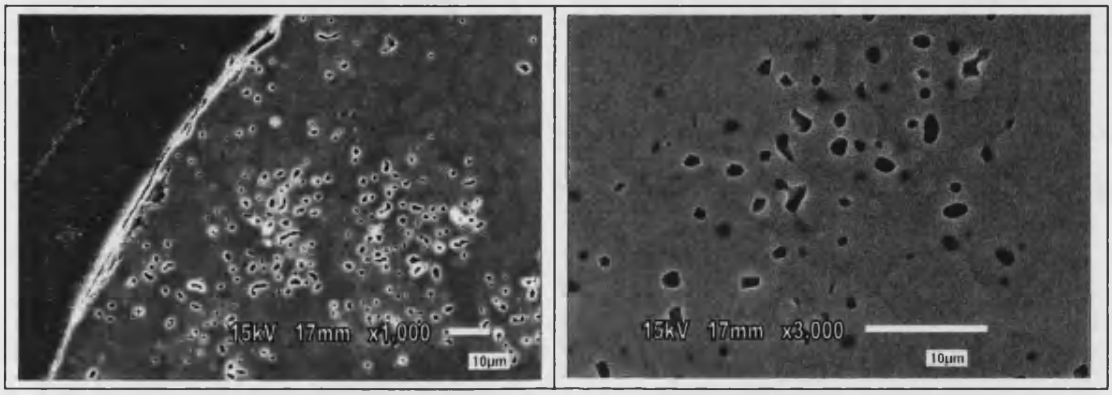

(c) Second method, single impregnation, 30 ppi foam and 11,200 cps viscosity.

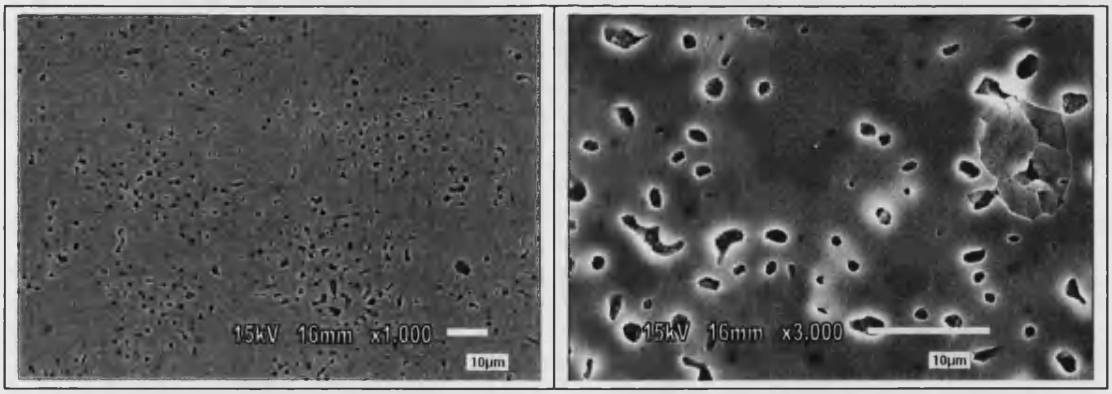

(b) Second method, single impregnation, 45 ppi foam and 11,200 cps viscosity.

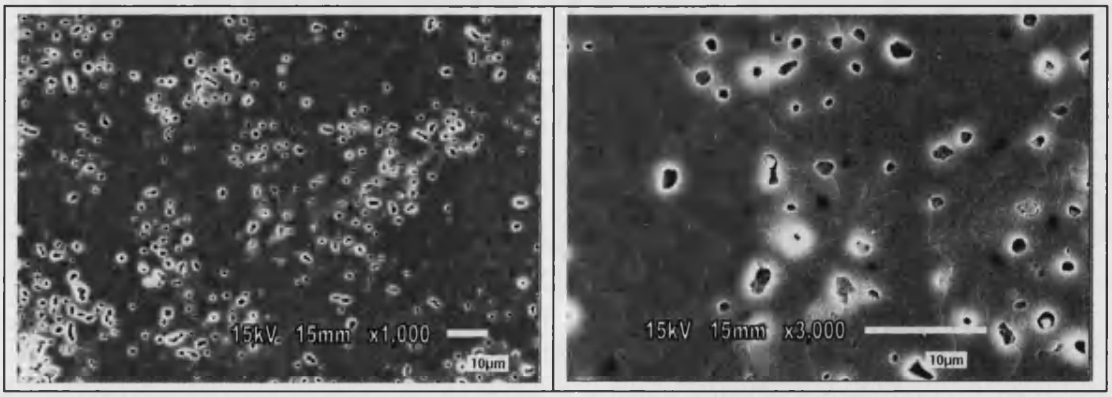

(c) Second method, double impregnation, 20 ppi foam and 11,200 cps viscosity.

Figure 4.31 Micropores produced by the slips of 120 wt% solid loading.

4.4.2 Microporosity and Micropore Size

Figures 4.32, 4.33 and 4.34 show the distributions of the micropores in the samples generated from the slips with 60 wt%, 100 wt% and 120 wt% solid loadings. The average micropore sizes and microporosities are shown in Table 4.6 which were 1.21 μm; 15.07%, 0.98 μm; 14.09% and 0.95 μm; 4.23% in each concentration. The highest micropore sizes and microporosities were produced from the slip of 60 wt% solid loading. The reason might be the looser packing of the powder in lower solid loading. The micropore sizes and microporosities both decreased as solid loading increased. The microporosity in the 120 wt% solid loading was 4.23 % which was obviously lower than that in the 60 and 100 wt% solid loading samples. This may result from the compact packing of the powders. However, there might be inaccuracy in the image analysis as descried in section 4.3.3 and an error of microporosity measurement might be arise as a result of grains which have a different contrast in the SEM micrographs. Compared to the density measurements, the microporosity of samples produced from 120 wt% solid loading measured by image analysis may be too low. More details will be discussed in section 4.5.1. Although the measurement of microporosity produced from 120 wt% solid loading might be too low, it can be seen clearly in Figure 4.31 that these micropores are smaller than those in other solid loadings and concentrated in some specific areas. The smaller micropores and inconsistent distribution in which there are no micropores in some areas should result in a lower overall microporosity relative to other samples. The results showed that the solid loading of the slip significantly influences micropore size and microporosity.

	Solid loading of ceramics slips		
Micropore	**60 wt%**	**100 wt%**	**120 wt%**
Sizes	1.21 μm	0.98 μm	0.95 μm
Porosities	15.07 ± 1.02 %	14.09 ± 0.84 %	4.23 ± 0.45 %
Shapes	Elongated More interconnected	Elongated	Circular Isolated
Distributions	Regular	Regular	Uneven

Table 4.6 The relationship between micropore structure and solid loading of slips.

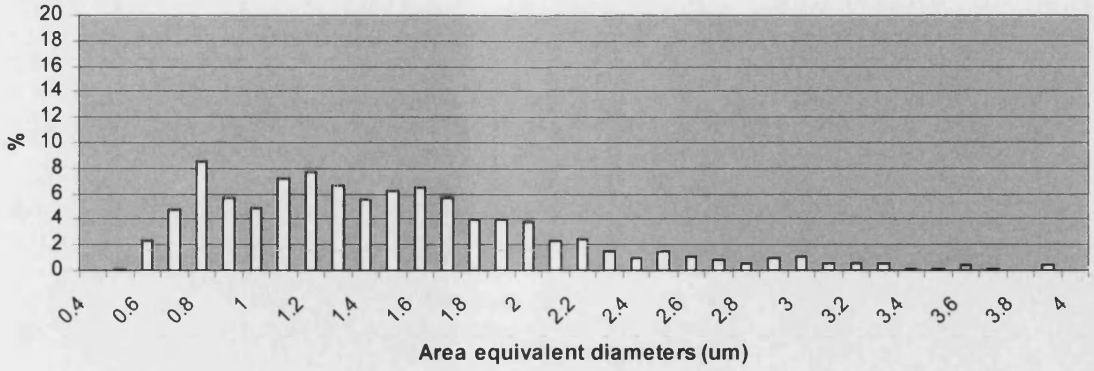

Figure 4.32 The micropore distribution of porous HA/TCP generated by the slip of 60 wt% concentration and 8,800 cps viscosity.

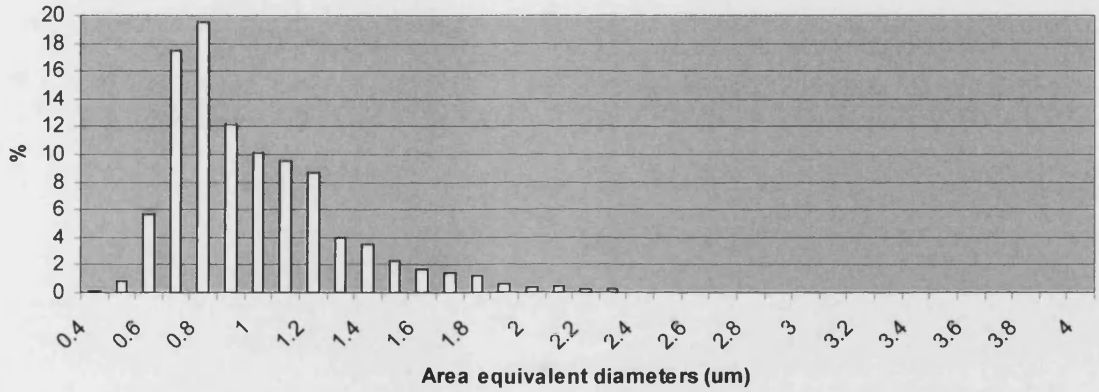

Figure 4.33 The micropore distribution of porous HA/TCP generated by the slip of 100 wt% concentration and 8,400 cps viscosity.

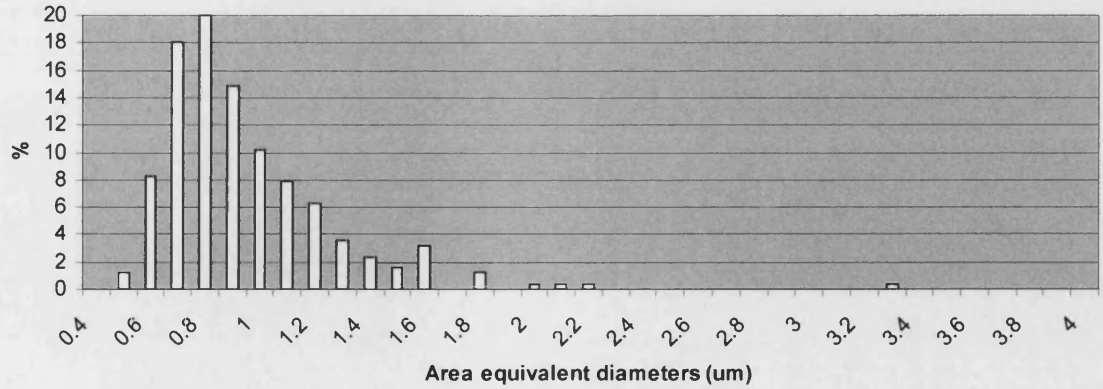

Figure 4.34 The micropore distribution of porous HA/TCP generated by the slip of 120 wt% concentration and 11,200 cps viscosity.

4.4.3 Summary of Results and Key Findings

- Micropore structures were obviously affected by the solid loading of slips. The micropores were more interconnected and larger and the distribution of the micropores was more regular when the solid loading of the slips was lower.
- Micropore shapes tended to be circular in shape when solid loading was high and elongated in shape in samples made with the low solid loading slip.
- The average micropore sizes were found to be 1.21 μm, 0.98 μm and 0.95 μm from slips with solid loadings of 60 wt%, 100 wt% and 120 wt% respectively.
- The average microporosities were found to be 15.07 ± 1.02 %, 14.09 ± 0.84 % and 4.23 ± 0.45 % for the samples made from slips of solid loadings of 60 wt%, 100 wt% and 120 wt% respectively.
- The micropores produced in 60 to 100 wt% solid loading samples were interconnected.

4.5 Physical and Mechanical Properties

Table 4.7 shows physical and mechanical properties of samples made from selected solid loading and ppi foams were measured. 60 to 140 wt% solid loading slips were used, as samples made from this range of solid loading were more efficient and reproducible. Porous samples made from 20 ppi foam were produced for all the solid loading as it produced samples with largest macropore size which could be more useful in clinical applications. Selected samples made from 30 and 45 ppi foams plus solid samples with the same chemical composition which were made from 100 wt% solid loading were produced for comparison purposes.

	Foam size (ppi)		
Solid loading	**20 ppi**	**30 ppi**	**45 ppi**
60 wt%	X	–	–
80 wt%	X	X	–
100 wt%	X	X	X
120 wt%	X	X	X
140 wt%	X	–	–
Solid	X		
X = Tested – = Non-Tested			

Table 4.7 Samples for physical and mechanical properties measurement.

4.5.1 Density

The apparent densities of the samples were determined by a geometric wt/vol method as outlined in section 3.4.1.

Apparent density in relation to solid loading:

The apparent density measurements of solid and porous blocks resulting from 20 ppi foam with various solid loadings are shown in Figure 4.35 (a). Figures 4.35 (b) and (c) show the densities resulting from 30 and 45 ppi foams where it can be seen that the densities of the porous samples increased with solid loading. This can be explained in terms of the slips with higher solid loadings producing lower levels of microporosity as confirmed by the microscopic analysis in section 4.4.

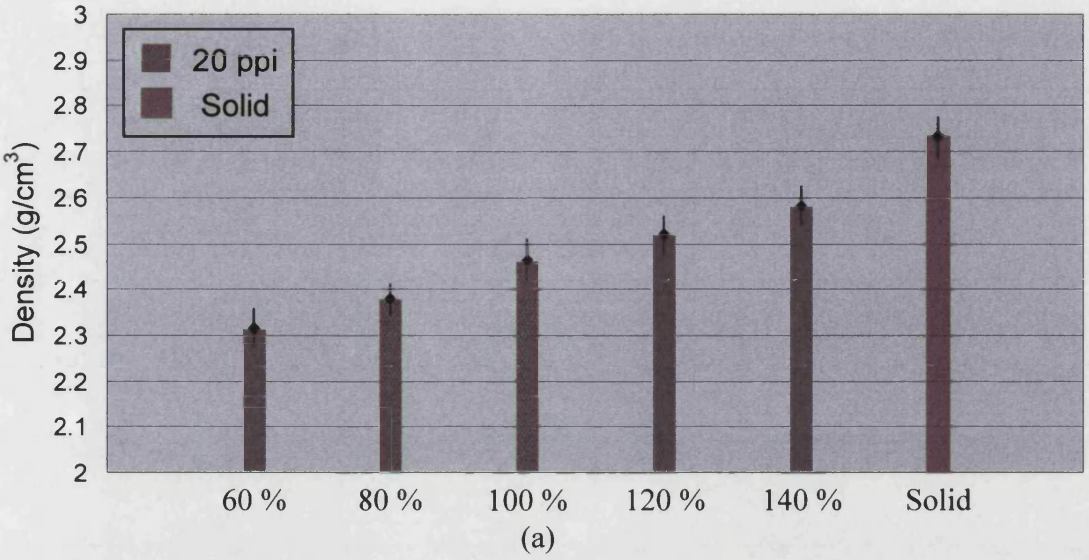

(a)

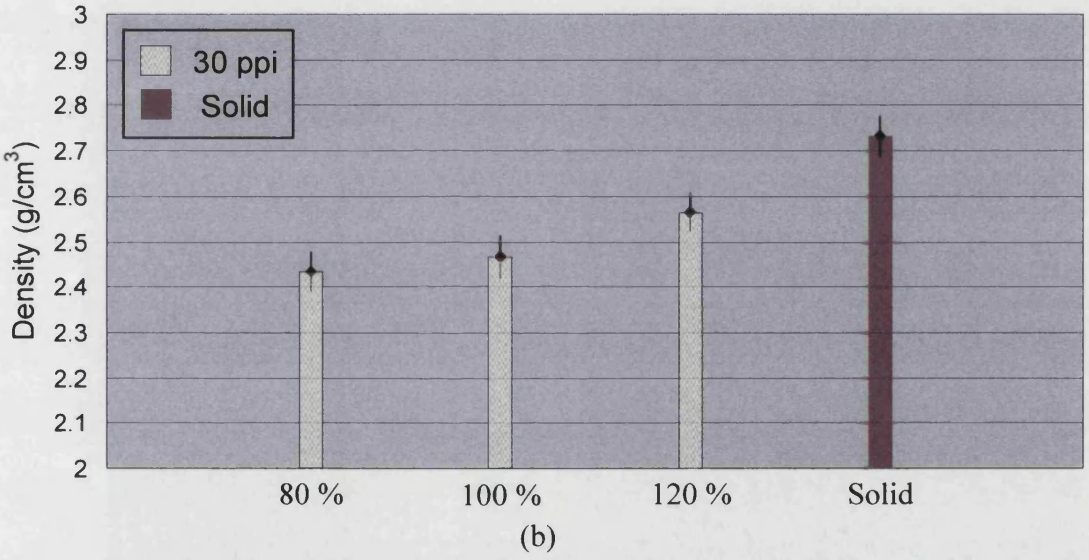

(b)

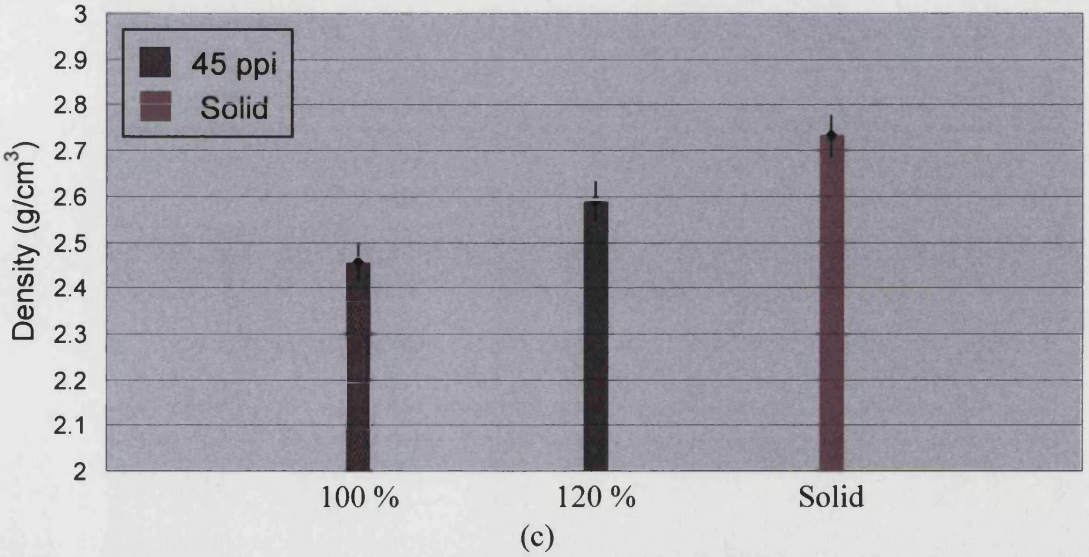

(c)

Figure 4.35 The apparent density measurements of porous blocks resulting from (a) 20 ppi (b) 30 ppi (c) 45 ppi foams and solid of the sintered HA/TCP bioceramics.

Apparent density in relation to grade of foam:

The different ppi foams did not seem to have a large effect on macroporosity as seen in the image analysis results in section 4.3.3. The porosities resulting from 20 ppi foams were slightly higher than those from the other two foams in 60 to 80 wt% solid samples loading but lower in 100 to 120 wt% solid loading samples. The 45 ppi foam tended to produce slightly higher porosities than the 30 ppi foam and the only exception was the 60 wt% solid loading. The apparent density measurements of porous blocks resulting from 80, 100 and 120 wt% solid loadings are shown in Figures 4.36 (a) (b) and (c), respectively. The densities from high to low were in ppi foam order. The 45 ppi foam produced the highest density sample and the 20 ppi foam resulted in the lowest density sample. The only exception was the samples made from 100 wt% solid loading, shown in Figure 4.36 (b), which had similar values for different foams.

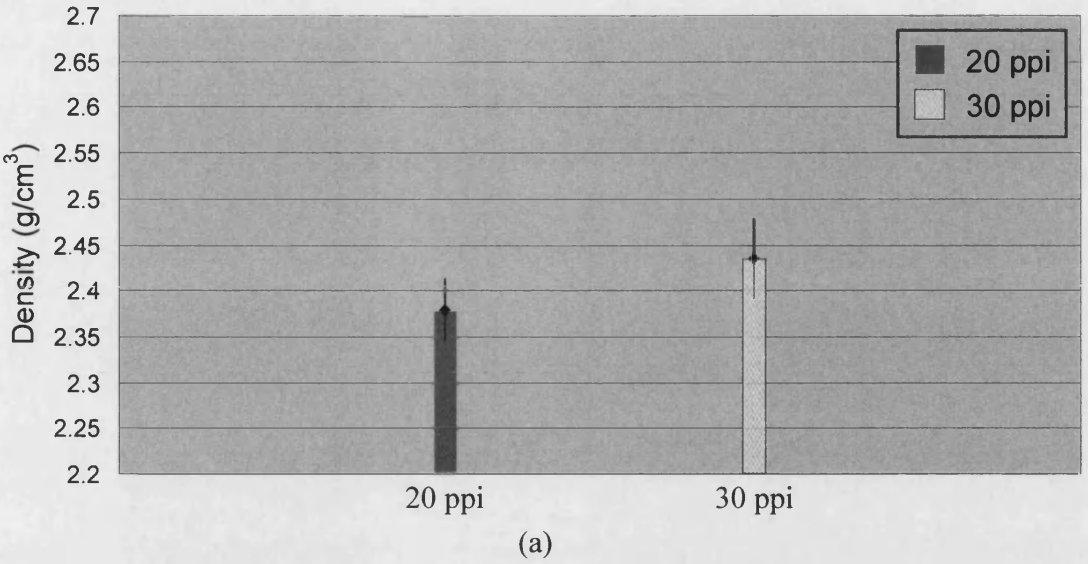

(a)

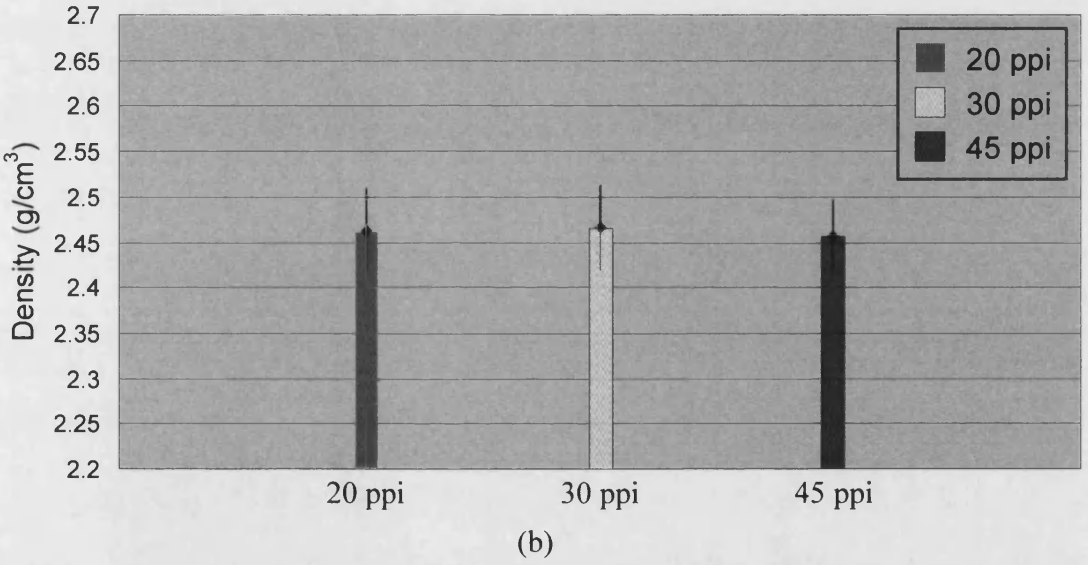

(b)

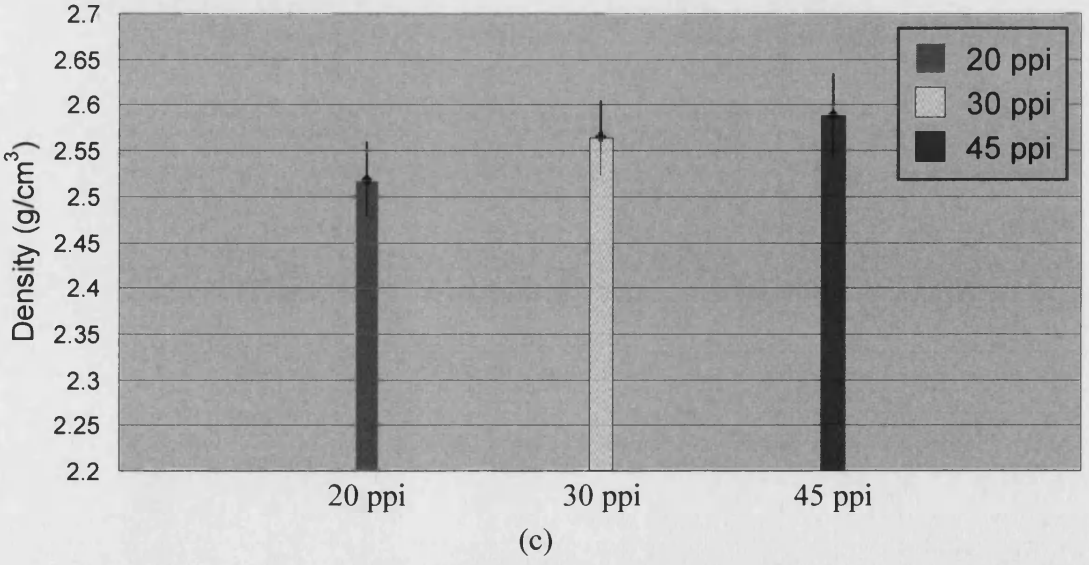

(c)

Figure 4.36 The apparent density measurements of porous blocks of the sintered HA/TCP bioceramics resulting from (a) 80 (b) 100 (c) 120 wt% solid loading slip.

Figure 4.37 and Table 4.8 summarize the apparent density of the solid sample compared to the densities of the porous blocks of the sintered HA/TCP with different solid loading of slips and the theoretical densities of dense HA, β-TCP and α-TCP. Table 4.9 shows the Student T-test results for the density measurements from solid and porous samples from various solid loading and ppi foam. The apparent density of the solid sample, made from the slip of 100 wt% solid loading, was highly significantly different to any other porous samples and was approximately 88 % of the theoretical density. According to the Student T-test results, the difference of the apparent density between the porous samples made from the same grade of foam but different solid loading were mostly of highly significant difference and significant difference. The density of the samples was mostly the same and possibly different for 20, 30 and 45 ppi samples with a specific slip loading. The major point to come out of this section was that not only solid loading but also ppi foam affected the apparent densities of porous samples. However, the grade of foam did not seem to have as great an effect as the solid loading on apparent density.

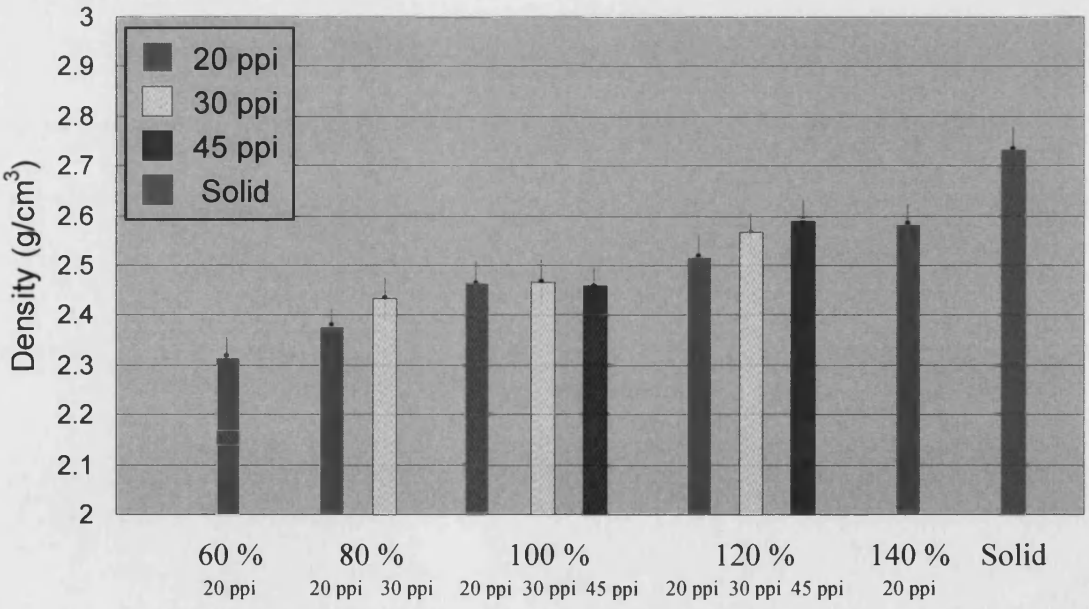

Figure 4.37 The apparent density measurements of solid and porous blocks of the sintered HA/TCP bioceramics.

	The apparent densities (g/cm^3)		
Solid loading	**20 ppi**	**30 ppi**	**45 ppi**
60 wt%	2.32 ± 0.04	–	–
80 wt%	2.38 ± 0.03	2.43 ± 0.04	–
100 wt%	2.46 ± 0.05	2.47 ± 0.05	2.46 ± 0.04
120 wt%	2.52 ± 0.04	2.56 ± 0.04	2.59 ± 0.04
140 wt%	2.58 ± 0.04	–	–
Solid	2.73 ± 0.05		

The theoretical densities (g/cm^3)[256,288]		
HA	β-TCP	α-TCP
3.16	3.07	2.86

Table 4.8 The apparent densities of porous blocks of the sintered HA/TCP and the theoretical densities of HA, β-TCP, α-TCP.

Solid loading (wt%)		60	80		100			120			140	Solid sample
	Foam (ppi)	20	20	30	20	30	45	20	30	45	20	
60	20		X	XX	XX	XX	XX	XX	XX	XX	XX	XX
80	20	X		#	X	X	X	XX	XX	XX	XX	XX
	30	XX	#		O	O	O	X	XX	XX	XX	XX
100	20	XX	X	O		O	O	#	XX	XX	XX	XX
	30	XX	X	O	O		O	#	XX	XX	XX	XX
	45	XX	X	O	O	O		#	XX	XX	XX	XX
120	20	XX	XX	X	#	#	#		△	#	#	XX
	30	XX	XX	XX	XX	XX	XX	△		O	O	XX
	45	XX	XX	XX	XX	XX	XX	#	O		O	XX
140	20	XX	XX	XX	XX	XX	XX	#	O	O		XX
Solid sample		XX	XX	XX	XX	XX	XX	XX	XX	XX	XX	

XX = Highly significant difference
X = Significant difference
# = Probable difference
△ = Possible difference
O = Difference not established

Table 4.9 Student T-test results for the densities of solid and porous samples from various solid loading and ppi foam.

The total porosity, which is the sum of the macro- and micro-porosity, can be calculated from the results of image analysis and apparent densities. The results obtained using these two methods are compared in Figure 4.38. It can be seen that for the 60 wt%, 100 wt% and solid samples the results were comparable. However, the relative porosities for the 120 wt% solid loading samples differ significantly. This difference could be accounted for in terms of the measurement of macroporosity, macroporosity or density. The error in the measurement of density should be less as the measurement of volume and weight should be accurate in samples with regular shape. In image analysis, both macroporosity and microporosity dropped significantly in the solid loading of 120 wt%. If the image analysis is correct for the porous samples made from the slip of 120 wt% solid loading then these porous samples would have a lower porosity than the solid sample, which is unlikely. There were also more variables in the image analysis measurement process which were discussed in section 4.3.3. Further tests need to be done to measure macroporosity and microporosity.

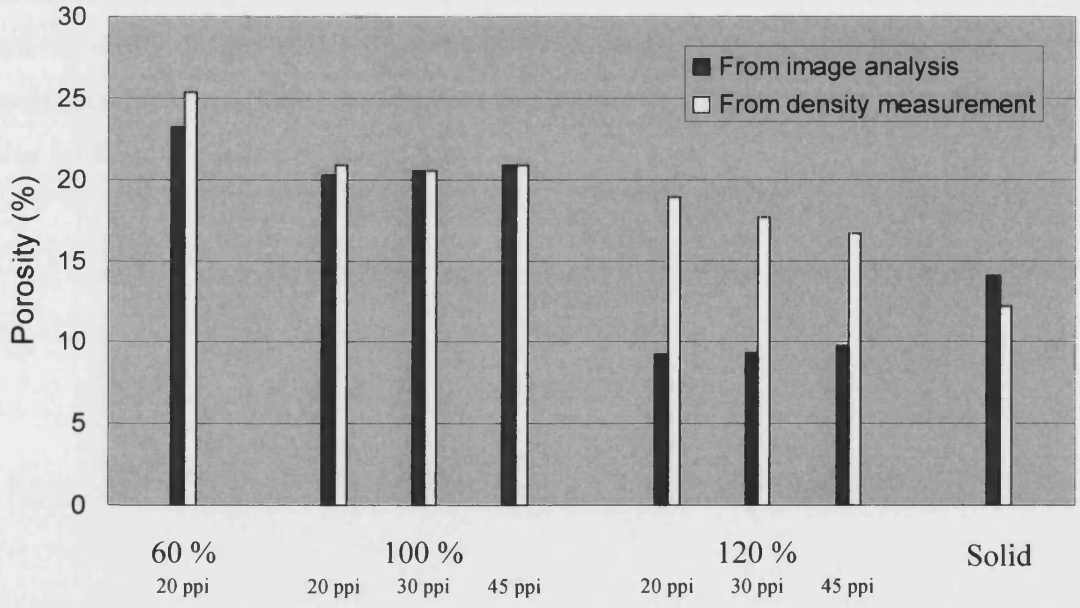

Figure 4.38 Total porosity of solid and porous blocks of the sintered HA/TCP calculated from the results of image analysis and density measurements.

4.5.2 Mechanical Testing

4.5.2.1 Four-Point Bend Testing

The four-point bend test was carried out using rectangular bars with dimensions of 45 × 5 × 4 mm as shown in section 3.4.2.1. The samples were tested with a crosshead speed of 0.5 mm/min and the span was 20 × 40 mm. Five to eight samples were tested in each condition.

Four-point bend strength in relation to solid loading:

Figures 4.39 (a) (b) and (c) show the four-point bend strengths of solid and porous HA/TCP blocks resulting from 20 ppi, 30 ppi and 45ppi foams, respectively. Comparing these porous samples made from 20 ppi foam but different solid loading slips shown in Figure 4.39 (a), there was no obvious relationship between four-point bend strengths and solid loading. Similar observations can be seen in samples made from 30 ppi foam in Figure 4.39 (b). Figure 4.39 (c) shows porous samples made from 45 ppi foam. Samples made from 120 wt% solid loading slip had slightly higher four-point bend strengths than samples made from 100 wt% solid loading. This illustrates that microporosity did not have a dramatic effect on four-point bend strengths especially for samples which have larger macropores. Microporosity might be below the critical flow size for failure in four-point bend test.

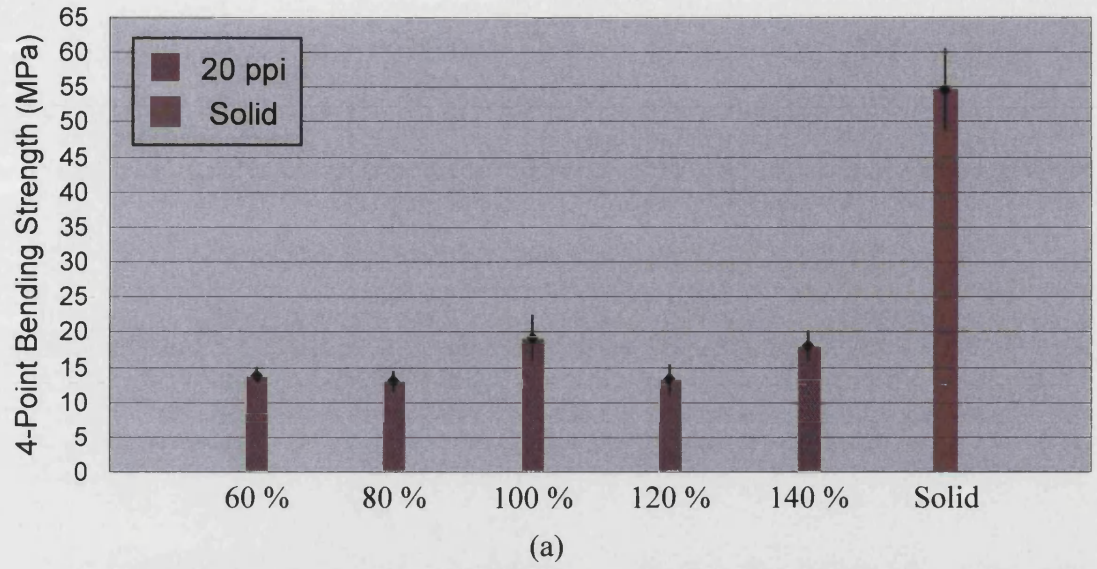

(a)

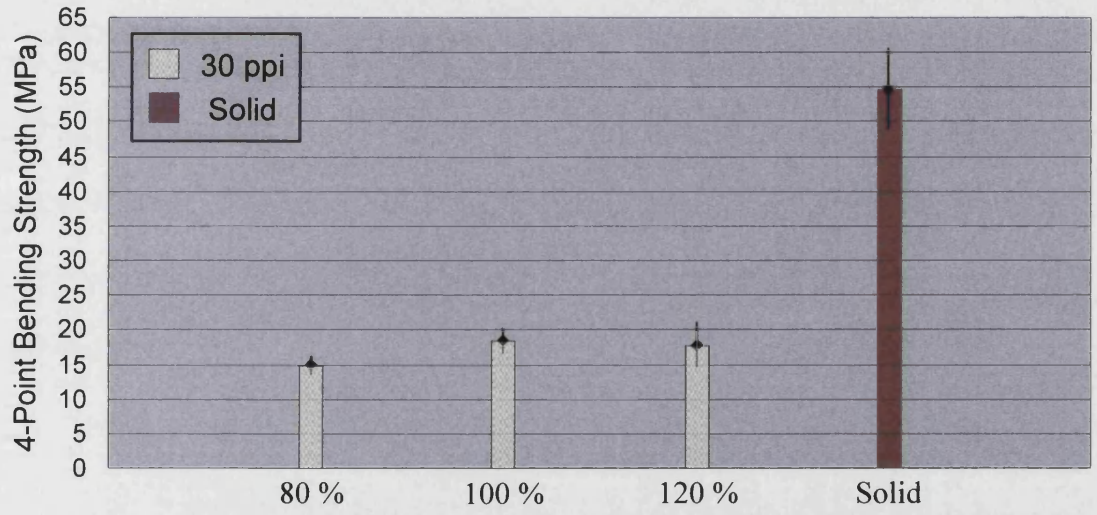

(b)

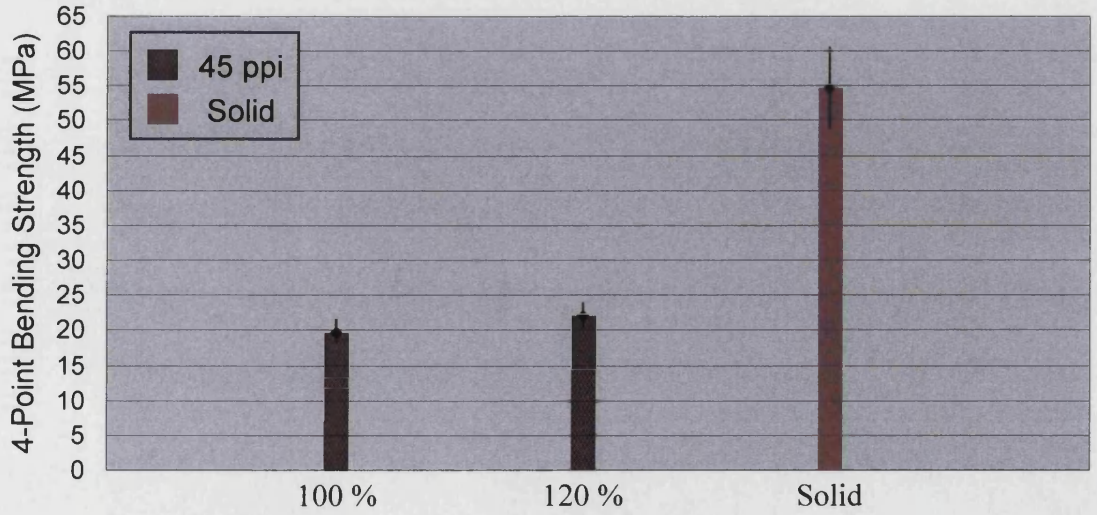

(c)

Figure 4.39 The four-point bend strengths of porous blocks resulting from (a) 20 ppi (b) 30 ppi (c) 45 ppi foams and solid sintered HA/TCP bioceramics.

Four-point bend strength in relation to grade of foam:

The four-point bend strengths of porous blocks resulting from 80, 100 and 120 wt% solid loading slips are shown in Figures 4.40 (a) (b) and (c), respectively. The strengths of samples made from 80 and 120 wt%, Figures 4.40 (a) and (c), from low to high are in the order of 20 ppi, 30 ppi and 45 ppi foams. The 45 ppi foam produced samples with the highest strength and the 20 ppi foam resulted in the lowest strength. This particular order can also be seen in the samples made from 100 wt% solid loading shown in Figure 4.40 (b). The average strength for samples made from 20 ppi foams may be high comparing to the others in Figure 4.40 (b). However, this may result from experimental error as the standard deviation for the 20 ppi sample is higher. This showed that macropore size had a noticeable effect on four-point bend strengths so starting foam structures had more effect than solid loading.

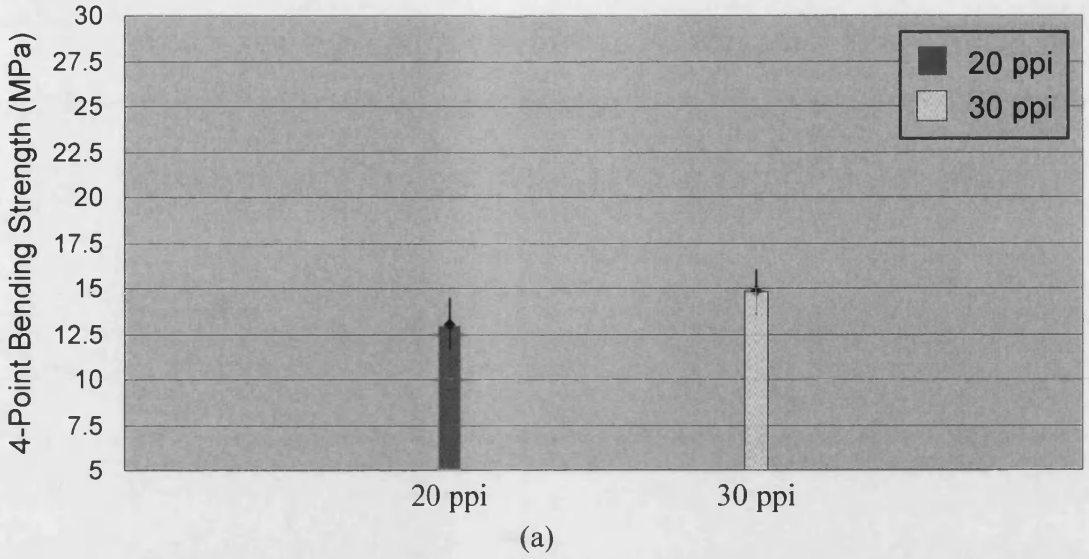

(a)

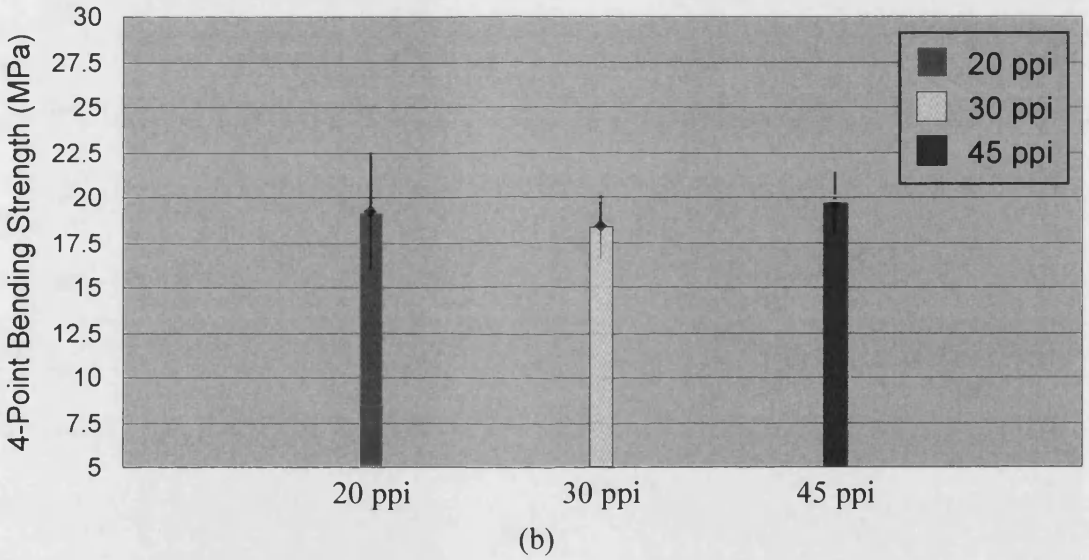

(b)

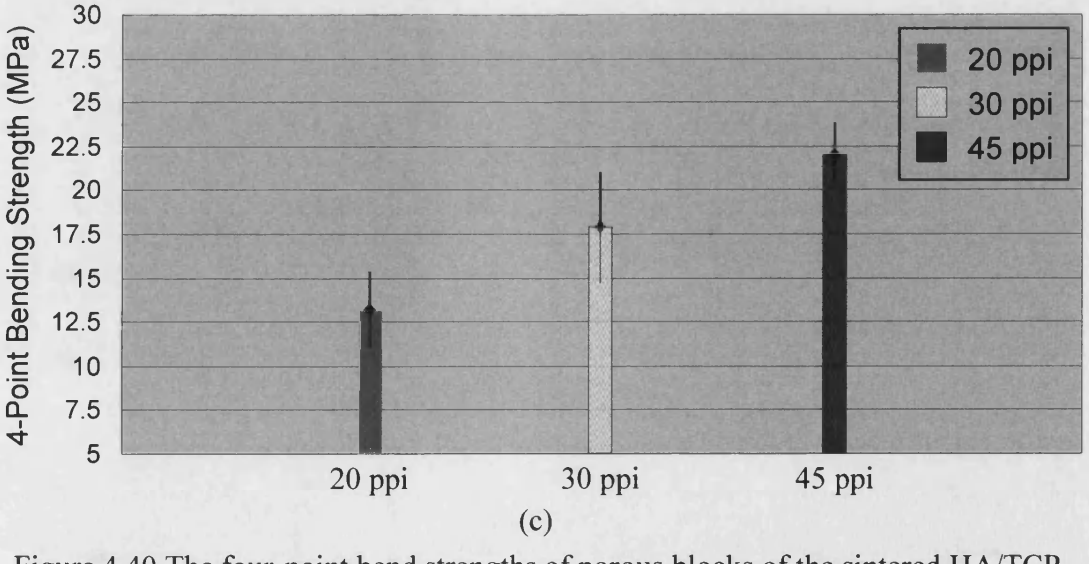

(c)

Figure 4.40 The four-point bend strengths of porous blocks of the sintered HA/TCP bioceramics resulting from (a) 80 (b) 100 (c) 120 wt% solid loading slip.

Figure 4.41 and Table 4.10 summarize the test results for solid and porous HA/TCP samples. The solid samples had the highest strengths which were in the order of 54.67 ± 5.83 MPa. The average four-point bend strengths for the porous samples were in the range of 13.03 to 22.03 MPa. Four-point bend strengths were sensitive to defects, especially on the surface of the materials, so the strengths of the porous HA/TCP were considerably lower and inherently more variable. Table 4.11 shows the Student T-test results for the four-point bend strengths from solid and porous samples with various solid loading and ppi foams. Unsurprisingly, the four-point bend strengths of porous samples were all highly significantly lower than that of the solid sample. The difference in four-point bend strengths between the porous samples made from the same grade of foam but different solid loading were significantly different and in some cases there was no difference. However, it was mentioned the four-point bend strengths of the porous samples had no particular order in relation to solid loading. The four-point bend strength of the porous samples is the same for 20, 30 and 45 ppi samples with 100 wt% slip loading but the strength of the porous samples showed a probable difference and highly significant difference for different ppi samples with 80 wt% and 120 wt% slip loading. These results showed different grade of foam had a notable effect on four-point bend strengths and the samples with a larger macropore size had lower four-point bend strengths but, in contrast, the micropore sizes and level of microporosity did not seem to have a dramatic effect on values of four-point bend strength.

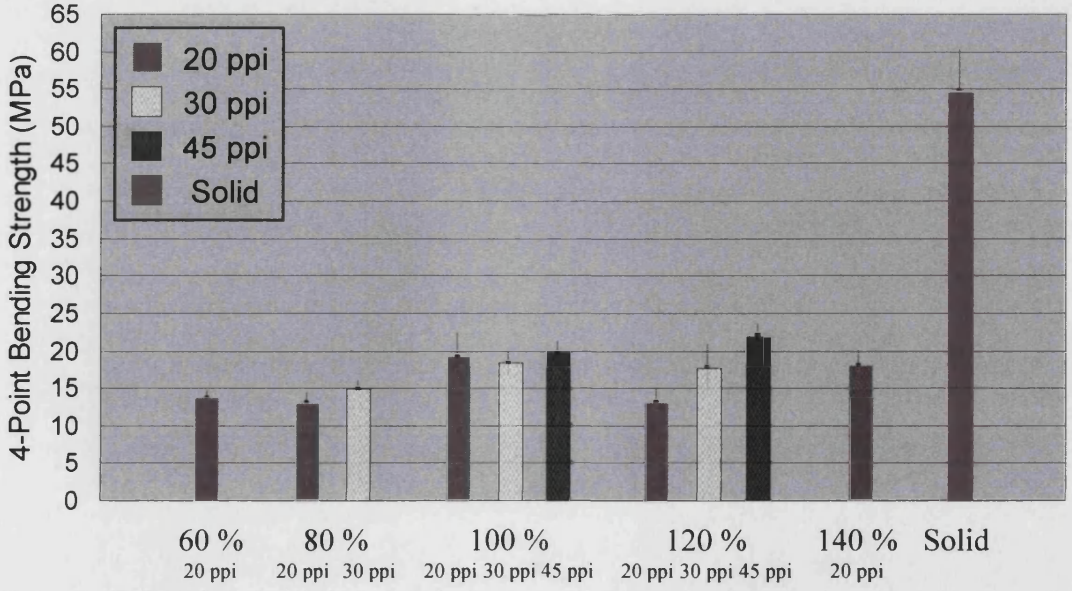

Figure 4.41 The four-point bend strengths of the solid and porous sintered HA/TCP bioceramic.

	4-Point Bend Strength (MPa)		
Solid loading	**20 ppi**	**30 ppi**	**45 ppi**
60 wt%	13.74 ± 1.07	–	–
80 wt%	13.03 ± 1.42	14.82 ± 1.23	–
100 wt%	19.20 ± 3.22	18.32 ± 1.81	19.65 ± 1.75
120 wt%	13.16 ± 2.17	17.84 ± 3.15	22.03 ± 1.76
140 wt%	17.98 ± 2.18	–	–
Solid	54.67 ± 5.83		

Table 4.10 The four-point bend strengths of solid and porous blocks of sintered HA/TCP bioceramics.

Solid loading (wt%)		60	80		100			120			140	Solid sample
	Foam (ppi)	20	20	30	20	30	45	20	30	45	20	
60	20		O	O	X	XX	XX	O	#	XX	X	XX
80	20	O		#	X	XX	XX	O	X	XX	XX	XX
	30	O	#		#	X	XX	O	△	XX	#	XX
100	20	X	X	#		O	O	#	O	O	O	XX
	30	XX	XX	X	O		O	X	O	X	O	XX
	45	XX	XX	XX	O	O		XX	O	#	O	XX
120	20	O	O	O	#	X	XX		#	XX	X	XX
	30	#	X	△	O	O	O	#		#	O	XX
	45	XX	XX	XX	O	X	#	XX	#		X	XX
140	20	X	XX	#	O	O	O	X	O	X		XX
Solid sample		XX	XX	XX	XX	XX	XX	XX	XX	XX	XX	

XX	=	Highly significant difference
X	=	Significant difference
#	=	Probable difference
△	=	Possible difference
O	=	Difference not established

Table 4.11 Student T-test results for the four-point bend strengths of solid and porous samples from various solid loading and ppi foam.

4.5.2.2 Work of Fracture (Tattersall-Tappin Testing)

The test was carried out using notched specimens with dimensions of 18 × 5 × 4 mm in three-point bending as illustrated in section 3.4.2.2. The samples were tested with a constant crosshead speed of 0.05 mm/min and the span was 15 mm. Five to eight samples were tested in each condition. The key feature of the test was that the crosshead speed should be sufficiently low to allow cracks to grow, rather than the sample to fail catastrophically, otherwise very variably results will be recorded. Figure 4.42 shows the load-deflection curve of the test with too fast a crosshead speed. The sample broke immediately after the applied force exceeded the yield strength and the resulting curve was totally different to the ideal curve in Figure 4.43. The highest force is at the end of the testing not in the middle of the testing. The typical curve for Tattersall-Tappin Testing is shown in Figure 4.43. The load verse deflection curve is linear before fracture begins (AB). When a crack is initiated the load falls. The region BC corresponds to rapid crack extension. The crack continues to grow in a controlled manner (CD). The cross-head speed should be low enough to allow crack growth in the sample during the tests.

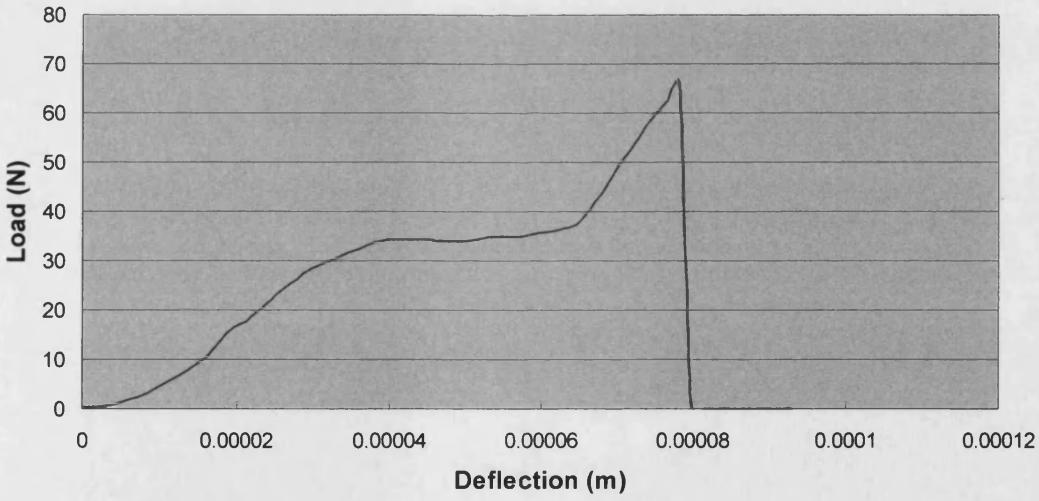

Figure 4.42 The load-deflection curve of Tattersall-Tappin Testing with too fast a crosshead speed.

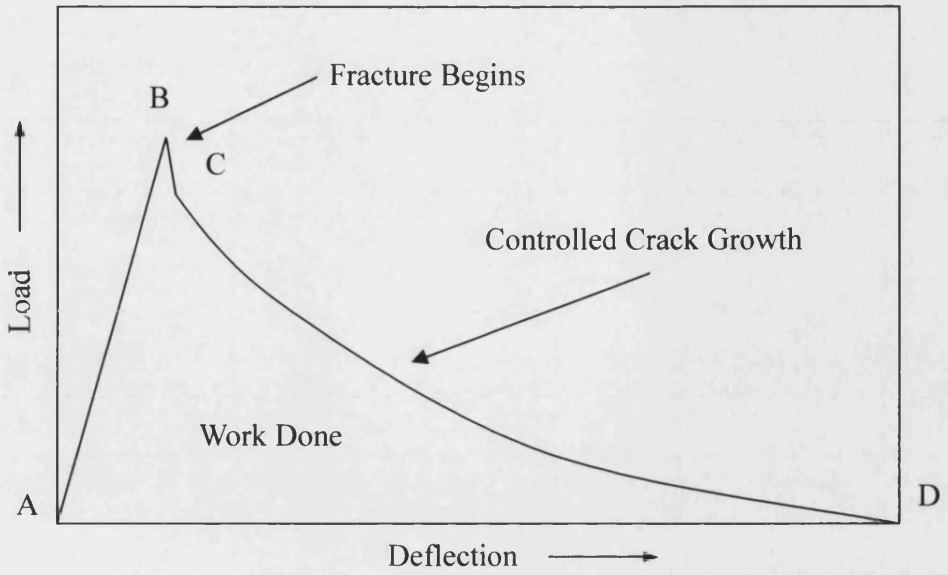

Figure 4.43 Typical Load-Deflection curve for a Tattersall-Tappin test.

Work of fracture in relation to solid loading:

The results of Tattersall-Tappin testing of solid and porous blocks resulting from 20, 30 and 45 ppi foams with various solid loading are shown in Figures 4.44 (a) (b) and (c), respectively. For all the different grade of foams the work of fracture generally increased with solid loading. This illustrates that microporosity had an effect on the work of fracture.

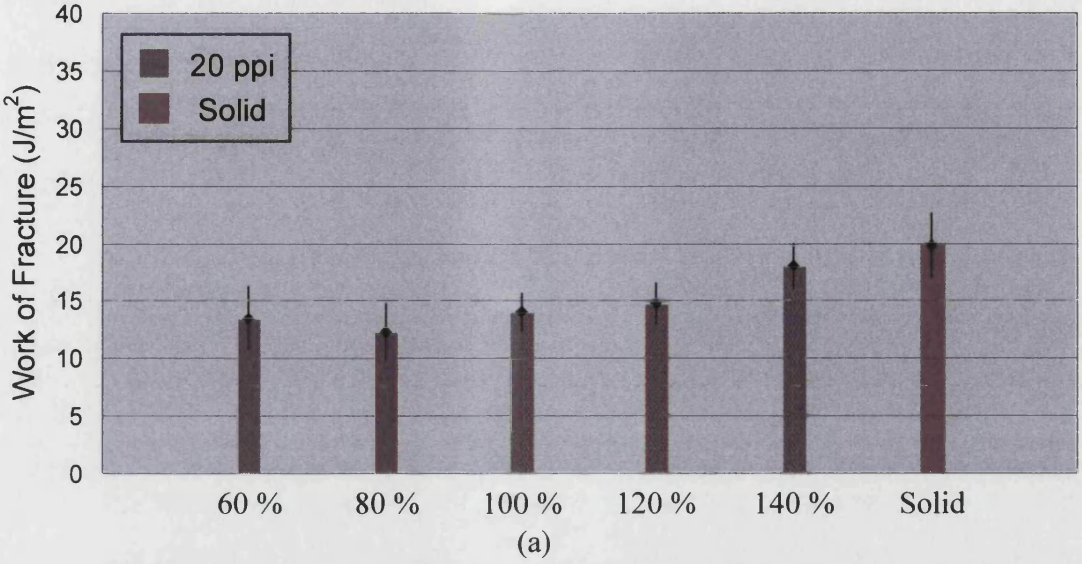

(a)

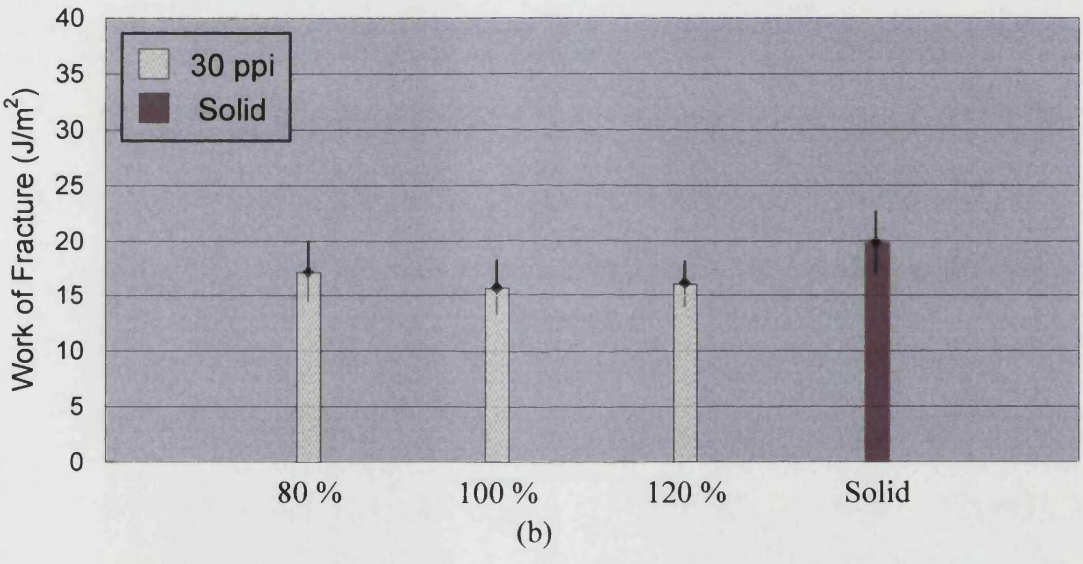

(b)

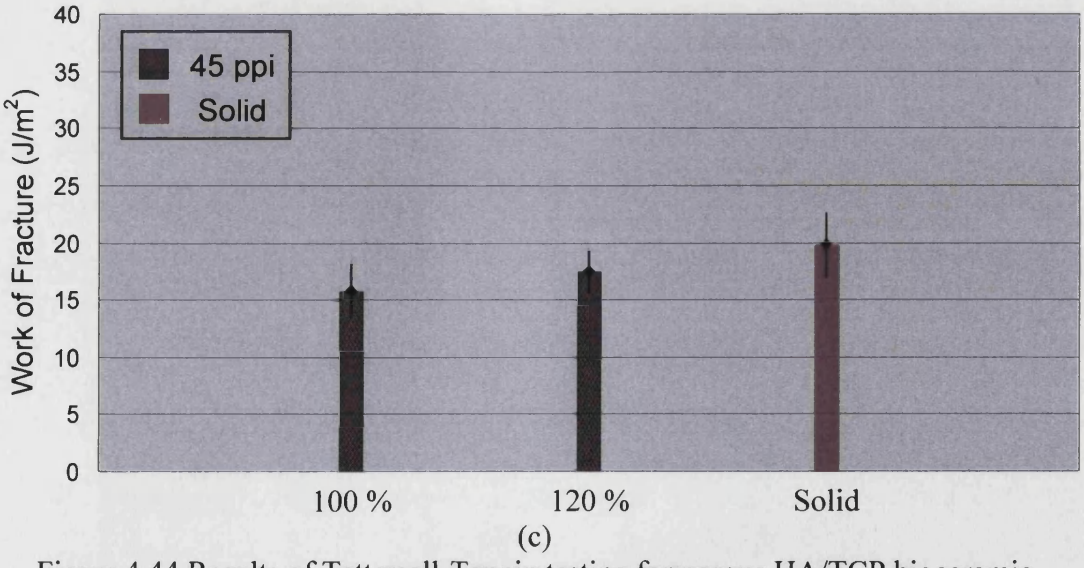

(c)

Figure 4.44 Results of Tattersall-Tappin testing for porous HA/TCP bioceramic produced from (a) 20 ppi (b) 30 ppi (c) 45 ppi foams and solid samples.

Work of fracture in relation to grade of foam:

Comparing the results from different foams, the work of fracture measured from lowest to the highest was in samples made from 20, 30 and 45 ppi foams. This was observed in 80, 100 and 120 wt% solid loading slips as shown in Figures 4.45 (a) (b) and (c). Samples made from 30 and 45 ppi foams with 100 wt% had similar values for work of fracture as shown in Figure 4.45 (b) but the samples made from 45 ppi foam still had higher value than the samples made from 30 ppi foam. The results showed similar trends to those observed for the measurement of density, four-point bend test and compressive tests. This is most likely the result of the different macropore sizes present in the samples.

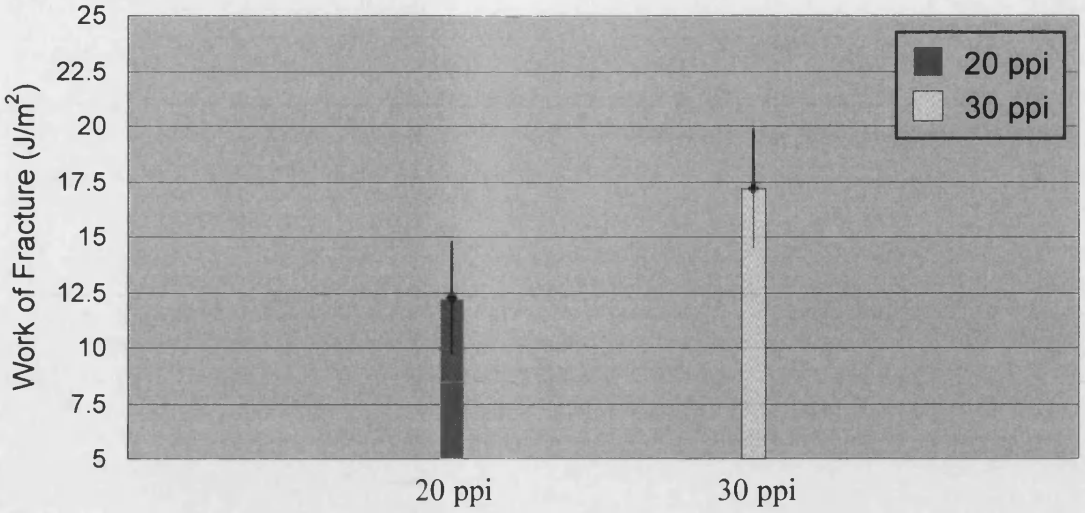

(a)

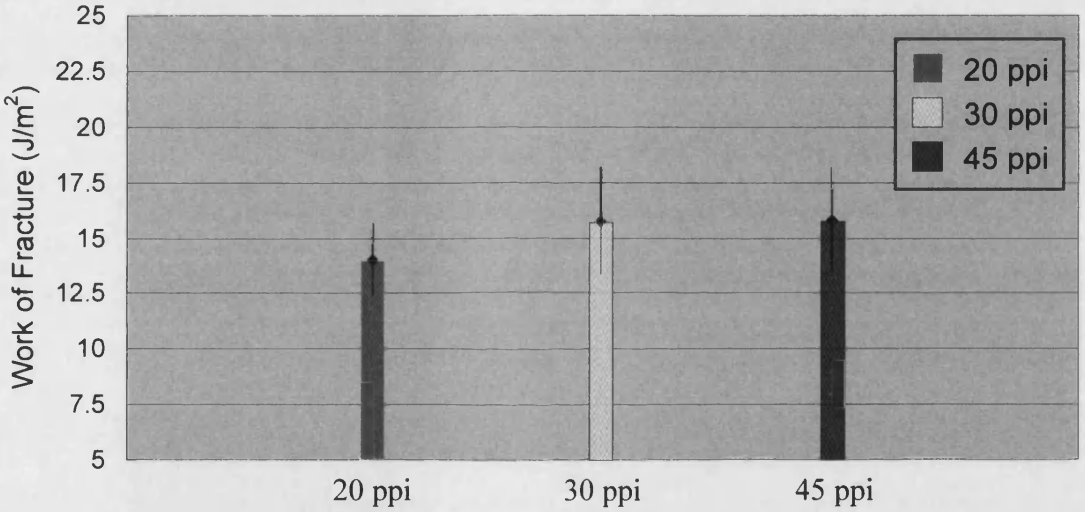

(b)

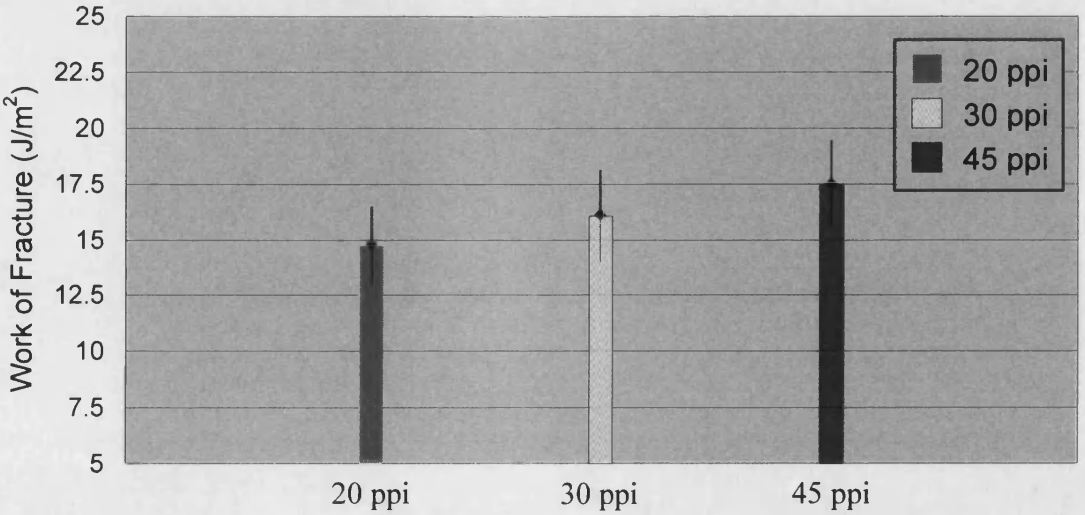

(c)

Figure 4.45 Results of Tattersall-Tappin testing for porous HA/TCP bioceramic produced from (a) 80 (b) 100 (c) 120 wt% solid loading slip.

Figure 4.46 and Table 4.12 summarize the results of Tattersall-Tappin testing of solid and porous HA/TCP samples. Table 4.13 shows the Student T-test results for the work of fracture from solid and porous samples from various solid loading and ppi foam. The results showed that the solid sample has the highest work of fracture but relatively, the difference when compared to the porous samples, is not as great as in the measurements from other mechanical tests. According to the Student T-test results, the differences of the work of fracture between the porous samples made from the same grade of foam but different solid loading are not significant and only a few of them show a significant difference or highly significant difference. The work of fracture of the porous samples is mostly the same with some possible difference for 20, 30 and 45 ppi samples with a specific slip loading. The results showed that work of fracture was slightly influenced by solid loading of slip and the grade of foam. Samples with a larger macropore size had lower work of fracture and the work of fracture also increased with solid loading. However, the differences between these porous samples made from various ppi foams and solid loading slips were relatively low compared to other mechanical tests. This may be because the Tattersall-Tappin test is not as sensitive to low levels of porosity.

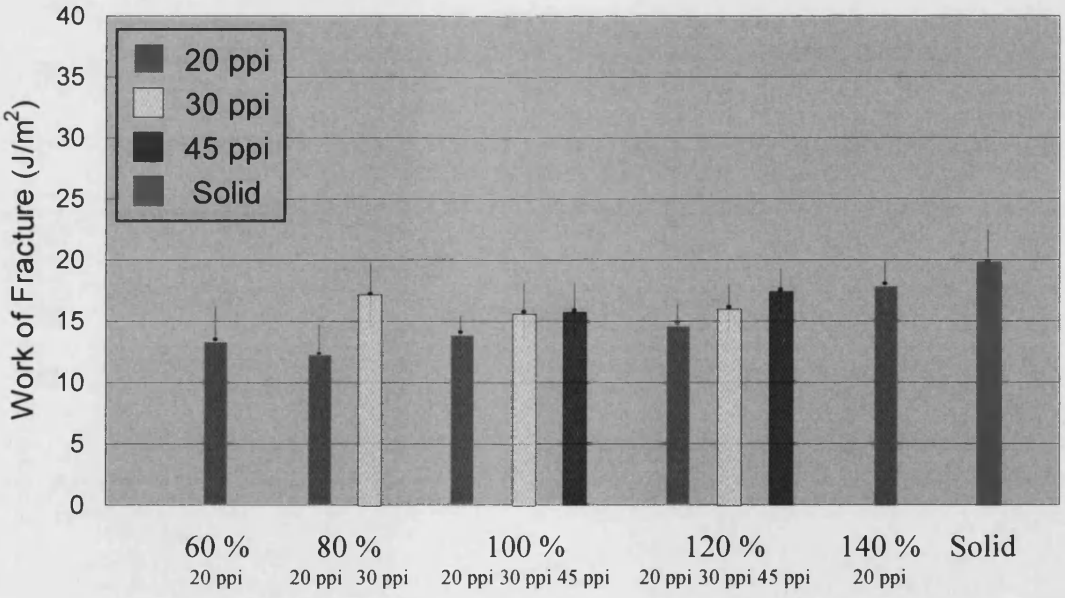

Figure 4.46 Results of Tattersall-Tappin testing for solid and porous HA/TCP bioceramic.

	Work of Fracture (J/m^2)		
Solid loading	**20 ppi**	**30 ppi**	**45 ppi**
60 wt%	13.50 ± 2.69	–	–
80 wt%	12.23 ± 2.52	17.17 ± 2.69	–
100 wt%	13.99 ± 1.60	15.71 ± 2.39	15.80 ± 2.35
120 wt%	14.71 ± 1.76	16.04 ± 2.04	17.49 ± 1.93
140 wt%	17.98 ± 1.98	–	–
Solid	19.72 ± 2.79		

Table 4.12 The work of fracture of solid and porous blocks of sintered HA/TCP bioceramics.

Solid loading (wt%)		60	80		100			120			140	Solid sample
	Foam (ppi)	20	20	30	20	30	45	20	30	45	20	
60	20		O	O	O	O	O	O	O	#	X	X
80	20	O		#	O	#	#	△	#	X	XX	XX
	30	O	#		△	O	O	O	O	O	O	O
100	20	O	O	△		O	O	O	O	#	X	X
	30	O	#	O	O		O	O	O	O	△	#
	45	O	#	O	O	O		O	O	O	△	#
120	20	O	△	O	O	O	O		O	#	X	X
	30	O	#	O	O	O	O	O		O	O	#
	45	#	X	O	#	O	O	#	O		O	O
140	20	X	XX	O	X	△	△	X	O	O		O
Solid sample		X	XX	O	X	#	#	X	#	O	O	

XX = Highly significant difference
X = Significant difference
# = Probable difference
△ = Possible difference
O = Difference not established

Table 4.13 Student T-test results for the work of fracture of solid and porous samples from various solid loading and ppi foam.

The results show that the work of fracture was slightly influenced by solid loading of slip and the foam structure. Samples with larger macropore sizes have lower values for work of fracture. However, the standard deviations in each group of the testing are high and are the highest when compared to other mechanical tests. The work of fracture results may be inaccurate for a number of reasons. The notches on these sample were made using a diamond-wafering saw and the samples were held manually. The width (g) of the gap as shown in Figure 4.47 could not be well controlled and as a result the two cuts were not exactly symmetrical. Consequently, the ratio of the base to the height (h/w) of specimens could not be properly controlled. According to the literature detailed in chapter 2.5.2, the work of fracture values might be affected by the notch depth ratio (h/w). In order to obtain more precise results, samples with regular notches should be made by using a purpose build jig and different notch depths could be further investigated.

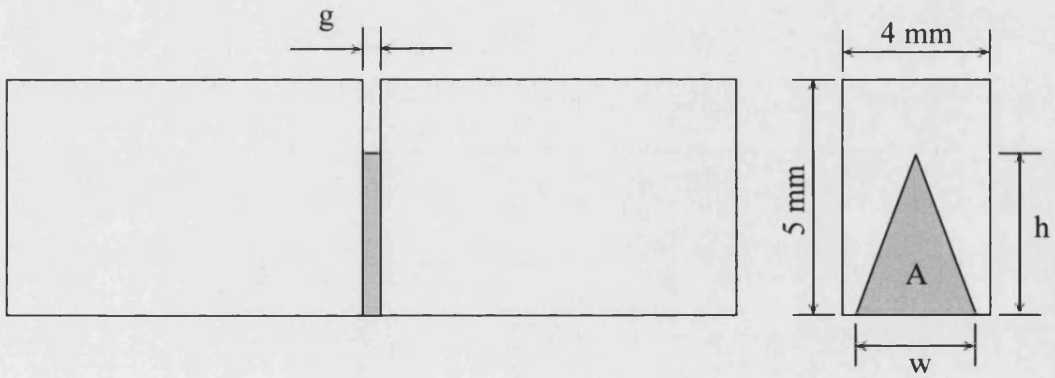

Figure 4.47 Schematic diagram showing the notched sample for the work of fracture test.

4.5.2.3 Compressive Testing

The testing was carried out using rectangular bars with dimensions of 15 × 5 × 4 mm as shown in section 3.4.2.3. The crosshead speed was 2 mm/min. Five to eight samples were tested in each condition. In order to reduce shear stress concentrations, a thin layer of rubber was inserted between each end of the sample and the loading plates of the machine during compressive tests. The difference between the testing without inserting rubbers and the testing with inserted rubber supports can be seen in Figure 4.48. The tests carried out with the rubber inserted resulted in higher compressive strengths and similar gradient curves in the elastic deformation region. This demonstrated that inserting the rubbers ensured more consistent results. Illustrations of compressive testing with and without inserting rubber supports can be seen in Figure 3.21 in the earlier experimental procedure section 3.4.2.3.

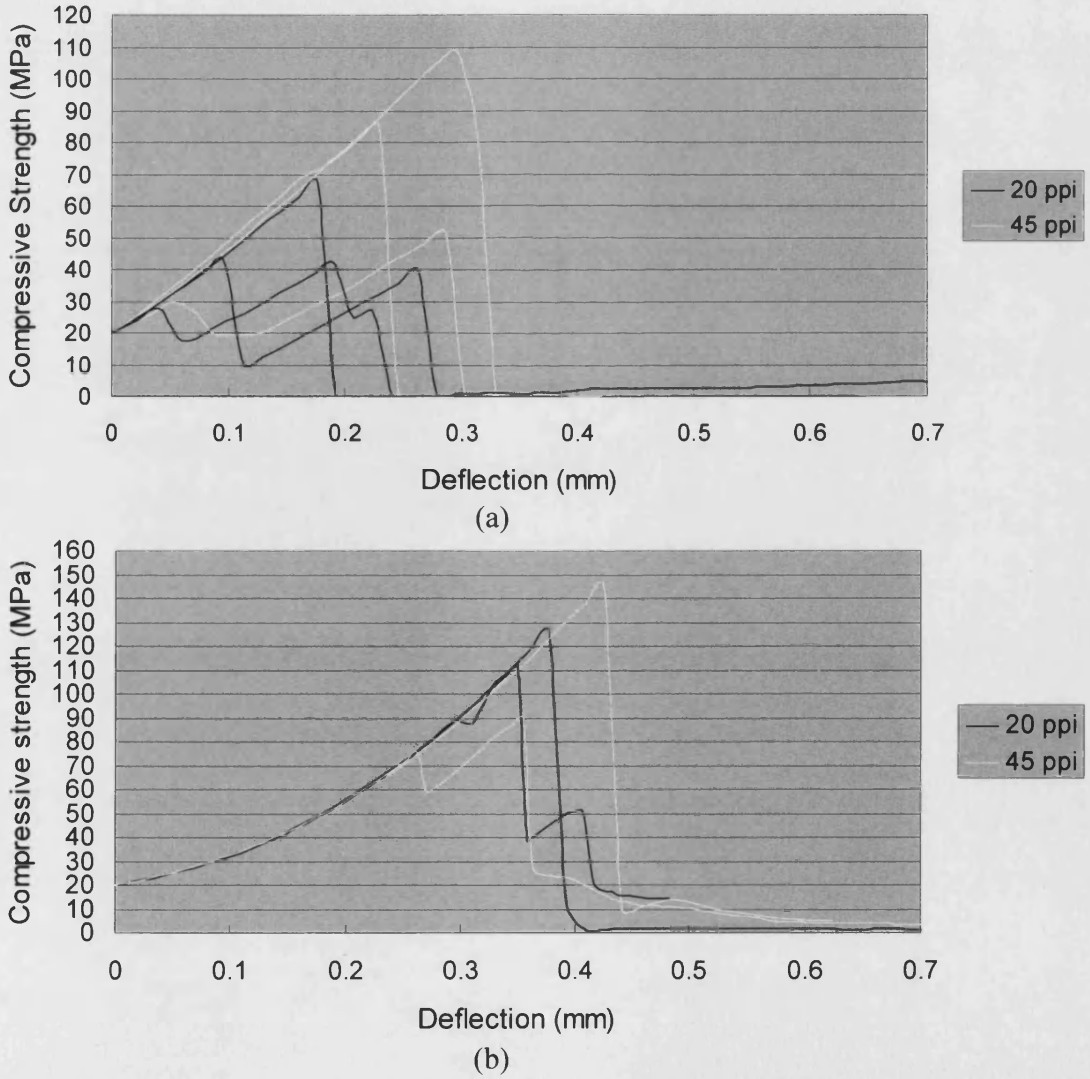

Figure 4.48 Results of compressive testing (a) without inserting rubbers (b) with inserted rubber supports

Compressive strength in relation to solid loading:

The results of compressive testing of solid and porous blocks resulting from 20, 30 and 45 ppi foams with various solid loadings are shown in Figures 4.49 (a) (b) and (c), respectively. Comparing the sample made from 20 ppi foams but different solid loading in Figure 4.49 (a), the compressive strengths increased slightly with the solid loading except in 80 wt% solid loading. This trend could also be seen in the samples made from 30 ppi foams in Figure 4.49 (b). The samples made from 45 ppi foams had similar values of compressive strength for the slips with 100 and 120 wt% solid loadings, which can be seen in Figure 4.49 (c). These results showed that generally the compressive strengths increased slightly with the solid loading. In the initial experiment, the compressive strengths decreased significantly when the solid loading was higher than 100 wt%. This was due to the fact that the samples contained many cracks when the slip had such a high solid loading. However, subsequently, it was found that the compressive strengths could be increased slightly when the solid loading was over 100 wt% by reducing the viscosity of the slip and extending the drying duration. This demonstrated that solid loading had an effect on compressive strength and higher solid loading results in higher compressive strengths. Figure 4.50 shows the unsuccessful porous HA/TCP generated by 20 and 30 ppi foams using the second vacuum impregnation method with slip of 120 wt% solid loading and 12,800 cps viscosity in the initial experiment. The successful samples using such a high solid loading can be seen in Figures 4.51 and 4.52.

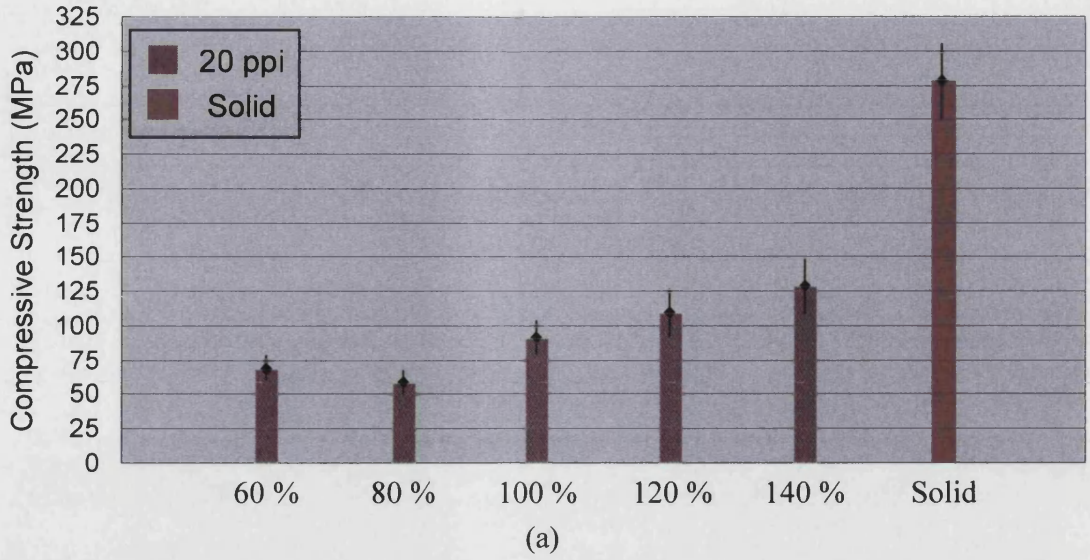

(a)

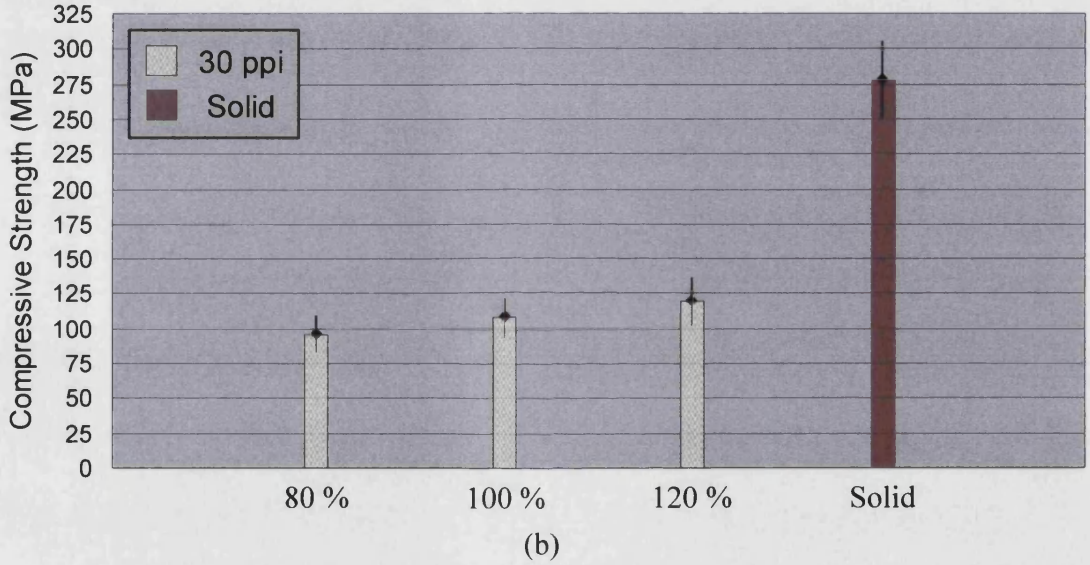

(b)

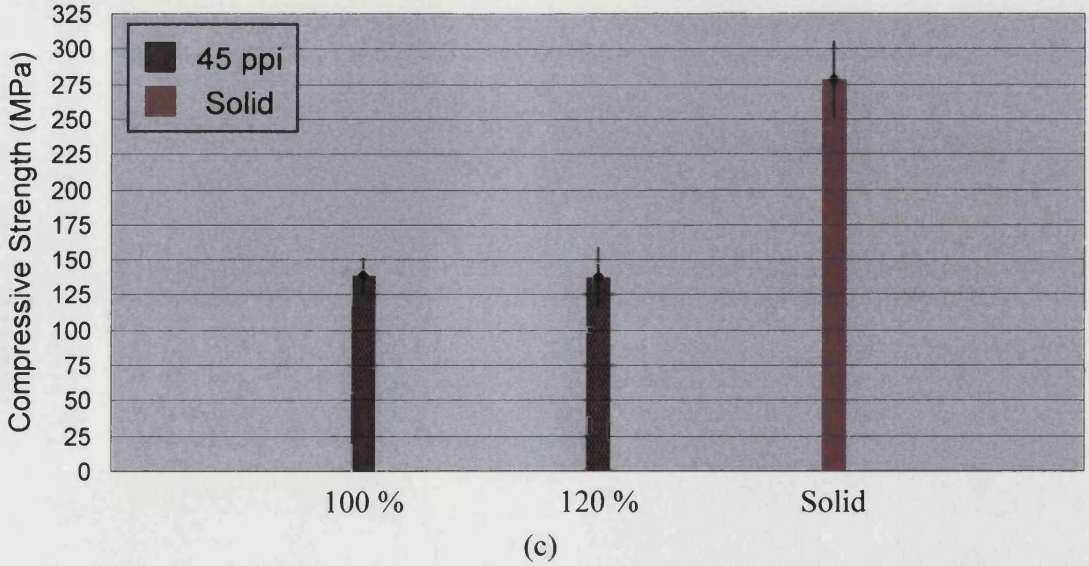

(c)

Figure 4.49 Compressive strengths of solid and porous HA/TCP bioceramics resulting from (a) 20 ppi (b) 30 ppi (c) 45 ppi foams.

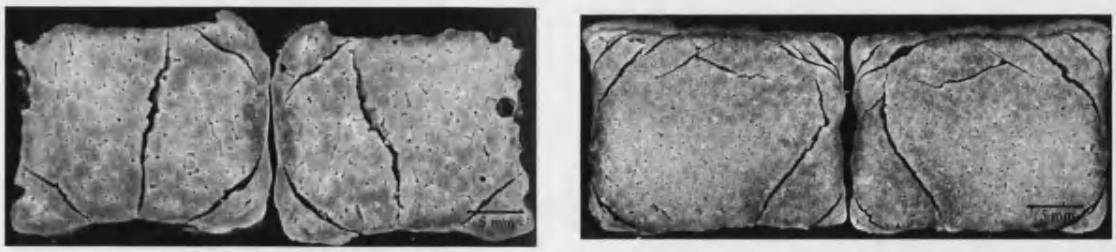

(a) 20 ppi (b) 30 ppi

Figure 4.50 A cross-section of porous HA/TCP generated by the second vacuum impregnation method with slip of 120 wt% solid loading and 12,800 cps viscosity.

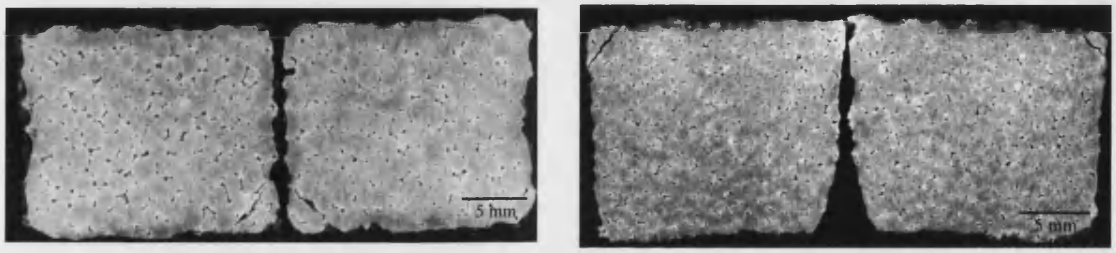

(a) 20 ppi (b) 30 ppi

Figure 4.51 A cross-section of porous HA/TCP generated by the second vacuum impregnation method with slip of 120 wt% solid loading and 8,800 cps viscosity.

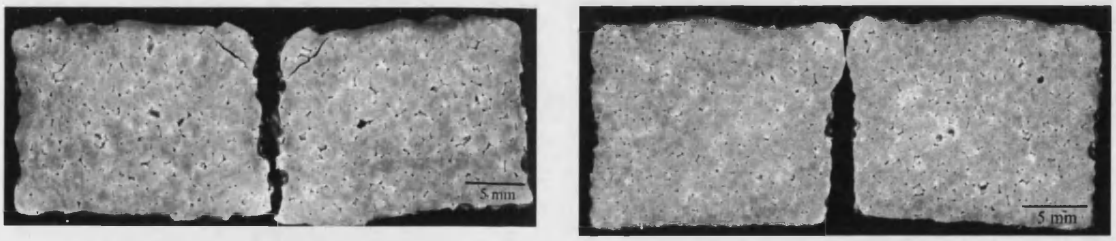

(a) 20 ppi (b) 30 ppi

Figure 4.52 A cross-section of porous HA/TCP generated by the second vacuum impregnation method with slip of 140 wt% solid loading and 9,600 cps viscosity.

Compressive strength in relation to grade of foam:

The compressive strengths of porous blocks resulting from 80, 100 and 120 wt% solid loading slips are shown in Figures 4.53 (a) (b) and (c), respectively. Comparing the samples made from the same solid loading but different ppi foams, the strengths from low to high are in the order of 20 ppi, 30 ppi and 45 ppi foams. This shows macropores have an influence on compressive strengths and larger macropore sizes result in lower compressive strengths.

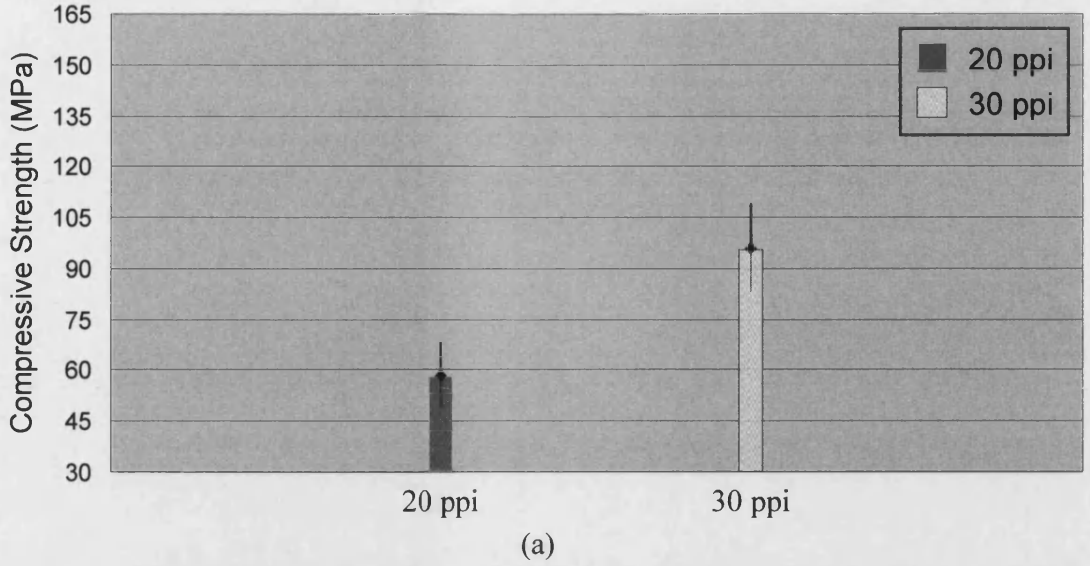

(a)

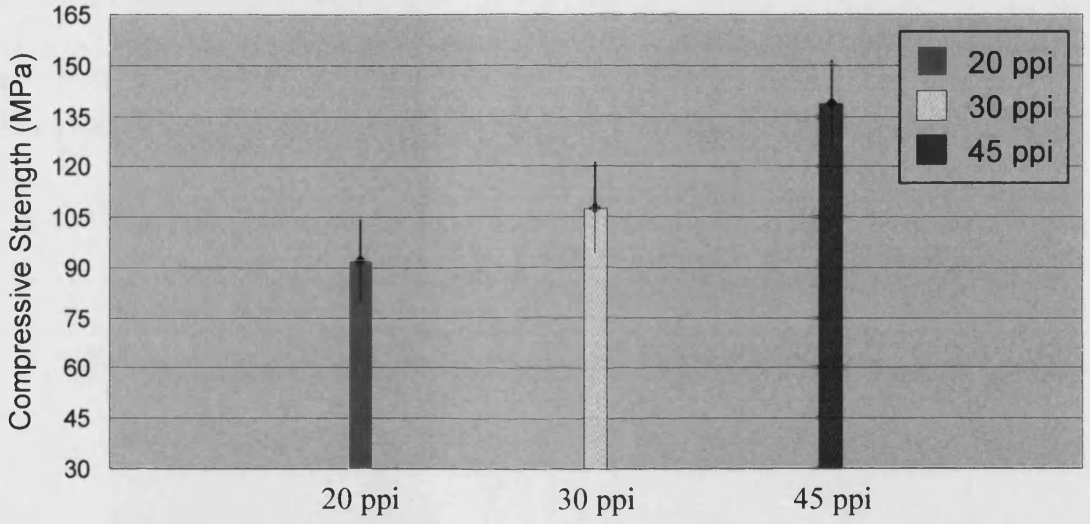

(b)

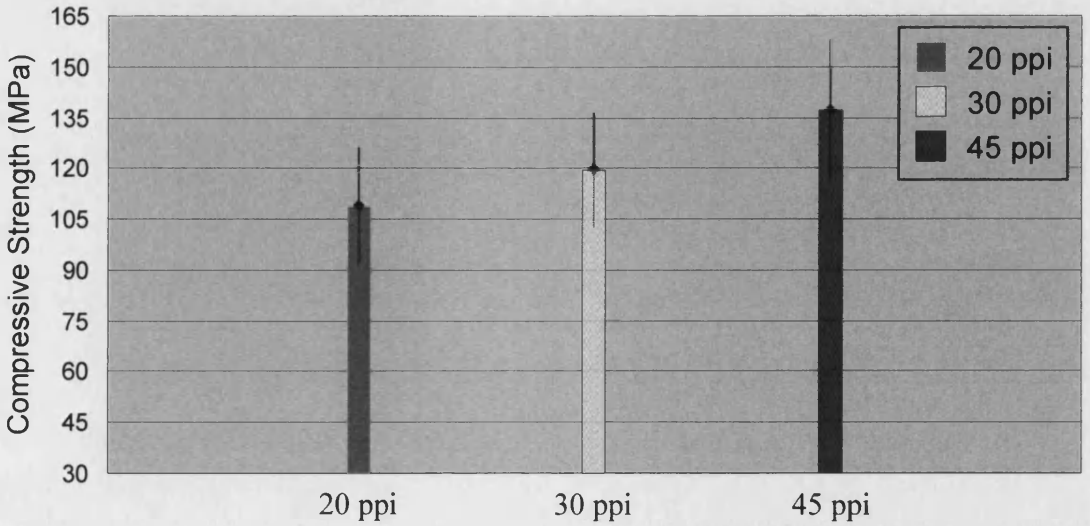

(c)

Figure 4.53 Compressive strengths of porous blocks of the sintered HA/TCP bioceramics resulting from (a) 80 (b) 100 (c) 120 wt% solid loading slips.

The compressive strengths of solid and porous HA/TCP samples are summarized in Figure 4.54 and Table 4.14. The average compressive strengths for porous sample were in the range of 58.46 to 138.72 MPa. The solid samples had the highest compressive strengths, which were 277.79 ± 26.97 MPa. Table 4.15 shows the Student T-test results for the four-point bend strengths from solid and porous samples from various solid loading and ppi foam. According to the Student T-test results, the compressive strength of the solid sample, made from the slip of 100 wt% solid loading, was highly significantly different to any other porous samples. The differences of the compressive strength between the porous samples made from the same grade of foam but different solid loading varied from no difference to a significant difference. The effect of foam size on compressive strength was similar to that of solid loading on compressive strength. The differences of the compressive strength between the porous samples made from the same solid loading but different grade of foam varied from no difference to a significant difference. According to the results, the compressive strengths were influenced by not only foam structures but also solid loading. Samples with larger macropore sizes and microporosities had lower compressive strengths.

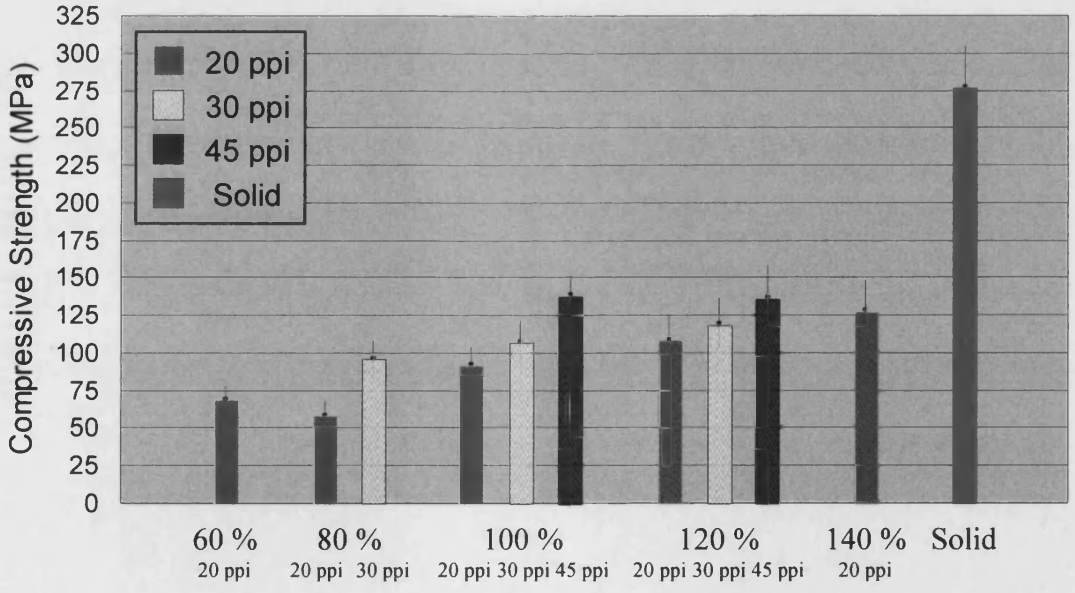

Figure 4.54 Compressive strengths of the solid and porous sintered HA/TCP bioceramic.

	Compressive strength (MPa)		
Solid loading	**20 ppi**	**30 ppi**	**45 ppi**
60 wt%	68.90 ± 9.03	–	–
80 wt%	58.46 ± 9.35	96.00 ± 12.73	–
100 wt%	92.00 ± 12.12	107.51 ± 13.75	138.72 ± 12.58
120 wt%	109.00 ± 17.17	119.46 ± 16.97	137.20 ± 20.73
140 wt%	128.30 ± 19.95	–	–
Solid	277.79 ± 26.97		

Table 4.14 The compressive strength of solid and porous blocks of sintered HA/TCP bioceramics.

Solid loading (wt%)		60	80		100			120			140	Solid sample
	Foam (ppi)	20	20	30	20	30	45	20	30	45	20	
60	20		O	△	△	X	XX	#	X	X	X	XX
80	20	O		#	#	X	XX	X	X	X	X	XX
	30	△	#		O	O	X	O	O	△	O	XX
100	20	△	#	O		O	X	O	O	#	△	XX
	30	X	X	O	O		X	O	O	#	O	XX
	45	XX	XX	X	X	X		#	O	O	O	XX
120	20	#	X	O	O	O	#		O	△	O	XX
	30	X	X	O	O	O	O	O		O	O	XX
	45	X	X	△	#	#	O	△	O		O	XX
140	20	X	X	O	△	O	O	O	O	O		XX
Solid sample		XX	XX	XX	XX	XX	XX	XX	XX	XX	XX	

XX = Highly significant difference
X = Significant difference
# = Probable difference
△ = Possible difference
O = Difference not established

Table 4.15 Student T-test results for the compressive strengths of solid and porous samples from various solid loading and ppi foam.

Ideally, fracture of sample in compression testing will be caused by maximum shear stresses and the fracture surfaces in the sample will be oriented at the angle of 45° to the axes of loading. Although inserting rubber supports at each end of the sample can reduce stress concentrations and result in higher compressive strengths, the failure mode observed was not the classic shear failure expected at 45° along the axis. This phenomenon can be seen in Figure 4.55. This was observed on both solid and porous samples made from various ppi foams and with and without inserting rubber supports. Figure 4.55 (a) shows the failure of a porous sample, made from 30 ppi foam, following compressive testing without inserting rubbers. Figures 4.55 (b) to (e) show porous samples made from various ppi foams with rubber supports inserted during compressive testing. The fracture for a solid sample is shown in Figure 4.55 (f). This illustrated the failure modes in the solid and porous samples with different macropore sizes were similar. The most common failure modes were fracture in the centre and at the corners of the samples. However, in both common failure modes the fracture lines in these samples were oriented parallel to the axes of loading.

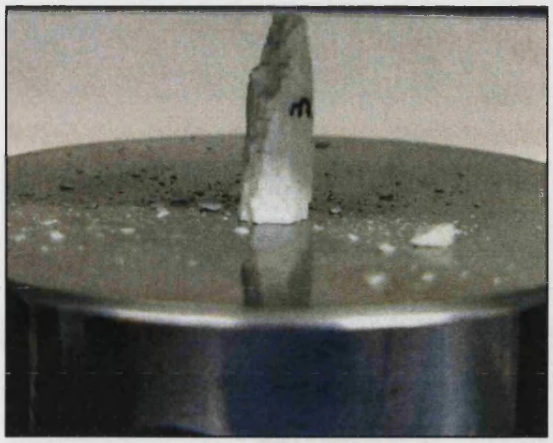

(a) porous sample made from 30 ppi foam broken at the corners

(b) porous sample made from 20 ppi foam broken to elongated pieces

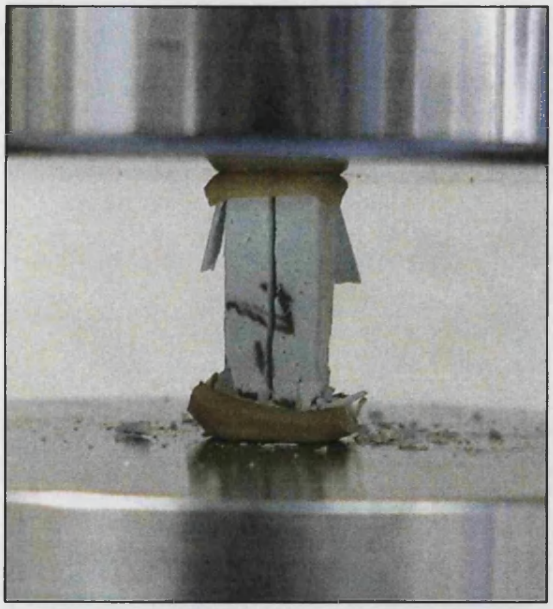

(c) porous sample made from 30 ppi foam broken in the centre

(d) porous sample made from 45 ppi foam broken at the corners

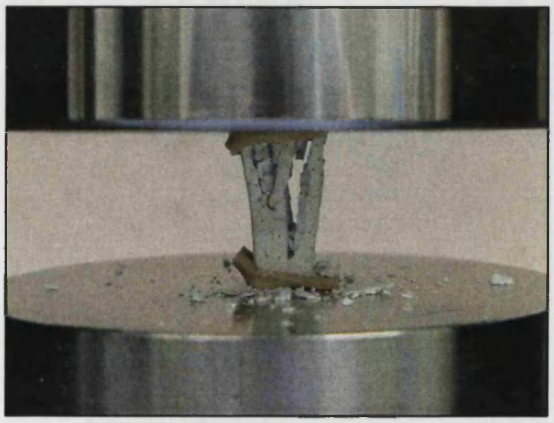

(e) porous sample made from 20 ppi foam broken in the centre

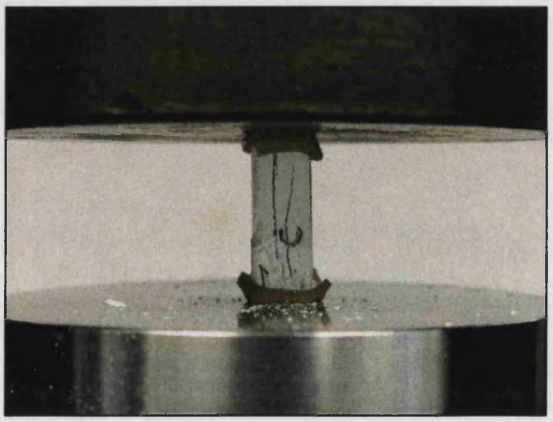

(f) solid sample broken in the centre

Figure 4.55 Illustration of the mode of the fracture for compressive tests.

According to literature[267], one explanation could be the friction between the sample and compression platens. The literature also mentioned that if the interface is dry, leading to strong friction between the samples and loading plate, then the fracture surfaces in the sample, in this situation, will be oriented at an angle of 45° to the axes of loading. If the interface is oily or wet, allowing some sliding along the interface in the transverse direction, then fracture will be caused by transverse strains arising during loading. The fracture line in the sample will be oriented parallel to the axes of loading. However, in the current study, the interface was dry. The samples might have experienced some sliding along the interface in the transverse direction when the test was carried out without inserting rubber supports. However, using the rubber supports, the friction between the samples and the surface of the platens should be increased, reducing the tendency to slip.

In contrast to this, it was reported[49,135] that friction could contribute to measurement error and the platens need to be lubricated. When a sample is compressed, most types of material will expand in the transverse direction due to the Poisson's effect. Friction at the interface will interfere with this expansion and change the apparent stiffness of the sample. Further work needs to be carried out on the failure mode to find out if friction is the cause of the unexpected failure modes observed.

4.5.2.4 Die-Plunger Testing

The test was employed to measure the compressive modulus, relaxation and energy absorption properties of granules. A 20 mm diameter and 150 mm length die-plunger was utilized to compress the granules and the cross-head speed was 2 mm/min. The first compression cycle was loading to 500 N and the second cycle was loading to 1000 N as outlined in section 3.4.2.4.

The HA/TCP granules, 4 mm in diameter, were made by the vacuum impregnation method from 20, 30 and 45 ppi foams. A commercially available synthetic material BoneSave® (Stryker Howmedica Osteonics, Limerick, Ireland), used for impaction grafting and space filling was used for comparison. Figures 4.56 (a) (b) and (c) show the compression force versus strain curves for porous HA/TCP granules made from 20, 30 and 45 ppi foams, respectively during the first compression cycle (0 to 500 N). The compression force increased exponentially up to a maximum peak in the first compression cycle up to the 500 N maximum load. The force-strain curves of the granules made by the vacuum impregnation method were quite irregular during the first compression from 0 to 500 N. In comparison, BoneSave® materials did not show this tendency. The reason might be the dimensions of these granules (4 mm) were greater compared to BoneSave® materials (2 to 4 mm), and this resulted in poorer packing initially. Granules of BoneSave® had a range of dimensions might result in better packing.

The granules made from 20 ppi foams had the highest average maximum strain up to 500 N which was 0.088. The average maximum strain for the granules made from 30 ppi foams was 0.067. The granules made from 45 ppi foams have the lowest average maximum strain which was 0.061. This indicated that the larger macropore size results in higher strain in the first compression cycle.

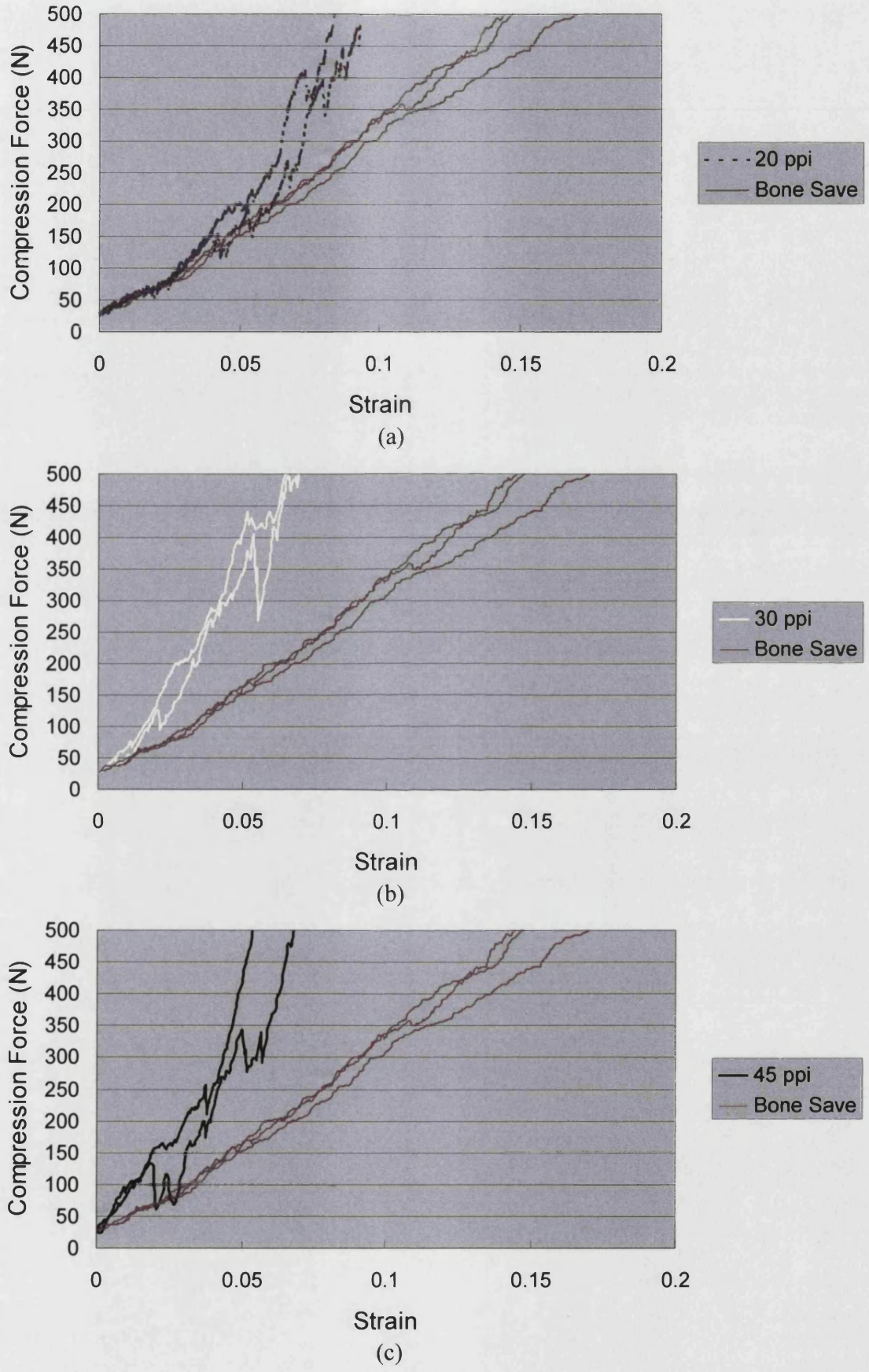

Figure 4.56 Compression force versus strain diagram for die-plunger testing of granules produced from (a) 20 ppi (b) 30 ppi (c) 45 ppi foam, up to 500 N.

Figures 4.57 (a) (b) and (c) show the compression force versus strain curves for porous HA/TCP granules made from 20, 30 and 45 ppi foams during the second compression cycle (0 to 1000 N), respectively. When the pre-compressed sample was loaded for the second time to 1000 N, the granules reacted in a stiffer manner than in the first compression and the curves from 0 to 500 N were relatively smooth. When the force exceeded 500 N, a visible decrease in the gradient of the force-strain correlation was noticed. However, this gradient was still much higher than during the first 0 to 500 N compression. Once the original peak load was exceeded, the compression force-strain relation became irregular.

The average maximum strain for the granules made from 20, 30 and 45 ppi foams were 0.040, 0.035 and 0.036, respectively. This shows that the strain order in the second compression cycle was similar to that in the first compression cycle. Larger macropore size results in higher strain.

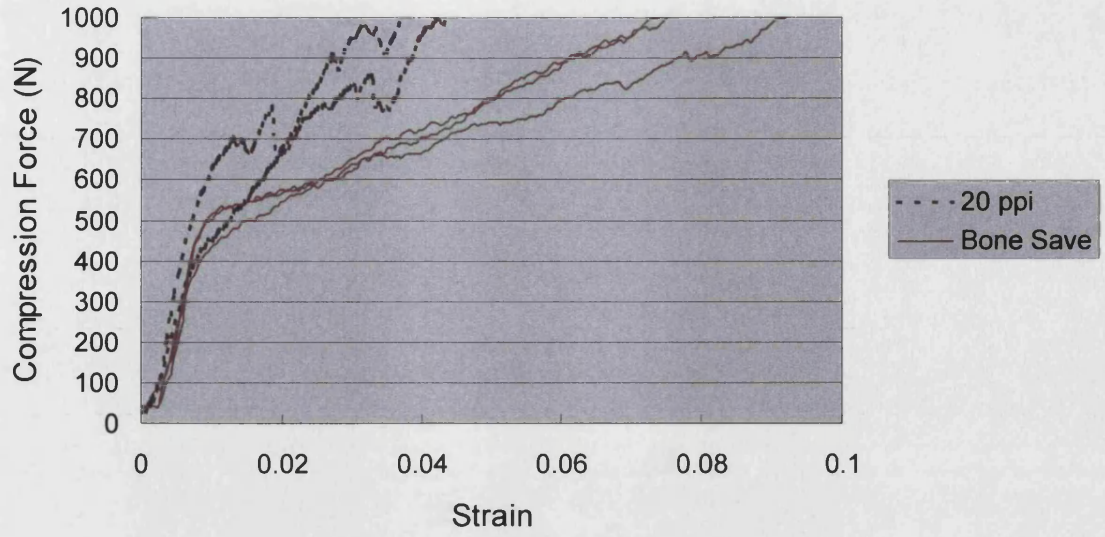

(a)

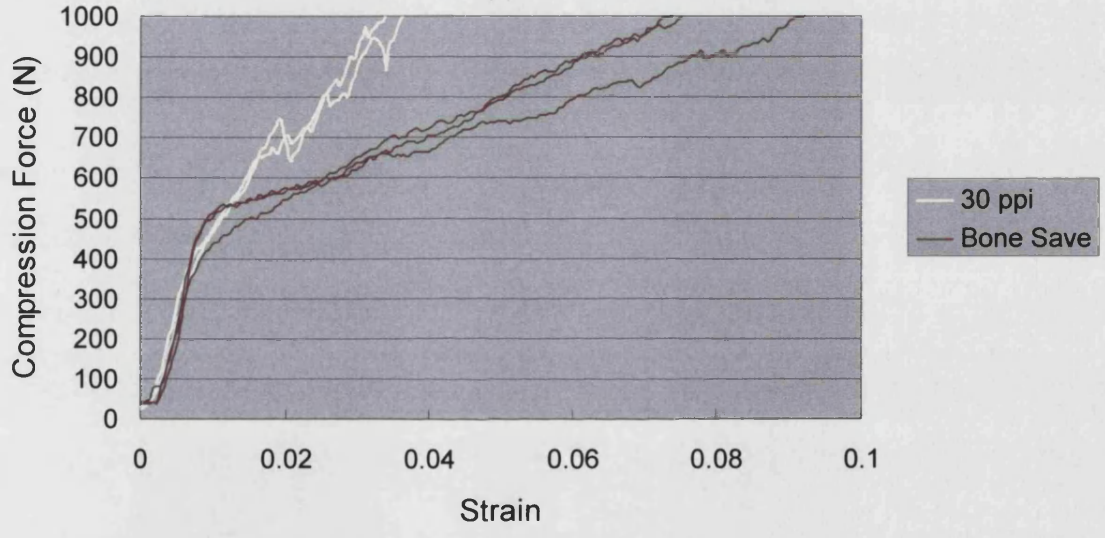

(b)

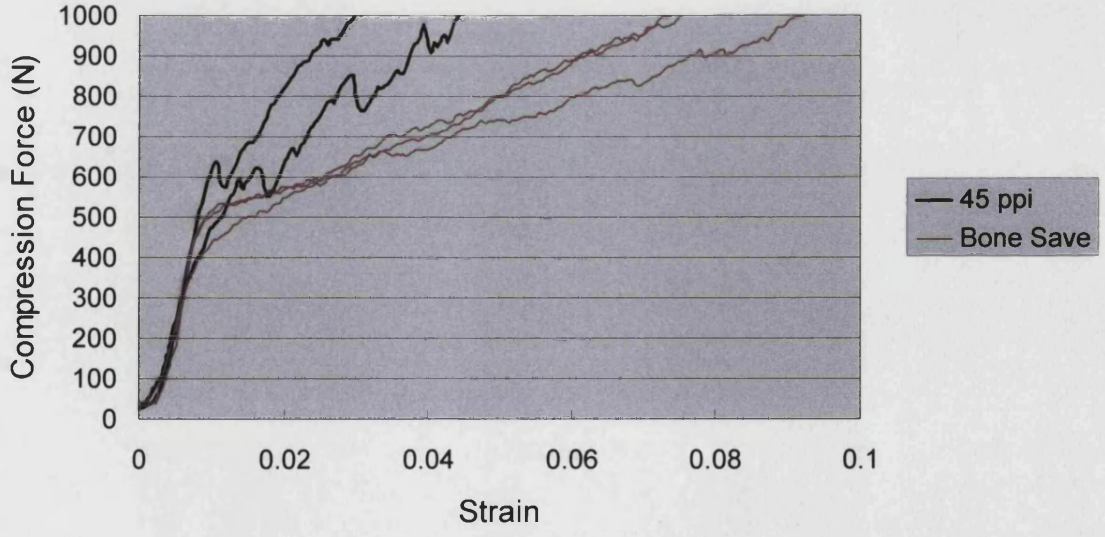

(c)

Figure 4.57 Compression force versus strain diagram for die-plunger testing of granules produced from (a) 20 ppi (b) 30 ppi (c) 45 ppi foam, up to 1000 N.

Figure 4.58 summarizes the compression force versus strain curves for porous HA/TCP granules during the first compression cycle (0 to 500 N) and the second compression cycle (0 to 1000 N). The granules made by the vacuum impregnation technique were stiffer than BoneSave® materials in both the first and the second compression cycle and did not crumble to powder after the testing. By comparison, many of BoneSave® granules crumbled to become smaller diameter powders. The commercial BoneSave® granules were produced by breaking a single large piece of material into smaller pieces. The sizes and shapes were not well controlled. The macro-pores in the commercial BoneSave® granules which were produced by burning out of organic particles were not interconnected. It can be concluded that the experimental granules could be useful for impaction grafting and space filling, with an improved capacity for retaining structural integrity.

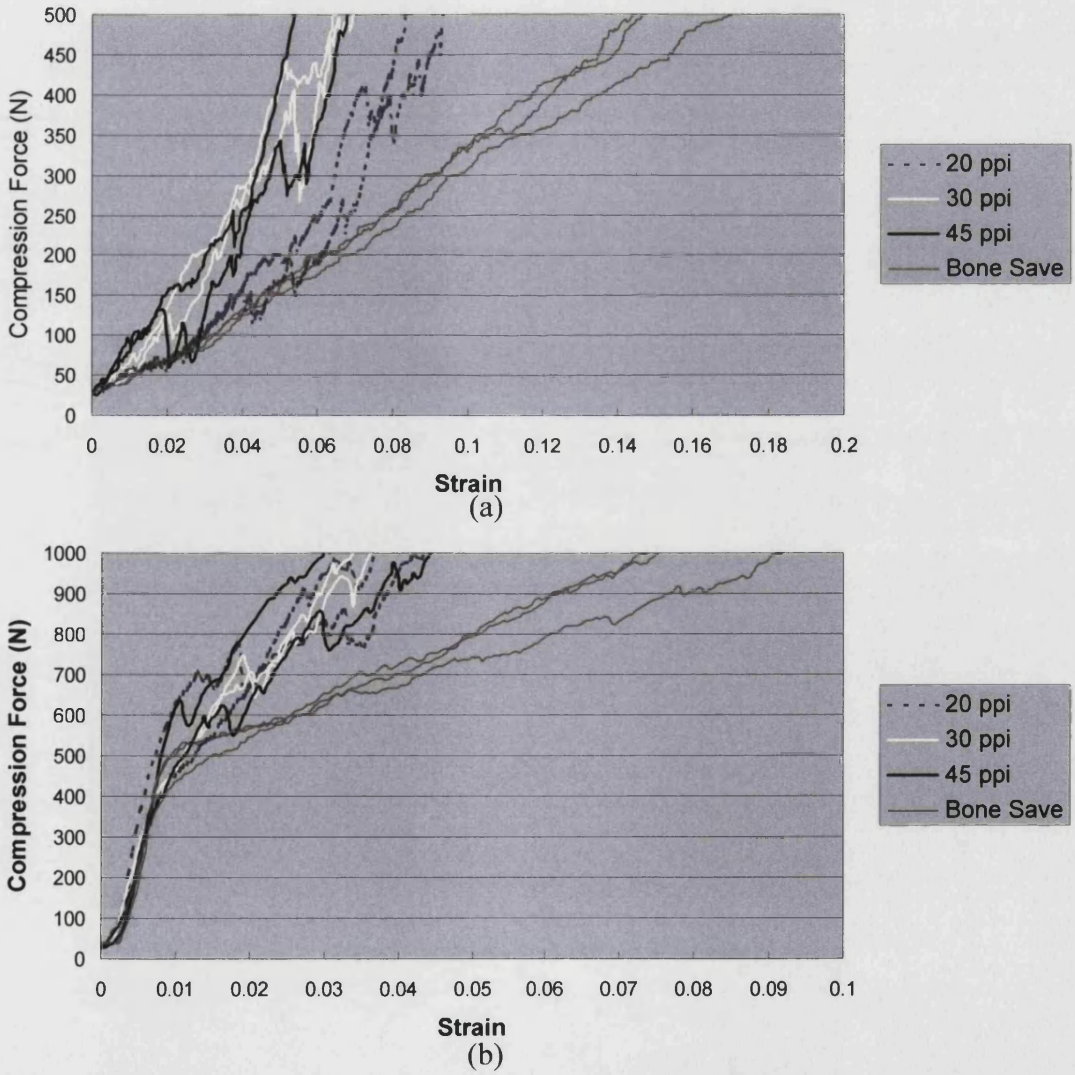

Figure 4.58 Compression force versus strain diagram for die-plunger testing of 4 mm granules and 2 – 4 mm BoneSave®. (a) up to 500 N (b) up to 1000 N.

Figure 4.59 shows results of testing granules with an average diameter of 6 mm. The curve in the first compression test from 0 to 500 N was extremely smooth and stable in Figure 4.59(a). However, the gradient of the curve was quite steep up to 600 N but dropped sharply and became unstable at 600 to 1000 N during the second compression in Figure 4.59(b). This may be explained in terms of the loose packing of the granules due to their large size. The larger granules tended to have a particular arrangement rather then random arrangement, the results will depend on the arrangement of these granules. Figure 4.60 shows the likely distribution of these granules during the test. Smaller granules have a more uniform packing factor. Larger granules could have quite a different arrangement. Figure 4.60 (a) shows the large granules pile up compactly in the right hand side but loosely on the left hand side. These different packing configurations could result in a diversity of results.

The force used for the testing in the first stage of compression was low for these granules and almost none of the granules broke, this resulted in the smooth and stable curve in Figure 4.59(a). Subsequently, for the test up to 1000 N, many of the granules were damaged or crushed. This resulted in the unsteady curve in Figure 4.59(b). The results showed that the test conditions were only suitable for small granules, which were smaller than 4 mm diameter due to the size of the granules in relation to the diameter of the die plunger. Furthermore, these granules are all in regular cubic shapes which may aggravate this problem. Using granules with a range of dimensions or a larger diameter die plunger may alleviate the problem.

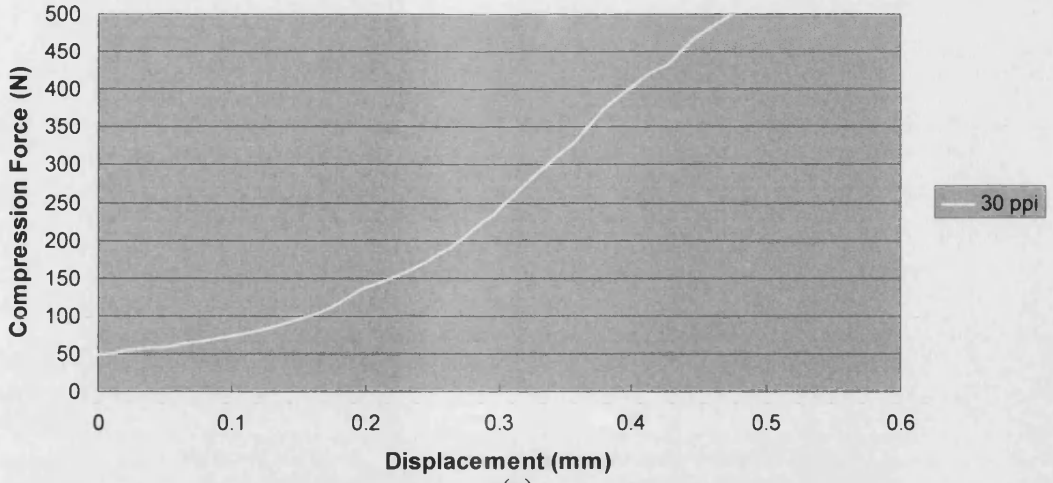

(a)

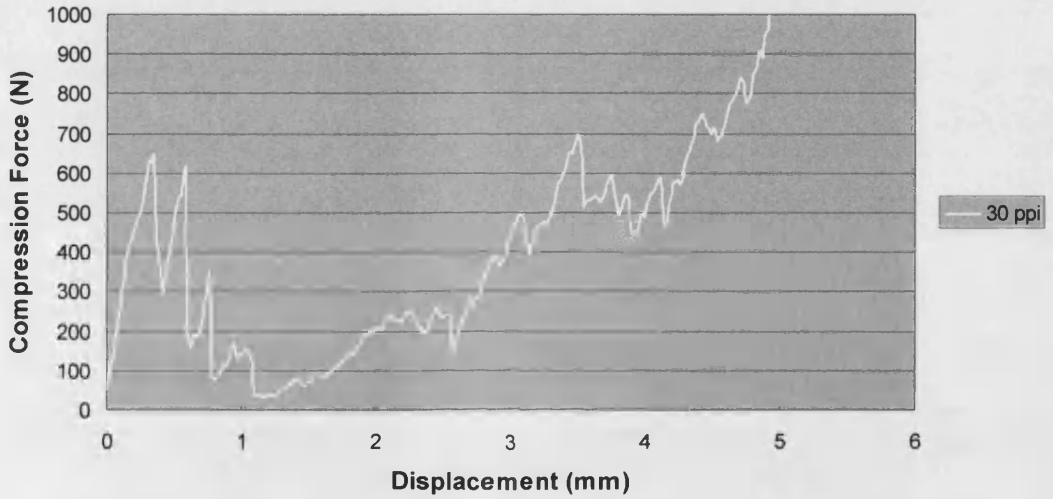

(b)

Figure 4.59 Force-deformation diagram for die-plunger testing of 6 mm granules. (a) up to 500 N (b) up to 1000 N.

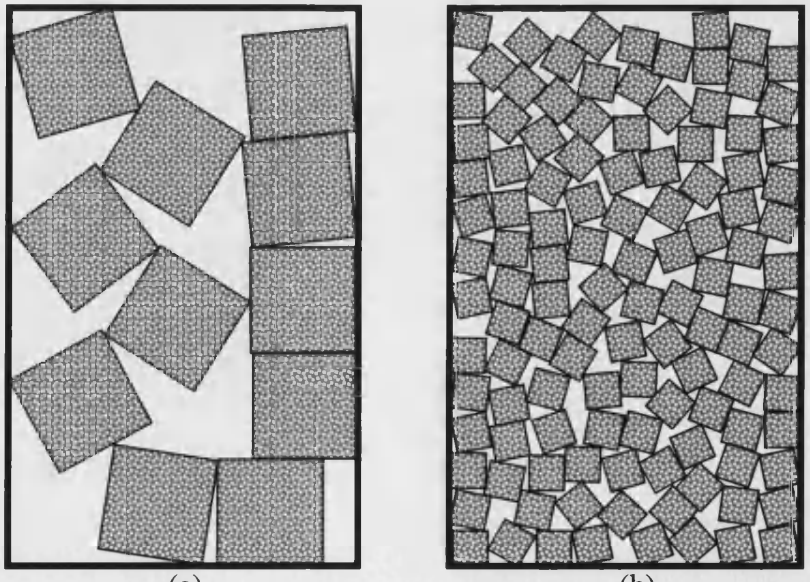

(a) (b)

Figure 4.60 Schematic representation of die-plunger testing for (a) large granules (b) small granules.

The relaxation behaviour of the granules made from various ppi foams and BoneSave® materials from the maximum load of 500 N are given in Figure 4.61. BoneSave® granules have higher relaxation than other granules. The average relaxations of granules from low to high are in the order of 30 ppi, 20 ppi and 45 ppi foams. This shows the average relaxations of granules have no particular order in relation to macropore sizes.

The relaxation behaviour of the granules and BoneSave® from the maximum load of 1000 N are given in Figure 4.62. The relaxations from the maximum load of 1000 N are higher than those from the maximum load of 500 N. The average relaxations of granules from low to high are in the order of 30 ppi, 20 ppi and 45 ppi foams. Granules made from 45 ppi foam had similar relaxation to BoneSave® granules. There is also no particular order in relation to macropore size for the relaxation behaviour from the maximum load of 1000 N. However, the average relaxations from low to high, in granules made from different ppi foams, are in the order of 30 ppi, 20 ppi and 45 ppi from the maximum load of both 500 and 1000 N. This coincidence may be caused by experimental error. Further work needs to be carried out to establish more accurate correlations between relaxation and macropore size.

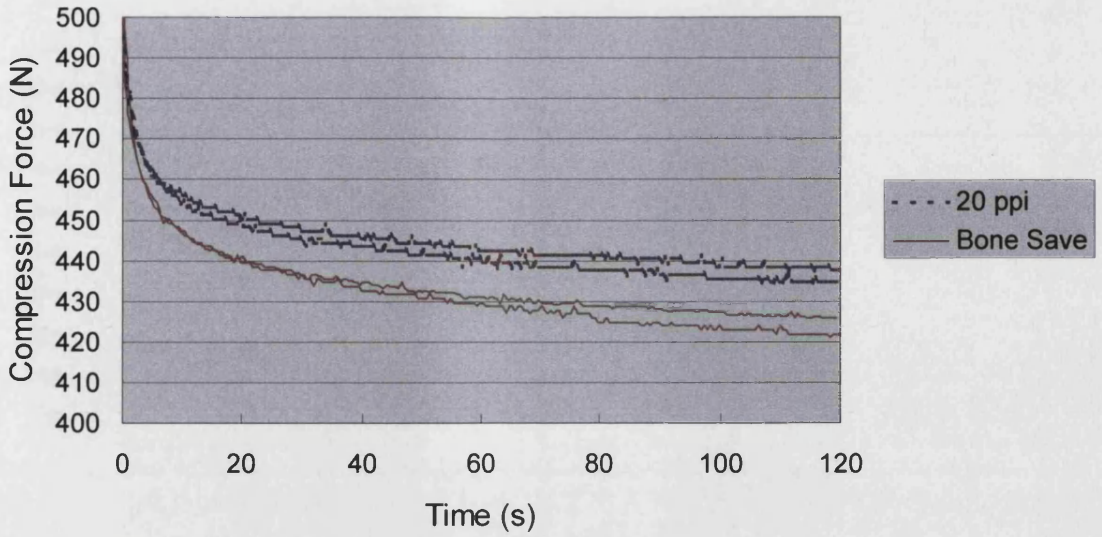

(a)

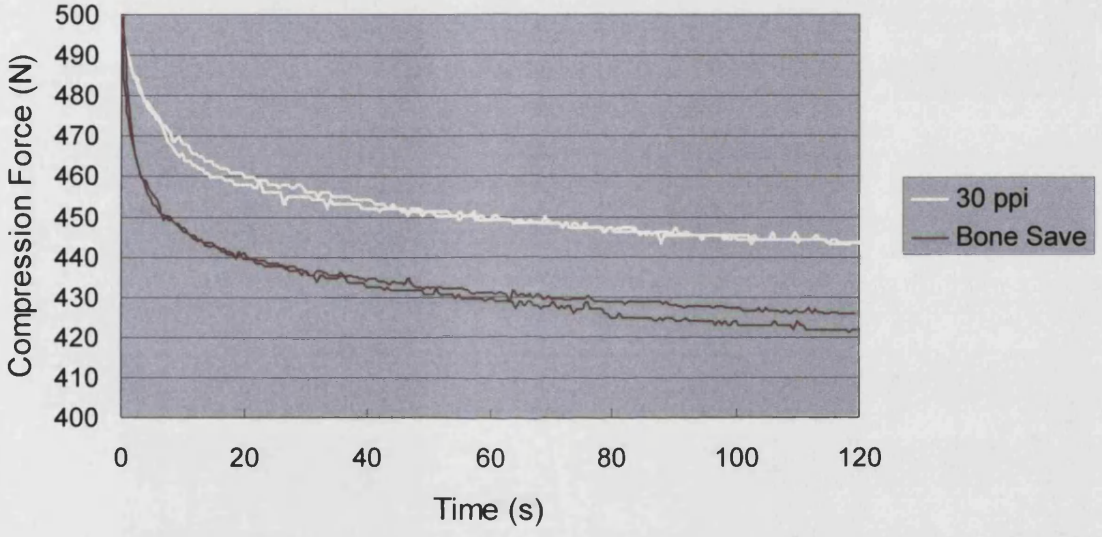

(b)

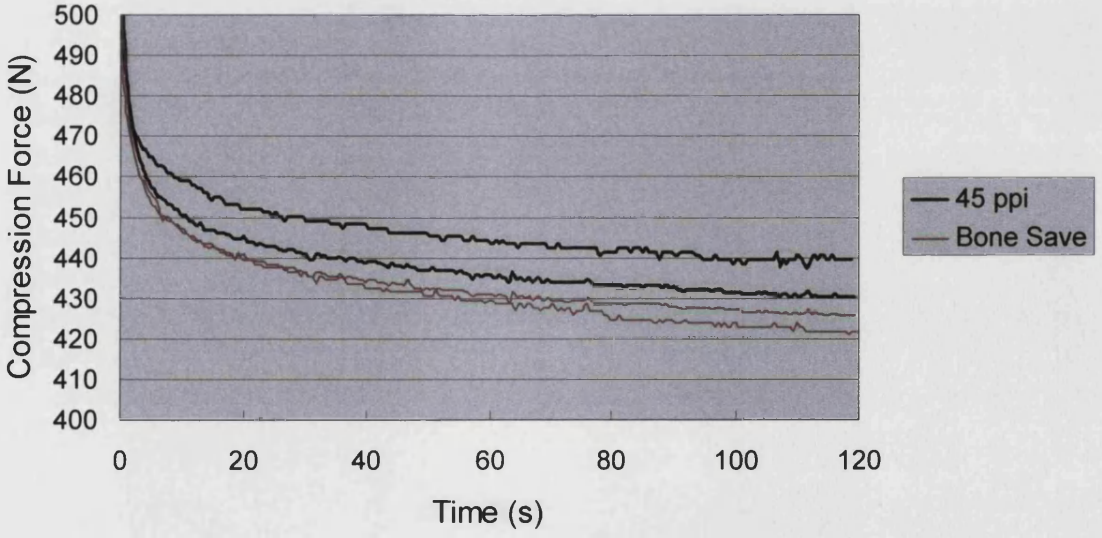

(c)

Figure 4.61 Compression force versus time curves for relaxation from 500 N of granules produced from (a) 20 ppi (b) 30 ppi (c) 45 ppi foam.

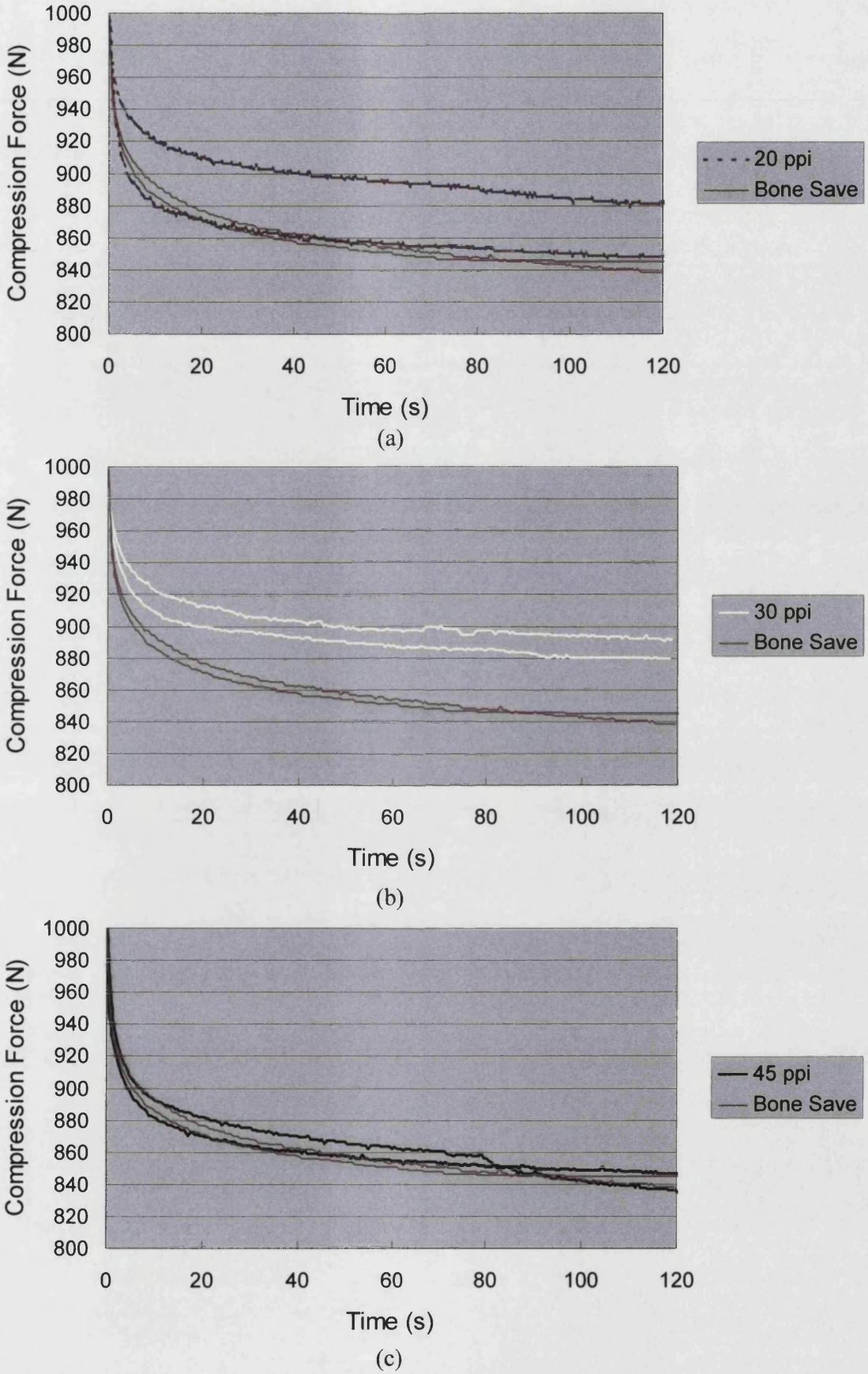

Figure 4.62 Compression force versus time curves for relaxation from 1000 N of granules produced from (a) 20 ppi (b) 30 ppi (c) 45 ppi foam.

The relaxation behaviour of the granules and BoneSave® granules from the maximum load of 500 N and from 1000 N are compared in Figure 4.63. BoneSave® granules seem to have higher relaxation from the maximum load of both 500 and 1000 N. However, the differences in relaxation behaviour between the granules and BoneSave® materials are not as great as the differences in the stiffness measurements.

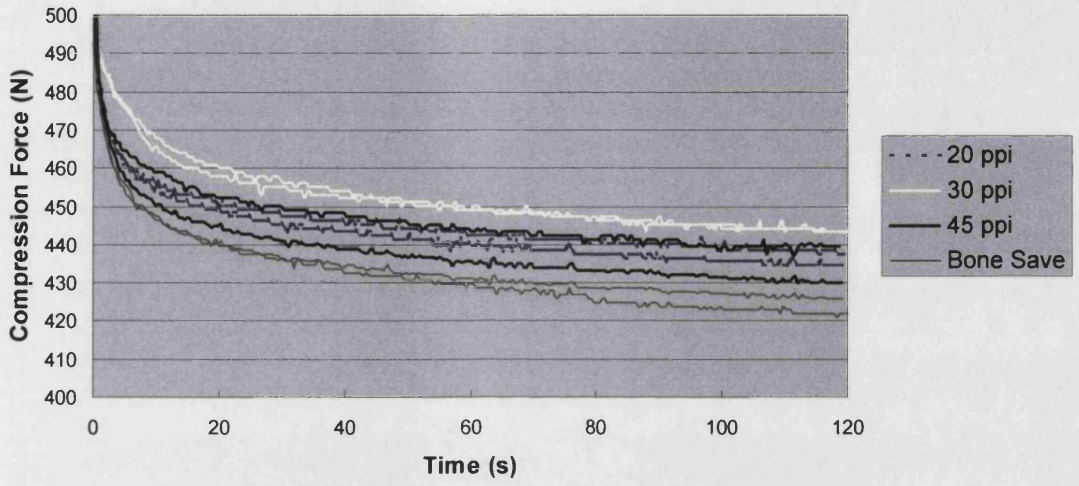

(a)

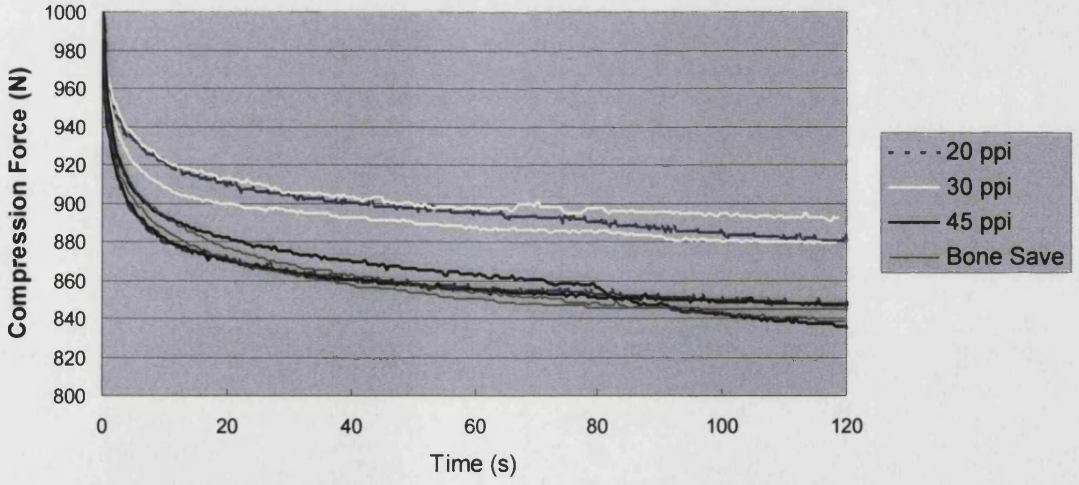

(b)

Figure 4.63 Compression force versus time curves for relaxation (a) from 500 N (b) from 1000 N.

4.5.3 Summary of Results and Key Findings

- The densities of the porous samples, 2.32 – 2.59 g/cm^3, increased with solid loading as the slips with higher solid loading resulted in a lower level of microporosity. The densities produced from the different ppi foams are in the order of 20 ppi, 30 ppi and 45 ppi from low to high. However, the grade of foam does not seem to have as great an effect as the solid loading on apparent densities.
- The average four-point bend strengths for the solid samples were in the order of 54.67 ± 5.66 MPa. For the porous sample, depending on the PU foam template and solid loading used, the strengths were in the order of 13.03 – 22.03 MPa which is significantly lower than the strength of the solid sample. Four-point bend strength was sensitive to defects, especially on the surface of the materials, so the strengths of the porous HA/TCP were considerably lower and inherently more variable. The samples with a larger macropore size had lower four-point bend strengths but, in contrast, the micropore sizes and level of microporosity did not seem to have a dramatic effect on values of four-point bend strength.
- The work of fracture was slightly influenced by the initial foam structures and solid loading. Samples with larger macropore size and microporosities had lower values of work of fracture. The average work of fracture for porous samples was in the range of 12.23 – 17.98 J/m^2. The solid sample has the highest work of fracture, 19.72 ± 2.79 J/m^2, but the difference in comparison to porous samples is not as great as in other mechanical tests. The Tattersall-Tappin test may not be sensitive to porosity. However, the standard deviations in each group of tests were high and were the highest compared to other mechanical tests. Inaccurate measurements may have arisen from poor control of the width and depth of the notch.
- Inserting rubber supports at the end of the compression samples reduced shear stress concentration resulting in higher compressive strengths and more equivalent curves in the elastic region of the stress-strain curve. The average compressive strengths for porous sample were in the range of 58.46 – 138.72 MPa depending on the PU foam template and solid loading used. The solid samples had the highest compressive strength, which was 277.79 ± 26.97 MPa. The results indicated that the compressive strengths were influenced by not only foam structures but also solid loading. Samples with larger macropore sizes and microporosities have lower compressive strengths.

- Macroporosities have a noticeable effect on four-point bend strength and a slight effect on compressive strength and work of fracture. Microporosities had an effect on compressive strength and work of fracture but did not seem to have an effect on four-point bend strengths.
- In compressive testing, the failure mode was not the classic shear failure expected 45° along the axis. This was observed in both solid and porous samples and with and without inserting rubber supports and could be as a result of the friction between the sample and compression platens. Further work needs to be carried out on the failure mode to establish if friction is the cause of this phenomenon.
- The granules made by the vacuum impregnation technique had interconnected porosity and with reproducible properties and could be manufactured in a controlled manner.
- The granules made by the vacuum impregnation technique were stiffer than commercial BoneSave® materials and did not crumble to powder during the die-plunger test. These experimental granules should be useful for impaction grafting and space filling, with an improved capacity for retaining structural integrity.
- The die-plunger test conditions used in this project were only suitable for small granules, which were 4 mm or less in diameter as it was difficult to pack the large particles into die plunger tube used in this test. A large diameter tube would be more appropriate for the testing of particles more than 4 mm in diameter.

4.6 Functional Gradient Materials (FGM)

4.6.1 Results

Figure 4.64 shows the sample generated from a template that consisted of sections of 20 ppi and 45 ppi foams joined together by stitching. The figure shows the external appearance (Figure 4.64(a)) and an internal cross-section view (Figure 4.64(b)) of the bioceramic block with the combination of two different porous structures. This technique demonstrated that porous HA/TCP with two or more different levels of porosity could be produced in a single block.

Figures 4.65 and 4.66 show the samples of 20 ppi and 45 ppi foams joined by pressfitting. The difference between them is described as follows. In Figure 4.65 the foam in the centre had almost the same diameter as the hole in the outer foam. The inner core was press fitted into the outer foam without compressing it. The structures of the square (20 ppi) foam and the hollow foam (45 ppi) remained the same. In order to get a more porous structure in the centre of the composite block, Figure 4.66, the diameter of the central foam block (37 mm) was made bigger than the hole (diameter: 25 mm) into which it was made to fit thus becoming a denser structure. The centre of the sample has higher porosity when compared to the sample in Figure 4.65. The results show that it is a potential method to obtain not only FGM ceramics but also tailored structures. The relative ratio of the centre foam to the hole could be changed to give different porosities in the centre. Foams with different porosities (20, 30, 45 ppi) could be utilized as the centre or hollow foam according to the desired application. However imperfections can occur as can be seen in Figure 4.66 (c) which shows a crack at the interface between the two different foam structures. This may originate from the hot cutting technique used to section the foams. The external structure of the foams may melt, resulting in a dense wall on the surface. When combined, the wall prevents slip crossing the interface, this results in a crack remaining after sintering. This could be avoided by trimming the surface which is to form the interface after hot cutting.

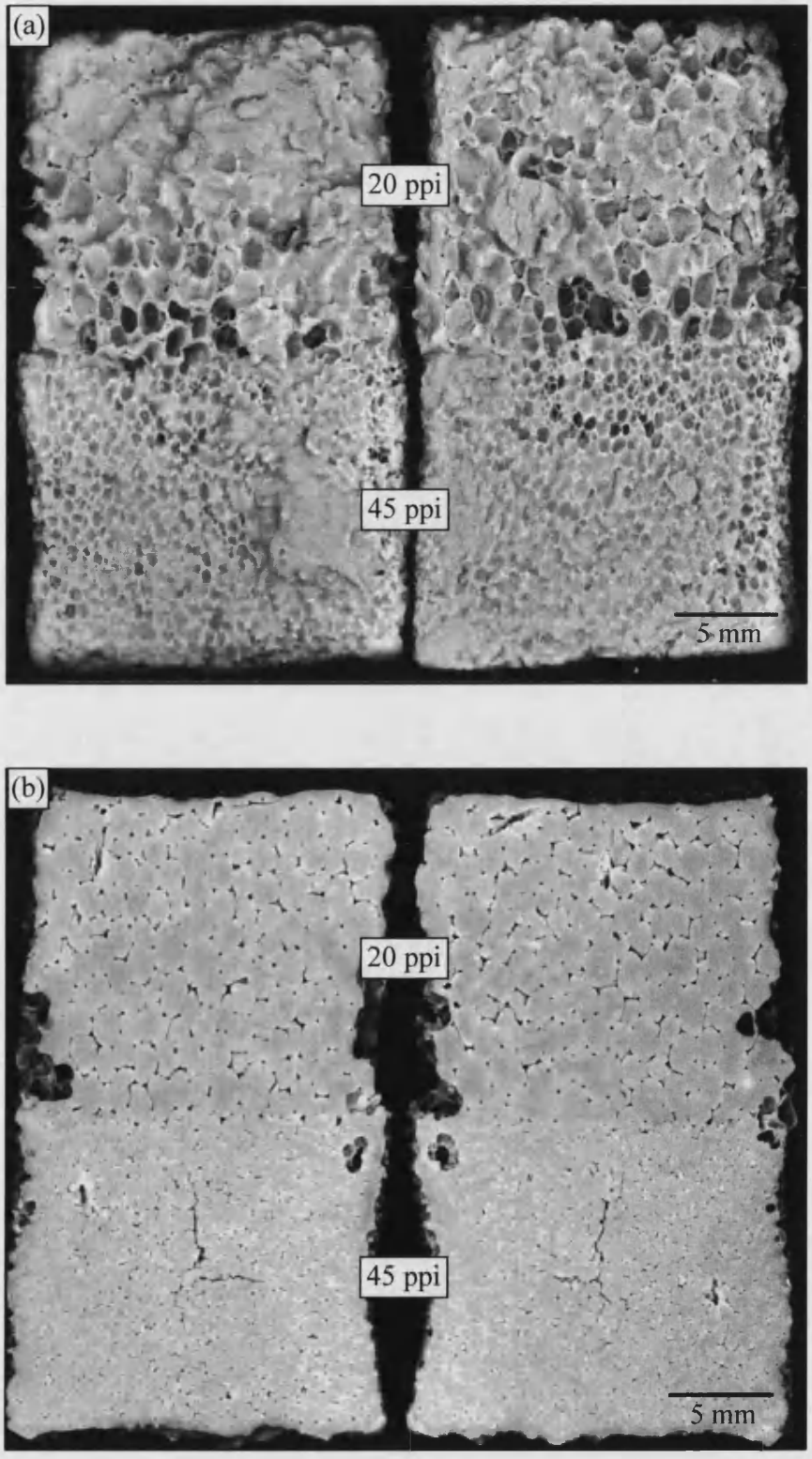

Figure 4.64 (a) The external appearance and (b) a transverse section of the HA/TCP with the combination two different pores sizes.

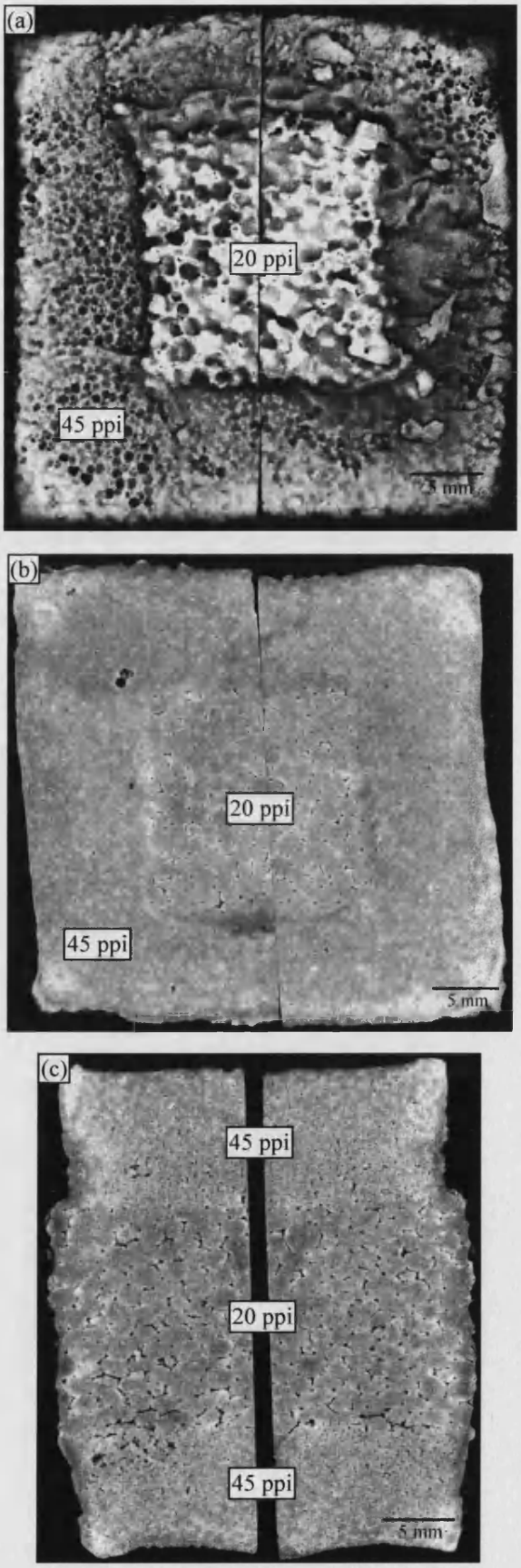

Figure 4.65 (a) The external appearance and (b, c) transverse sections of the HA/TCP with the combination two different pore sizes.

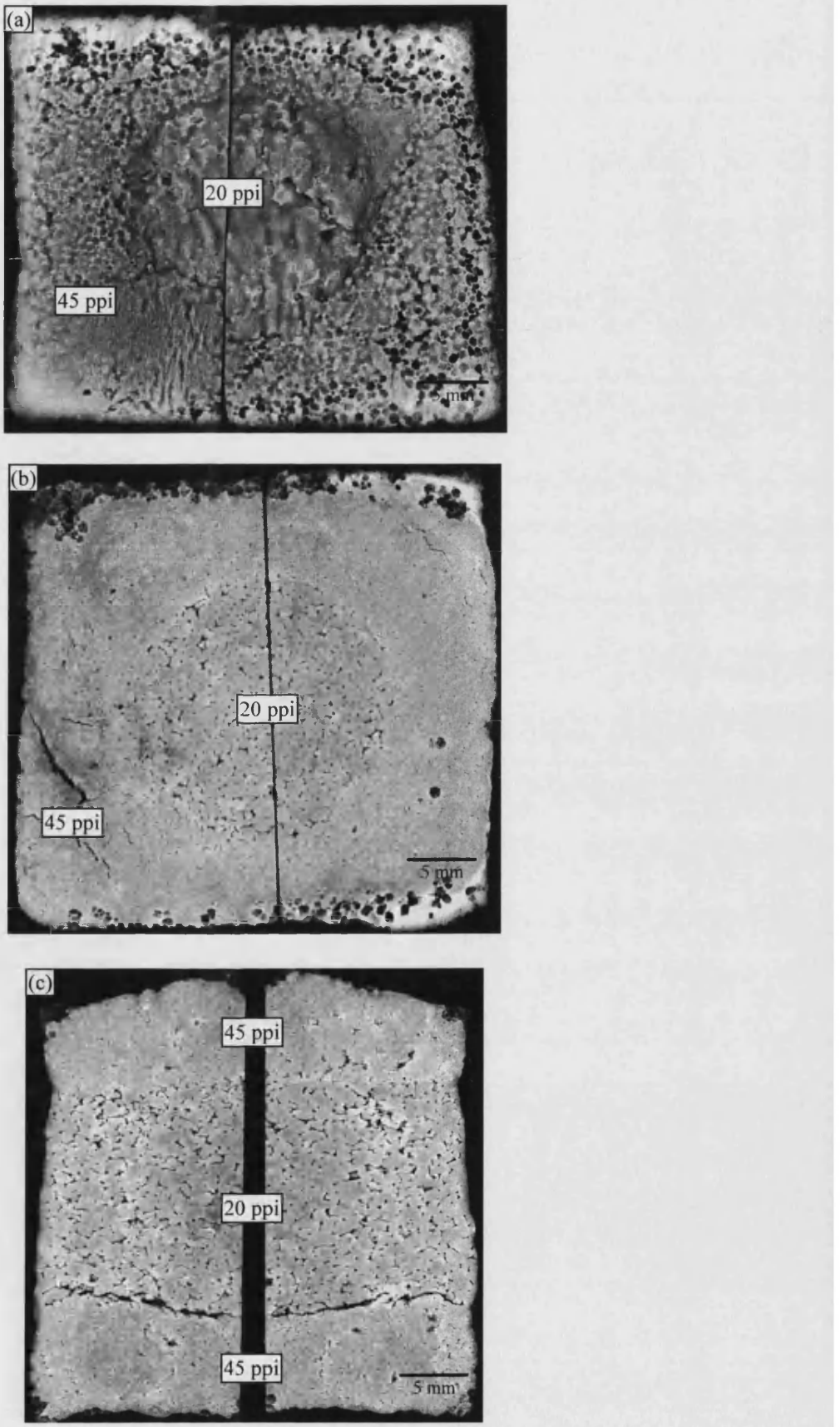

Figure 4.66 (a) The external appearance and (b, c) transverse sections of the HA/TCP with the combination two different pore sizes.

Figure 4.67 is an SEM micrograph of the interface of sample contains two different porous structures. No defects could be seen at the interface between the two different foam structures. Using this method to make a FGM ensured that the pores present in different parts of the composite structure were interconnected. The polymer foams were joined by stitching or pressfitted together, consequently, the interface of the two foams had a number of definite points of contact. These converted to interconnected channels in the resultant ceramic blocks.

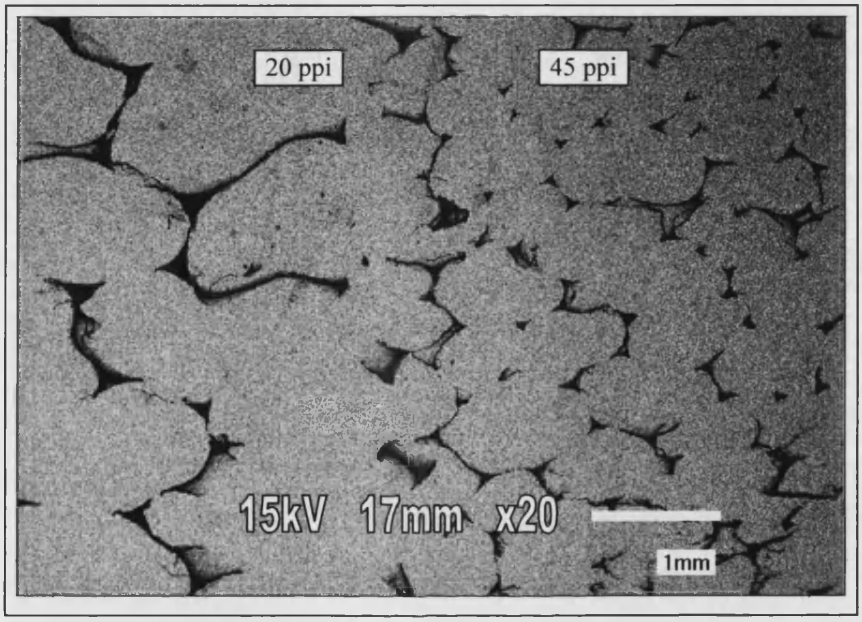

Figure 4.67 Micrograph of the interface of the sample which consisted of 20 ppi and 45 ppi foams.

A sample with a graded porous structure which is much closer to the human bone morphology is shown in Figure 4.68. The outside denser structure was made by vacuum impregnation and inside, the more porous structure, was made by a dipping method. These two structures were conspicuously different but joined together firmly.

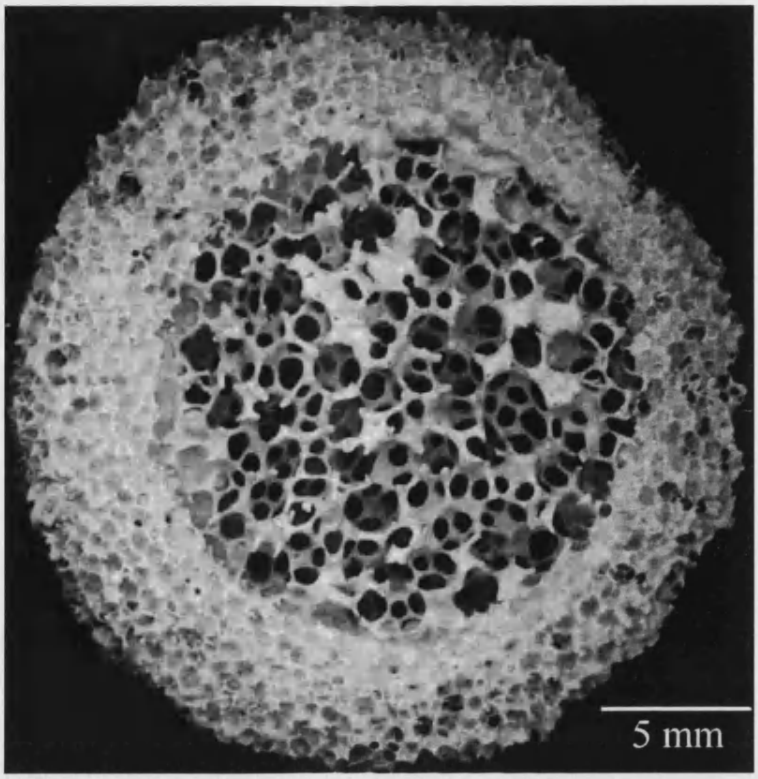

Figure 4.68 The external appearance of a sample produced by joining two porous structures made by vacuum impregnation and dipping.

Novel techniques have been developed for the manufacture of functional gradient materials. It has been demonstrated that FGM with two different pore sizes with no fractures at the interface can be fabricated successfully. The technique developed is efficient and reproducible. Integrity and continuity across the interface indicate the enormous potential to produce complex shapes when compared to most existing methods which can only be used to manufacture flat layered porous graded structures.

Simulation of a bimodal structure closer to that found in natural bone is possible. Many potential biomedical applications could be developed utilising graded porous structures. The ease of processing will make it possible to fabricate a range of complex shape for different applications.

4.6.2 Four-Point Bend Testing

In order to compare the strengths of the FGM and homogeneous materials and to investigate if the interface of the FGM was a source of weakness, four-point bend testing was employed. The FGM samples made from a slip of 100 wt% solid loading were tested with a crosshead speed of 0.5 mm/min and the span was 20 mm × 40 mm.

Figure 4.69 shows rectangular bars with dimension of 45 × 5 × 4 mm comprising two different porosity structures made from a slip of 100 wt% solid loading. The interface of the two structures was within the upper span which meant that it sustained the highest loading. Figure 4.70 shows the bars after four-point bend testing. The interface of the FGM was not a source of weakness as the fracture was not at the interface between the two areas. Figure 4.71 and Table 4.16 show the four-point bend strengths of porous HA/TCP bioceramics resulting from 20, 30 and 45 ppi foams with 100 wt% solid loading slip and FGM samples. The average four-point bending strength of the porous samples made from various ppi foams was in the range of 18.32 to 19.65 MPa and the FGM was 15.61 ± 2.72 MPa. FGM had the lowest average four-point bend strength. Table 4.17 shows the Student T-test results for the strengths of porous HA/TCP bioceramics from various ppi foam and FGM samples. The results show there was no difference between the FGM and samples made from 20 and 30 ppi foam but the FGM had probably lower strength than that in the sample made from 45 ppi foam. The lower strength of FGM might result from poor compression step during impregnation as intense compression may damage the structure of stitching. A longer vacuum period might improve the impregnation and result in an increase the in strength of the FGM. However, the fracture of the FGM was in the area made from 20 ppi foam which had lower strength than that from 45 ppi foam. The strength of FGM was comparable to that in the sample made from 20 ppi foam. This confirmed that the four-point bend strengths of the FGM made by this method were similar to the homogeneous porous sample and the interface was not a source of weakness.

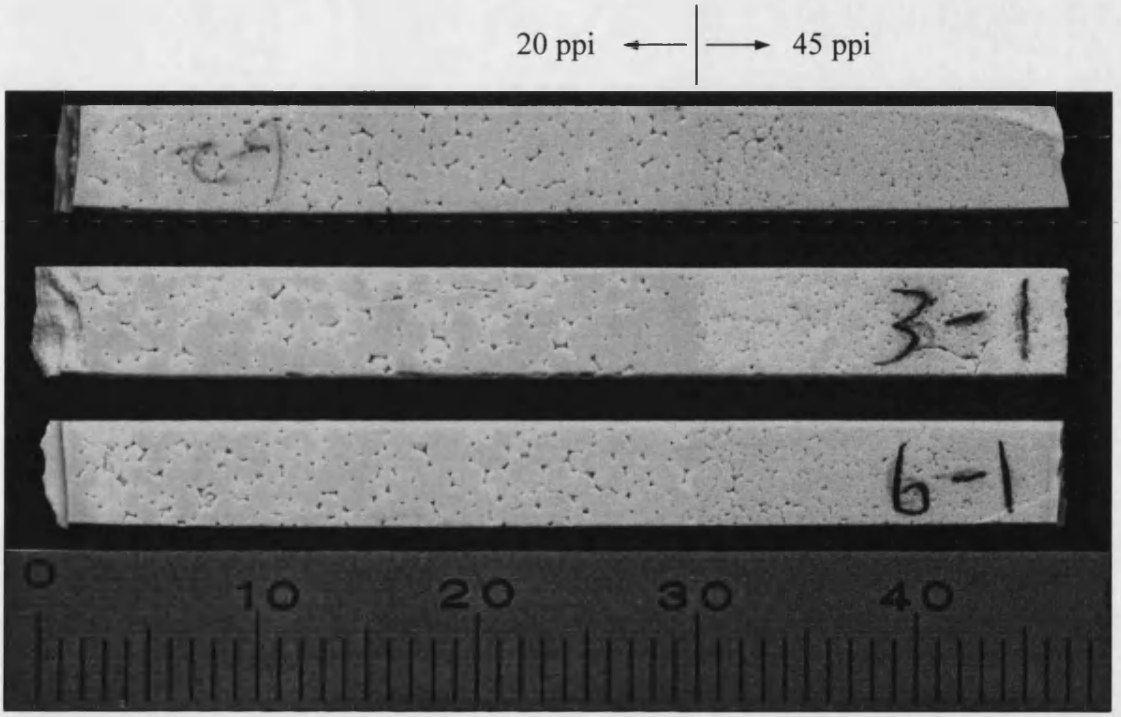

Figure 4.69 Bars of FGM sectioned from a large block for four-point bending testing.

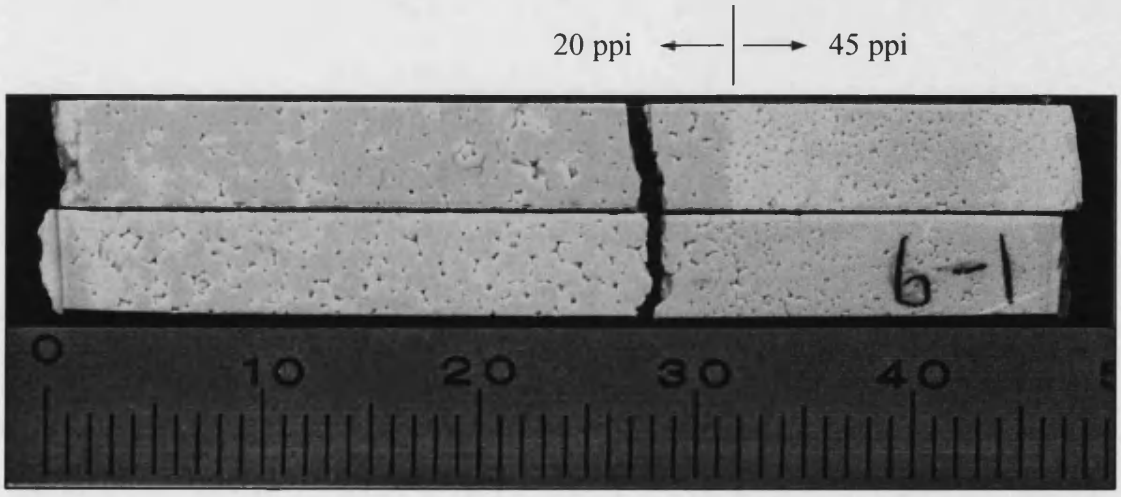

Figure 4.70 The fracture mode of the FGM bars after four-point bend testing.

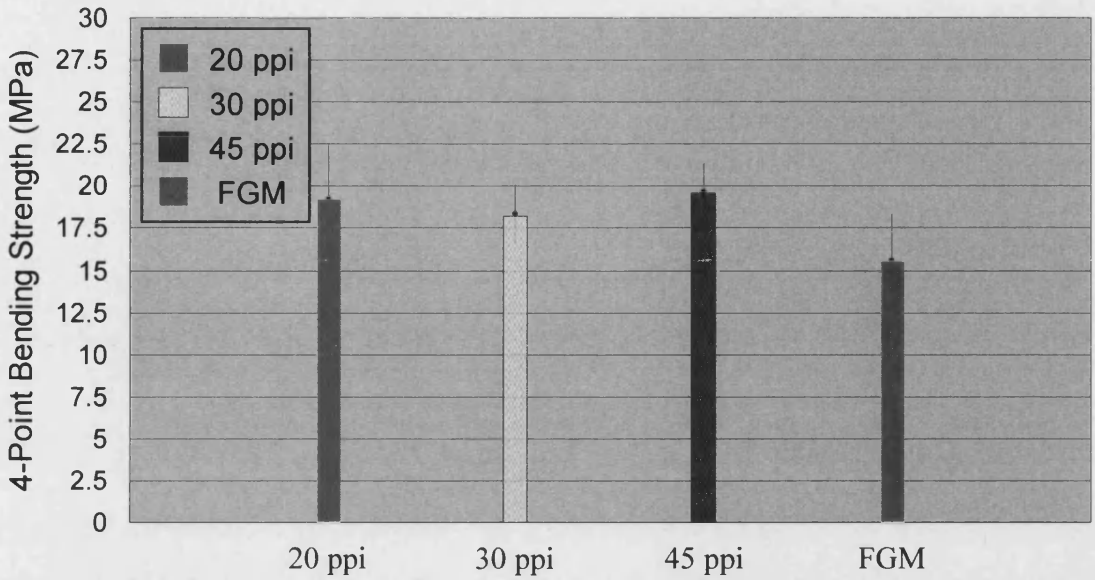

Figure 4.71 The four-point bending strengths of porous HA/TCP bioceramics resulting from 100 wt% solid loading slip and FGM samples.

4-Point Bend Strength (MPa)			
20 ppi	**30 ppi**	**45 ppi**	**FGM**
19.20 ± 3.22	18.32 ± 1.81	19.65 ± 1.75	15.61 ± 2.72

Table 4.16 The four-point bend strengths of porous HA/TCP bioceramics resulting from 100 wt% solid loading slip and FGM samples.

Foam (ppi)	20	30	45	FGM
20		O	O	O
30	O		O	O
45	O	O		#
FGM	O	O	#	

XX = Highly significant difference
X = Significant difference
# = Probable difference
△ = Possible difference
O = Difference not established

Table 4.17 Student T-test results for the four-point bend strengths of porous HA/TCP bioceramics from various ppi foams and 100 wt% solid loading slip and FGM samples.

4.6.3 Summary of Results and Key Findings

- By joining different ppi foams together by either stitching or pressfitting to form templates, porous ceramics with two or more different levels of porosity could be produced in a single block. No weakness could be seen at the interface between the two different porosity sections.
- It is feasible to vary the porosity of HA/TCP ceramics by compressing one foam into a recess in another foam.
- Using this method to make a FGM ensured that the pores present in different parts of the composite structure were interconnected. The polymer foams were joined by stitching or pressfitting together, consequently, the interface of the two foams had a number of definite points of contact. These converted to interconnected channels in the resultant samples.
- The sample with a graded porous structure, which is much closer to human bone morphology could be produced by vacuum impregnation and dipping methods.
- The average four-point bend strength of the FGM was comparable to the homogeneous porous samples. The interface of the FGM was not a source of weakness.

CHAPTER 5

GENERAL DISCUSSION AND CONCLUSIONS

This chapter covers general discussion and conclusions to this project

5. General Discussion and Conclusions

The main aim of this study was to fabricate porous calcium phosphate bioceramics with completely interconnected porosity combined with good mechanical properties to enable their use in heavy load-bearing applications. Further, achievements were the manufacture of porous granules which could be used for impaction grafting and space filling and the development of a functional gradient material (FGM) with graded pore structures similar to the bimodal structures of cortical and spongy bone.

Many methods have been developed by other groups to fabricate porous ceramics, including organic particle embedding techniques[204], production of gas bubbles in slips[212] and the replication of reticulated porous structures[218]. However, up until now the hydroxyapatite (HA) and tricalcium phosphate (TCP) bioceramics developed have had isolated porosity which constrains their potential for bone ingrowth[148] or have poor mechanical properties so that they cannot currently be used in heavy load-bearing applications[44].

Evidence from the literature shows that current porous calcium phosphate samples made from both organic particle embedding and production of gas bubbles in slips have poor connectivity between macropores especially for samples with low levels of porosity[82,148]. The replication of reticulated porous structures method produces porous calcium phosphate samples with insufficient mechanical properties[240]. To date, porous calcium phosphates which combine interconnected porosity with good mechanical strengths have not been reported.

In this study, porous HA/TCP bioceramics with interconnected porosity combined with good mechanical properties were fabricated successfully by a novel technique of vacuum impregnation of reticulated polymeric foams with ceramic slip. By varying the characteristics of the slips and using foams of different pores per inch (ppi), samples of porous HA/TCP, blocks and granules, with a wide range of pore sizes were successfully manufactured. The vacuum impregnation method can be used to produce porous HA/TCP bioceramics with both regular and irregular three-dimensonal shapes. The successful samples have an excellent porous structure without isolated holes. Nearly 100% of the macroporosity arises from the PU foam structure.

The macropore size of the HA/TCP bioceramics was in the range of 197 to 254 μm (for 20 ppi foam), 143 to 182 μm (for 30 ppi foam) and 105 to 135 μm (for 45 ppi foam) and

the macroporosities made from three different porosity foams were similar in the range of 5.24 to 9.67 %. This demonstrated that the major determinant of the macropore structures is the initial structure of PU foams. The macropore sizes produced in this research were larger than 100 μm in diameter which were appropriate for bone ingrowth. The macroporosity of most current porous calcium phosphate is in the range of 28 to 92 %[97,150,151,209] which is similar to spongy bone. The macroporosity of the HA/TCP bioceramic produces in this project was close to that of compact bone. Porous calcium phosphate bioceramics with interconnected porosity combined with macroporosity in the compact bone range have not been reported in the literature.

Micropore structures are obviously affected by the solid loading of slips. The average micropore sizes and microporosities were found to be 1.21 μm; 15.07 ± 1.02 %, 0.98 μm; 14.09 ± 0.84 % and 0.95 μm; 4.23 ± 0.45 % respectively for slips with solid loadings of 60 wt%, 100 wt% and 120 wt%. The micropores were more interconnected and larger and the distributions of the micropores were more regular when the solid loading of the slip was lower. Micropore shapes tend to be circular shape when solid loading is high and elongated in shape in low solid loading slip. The micropores produced from 60 to 100 wt% solid loading were all interconnected which demonstrates the potential of these materials to act as a carrier for bone morphogenetic proteins (BMPs).

The apparent density of the porous HA/TCP bioceramics fabricated by the vacuum impregnation technique was in the range of 2.32 to 2.60 g/cm^3. The density increased with solid loading as the slips with higher solid loading resulted in a lower level of microporosity. The densities produced from the different ppi foams were in the order of 20 ppi, 30 ppi and 45 ppi from low to high. However, the foam does not seem to have as large an effect as solid loading on apparent densities.

Various mechanical tests have been carried out on these porous HA/TCP samples. Table 5.1 shows the mechanical properties of porous calcium phosphate bioceramics fabricated by the vacuum impregnation technique relative to the mechanical properties values published in the literature. The mechanical properties for the porous sample made in this project depended on the PU foam template and solid loading used.

	Vacuum impregnation technique		Data shown in the literature	
Mechanical properties	Average	Range	Most probable range	Highest
Bending strength (MPa)	16.98	13.03 to 22.03	< 11	40
Work of fracture (J/m^2)	15.46	12.23 to 17.98	–	–
Compressive strength (MPa)	105.56	58.46 to 138.72	0.2 to 15	36

Table 5-1 Comparison of the mechanical properties of porous calcium phosphate bioceramics fabricated by the vacuum impregnation technique and values from the literature.

The average four-point bending strength for porous calcium phosphate bioceramics fabricated by the vacuum impregnation technique was 16.98 MPa (range: 13.03 to 22.03 MPa). The porous samples with a larger macropore size have lower four-point bending strengths but micropore sizes and microporosity do not seem to have a dramatic effect on four-point bending strengths. Microporosity might be below the critical flaw size for failure in four-point bending test. The bending strengths in the literature were carried out by either four-point bending or three-point bending tests. Almost all of the bending strengths of porous calcium phosphate ceramics in the literature are below 11 MPa[208,210,220] which is lower than that of porous samples produced in this project. The highest bending strength of porous calcium phosphate ceramics in the literature is ~ 40 MPa[202] which is much higher than that of the samples made by vacuum impregnation technique. This may be as a consequence of the interconnected porosity in the samples which may encourage crack growth in the samples resulting in lower bending strengths.

The average value of work of fracture for the porous calcium phosphate bioceramics fabricated by the vacuum impregnation technique was 15.46 J/m^2 (range: 12.23 to 17.98 J/m^2). Samples with larger macropore sizes have slightly lower values of work of fracture. Higher micropore sizes and microporosity also tend to produce samples with slightly lower values of work of fracture. However, the influence of both macro- and microporosity are not as large as in other mechanical tests with the exception of microporosity on four-point bending strength. The work of fracture may not be sensitive to porosity. Few results for the work of fracture for calcium phosphate can be found in the literature. The only data reported for calcium phosphate based ceramics are dense

HA samples reinforced with Ti particles and dense calcium phosphate reinforced with fibres. Their values of work of fracture are 12.8 J/m^{2}[257] and $1.5 - 3.5 \times 10^{3}$ J/m^{2}[107], respectively. However, these values of work of fracture are significantly different to each other probably as a result of the different reinforcement mechanisms. Both of the tests were carried out on dense samples without notches which are not directly comparable with the porous samples made by the vacuum impregnation technique in this study.

Most of the values for compressive strengths of porous calcium phosphate shown in the literature are in the range 0.2 – 18 MPa[73,76,108,118,150,220,228] and the highest is ~ 36 MPa[201]. These porous samples shown in the literature are not useful for heavy load-bearing applications. The compressive strengths of these samples are much lower than those of samples made by the vacuum impregnation technique which were in the range of 58.46 to 138.72 MPa. The compressive strengths of samples in this project were obviously influenced by not only foam structures but also solid loading. Samples with larger macropore sizes and microporosities had lower compressive strengths.

These results show macroporosity has a noticeable effect on four-point bend strength and slight effect on compressive strengths and work of fracture. Microporosities have an effect on compressive strength and work of fracture but do not appear to have an effect on four-point bending strengths.

Comparing the results obtained in the current study with the mechanical strengths of porous calcium phosphate published in the literature indicates that it is possible to manufacture open pore HA/TCP bioceramics with mechanical strengths exceeding these recorded for existing porous calcium phosphate ceramics. The porous HA/TCP samples made by the vacuum impregnation technique may have much more potential for heavy load-bearing applications which could be of clinical interest.

The method developed can be used to make porous HA/TCP granules in the size range of 2 to 8 mm with interconnected porosity and controlled size and shape – hitherto not possible using existing manufacturing techniques. The technique is efficient when compared to making a large block of material and subsequently breaking up the sintered product into smaller pieces[193], as is the current practice by one manufacturer. Size and shape can be controlled and waste minimised. Some other existing methods can be used to produce granules with a controlled porosity and good shapes, which are spherical or near-spherical shapes[189,197,198]. However, the porous network of these granules is not

highly interconnected especially for the sample with low porosity. The granules made by the vacuum impregnation technique have guaranteed interconnected porosity, reproducible properties and can be manufactured in a more controlled manner. The results of the die-plunger testing showed that the granules made by the vacuum impregnation technique were stiffer than commercial BoneSave® materials and did not crumble to powder after the die-plunger test. By comparison, many of BoneSave® samples crumbled to become smaller diameter powders. It is therefore evident that these experimental granules would be useful for impaction grafting and space filling, with an improved capacity for retaining structural integrity.

Functional gradient materials (FGM) with graded porosity have been manufactured by novel techniques. By joining different ppi foams together by either stitching or pressfitting, porous ceramics with two or more different levels of porosity could be produced in a single block. No weakness could be seen at the interface between the two different porosity sections. The average four-point bending strength of the FGM was similar to the homogeneous porous samples. The interface of the FGM was not a source of weakness as the fracture was not at the interface between the two areas after bending test. This demonstrates FGM which have two different porous structures with no inter-layer fractures can be fabricated. Functional gradient materials (FGM) with porosity gradients close to the bimodal structure of cortical and cancellous bone could also be produced by the vacuum impregnation and dipping method. These two structures were conspicuously different but joined together firmly.

The technique developed to make FGM is efficient and reproducible. Integrity and continuity across the interface indicate the enormous potential to produce complex shapes when compared to most existing methods which can only be used to manufacture flat layered porous graded structures[203,207,214] which are not close to common circular shape of transverse section of lone bone.

Furthermore, using this method to make a FGM ensured that the pores present in different parts of the composite structure were interconnected. The polymer foams were joined by sewing or pressfitted together, consequently, the interface of the two foams had a number of definite points of contact. These converted to interconnected channels in the resultant ceramic blocks.

In this study, the novel technique of vacuum impregnation of reticulated polymeric foams with ceramic slip was introduced to fabricate porous HA/TCP bioceramics with

interconnected porosity combined with good mechanical properties. The information gathered from this research will provide a useful platform for further study. Recommendations for future work will be outlined in the next chapter.

CHAPTER 6

SUGGESTIONS FOR FUTURE WORK

Suggestion for future work to this project

6. Suggestions for Future Work

A range of HA/TCP bioceramics with interconnected macroporosity have been made successfully by the novel method. This has many advantages such as the interconnected porosity and high compression strength compared to ceramics produced using other methods. On the basis of the results obtained in this study, the following suggestions could be made for the further research.

(1) With an aim of making a more porous HA/TCP, the method of dipping foams into the slip of lower viscosity (less than 6,000 cps) could be further experimented. Although many research groups have utilized this method, most of their products have cracks in the cellular struts. These cracks are known to decrease the mechanical properties drastically. This might be able to be overcome by dipping more the once and the effect of dipping time on the porosity and pore size could be also analysed.

(2) The main shapes of macropore in this research are bow tie and triangle shapes, which replicated the original shape of the struts of the PU stating foam. Most of the currently used products are based on a circular shape pore as in cancellous bone. The samples should be further investigated to see if the shape effects bone ingrowth.

(3) Foams with required density and strut shape could be obtained to enable manufacture porous samples with specific pore size, shape and volume for various clinic applications.

(4) Although porous samples with various shapes have been manufactured successfully, more complex shapes such as those for jaw reconstruction could be investigated and in order to understand the limitations in shape imposed by this method.

(5) With the aim of obtaining samples with graded pore structures as close as possible to the human bone morphology, different means of combining foams of different shapes could be further experimented with.

(6) With the purpose of obtaining more precise results of work of fracture, samples with more regular notches should be made and Tattersall-Tappin test should be further investigated on samples with various notch depth ratios.

(7) More work could be carried out on the compressive failure mode to find out the reason for the deviation from the classic shear failure expected of 45° along the axis.

(8) In order to measure the mechanical properties of granules which are bigger than six mm, a larger diameter plunger for the die-plunger test could be prepared. It may give more consistent results for bigger granules and could also be used to compare the effect of varying the plunger dimension on granules of different sizes. Granules with mixed size could also be experimented on.

(9) More mechanical tests could be carried out on FGM especially for the sample closer to the human bone morphology made by vacuum impregnation and dipping method.

(10) *In-vitro* and *in-vivo* experiments could be used to investigate solubility rates and biological response of the HA/TCP samples.

7. References

1. D.C. Tancred, A.J. Carr and B.A.O. Mccormack. (1998). Development of a new synthetic bone graft. Journal of Materials Science: Materials in Medicine, 9, 819-823.

2. W. Suchanek and M. Yoshimura. (1998). Processing and properties of hydroxyapatite-based biomaterials for use as hard tissue replacement implants. Journal of Materials Research, 13, 94-117.

3. G. Daculsi and N. Passuti. (1990). Effect of the macroporosity for osseous substitution of calcium phophate ceramics. Biomaterials, 11, 86-87.

4. G. Carotenuto, G. Spagnuolo, L. Ambrosio and L. Nicolais. (1999). Macroporous hydroxyapatite as alloplastic material for dental applications. Journal of Materials Science: Materials in Medicine, 10, 671-676.

5. V. Karageorgiou and D. Kaplan. (2005). Porosity of 3D biomaterial scaffolds and osteogenesis. Biomaterials, 26, 5474-5491.

6. J.X. Lu, B. Flautre, K. Anselme and P. Hardouin. (1999). Role of interconnections in porous bioceramics on bone recolonization in vitro and in vivo. Journal of Materials Science: Materials in medicine, 10, 111-120.

7. J.H. Kuhne, R. Bartl, B. Frish, C. Hanmer, V. Jansson and M. Zimmer. (1994). Bone formation in coralline hydroxyapatite-effects of pore size studied in rabbits. Acta Orthopaedica Scandinavia, 65(3), 246-152.

8. L.L. Hench. (1998). Bioceramics. Journal of the American Ceramic Society, 81(7), 1705-1728.

9. J.D. Currey, K. Brear and P. Zioupos. (1996). The effects of ageing and changes in mineral content in degrading the toughness of human femora. Journal of Biomechanics, 29(2), 257-260.

10. W.K. Sietsema. (1995). Animal models of cortical porosity. Bone, 17(4) Supplement, 297s-303s.

11. D. Green, D. Walsh, S. Mann and R.O.C. Oreffo. (2002). The potential of biomimesis in bone tissue engineering: lessons from the design and synthesis of invertebrate skeletons. Bone, (30)6, 810-815.

12. V. Olivier, N. Faucheux and P. Hardouin. (2004). Biomaterial challenges and approaches to stem cell use in bone reconstructive surgery. Drug Discovery Today, 9(18), 803-811.

13. A.K. Jain and R. Panchagula. (2000). Review: Skeletal drug delivery system. International Journal of Pharmaceutics, 206, 1-12.

14. L.L. Hench. (1998). Biomaterials: a forecast for the future. Biomaterials, 19, 1419-1423.

15. T.E. Orr, P.A. Villars, S.L. Mitchell, H.P. Hsu and M. Spector. (2001). Compressive properties of cancellous bone defects in a rabbit model treated with particles of natural bone mineral and synthetic hydroxyapatite. Biomaterials, 22, 1953-1959.

16. S.B.T Bolder, N. Verdonschot, B.W. Schreurs and P. Buma. (2002). Acetabular defect reconstruction with impacted morsellized bone grafts or TCP/HA particles. A study on the mechanical stability of cemented cups in an artificial acetabulum model. Biomaterials, 23, 659-666.

17. N. Koc, M. Timucin and F. Korkusuz. (2004). Fabrication and characterization of porous tricalcium phosphate ceramics. Ceramics International, 30, 205-211.

18. M. Trecant, J. Deleccrin, J. Royer, E. Geoyenvalle and G. Daculsi. (1994). Mechanical changes in macroporous calcium phosphate ceramics after implantation in bone. Clinical Materials, 15, 233-240.

19. R.O.C. Oreffo and J.T. Triffitt. (1999). Future potentials for using osteogenic stem cells and biomaterials in orthopedics. Bone, 25(2), supplement, 5s-9s.

20. Y.M. Lee, Y.J. Soel, Y.T. Lim, S. Kim, S.B. Han, I.C. Rhyu, S.H. Baek, S.J. Heo, J.Y. Choi, P.R. Klokkevold and C.P. Chung. (2001). Tissue-engineered growth of bone by marrow cell transplantation using porous calcium metaphosphate matrices. Journal of Biomedical Materials Research, 54, 216-223.

21. W. Baer, P. Schaller and H.D. Carl. (2002). Spongy hydroxyapatite in hand surgery-a five year follow-up. The Journal of Hand Surgery, 27B(1), 101-103.

22. S. Itoh, M. Kikuchi, Y. Koyama, K. Takakuda, K. Shinomiya and J. Tanaka. (2002). Development of an artificial vertebral body using a novel biomaterial, hydroxyapatite/collagen composite. Biomaterials, 23, 3919-3926.

23. D. Tadic and M. Epple. (2004). A thorough physicochemical characterisation of 14 calcium phosphate-based bone substitution materials in comparison to natural bone. Biomaterials, 25, 987-994.

24. R. Schnettler, V. Alt, E. Dingeldein, H.J. Pfefferle, O. Kilian, C. Meyer, C. Heiss and S. Wenisch. (2003). Bone ingrowth in bFGF-coated hydroxyapatite ceramic implants. Biomaterials, 24, 4603-4608.

25. J.W. Vahey, P.T. Simonian and E.U. Conrad. (1995). Carcinogenicity and metallic implants. American Journal of Orthodontics and Dentofacial Orthopedics, 24, 319-324.

26. K. Arvideon, M. Cottler-Fox and V. Friberg. (1986). Cytotoxic effects of Co-Cr alloys on fibroblast derived form human gingiva. Scand J Dent Res, 95, 356-363.

27. N. Jacobsen and A. Hensten-Pettersen. (1989). Occupational health problems and adverse patient reactions in orthodontics. Eur J Orthodon, 11, 254-264.

28. Z. Lin Sun, J.C. Wataha and C.T. Hanks. (1997). Effects of metal ions on osteoblastlike cell metabolism and differentiation. Journal of Biomedical Materials Research, 34, 29-37.

29. D.W. Hutmacher. (2000). Scaffolds in tissue engineering bone and cartilage. Biomaterials, 21, 2529-2543.

30. J.R. Jones and L.L. Hench. (2001). Biomedical materials for new millennium: perspective on the future. Materials Science and Technology, 17, 891-900.

31. J.E. Lemons. (1996). Ceramics: past, present and future. Bone, (19)1, Supplement 1, 121s-128s.

32. R.M. Pilliar, M.J. Filiaggi, J.D. Wells, M.D. Grynpas and R.A. Kandel. (2001). Porous calcium polyphosphate scaffolds for bone substitute applications-in virto characterization. Biomaterials, 22, 963-972.

33. L.M.R. Lorenzo and J.M.F. Ferreira. (2004). Development of porous ceramic bodies for applications in tissue engineering and drug delivery systems. Materials Research Bulletin, 39, 83-91.

34. A.R. Boccaccini and V. Maquet (2003). Bioresorbable and bioactive polmer/Bioglass® composites with tailored pore structure for tissue engineering applications. Composites Science and Technology, 63, 2417-2429.

35. K.E. Tanner, R.D. Downes and W. Bonfield. (1994). Clinical applications of hydroxyapatite reinforced materials. British Ceramic Transations, 93(3), 104-107.

36. M.H. Fathi, M. Salehi, A. Saatchi, V. Mortazavi and S.B. Moosavi. (2003). In vitro corrosion behavior of bioceramic, metallic, and bioceramic-metallic coated stainless steel dental implants. Dental Materials, 19, 188-198.

37. M. Wang. (2003). Developing bioactive composite materials for tissue replacement. Biomaterials, 24, 2133-2151.

38. L.L. Hench. (1991). Bioceramics: from concept to clinic. Journal of the American Ceramic Society, 74(7), 1487-1510.

39. L.L. Hench and J. Wilson ed. (1993). An Introduction to Bioceramics. Singapore: World Scientific.

40. L.L. Hench and J. Wilson. (1984). Surface-active biomaterials. Science, 226, 630-636.

41. M. Jarcho. (1981). Calcium phosphate ceramics as hard tissue prosthetics. Clinical Orthopaedics and Related Research, 157, 259-278.

42. H. Yuan, K. Kurashina, J.D.D. Bruijn, Y. Li, K. de Groot, X. Zhang. (1999). A preliminary study on osteoinduction of two kinds of calcium phosphate ceramics. Biomaterials, 20, 1799-1806.

43. C.D. Friedman, P.D. Costantino, S. Takagi and L.C. Chow. (1998). BoneSource™ hydroxyapatite cement: a novel biomaterial for craniofacial skeletal tissue engineering and reconstruction. Journal of Biomedical Materials Research (Appl Biomater), 43(4), 428-432.

44. T. Kitsugi, T. Yamamuro, T. Nakamura, S. Kotani, T. Kokubo, H. Takeuchi. (1993). Four calcium phosphate ceramics as bone substitutes for non-weight-bearing. Biomaterials, 14(3), 216-224.

45. V.I. Sikavitsas, J.S. Temenoff and A.G. Mikos. (2001). Review: Biomaterials and bone mechanotransduction. Biomaterials, 22, 2581-2593.

46. V.C. Scanlon and T. Sanders. (1999). Essentials of anatomy and physiology. Third edition. Philadelphia: F.A. Davis Company.

47. D. Shier, J. Butler and R. Lewis (2003) Hole's essentials of human anatomy and physiology. Eight edition McGraw-Hill companies: Boston.

48. G.A. Thibodeau, K.T. Patton. (2003). Anatomy and physiology. St. Louis: Mosby.

49. S.C. Cowin ed. (2001). Bone mechanics handbook. 2nd ed. New York: CRC Press.

50. S.C. Cowin ed. (1989). Bone Mechanics. Florida: CRC Press.

51. J.T. Tiffit. (1980). The Organic Matrix of Bone Tissue, in Fundamental and Clinical Bone Physiology, M. R. Urist (ed.), J. B. Lippincott Co., Philadelphia.

52. W. Linhard, F. Peters, W. Lehmann, K. Schwarz, A.F. Schilling, M. Amling, J.M. Reuger and M. Epple. (2001). Biologically and chemically optimised composites of carbonated apatite and polyglycolide as bone substitution materials. Journal of Biomedical Materials Research, 54, 162-171.

53. D. Tadic, F. Peters and M. Epple. (2002). Continuous synthesis of amorphous carbonated apatites. Biomaterials, 23, 2553-2559.

54. C. Ergun, T.J. Webster, R. Bizios and R.H. Doremus. (2002). Hydroxyapatite with substituted magnesium, zinc, cadmium and yttrium. I. Structure and microstructure. Journal of Biomedical Materials Research, 59, 305-311.

55. J. Barralet, S. Best, W. Bonfield. (1998). Carbonate substitution in precipitated hydroxyapatite: an investigation into the effects of reaction temperature and bicarbonate ion concentration. Journal of Biomedical Materials Research, 41, 79-86.

56. E. Landi, G. Celotti, G. Logroscino and A. Tampieri. (2003). Carbonated hydroxyapatite as bone substitute. Journal of the European Ceramic Society, 23, 2931-2937.

57. M. Okazaki and J. Takahashi. (1999). Synthesis of functionally grades CO_3 apatite as surface biodegradable crystals. Biomaterials, 20, 1073-1078.

58. M.J. Glimcher, L.C. Bonar, M.D. Grynaps, W.J. Landis and A.H. Roufosse. (1981). Recent studies of bone mineral: is the amorphous calcium phosphate theory valid? Journal of Crystal Growth, 53(1), 100-119.

59. D. Tadic and M. Epple. (2003). Mechanically stable implants of synthetic bone mineral by cold isostatic pressing. Biomaterials, 24, 4565-4571.

60. D. Tadic, F. Beckmann, K. Schwarz and M. Epple. (2004). A novel method to produce hydroxyapatite objects with interconnecting porosity that avoids sintering. Biomaterials, 25, 3335-3340.

61. J.C. Merry, I.R. Gibson, S.M. Best, W. Bonfield. (1998). Synthesis and characterization of carbonate hydroxyapatite. Journal of Materials Science: Materials in Medicine, 9, 779-783.

62. B.B. Nissan. (2003). Natural bioceramics: from coral to bone and beyond. Current Opinion in Solid State and Materials Science, 7, 283-288.

63. Y. Doi, T. Shibutani, Y. Moriwaki, T. Kajimoto and Y. Iwayama. (1998). Sintered carbonate apatites as bioresorbable bone substitutes. Journal of Biomedical Materials Research, 39, 603-610.

64. J.B. Park and R.S. Lakes. (1992). Biomaterials: An Introduction. 2nd ed. New York: Plenum Press.

65. C.C. Silva, D. Thomazini, A.G. Pinheiro, F. Lanciotti Jr, J.M. Sasaki, J.C. Goes and A.S.B. Sombra. (2002). Optical properties of hydroxyapatite obtained by mechanical alloying. Journal of Physics and Chemistry of Solids, 63, 1745-1757.

66. J.D. Currey. (2004). Incompatible mechanical properties in compact bone. Journal of Theoretical Biology, 231, 569-580.

67. S. Yang, K.F. Leong, Z. Du and C.K. Chua. (2001). The design of scaffolds for use in tissue engineering. Part 1. Traditional factors. Tissue Engineering, 7(6), 679-689.

68. S.R. Levitt, P.H. Crayton, E.A. Monroe and R.A. Condrate. (1969). Forming method for apatite prostheses. Journal of Biomedical Materials Research, 3, 683-685.

69. D.M. Liu, T. Troczynski and W.J. Tseng. (2001). Water-based sol-gel synthesis of hydroxyapatite: process development. Biomaterials, 22, 1721-1730.

70. W. Paul and C.P. Sharma. (1999). Development of porous spherical hydroxyapatite granules: application towards protein delivery. Journal of Materials Science: Materials in Medicine, 10, 383-388.

71. J.W. Frame and C.L. Brady. (1987). The versatility of hydroxyapatite blocks in maxillofacial surgery. British Journal of Oral and Maxillofacial Surgery, 25(6), 452-464.

72. A. Almirall, G. Larrecq, J.A. Delgado, S. Martinez, J.A. Planell and M.P. Ginebra. (2004). Fabrication of low temperature macroporous hydroxyapatite scaffolds by foaming and hydrolysis of an α-TCP paste. Biomaterials, 25, 3671-3680.

73. P. Sepulveda, J.G.P. Binner, S.O. Rogero, O.Z. Hiha and J.C. Bressiani. (2000). Production of porous hydroxyapatite by the gel-casting of foams and cytotoxic evaluation. Journal of Biomedical Materials Research, 50, 27-34.

74. A. Ratier, I.R. Gibson, S.M. Best, M. Freche, J.L. Lacout and F. Rodriguez. (2001). Setting characteristics and mechanical behaviour of a calcium phosphate bone cement containing tetracycline. Biomaterials, 897-901.

75. A.E. Porter, N. Patel, J.N. Skepper, S.M. Best and W. Bonfield. (2003). Comparison of in vivo dissolution processes in hydroxyapatite and silicon substituted hydroxyapatite bioceramics. Biomaterials, 24, 4609-4620.

76. K.A. Hing, S.M. Best and W. Bonfield. (1999). Characterization of porous hydroxyapatite. Journal of Materials Science: Materials in Medicine, 10, 135-145.

77. N. Patel, I.R. Gibson, S.M. Best, P.A Revell and W. Bonfield. (2002). A comparative study on the in vivo behaviour of hydroxyapatite and silicon substituted hydroxyapatite granule. Journal of Materials Science: Materials in Medicine, 13, 1199-1206.

78. A.E. Porter, N. Patel, J.N. Skepper, S.M. Best and W. Bonfield. (2004). Effect of sintered silicate-substituted hydroxyapatite on remodelling processes at the bone-implant interface, Biomaterials, 25, 3303-3314.

79. S.M. Rea, R.A. Brooks, S.M. Best, T. Kokubo and W. Bonfield. (2004). Proliferation and differentiation of osteoblast-like cells on apatite-wollastonite/ polyethylene composites. Biomaterials, 25, 4503-4512.

80. T.S.B. Narasaraju and D.E. Phebe. (1996). Review: Some physico-chemical aspects of hydroxyapatite. Journal of Materials Science, 31, 1-21.

81. S. Puajindanetr, S.M. Best and W. Bonfield. (1994). Characterisation and sintering of precipitated hydroxyapatite. British Ceramic Transactions, 93(3), 96-99.

82. J.M. Bouler, M. Trecant, J. Delecrin, J. Royer, N. Passuti and G. Daculsi. (1996). Macroporous biphasic calcium phosphate ceramics: Influence of five synthesis parameters on compressive strength. Journal of Biomedical Materials Research, 32, 603-609.

83. J. Ma, C. Wang and K.W. Peng. (2003). Electrophoretic deposition of porous hydroxyapatite scaffold. Biomaterials, 24, 3505-3510.

84. I.R. Gibson, S.M. Best, W. Bonfield. (1999). Chemical characterization of silicon-substituted hydroxyapatite. Journal of Biomedical Materials Research, 44, 422-428.

85. M.H.P.D. Silva, J.H.C Lima, G.A. Soares, C.N. Elias, M.C. de Andrade, S.M. Best and I.R. Gibson. (2001). Transformation of monetite to hydroxyapatite in bioactive coating on titanium. Surface and Coatings Technology, 137, 270-276.

86. I.R. Gibson, K.A. Hing, S.M. Best and W. Bonfield. (1999). Enhanced in vitro cell activity and surface apatite layer formation on novel silicon-substituted hydroxyapatites. Biomaterials, 12, 191-194.

87. M. Aizawa, A.E. Porter, S.M. Best and W. Bonfield. (2005). Ultrastructural observation of single-crystal apatite fibres. Biomaterials, 26, 3427-3433.

88. E.S. Thian, J. Huang, S.M. Best, Z.H. Barber and W. Bonfield. (2005). Magnetron co-sputtered silicon-containing hydroxyapatite thin films-an in vitro study. Biomaterials, 26, 2947-2956.

89. E.S. Thian, J. Huang, S.M. Best and W. Bonfield. (2004). Fabrication of hydroxyapatite ceramics via a modified slip casting route. Key Engineering Materials, 254-256, 111-114.

90. G. Daculsi, N. Passuti, S. Martin, C. Deudon, R.Z. Legeros and S. Raher. (1990). Macroporous calcium phosphate ceramic for long bone surgery in humans and dogs. Clinical and histological study. Journal of Biomedical Materials Research, 24, 379-396.

91. Z. Zyman, I. Ivanov, V. Glushko, N. Dedukh and S. Malyshkina. (1998). Inorganic phase composition of remineralisation in porous CaP ceramics. Biomaterials, 19, 1269-1273.

92. R.B. Martin, M.W. Chapman, R.E. Holmes, D.J. Sartoris, E.C. Shors, J.E. Gordon, D.O. Heitter, N.A. Sharkey and A.G. Zissimos. (1989). Effects of bone ingrowth on the strength and non-invasive assessment of a coralline hydroxyapatite material. Biomaterials, 10, 481-488.

93. O. Gauthier, J.M. Bouler, E. Aguado, P. Pilet and G. Daculsi. (1998). Macroporous biphasic calcium phosphate ceramics; influence of macropore diameter and macroporosity percentage on bone ingrowth. Biomaterial, 19, 133-139.

94. K. de Groot. (1980). Bioceramics consisting of calcium phosphate salts. Biomaterials, 1(1), 47-50.

95. C.J. Damien and J.R. Parsons. (1990). Bone graft and bone graft substitutes: a review of current technology and applications. Journal of Applied Biomaterials, 2, 187-208.

96. H. Oonishi. (1991). Orthopaedic applications of hydroxyapatite. Biomaterials, 12, 171-178.

97. H.W. Kim, S.Y. Lee, C.J. Bae, Y.J. Noh, H.E. Kim, H.M. Kim and J.S. Ko. (2003). Porous ZrO_2 Bone scaffold coated with hydroxyapatite with fluorapatite intermediate layer. Biomaterials, 24, 3277-3284.

98. R.B. Mattin, M.W. Chapman, N.A. Sharkey, S.L. Zissimos, B. Bay and E.C. Shors. (1993). Bone ingrowth and mechanical properties of coralline hydroxyapatite 1 yr after implantation. Biomaterials, 14(5), 341-348.

99. A. Okazaki, T. Koshino, T. Saito and T. Takagi. (2000). Osseous tissue reaction around hydroxyapatite block implanted into proximal metaphysis of tibia of rat with collagen-induced arthritis. Biomaterials, 21, 483-487.

100. J. Vuola, H. Goransson, T. Bohling and S.A. Seljavaara. (1996). Bone marrow induced osteogenesis in hydroxyapatite and calcium carbonate implants. Biomaterials, 17, 1761-1766.

101. T. Koshino, T. Murase, T. Takagi and T. Saito. (2001). New bone formation around porous hydroxyapatite wedge implanted in opening wedge high tibial osteotomy in patients with osteoarthritis. Biomaterials, 22, 1579-1582.

102. H.H.K. Xu and C.G.S. Jr. (2005). Fast setting calcium phosphate-chitosan scaffold: mechanical properties and biocompatibility. Biomaterials, 26, 1337-1348.

103. H.H.K. Xu, J.B. Quinn, S. Takagi and L.C. Chow. (2004). Synergistic reinforcement of in situ hardening calcium phosphate composite scaffold for bone tissue engineering. Biomaterials, 25, 1029-1037.

104. L.A. Dos Santos, L.C. De Oliveira, E.C.S. Rigo, R.G. Carrodeguas, A.O. Boschi and A.C.F. De Arruda. (1999). Influence of polymeric additives on the mechanical properties of α-tricalcium phosphate cement. Bone, 25(2), Supplement 1, 99s-102s.

105. S. Takagi and L.C. Chow. (2001). Formation of macropores in calcium phosphate cement implants. Journal of Materials Science: Materials in Medicine, 12, 135-139.

106. E.M. Ooms, J.G.C. Wolke, M.T. van de Heuvel, B. Jeschke and J.A Jansen. (2003). Histological evaluation of the bone response to calcium phosphate cement implanted in cortical bone. Biomaterials, 24, 989-1000.

107. H.H.K. Xu and J.B. Quinn. (2002). Calcium phosphate cement containing resorbable fibers for short-term reinforcement and macroporosity. Biomaterials, 23, 193-202.

108. R.P.del Real, J.G.C. Wolke, M. Vallet-Regi and J.A. Jansen. (2002). A new method to produce macropores in calcium phosphate cements. Biomaterials, 23, 3673-3680.

109. E. Charriere, S. Terrazzoni, C. Pittet, P. Mordasini, M. Dutoit, J. Lemaitre and P. Zysset. (2001). Mechanical characterization of brushite and hydroxyapatite cements. Biomaterials, 22, 2937-2945.

110. S. Stea, M. Visentin, L. Savarino, M.E. Donati, A. Pizzoferrato, A. Moroni and V. Caja. (1995). Quantitative analysis of the bone-hydroxyapatite coating interface. Journal of materials Science: Materials in Medicine, 6, 455-459.

111. P. Habibovic, F. Barrere, C.A. van Blitterswijk, K de Groot and P. Layrolle. (2002). Biomimetic hydroxyapatite coating on metal implants. Journal of the American Ceramic Society, 85, 517-522.

112. S.R. Sousa and M.A. Barbosa. (1996). Effect of hydroxyapatite thickness on metal ion release from Ti_6Al_4V substrates, Biomaterials, 17(4), 397-404.

113. W.J. Weng and J.L. Baptista. (1998). Sol-gel derived porous hydroxyapatite coatings. Journal of Materials Science: Materials in Medicine, 9, 159-163.

114. C. Tanaka, J. Shikata, M. Ikenaga and M. Takahashi. (2003). Acetabular reconstruction using a kerboull-type acetabular reinforcement device and hydroxyapatite granules. The Journal of Arthroplasty, 18(6), 719-725.

115. V.S. Komlev, S.M. Barinov and E.V. Koplik. (2002). A method to fabricate porous spherical hydroxyapatite granules intended for time-controlled drug release. Biomaterials, 23, 3449-3454.

116. W.L.W. van Hemert, K. Willems, P.G. Anderson, R.J. van Heerwaarden and A.B. Wymenga. (2004). Tricalcium phosphate granules or rigid wedge preforms in open wedge high tibial osteotomy: a radiology study with a new evaluation system. The Knee, 451-456.

117. J. Reichert and J.G.P. Binner. (1996). An evaluation of hydroxyapatite-based filters for removal of heavy metal ions from aqueous solutions. Journal of Materials Science, 31, 1231-1241.

118. P. Sepulveda, F.S. Ortega, M.D.M. Innocentini and V.C. Pandolfelli. (2000). Properties of highly porous hydroxyapatite obtained by the gelcasting of foams. Journal of the American Ceramic Society, 83(12), 3021-3024.

119. J.B.P. Binner. (1997). Production and properties of low density engineering ceramic foams. British Ceramic Transactions. 96(6), 247-249.

120. R. Brezny and D.J. Green. (1989). Fracture behavior of open-cell ceramics. Journal of the American Ceramic Society, 72(7), 1145-1152.

121. T. Fujiu, G.L. Messing and W. Huebner. (1990). Processing and properties of cellular Silica synthesized by foaming sol-gels. Journal of the American Society, 73(1), 85-90.

122. P. Sepulveda. (1997). Gelcasting foams for porous ceramics. The American Ceramic Society Bulletin, 76(10), 61-65.

123. M. Wu, T. Fujiu and G.L. Messing. (1990). Synthesis of cellular inorganic materials by foams sol-gels. Journal of Non-Crystalline Solides, 121, 407-412.

124. L. Montanaro, Y. Jorand, G. Fantozzi and A. Negro. (1998). Ceramic foams by powder processing. Journal of the European Ceramic Society, 18, 1339-1350.

125. P. Sepulveda and J.G.P. Binner. (1999). Processing of cellular ceramics by foaming and in situ polymerisation of organic monomers. Journal of the European Ceramic Society, 19(12), 2059-2066.

126. J.S. Lee and J.K. Park. (2003). Processing of porous ceramic spheres by pseudo-double-emulsion method. Ceramics International, 29, 271-278.

127. C.Y. Chen, S.Y. Chen and D.M. Liu. (1999). Electrophoretic deposition forming of porous alumina membranes. Acta Materialia, 47(9), 2717-2726.

128. G. Li, Z. Jiang, A. Jiang and L. Zhang. (1997). Strengthening of porous Al_2O_3 ceramics through nanoparticle addition. NanoStructured Materials, 8(6), 749-754.

129. X.J. Ding, J.Z. Zhang, R.D. Wang and C.D. Feng. (2001). A novel preparation of porous alumina with parallel channels. Materials Letters, 51, 429-433.

130. H.T. Wang, X.Q. Liu and G.Y. Meng. (1997). Porous α-Al_2O_3 ceramics prepared by gelcasting. Materials research Bulletin, 32(12), 1705-1712.

131. X. Zhu, D. Jiang and S. Tan. (2002). The control of slurry rheology in the processing of reticulated porous ceramics. Materials Research Bulletin, 37, 541-553.

132. Y. Inagaki, N. Kondo and T. Ohji. (2002). High performance porous silicon nitrides. Journal of the European Ceramic Society, 22, 2489-2494.

133. Y. Shigegaki, M.E. Brito, K. Hirao, M. Toriyama and S. Kanzaki. (1997). Strain tolerant porous silicon nitride. Journal of the American Ceramic Society, 80, 495-498.

134. F. Tang, H. Fudouzi, T. Uchikoshi and Y. Sakka. (2004). Preparation of porous materials with controlled pore size and porosity. Journal of the European Ceramic Society, 24, 341-344.

135. M. Kiser, M.Y. He and F.W. Zok. (1999). The mechanical response of ceramic microballoon reinforced aluminum matrix composites under compressive loading. Acta Materialia, 47(9), 2685-2694.

136. M.R. Nangrejo, X. Bao and M.J. Edirisinghe. (2000). Preparation of silicon carbide-silicon nitride composite foams from pre-ceramic polymers. Journal of the European Ceramic Society, 20, 1777-1785.

137. A.J. Sherman, R.H. Tuffias and R.B. Kaplan. (1991). Refractory ceramic foams: A novel, new high-temperature structure. American Ceramic Society Bulletin, 70(6), 1025-1029.

138. Y.W. Kim and C.B. Park. (2003). Processing of microcellular preceramics using carbon dioxide. Composites Science and Technology, 63(16), 2371-2377.

139. J. Saggio-Woyansky, C.E. Scott and W.P. Minnear. (1992). Processing of porous ceramics. American Ceramic Society Bulletin. 71(11), 1674-1682.

140. M.E. Davis. (2002). Ordered porous materials for emerging applications. Nature, 417, 813-821.

141. D.M. Liu. (1997). Fabrication of hydroxyapatite ceramic with controlled porosity. Journal of Materials Science: Materials in Medicine, 8, 227-232.

142. P. Layrolle, A. Ito and T. Tateishi. (1998). Sol-gel synthesis of amorphous calcium phosphate and sintering into microporous hydroxyapatite bioceramics. Journal of the American Ceramic Society, 81(6), 1421-1428.

143. P. Frayssinet and N. Rouquet. (1998). High compressive strength macroporous calcium phosphate ceramics for bone repair. Journal of Biomechanics, 31(Supplement 1), 50.

144. M. Itokazu, W. Yang, T. Aoki, A. Ohara and N. Kato. (1998). Synthesis of antibiotic-loaded interporous hydroxyapatite blocks by vacuum method and in vitro drug release testing. Biomaterials, 19, 817-819.

145. D.J.A. Netz, P. Sepulveda, V.C. Pandolfelli, A.C.C. Spadaro, J.B. Alencastre, M.V. L.B. Bentley and J.M. Marchetti. (2001). Potential use of gelcasting hydroxyapatite porous ceramic as an implantable drug delivery system. International Journal of Pharmaceutics, 213, 117-125.

146. L.L. Hench, R.J. Splinter, W.C. Allen and T.K.J. Greenlee. (1972). Bonding mechanism at the interface of ceramic prosthetic materials. Journal of Biomedical Materials Research, 2, 117-141.

147. H. Ohgushi, M. Okumura, T. Yoshikawa, K. Inoue, N. Sepuku and S. Tamai. (1992). Bone formation process in porous calcium carbonate and hydroxyapatite. Journal of Biomedical Materials Research, 26, 885-895.

148. T.M.G. Chu, D.G. Orton, S.J. Hollister, S.E. Feinberg and J.W. Halloran. (2002). Mechanical and in vivo performance of hydroxyapatite implants with controlled architectures. Biomaterials, 23, 1283-1293.

149. T.M.G. Chu, J.W. Hallorann, S.J. Hollister and S.E. Feinberg. (2001). Hydroxyapatite implants with designed internal architecture. Journal of Materials Science: Materials in medicine, 12, 471-478.

150. Jintao Tian and Jiemo Tian. (2001). Preparation of porous hydroxyapatite. Journal of Materials Science, 36, 3061-3066.

151. B. Flautre, M. Descamps, C. Delecourt, M.C. Blary and P. Hardouin. (2001). Porous HA ceramic for bone replacement: role of the pores and interconnections-experimental study in the rabbit. Journal of Materials Science: Materials in Medicine, 12, 679-682.

152. J.F. Piecuch, A.J. Goldberg, C.V. Shastry and R.B. Chrzanowski. (1984). Compressive strength of implanted porous replamineform hydroxyapatite. Journal of Biomedical Materials Research, 18, 39-45.

153. B.S. Chang, C.K. Lee, K.S. Hong, H.J. Youn, H.S. Ryu, S.S. Chung and K.W. Park. (2000). Osteoconduction at porous hydroxyapatite with various pore configurations. Biomaterials, 21, 1291-1298.

154. G.D. With, H.J.A.V. Dijk, N. Hattu and K. Prijs. (1981). Preparation, microstructure and mechanical properties of dense polycrystalline hydroxy apatite. Journal of Materials Science, 16, 1592-1598.

155. J. Vuola, R. Taurio, H. Goransson and S.A. Seljavaara (1998). Compressive strength of calcium carbonate and hydroxyapatite implants after bone-marrow-induced osteogenesis. Biomaterials, 19, 223-227.

156. J.C. Le Huec, T. Schaeverbeke, D. Clement, J. Faber and A. Le Rebeller. (1995). Influence of porosity on the mechanical resistance of hydroxyapatite ceramics under compressive stress. Biomaterials, 16, 113-118.

157. R.E. Holmes, R.W. Bucholz and V. Mooney. (1986). Porous hydroxyapatite as a bone-graft substitute in metaphyseal defects. Journal of Bone and Joint Surgery, 68-A, 904-911.

158. N. Tamai, A. Myoui, T. Tomita, T. Nakase, J. Tanaka, T. Ochi and H. Yoshikawa. (2002). Novel hydroxyapatite ceramics with an interconnective porous structure exhibit superior osteoconduction in vivo. Journal of Biomedical Materials Research, 59(1), 110-117.

159. D.C. Tancred, B.A.O. McCormack and A.J. Carr. (1998). A synthetic bone implant macroscopically identical to cancellous bone. Biomaterials, 19, 2303-2311.

160. K. de Groot. (1993). Clinical applications of calcium phosphate biomaterials: a review. Ceramics International, 19, 363-366.

161. I. Collin, B. Lamy, O. Gauthier and J.M. Bouler. (2005). Improvement of macroporous biphasic phosphocalcic ceramics for the filling of bone defects. ITBM-RBM, 26, 247-248.

162. E. White and E.C. Shors. (1986). Biomaterial aspects of interpore 200 porous hydroxyapatite. Dental Clinics of North America, 30(1), 49-67.

163. S.F. Hulbert, S.J. Morrison and J.J. Klawitter. (1970). Compatibility of porous ceramics with soft tissue; application to tracheal prostheses. Journal of Biomedical Materials Research Symposium, 2(1), 269-279.

164. E. Tsuruga, H. Takita, H. Itoh, Y. Wakisaka and Y. Kuboki (1997). Pore size of porous hydroxyapatite as the cell-substratum controls BMP-induced osteogenesis. Journal of Biomedical Materials Research, 121, 317-324.

165. R.E. Holmes. (1979). Bone regeneration within a coralline hydroxyapatite implant. Plast Reconstr Surg., 63, 626-633.

166. W.L. Suchanek and M. Yoshimura . (1998). Preparation of Fibrous, porous hydroxyapatite ceramics from hydroxyapatite whiskers. Journal of the American Ceramic Society, 81(3), 765-767.

167. P.S. Eggli, W. Muller and R.K. Schenk. (1988). Porous hydroxyapatite and tricalcium phosphate cylinders with two different pore size ranges implanted in the cancellous bone of rabbits. Clinical Orthopaedics and Related Research, 232, 127-138.

168. E. Ryshkewitch. (1953). Compression strength of porous sintered alumina and zirconia. Journal of the American Ceramic Society, 36(2), 65-68.

169. W. Duckworth. (1953). Discussion of Ryshkewitch paper, Journal of the American Ceramic Society, 36(2), 68.

170. W.D. Kingery, H.K. Bowen and D.R. Uhlmann. (1976) Introduction to Ceramics, 2nd. New York: A. Wiley-Interscience Publication

171. L.L. Hench and E.C. Ethridge. (1982). Biomaterial. Academic Press. Inc.

172. W. Cao and L.L. Hench. (1996). Bioactive Materials. Ceramics International, 22, 493-507.

173. A.M. Gatti, D. Zaffe and G.P. Poli. (1990). Behaviour of tricalcium phosphate and hydroxyapatite granules in sheep bone defects. Biomaterials, 11(7), 513-517.

174. S. Yamaha, D. heymann, J.M. Bouler and G. Daculsi. (1997). Osteoclastic resorption of calcium phosphate ceramics with different hydroxyapatite/β-tricalcium phosphate ratios. Biomaterials, 18(15), 1037-1041.

175. M.T. Fulmer, I.C. Ison, C.R. Hankermayer, B.R. Constantz and J. Ross. (2002). Measurements of the solubilities and dissolution rates of several hydroxyapatites. Biomaterials, 23, 751-755.

176. D.M. Liu, Q. Yang, T. Troczynski and W.J. Tseng. (2002). Structural evolution of sol-gel derived hydroxyapatite. Biomaterials, 23, 1679-1687.

177. J.O. Hollinger and G.C. Battistone. (1986). Biodegradable bone repair materials. Clinical Orthopaedics and Related Research, 207, 290-305.

178. K. Kurashina, H. Kurita, H. Takeuchi, Mi. Hirano, C.P.A.T. Klein and K. de Groot. (1995). Osteogenesis in muscle with composite graft of hydroxyapatite and autogenous calvarial periosteum: a preliminary report. Biomaterials, 16, 119-123.

179. J. Dong, T. Uemura, Y. Shirasaki and T. Tateishi. (2002). Promotion of bone formation using highly pure porous β-TCP combined with bone marrow-derived osteoprogenitor cells. Biomaterials, 23, 4493-4502.

180. Z. Yang, H. Yuan, W. Tong, P. Zou, W. Chen and X.D. Zhang. (1996). Osteogenesis in extraskeletally implanted porous calcium phosphate ceramics: variability among different kinds of animals. Biomaterials, 17, 2131-2137.

181. K. Kurashina, H. Kurita, Q. Wu, A. Ohtsuka and H. Kobayashi. (2002). Ectopic osteogenesis with biphasic ceramics of hydroxyapatite and tricalcium phosphate in rabbits. Biomaterials, 23(2), 407-412.

182. H. Schliephake and T. Kage. (2001). Enhancement of bone regeneration using resorbable ceramics and a polymer-ceramic composite material. Journal of Biomedical Materials Research, 56, 128-136.

183. K.J.L. Burg, S. Porter and J.F. Kellam. (2000). Biomaterial developments for bone tissue engineering. Biomaterials, 21, 2347-2359.

184. M. Kohri, K. Miki, D.E. Waite, H. Nakajima and T. Okabe. (1990). In vitro stability of biphasic calcium phosphate ceramics. Biomaterials, 14(4), 299-304.

185. C. Klein, K. de Groot, C. Weiqun, L. Yubao and X.D. Zhang. (1994). Osseous substance formation induced in porous calcium phosphate ceramics in soft tissues. Biomaterials, 15(1), 31-34.

186. G. Daculsi. (1998). Biphasic calcium phosphate concept applied to artificial bone, implant coating and injectable bone substitute. Biomaterials, 19, 1473-1478.

187. D.C. Tancred, B.A.O. McCormack and A.J. Carr. (1998). A quantitative study of the sintering and mechanical properties of hydroxyapatite/phosphate glass composites. Biomaterials, 19, 1735-1743.

188. U. Ripamounti. (1996). Osteoinduction in porous hydroxyapatite implanted in heterotopic sites of different animal models. Biomaterials, 17, 31-35.

189. M. Fabbri, G.C. Celotti and A. Ravaglioli. (1994). Granulates based on calcium phosphate with controlled morphology and porosity for medical applications: physico-chemical parameters and production technique. Biomaterials, 15(6), 474-477.

190. R.E. Grundel, M.W. Chapman, T. Yee and M.S. Moore. (1991). Autogeneic bone marrow and porous biphasic calcium phosphate ceramic for segmental bone defects in the canine ulna. Clinical Orthopaedics and Related Research, 266, 244-258.

191. K.D. Johnson, K.E. Frierson, T.S. Keller, C. Cook, R. Scheinberg, J. Zerwekh, L. Meyers and M.F. Sciadini. (1996). Porous ceramics as bone graft substitutes in long bone defects: a biomechanical, histological and radiographic analysis. Journal of Orthopaedic Research, 14, 351-369.

192. D.C. Moore, M.W. Chapman and D. Manske. (1987). The evaluation of a biphasic calcium phosphate ceramic for use in grafting long bone diaphyseal defects. Journal of Orthopaedics Research, 5, 356-365.

193. M.T. Mushipe, P.A. Revell and J.C. Shelton. (2002). Cancellous bone repair using bovine trabecular bone matrix particulates. Biomaterials, 23, 365-370.

194. D.M. Roy and S.K. Linnehan. (1974). Hydroxyapatite formed from coral skeletal carbonate by hydrothermal exchange. Nature, 247, 220-222.

195. M. Sivakumar, T.S.S. Kumar, K.L. Shantha and K.P. Rao. (1996). Development of hydroxyapatite derived from Indian coral. Biomaterials, 17, 1709-1714.

196. D.M. Liu. (1996). Fabrication and characterisation of porous hydroxyapatite granules, Biomaterials, 17, 1955-1957.

197. E.R. Munoz, J.R. Diaz, J.R. Rodriguez and W. Brostow. (2001). Hydroxyapatite spheres with controlled porosity for eye ball prosthesis: processing and characterization. Journal of Materials Science: Materials in Medicine, 12, 305-311.

198. V.S. Komlev, S.M. Barinov, E. Girardin, S. Oscarsson, A. Rosengren, F. Rustichelli and V.P. Orlovskii. (2003). Porous spherical hydroxyxapatite and fluorhydroxyapatite granules: processing and characterization. Science and Technology of Advanced Materials, 4, 503-508.

199. B. Sounporlak and I.A. Aksay. (1988). Process for the production of porous ceramics using decomposable polymeric microsphere and the resultant product, United States Patent, No. 4,777,153.

200. D.M. Liu. (1996). Control of pore geometry on influencing the mechanical property of porous hydroxyapatite bioceramic. Journal of Materials Science Letters, 15, 419-421.

201. D.M. Liu. (1997). Influence of porosity and pore size on the compression strength of porous hydroxyapatite ceramics. Ceramics International, 23, 135-139.

202. D.M. Liu. (1998). Preparation and characterisation of porous hydroxyapatite bioceramic via a slip-casting route. Ceramics International, 24, 441-446.

203. L. Vaz, A.B. Lopes and M. Almeida. (1999). Porosity control of hydroxyapatite implants. Journal of Materials Science: Materials in Medicine, 10, 239-242.

204. K. Lin, J. Chang, Y. Zeng and W. Qian. (2004). Preparation of macroporous calcium silicate ceramics. Materials Letters, 58, 2109-2113.

205. F.H. Lin, C.C. Lin, H.C. Liu, Y.Y. Huang, C.Y. Wang and C.M. Lu. (1994). Sintered porous DP-bioactive glass and hydroxyapatite as bone substitute. Biomaterials, 15(13), 1087-1098.

206. T.R. Shrout, W. A. Schulze and J.V. Biggers. (1979). Simplified fabrication of PZT/Polymer composites. Materials Research Bulletin, 14, 1553-1559.

207. J. Werner, B. Linner-krcmar, W. Friess and P. Greil. (2002). Mechanical properties and in vitro cell compatibility of hydroxyapatite ceramics with graded pore structure. Biomaterials, 23(21), 4285-4294.

208. M. Milosevski, J. Bossert, D. Milosevski and N. Gruevska. (1999). Preparation and properties of dense and porous calcium phosphate. Ceramics International, 25, 693-696.

209. A. Slosarczyk, E. Stobierska and Z. Paszkiewicz. (1999). Porous hydroxyapatite ceramics. Journal of Materials Science Letters, 18, 1163-1165.

210. N.O. Engin and A.C. Tas. (1999). Manufacture of macroporous calcium hydroxyapatite bioceramics. Journal of the European Ceramic Society, 19, 2569-2572.

211. E. Sundermann and J. Viedt. (1973). Method of manufacturing ceramic foam bodies. U.S. Patent No. 3,745,201.

212. I.H. Arita, D.S. Wilkinson, M.A. Mondragonn and V.M. Castano. (1995). Chemistry and sintering behaviour of thin hydroxyapatite ceramics with controlled porosity. Biomaterials, 16, 403-408.

213. I.H. Arita, V.M. Castano. and D.S Wilkinson. (2000). Tape casting of porous hydroxyapatite ceramics. Journal of Materials Science Letter, 19, 33-35.

214. I.H. Arita, V.M. Castano and D.S Wilkinson. (1995). Synthesis and processing of hydroxyapatite ceramic tapes with controlled porosity. Journal of Materials Science: Materials in Medicine, 6, 19-23.

215. J.G.P. Binner and J. Reichert. (1996). Processing of hydroxyapatite ceramic foams. Journal of Materials Science, 31, 5717-5723.

216. L. Yubao, C.P.A.T. Klein, X.D. Zhang and K. de Groot. (1994). Formation of a bone apatite-like layer on the surface of porous hydroxyapatite ceramics. Biomaterials, 15(10), 835-841.

217. K. Schwartzwalder and A.V. Somers. (1963). Method of making porous ceramic articles. U.S. Patent No. 3,090,094.

218. H.R.R. Ramay and M. Zhang. (2004). Biphasic calcium phosphate nanocomposite porous scaffolds for load-bear bone tissue engineering. Biomaterials, 25, 5171-5180.

219. X. Miao, Y. Hu, J. Liu and A.P. Wong. (2004). Porous calcium phosphate ceramics prepared by coating polyurethane foams with calcium phosphate cements. Materials Letters, 58, 397-402.

220. M. Fabbri, G.C. Celotti and A. Ravaglioli. (1995). Hydroxyapatite-based porous aggregates: physico-chemical nature, structure, texture and architecture. Biomaterials, 16, 225-228.

221. F.F. Lange, B.V. Velamakanni and A.G. Evans. (1990). Method for processing metal-reinforced ceramic composites. Journal of the American Society, 73(2), 388-393.

222. D.D. Brown and D.J. Green. (1994). Investigation of strut crack formation in open cell alumina ceramics. Journal of the American ceramic Society, 77(6), 1467-1472.

223. S.H. Kwon, Y.K. Jun, S.H. Hong, I.S. Lee, H.E. Kim and Y.Y. Won. (2002). Calcium phosphate bioceramics with various porosities and dissolution rates. Journal of the American Ceramic Society, 85(12), 3129-3131.

224. Y.K. Jun, W.H. Kim, O.K. Kweon and S.H. Hong. (2003). The fabrication and biochemical evaluation of alumina reinforced calcium phosphate porous implants. Biomaterials, 24, 3731-3739.

225. Y.S. Han, J.B. Li, Y.J. Chen and Q.M. Wei. (2002). A study on the factors involved in collapse of macroporous α-Al_2O_3 structure. Journal of Materials Processing Technology, 128, 313-317.

226. H.X. Peng, Z. Fan, J.R.G. Evans and J.J.C. Busfield. (2000). Microstructure of ceramic foams. Journal of the European Ceramic Society, 20(7), 807-813.

227. Y.S. Han, J.B. Li and Y.J. Chen. (2003). Fabrication of bimodal porous alumina ceramics. Materials Research Bulletin, 38, 373-379.

228. H. R. Ramay and M. Zhang. (2003). Preparation of porous hydroxyapatite scaffolds by combination of the gel-casting and polymer sponge methods. Biomaterials, 24, 3293-3302.

229. H.X. Peg, Z. Fan and J.R.G. Evans. (2000). Factors affecting the microstructure of a fine ceramic foam. Ceramics International, 26, 887-895.

230. D.P Shinner, R.E. Newnham and L.E. Cross. (1978). Flexible composite transducers. Materials Research Bulletin, 13, 599-607.

231. I.J. Holland. (1963). Method of making a porous shape of sintered refractory material. U.S. Patent No. 3,097,930.

232. J.A. Lewis. (2000). Colloidal Processing of ceramics. Journal of the American Ceramic Society, 83(10), 2341-2359.

233. E.G. Nordstrom and K.H. Karlsson. (1990). Slip cast apatite ceramics. Ceramic Bulletin, 69(5), 824-827.

234. D.M. Liu. (2002). Theoretical determination of floc size in highly-concentrated zirconia-wax suspensions. Acta Materailia, 50(8), 1927-1935.

235. J.M.F. Ferreira and H.M.M. Diz. (1999). Effect of solids loading on slip-casting performance of silicon carbide slurries. Journal of the American Ceramic Society, 82(8), 1993-2000.

236. L.M.R. Lorenzo, M.V. Regi and J.M.F. Ferreira. (2001). Colloidal processing of hydroxyapatite. Biomaterials, 22, 1847-1852.

237. G. Tari and J.M.F. Ferreira. (1998). Colloidal processing of calcium carbonate. Ceramics International, 24, 527-532.

238. S. Gautier, E. Champion, D. Bernache-Assollant and T. Chartier. (1999). Rheological Characteristics of alumina platelet-hydroxyapatite composite suspensions. Journal of the European Ceramic Society, 19, 469-477.

239. M. Toriyama, A. Ravaglioli, A. Krajewski, C. Galassi, E. Roncari and A. Piancastell. (1995). Slip casting of mechanochemically synthesized hydroxyapatite. Journal of Materials Science, 30, 3216-3221.

240. P. Colombo and E. Bernardo. (2003). Macro- and micro-cellular porous ceramics from preceramic polymers. Composites Science and Technology, 63(16), 2353-2359.

241. R. Brezny and D.J. Green. (1990). The effect of cell size on the mechanical behavior of cellular materials. Acta Metallurgica et Materialia., 38(12), 2517-2526.

242. R. Brezny, D.J. Green and C.Q. Dam. (1989). Evaluation of strut strength in open-cell ceramics. Journal of the American Ceramic Society, 72(6). 885-889.

243. R. Brezny and D.J. Green. (1991). Factors controlling the Fracture resistance of brittle cellular materials. Journal of the American Ceramic Society, 74(5), 1061-1065.

244. E. Charriere, J. Lemaitre and Ph. Zysset. (2003). Hydroxyapatite cement scaffolds with controlled macroporosity: fabrication protocol and mechanical properties. Biomaterials, 24, 809-817.

245. V.L. Tsang and S.N. Bhatia. (2004). Three-dimensional tissue fabrication. Advanced Drug Delivery Reviews, 56, 1635-1647.

246. C.Y. Lin, N. Kikuchi and S.J. Hollister. (2004). A novel method for biomaterial scaffold internal architecture design to match bone elastic properties with desired porosity. Journal of Biomechanics, 37, 623-636.

247. Z. Fang, B. Starly and W. Sun. (2005). Computer-aided characterization for effective mechanical properties of porous tissue scaffolds. Computer-Aided Design, 37, 65-72.

248. G.D. Quinn. (1991). Design data for engineering ceramics: a review of the flexure test. Journal of the American Ceramic Society, 74(9) 2037-2066.

249. M.B. Thomas, R.H. Doremus, M. Jarcho and R.L. Salsbury. (1980). Dense hydroxyapatite: fatigue and fracture strength after various treatments from diametral tests. Journal of Materials Science, (15), 891-894.

250. H.W. Chandler, R.J. Henderson, M.N. Al-Zubaidy, M. Saribiyik and A. Muhaidi. (1997). A fracture test for brittle materials. Journal of the European Ceramic Society, 17, 759-763.

251. L.V. Griffin, J.C. Gibeling, R.B. Martin, V.A. Gibson and S.M. Stover. (1999). The effects of testing methods on the flexural fatigue life of human cortical bone. Journal of Biomechanics. 32, 105-109.

252. P.E. Wang and T.K. Chaki. (1993). Sintering behaviour and mechanical properties of hydroxyapatite and dicalcium phosphate. Journal of Materials Science: Materials in Medicine, 4, 150-158.

253. H.Y. Juang and M.H. Hon. (1997). The effect of calcination temperature on the behaviour of HA powder for injection moulding. Ceramics International, 23, 383-387.

254. R.R. Rao and T.S. Kannan. (2001). Dispersion and slip casting of hydroxyapatite. Journal of the American Ceramic Society, 84(8). 1710-1716.

255. M. Akao, H. Aoki and K. Kato. (1981). Mechanical properties of sintered hydroxyapatite for prosthetic applications. Journal of Materials Science, 16, 809-812.

256. J.D. Santos, J.C. Knowles, R.L. Reis, F.J. Monteiro and G.W. Hasting. (1994). Microstructural characterization of glass-reinforced hydroxyapatite composites. Biomaterials, 15(1), 5-10.

257. C. Chu, P. Lin, Y. Dong, X. Xue, J. Zhu and Z. Yin. (2002). Fabrication and characterization of hydroxyapatite reinforced with 20 vol % Ti particles for use as hard tissue replacement. Journal of Materials Science: Materials in Medicine, 13, 985-992.

258. N.O. Engin and A.C. Tas. (2000). Preparation of porous $Ca_{10}(PO_4)_6(OH)_2$ and β-$Ca_3(PO_4)_2$ bioceramics. Journal of the American Ceramic Society, 83(7), 1581-1584.

259. H.G. Tattersall and G. Tappin. (1966). The work of fracture and its measurement in metals, ceramics and other materials. Journal of Materials Science, 1, 296-301.

260. J. Nakayama. (1965). Direct measurement of fracture energies of brittle heterogeneous materials. Journal of the American Ceramic Society, 48(11), 583-587.

261. R.W. Davidge and C.D. Phillips. (1972). The significance of impact data for non-metallic materials. Journal of Materials Science, 7, 1308-1314.

262. L.L. Rogers and D.D. Moyle. (1988). Effect of specimen size on work-of – fracture measurements. Journal of Biomechanics, 21(11), 919-926.

263. R.W. Davidge and G. Tappin. (1968). The effective surface energy of brittle materials. Journal of Materials Science, 3, 165-173.

264. L.A. Simpson. (1972). Effect of microstructure on measurements of fracture energy of Al_2O_3. Journal of the American Ceramic Society, 56(1), 7-11.

265. K. Piekarski. (1970). Fracture of bone. Journal of Applied Physics, 41(1), 215-223.

266. C. H. Turner and D. B. Burr. (1993) Basic biomechanical measurements of bone: A tutorial, Bone, 14(4), 595-608.

267. Yuehuei H. An. and Robert A. Draughn ed. (2000) Mechanical testing of bone and the bone-implant interface. Boca Raton; London: CRC Press.

268. M. Jarcho, C.H. Bolen, M.B. Thomas, J. Bobick, J.F. Kay and R.H. Doremus. (1976). Hydroxyapatite synthesis and characterization in dense polycrystalline form. Journal of Materials Science, 11, 2027-2035.

269. B. Grimm (2003) Mechanical properties of morsellised bone graft and synthetic graft extenders for impaction grafting. Thesis (Ph.D.), University of Bath, Bath.

270. A. Mortensen and S. Suresh. (1995). Functionally graded metals and metal-ceramic composites: Part 1 Process. International Materials Reviews, 40(6). 239-265.

271. B. Kieback, A. Neubrand and H. Riedel. (2003). Processing techniques for functionally graded materials. Materials Science and Engineering, A362, 81-105.

272. M. Okazaki, Y. Miake, H Tohda, T. Yanagisawa. T. Matsumoto and J. Takahashi. (1999). Functionally graded fluoridated apatites. Biomaterials, 22, 1421-1426.

273. A. Tampieri, G. Celotti, S. Sprio, A. Delcegliano and S. Franzese. (2001). Porosity-graded hydroxyapatite ceramics to replace nature bone. Biomaterials, 22, 1365-1370.

274. R. Carola, J.P. Harley, C.R. Noback. (1990). Human Anatomy and Physiology. New York; London: McGraw-Hill.

275. K. Maca, P.Dobsak and A.R. Boccaccini. (2001). Fabrication of graded porous ceramics using alumina-carbon powder mixture. Ceramics International, 27, 577-584.

276. J. Moon, A.C. Caballero, L. Hozer, Y.M. Chiang and M.J. Cima. (2001). Fabrication of functionally graded reaction infiltrated SiC–Si composite by three-dimensional printing (3DP™) process. Materials Science and Engineering A, 298, 110-119.

277. Y. Kinemuchi, K. Watari and S. Uchimura. (2003). Grading porous ceramics by centrifugal sintering. Acta Materialia, 51(11), 3225-3231.

278. E. Roncari and C. Galassi. (2000). Tape casting of porous hydroxyapatite ceramics. Journal of Materials Science Letter, 19, 33-35.

279. S.F. Corbin, X. Zhao-jie, H. Henein and P.S. Apte. (1999). Functionally graded metal/ceramic composites by tape casting, lamination and infiltration. Materials Science and Engineering A, 262, 192-203.

280. P. Colombo and J.R. Hellmann. (2002). Materials Research Innovations, 6, 260.

281. J. Zeschky, T. Hofner, C. Arnold, R. Weibmann, D.B. Hourlier, M. Scheffler and P. Greil. (2005). Polysilsesquioxane derived ceramic foams with gradient porosity. Acta Materialia, 53, 927-937.

282. F.R.C. Jr, K.P. Trumble and J. Rodel. (1998). Tailored porosity gradients via colloidal infiltration of compression-molded sponges. Journal of American Ceramic Society, 81(6), 1661-1664.

283. W. Pompe, H. Worch, M. Epple, W. Friess, M. Gelinsky, P. Greil, U. Hempel, D. Scharnweber and K. Schulte. (2003). Functionally graded materials for biomedical applications. Materials Science and Engineering, A362, 40-60.

284. M. Wang, X.Y. Yang, K.A. Khor and Y. Wang. (1999). Preparation and characterization of bioactive monolayer and functionally graded coatings. Journal of Materials Science: Materials in Medicine, 10, 269-273.

285. M. Kon, K. Ishikawa and Y. Miyamoto. (1995). Development of calcium phosphate based functional gradient bioceramics. Biomaterials, 16, 709-714.

286. B. P. Casey. (2003). Novel fabrication techniques for the production of porous biphasic calcium phosphate ceramics for bone substitute application. Thesis (Ph.D.), University of Bath, Bath.

287. L. Yubao, C.P.A.T. Klein, X.D. Zhang and K.D. Groot. (1993). Relationship between the colour change of hydroxyapatite and the trace element manganese. Biomaterials, 14(13), 969-972.

288. R.A. Young and J.C. Elliot. (1966). Atomic-Scale Bases for Several Properties of Apatites. Archives of Oral Biology, 11, 699-707.

8. Appendix

Appendix A

	United States	Japan	Germany	France
Title (Year)	MIL-STD 1942 (1983) ASTM C 1161 (1990)	JIS R 1601 (1981)	DIN 51 110 Part 1 (1989)	AFNOR B41-104 (1989, tentative)
Fixture	Three or four point	Three or four point	Four point	Three or four point
Spans (four point)	10 × 20 mm 20 × 40 mm 40 × 80 mm 0.75 × 1.5 in.*	10 × 30 mm	20 × 40 mm	10 × 20 mm 20 × 40 mm
Fixture	Semiarticulating or fully articulating	Fixed**	Fully articulating	Fully articulating
Fixture load pins	Rotating	Fixed***	Rotating	Rotating
Specimen sizes	1.5 × 2 × 25 mm 3 × 4 × 45 mm 6 × 8 × 85 mm 0.13 × 0.25 × 2 in.*	3 × 4 × 35 mm	3 × 4 × 45 mm	2 × 4 × 25 mm 3 × 4 × 45 mm
Specimen chamfers	Up to 0.15 mm	Up to 0.3 mm****	Up to 0.3 mm****	Up to 0.3 mm****
Specimen preparation	(a) As-fired (b) Application matched (c) Three steps prescribed (wheel, grits, rates, etc.) (d) Other (Most flexible)	(a) As-fired (b) Polish (final finish may merely conceal damage?)	(a) As-fired (b) Three steps prescribed (wheel, grits, rates, etc.)	(a) Polish, deeply (tensile face) (b) Grinding optional (c) Other (Polish at least 100 μm deep to remove damage; roughness of 2 μm)
Number of specimens (minimum)	10 for mean, 30 for Weibull analysis	10	15, preferably 30	10
Loading rate	0.5 mm/min (for B size)	0.5 mm/min	5 - 10 s	0.2 mm/min 0.5 mm/min (or higher)
Comments	Most flexible; B configuration is most common; Tutorial and discussion of flexure testing	Less stringent in some technical details; simple to use	Tolerances similar to MIL STD	Tolerances similar to MIL STD; Special inspection require for 20% of specimens; Includes Weibull analysis
*ASTM. **Specimens must be parallel, but no specifications on fixture. ***5% to 15% error? ****4% stress error.				

Table 8.1 A comparison of flexure standards[248].

Appendix B

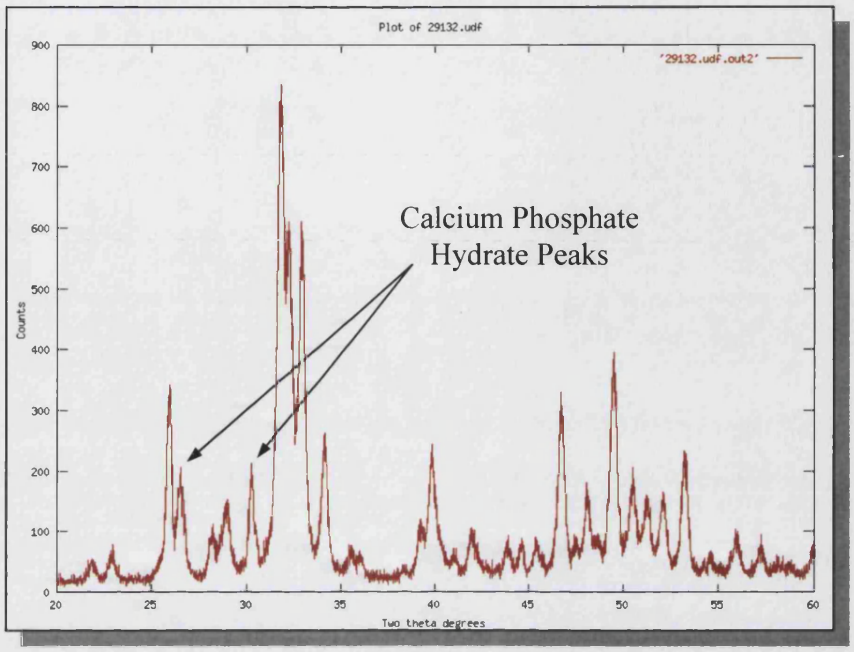

(a)

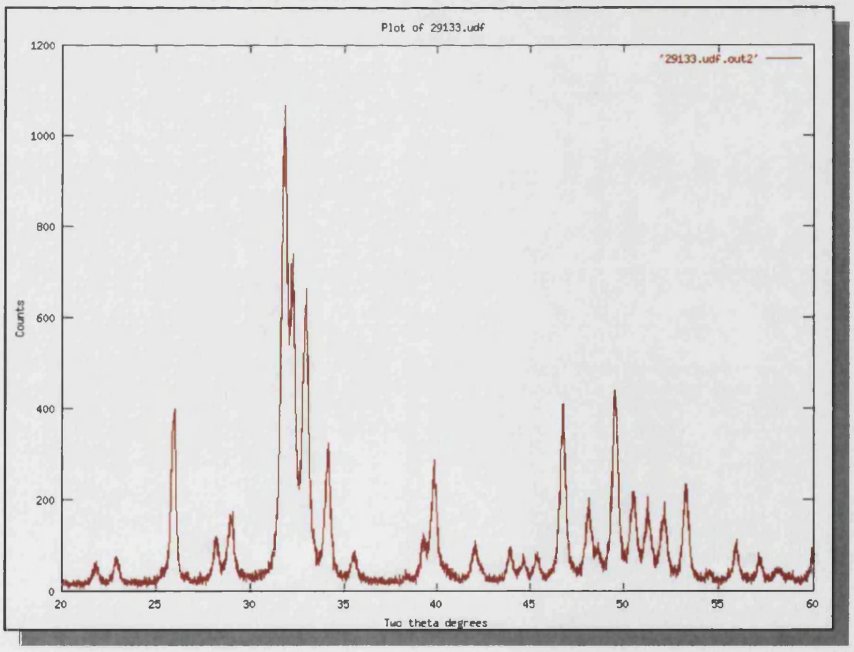

(b)

Figure 8.1 XRD trace for (a) grade 118 and (b) grade 130 powders as received[286].

List of publications

1. Y.H. Hsu, I.G. Turner and A.W. Miles. Fabrication of porous calcium phosphate bioceramics as synthetic cortical bone graft. British Orthopaedic Research Society (BORS) Spring Meeting, 29-30 March 2004, Bristol, UK.

2. Y.H. Hsu, I.G. Turner and AW Miles. Fabrication of porous calcium phosphate bioceramics as synthetic cortical bone graft. 7th World Biomaterials Congress,17-21 May 2004, Sydney, Australia.

3. Y.H. Hsu, I.G. Turner, and A.W. Miles. Fabrication of porous calcium phosphate bioceramics as synthetic cortical bone graft. 17th annual meeting (Bioceramics 17) of The International Society for Ceramics in Medicine (ISCM), 8-12 December 2004, New Orleans, USA.

4. Y.H. Hsu, I.G. Turner and A.W. Miles. (2005). Fabrication of porous calcium phosphate bioceramics as synthetic cortical bone graft. Key Engineering Materials, Vols. 284-286, 305-308.

5. British Patent Application No. 0318902.4; Bone substitute material, August 2003.

1. BORS Spring Meeting, 29-30 March 2004, Bristol, UK.

Fabrication of Porous Calcium Phosphate Bioceramics as Synthetic Cortical Bone Graft

Y.H. Hsu[1], I.G. Turner [1], A.W. Miles [2]
[1]Dept of Engineering & Applied Science, University of Bath, Claverton Down, Bath, BA2 7AY
[2]Dept of Mechanical Engineering, University of Bath, Claverton Down, Bath, BA2 7AY

Introduction

Calcium phosphate based ceramics with a porous configuration are attractive for use as synthetic bone grafts as the porous network allows tissue ingrowth, which further enhances the implant-tissue attachment. The degree of interconnectivity and the nominal pore size are the critical factors that determine the success of the implants. It is generally accepted that a minimum pore size of 100 μm is necessary for the porous implant materials to function well and a pore size greater than 200 μm is an essential requirement for osteo-conduction. However, research has suggested that the degree of interconnectivity is more critical than the pore size.

In this study, porous Hydroxyapatite/Tricalcium phosphate (HA/TCP) bioceramics with interconnected porosity and controlled pore sizes were fabricated by a novel technique involving vacuum impregnation of reticulated polymeric foams with ceramic slip. HA/TCP samples with a range of pore sizes and functionally gradient materials (FGM) with porosity gradients were made.

Materials and Methods

Two grades of calcium phosphate powder, TCP 118 and TCP 130, were used. Varying the blend ratios could change the ratios of HA and TCP in the sintered samples. The foams used comprised polyurethane (PU) which had one of three different porosities 20, 30 and 45 pores per inch (ppi). In order to make a FGM with porosity gradients mimicking the bimodal structure of cortical and cancellous bone, two different foams were either joined together by sewing or pressfitting together. The foams were substantially impregnated with slip by vacuum impregnation. The impregnated foams were removed from the vacuum chamber and dried on tissue for at least 24 hours then sintered at temperatures of up to 1280°C.

Results and Discussion

Using a slip with the appropriate viscosity, porous HA/TCP bioceramics having interconnecting pores and a range of pore sizes can be produced successfully. By joining different ppi foams together, it is possible to develop functional gradient materials in which the porosity varies through the thickness of the samples. No weakness could be seen at the interface between the two different structures. This demonstrated that porous HA/TCP with two or more different levels of porosity could be produced in a single block. Image analysis shows the porosity measured for the three different foams was similar. The area equivalent diameters of the pore structure are 197-254 μm with 20ppi foam, 143-183 μm with 30ppi foam and 105-127 μm with 45ppi foam. The compressive strengths of the HA/TCP samples are in the range of 30-170 MPa and the apparent densities were 2.34-2.76 g/cm^3. The technique developed for fabricating porous bioceramics can be extended to produce a range of bone substitute materials with properties tailored to specific clinical applications.

Acknowledgements

The authors would like to thank the University of Bath and Stryker Howmedica Osteonics for their support.

2. 7th World Biomaterials Congress,17-21 May 2004, Sydney, Australia.

Fabrication of Porous Calcium Phosphate Bioceramics as Synthetic Cortical Bone Graft

Hsu, Y.H.[1], Turner, I.G.[1], Miles, A.W.[2]
[1]Dept of Engineering and Applied Science, University of Bath, Claverton Down, Bath, BA2 7AY, U.K.
[2]Dept of Mechanical Engineering, University of Bath, Claverton Down, Bath, BA2 7AY, U.K.

Introduction

In recent years attention has particularly focussed on the fabrication of calcium phosphate ceramics with a porous configuration as synthetic bone grafts because the porous network promotes tissue ingrowth, which further enhances the implant-tissue attachment[1-6]. The degree of interconnectivity and the nominal pore size are the critical factors that determine the success of the implants. Hulbert *et al.*[7] particularly claimed that a minimum pore size of 100 μm is necessary for the porous implant materials to function well and a pore size greater than 200 μm was an essential requirement for osteo-conduction. However, a number of groups have suggested that the degree of interconnectivity is more critical than the pore size[8, 9].

In this study, porous Hydroxyapatite/Tricalcium phosphate (HA/TCP) bioceramics with interconnected porosity and controlled pore sizes were fabricated by a novel technique involving vacuum impregnation of reticulated polymeric foams with ceramic slip. HA/TCP samples with a range of pore sizes and functionally gradient materials (FGM) with porosity gradients were made.

Materials and Methods

Two grades of calcium phosphate powder, TCP 118 and TCP 130, were used. Varying the blend ratios could change the ratios of HA and TCP in the sintered samples. The foams used were made of polyurethane (PU) and had three different porosities 20, 30 and 45 pores per inch (ppi). In order to make a FGM with porosity gradients mimicking the bimodal structure of cortical and cancellous bone, two different foams were joined together by sewing and push fit. Slips of 600 – 1400 g of powder per litre (60 – 140 wt%) were prepared by ball milling. Dispex A40 was added as a dispersant to adjust the viscosity. The rheological properties of the slip were characterised using a Brookfield viscometer. The foams were substantially impregnated with slip by vacuum impregnation. The foams were removed from the vacuum chamber and dried on tissue for at least 24 hours. The samples were then sintered at temperatures of up to 1280°C.

Results and Discussion

Figure 1(a) shows the many large isolated holes resulting from the single vacuum process. This problem was overcome by double impregnation, Figure 1(b).

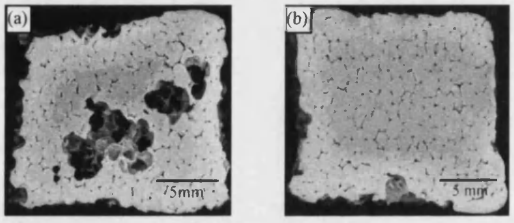

Figure 1 Porous HA/TCP generated by (a) single impregnation (b) double impregnation.

Figure 2 shows the samples generated by joining 20 and 45 ppi foams together. No weakness could be seen at the interface between the two different structures. This demonstrated that porous HA/TCP with two or more different levels of porosity could be produced in a single block.

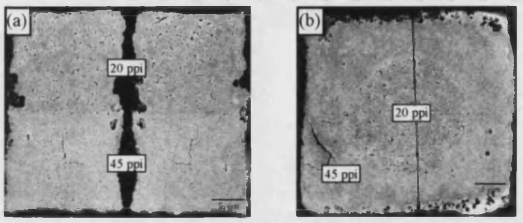

Figure 2 The HA/TCP ceramics combining two different pores sizes by (a) sewing and (b) push fit.

Image analysis shows the porosity measured for the three different foams was similar. The area equivalent diameters of the pore structure are 197-254 μm with 20ppi foam, 143-183 μm with 30ppi foam and 105-127 μm with 45ppi foam. The compressive strengths of the HA/TCP samples are in the range of 30-170 MPa and the apparent densities were 2.34-2.76 g/cm^3.

Conclusions

Using a slip with the appropriate viscosity, porous HA/TCP bioceramics having interconnecting pores and a range of pore sizes can be produced successfully. Double vacuum impregnation is more successful than a single vacuum process. By joining different ppi foams together, it is possible to develop functional gradient materials in which the porosity varies through the thickness of the samples. The technique developed for fabricating porous bioceramics can be extended to produce a range of bone substitute materials with properties tailored to specific clinical applications.

Acknowledgements

The authors would like to thank the University of Bath and Stryker Howmedica Osteonics for their support.

References

1. A. Tampieri *et al.* (2001). Biomater., **22**, 1365-1370.
2. T.M.G. Chu ea al. (2002). Biomater., **23**, 1283-1293.
3. J. Tian *et al.* (2001). J. Mat. Sci., **36**, 3061-3066.
4. D.J.A. Netz et al. (2001). Inter. J. Pharm., **213**, 117-125.
5. B. Flautre *et al.* (2001). J. Mat. Sci.: Mat. Med., **12**, 679-682.
6. J.X. Lu *et al.* (1999). J. Mat. Sci.: Mat. Med., **10**, 111-120.
7. S.F. Hulbert *et al.* (1970) J. Biomed. Mater. Res. Symp., **2**(1), 269-279.
8. J.H. Kuhne *et al.* (1994). Acta Orthop. Scand., **65**, 246.
9. P.S. Eggli *et al.* (1988). Clin. orthop. Rel. Res., **232**,127-138.

3. Bioceramics 17, 8-12 December 2004, New Orleans, USA.

Fabrication of Porous Calcium Phosphate Bioceramics as Synthetic Cortical Bone Graft

Y.H. Hsu[1], I.G. Turner [1], A.W. Miles [2]
[1]Dept of Engineering & Applied Science, University of Bath, Claverton Down, Bath, BA2 7AY
[2]Dept of Mechanical Engineering, University of Bath, Claverton Down, Bath, BA2 7AY

Introduction

Bone grafts are necessary in orthopaedic surgery for filling bone cavities, treatment of nonunion and replacement of bone lost during trauma and tumour removal. Porous calcium phosphate based ceramics are attractive for use as synthetic bone grafts allowing successful tissue ingrowth, which further enhances the implant-tissue attachment. The degree of interconnectivity and the nominal pore size are critical factors that determine the success of the implants. It is generally accepted that a minimum pore size of 100 μm is necessary for the porous implant materials to function well and a pore size greater than 200 μm is an essential requirement for osteoconduction. However, research has suggested that the degree of interconnectivity is more critical than the pore size.

In this study, porous hydroxyapatite/tricalcium phosphate (HA/TCP) bioceramics with interconnected porosity and controlled pore sizes were fabricated by a novel technique involving vacuum impregnation of reticulated polymeric foams with ceramic slip. Porous HA/TCP blocks, granules and functionally gradient materials (FGM) with porosity gradients were made.

Materials and Methods

Two grades of calcium phosphate powder, TCP 118 and TCP 130, were used. Varying the blend ratios changed the ratios of HA and TCP in the sintered samples. The foams used comprised polyurethane (PU) which had one of three porosities 20, 30 and 45 pores per inch (ppi) and varying dimensions. In order to make a FGM with porosity gradients mimicking the bimodal structure of cortical and cancellous bone, two different foams were either joined together by sewing or pressfitted together. The foams were substantially impregnated with slip by vacuum impregnation, dried on tissue for at least 24 hours then sintered at temperatures of up to 1280°C.

Results

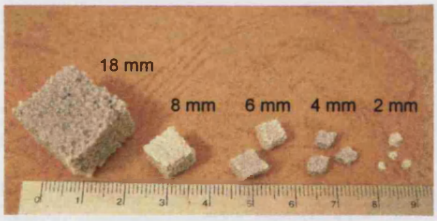

Figure 1 Porous HA/TCP bioceramics with different dimensions.

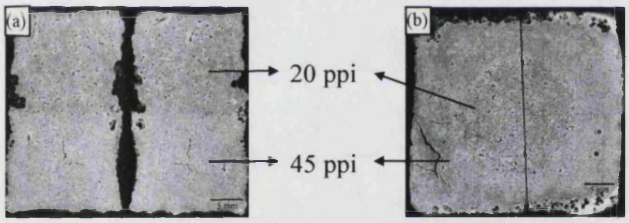

Figure 2 The HA/TCP ceramics combining two different pores sizes by (a) sewing and (b) pressfitting.

Figure 1 shows porous HA/TCP bioceramics with different dimensions fabricated by the vacuum impregnation method. Figure 2 shows the sample generated by joining 20 and 45 ppi foams together. No weakness could be seen at the interface between the two different structures. This demonstrated that porous HA/TCP with two or more different levels of porosity could be produced in a single block. Image analysis revealed the porosity measured for the three different foams was in the range of 5-10%. The area equivalent diameters of the pores were 197-254 μm for 20ppi foam, 143-183 μm for 30ppi foam and 105-127 μm for 45ppi foam. The compressive strengths of the HA/TCP samples were in the range of 30-170 MPa and the apparent densities were 2.34-2.76 g/cm^3.

Discussion and Conclusions

Using a slip with the appropriate viscosity, large blocks of porous HA/TCP bioceramic with interconnected pores and a range of pore sizes were produced successfully. The method was also used to make HA/TCP granules in the size range of 2-8 mm with interconnected porosity and controlled size and shape – hitherto not possible using existing manufacturing techniques. By joining different ppi foams together, it was possible to produce functional gradient materials with porosity which varied through the thickness of the samples. The techniques developed for fabricating porous bioceramics can be extended to produce a range of bone substitute materials with properties tailored to specific clinical applications.

Acknowledgements

The authors would like to thank the University of Bath and Stryker Howmedica Osteonics for their support.

4. Key Engineering Materials, Vols. 284-286, 305-308, (2005).

Fabrication of Porous Calcium Phosphate Bioceramics as Synthetic Cortical Bone Graft

Y.H. Hsu[1,a], I.G. Turner[1,b] and A.W. Miles[2,c]

[1]Dept of Engineering & Applied Science, University of Bath, Claverton Down, Bath, BA2 7AY.

[2]Dept of Mechanical Engineering, University of Bath, Claverton Down, Bath, BA2 7AY.

[a]Y.Hsu@bath.ac.uk, [b]I.G.Turner@bath.ac.uk, [c]A.W.Miles@bath.ac.uk

Keywords: Calcium phosphate, Hydroxyapatite and Bioceramics

Abstract. The aim of this study was to fabricate porous Hydroxyapatite/Tricalcium phosphate (HA/TCP) bioceramics with an adequate degree of interconnected porosity combined with optimal mechanical properties. Porous HA/TCP bioceramics with interconnected porosity and the controlled pore sizes necessary to simulate natural bone tissue morphology were fabricated by a novel technique of vacuum impregnation of reticulated polymeric foams with ceramic slip. By varying the characteristics of the slips and using foams of different pores per inch (ppi), samples of porous HA/TCP, blocks and granules, with a wide range of pore sizes were successfully manufactured. Functionally gradient materials (FGM) with porosity gradients were also made and no weakness was found at the interface. The pore size of the HA/TCP bioceramics was in the range of 197 – 254 μm (for 20 ppi foam), 143 – 182 μm (for 30 ppi foam) and 105 – 127 μm (for 45 ppi foam). The compressive strengths and the apparent densities of the HA/TCP samples were in the range of 30 – 170 MPa and 2.34 – 2.76 g/cm^3 respectively. These results indicate that it is possible to manufacture open pore HA/TCP bioceramics with compressive strengths comparable to human bone which could be of clinical interest.

Introduction

Bone grafts are necessary in orthopaedic surgery for filling bone cavities, treatment of nonunion and replacement of bone lost during trauma and tumour removal. Porous calcium phosphate based ceramics are attractive for use as synthetic bone grafts allowing successful tissue ingrowth, which further enhances the implant-tissue attachment [1-5]. The degree of interconnectivity and the nominal pore size are critical factors that determine the success of the implants. It is generally accepted that a minimum pore size of 100 μm is necessary for the porous implant materials to function well and a pore size greater than 200 μm is an essential requirement for osteoconduction. However, research has suggested that the degree of interconnectivity is more critical than the pore size [6,7]. The aim of this study was to produce open pore HA/TCP samples with connected porosity combined with good mechanical properties.

Materials and Methods

Two grades of powder, TCP 118 and TCP 130, were used in this study. Varying the blend ratios of TCP 118 and TCP 130 and sintering temperature, changed the ratios of HA and TCP in the sintered samples. TCP 118 is a low crystalline (i.e. imperfect and unstable) hydroxyapatite, that contains the phase calcium phosphate hydrate (CPH) which allows the final sintered products to comprise β-tricalcium phosphate (β-TCP) and α-tricalcium phosphate (α-TCP) as well as some hydroxyapatite (HA) depending on the sintered temperature. TCP 130 is a stable, highly crystalline form of HA and does not undergo phase transition on subsequent firing.

The organic foams, which were completely burnt out during sintering were made of polyurethane (PU) which had one of three porosities – 20 ppi, 30 ppi and 45 ppi and varying dimensions. The PU foams were sectioned to the desired shape and size, then soaked in water

for 24 hours. This stage of the process removed dust and impurities from the foams. The standard foams dimensions used in this research were 30 × 30 × 25 mm. The method can utilize PU foams in a full range of sizes, encompassing a range of geometries from small granules up to large blocks. In order to make a FGM with porosity gradients mimicking the bimodal structure of cortical and cancellous bone, two different foams were either joined together by sewing or pressfitted as shown in Figure 1.

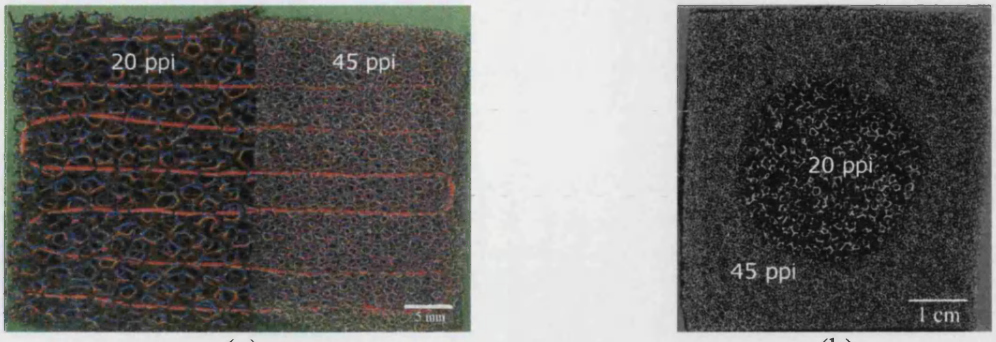

(a) (b)

Fig. 1 Two different ppi foams joined together by (a) sewing (b) pressfitting.

The ceramic suspensions were prepared by first adding the dispersing agent, Dispex A40, to distilled water. This decreases the slip viscosity and improves the flow properties without decreasing the solids loading. While stirring, TCP 118 and TCP 130 powders were gradually added in different proportions in order to achieve various solid loading of slips. After adding the required amounts of powder, the mixtures were ball milled, using ZrO_2 balls as the milling media, for 24 hours. This process improves the rheological properties of the suspensions and the packing ability during consolidation. After ball milling, another amount of dispersant was added to adjust the slip to an exact viscosity. The viscosity characteristics of the slip were measured using a Brookfield viscometer via a constant spindle speed of 10 rpm using a No. 5 spindle. The viscosity of the slip must be sufficiently low to enter and fill the foams. However, it should also be high enough to avoid the ceramic slips draining from the foams. Hence, the slip was vacuumed for ten minutes before impregnation to remove any entrapped air bubbles which could decrease the density and compromise the mechanical strength of the bioceramics.

An important feature of the method is that the slip substantially fills the foams as opposed to only coating the walls. In the latter case, the resulting product would be a replica of the reticulated foam material and the ceramic parts of the structure would be hollow and therefore less strong. These differences are illustrated in Figure 2.

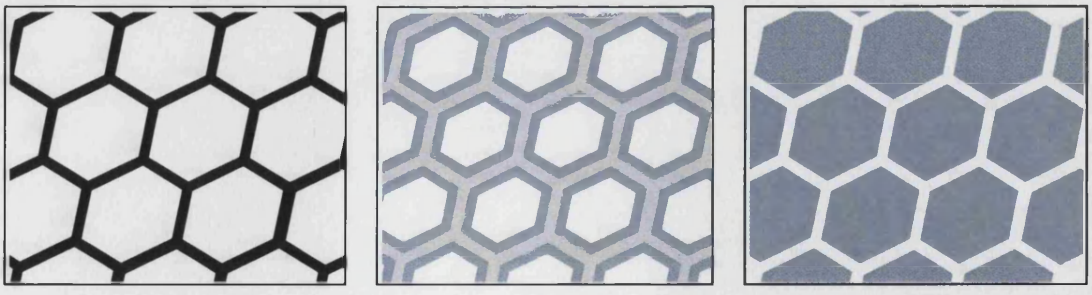

(a) (b) (c)

Fig. 2 (a) the reticulated structure of the polymer foam (b) result of coating just the walls of the polymer foam (c) result of substantially filling the foams with slips.

The foams were substantially impregnated with ceramic slip by vacuum impregnation. The procedure is shown in Figure 3. The slip was placed in a small beaker. The PU foam was compressed to remove air, immersed in the slip, then allowed to expand. The compression and expansion procedures while submerged were repeated in order to fill all the pores. The beaker

was then vacuumed for five minutes to remove the air in the foam and the slip. The impregnated foams were taken out and allowed to dry on tissue at room temperature. The time takes for this step was at least 24 hours, followed by drying in an oven at 40°C for another 24 hours. When the samples were made from the slips with higher solid loading, the drying time was increased. The dried green samples were fired in a programmable furnace at 1280°C.

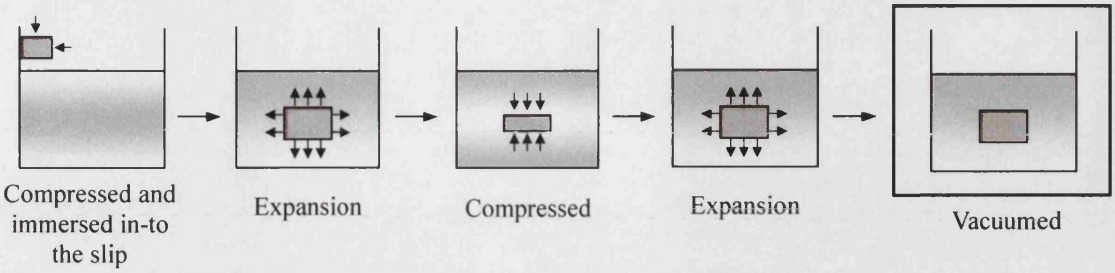

Fig. 3 Schematic representation of the vacuum impregnation technique.

Results

Figure 4 shows porous HA/TCP bioceramics with different dimensions fabricated by the vacuum impregnation method. Figure 5 shows the samples generated by joining 20 and 45 ppi foams together. No weakness could be seen at the interface between the two different structures. This demonstrated that porous HA/TCP with two or more different levels of porosity could be produced in a single block. Image analysis revealed the porosity measured for the three different foams was in the range of 5-10 %. The ranges of both the apparent densities of the porous HA/TCP samples and the theoretical densities of dense HA, β -TCP and α - TCP are shown in Table 1. The area equivalent diameters of the pore structure are shown in Figure 6. The 20 ppi foam produced a pore size range of 197-254 μm; the 30 ppi produced a pore size range of 143-182 μm and the 45 ppi a range of 105-127 μm. The compressive strengths of the HA/TCP samples were found to be 30-170 MPa.

Fig. 4 Porous HA/TCP bioceramics with different dimensions.

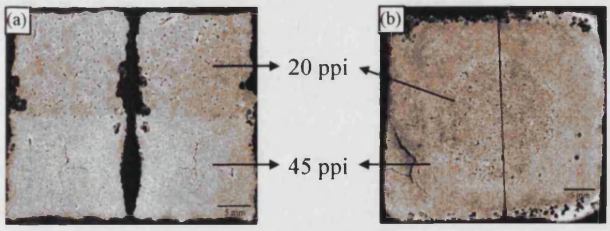

Fig. 5 The HA/TCP ceramics combining two different pores sizes by (a) sewing and (b) pressfitting.

Table 1 The apparent densities of porous blocks of the sintered HA/TCP and the theoretical densities of HA, β - TCP, α - TCP.

The apparent densities (g/cm^3)			The theoretical densities (g/cm^3) [8]		
20 ppi	30 ppi	45 ppi	HA	β - TCP	α - TCP
2.34 – 2.76	2.35 – 2.66	2.44 – 2.66	3.16	3.07	2.86

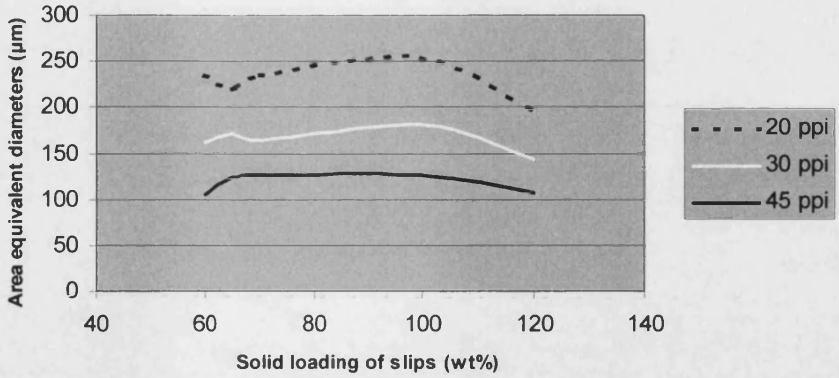

Fig. 6 The area equivalent diameters of the porous HA/TCP.

Discussion and Conclusions

Using a slip with the appropriate viscosity, large blocks of porous HA/TCP bioceramic with interconnected pores and a range of pore sizes combined with good mechanical properties were produced successfully. The method was also used to make HA/TCP granules in the size range of 2-8 mm with interconnected porosity and controlled size and shape – hitherto not possible using existing manufacturing techniques. Granules with reproducible properties can be manufactured in a more controlled manner relative to the alternative method of producing a single large piece of material which is broken into smaller pieces which are then sintered. By joining different ppi foams together, it was possible to produce functional gradient materials with porosity which varied through the thickness of the samples. Using this method to make a FGM ensured that the pores present in different parts of the composite structure were interconnected. The polymer foams were joined by sewing or pressfitted together, consequently, the interface of the two foams had a number of definite points of contact. These converted to interconnected channels in the resultant HA/TCP samples. The techniques developed for fabricating porous bioceramics can be extended to produce a range of bone substitute materials with properties tailored to specific clinical applications.

Acknowledgements

The authors would like to thank the University of Bath and Stryker Howmedica Osteonics for their support.

References

[1] A. Tampieri, G. Celotti, S. Sprio, A. Delcegliano and S. Franzese: Biomaterials, 22 (2001), p. 1365
[2] T.M.G. Chu, D.G. Orton, S.J. Hollister, S.E. Feinberg and J.W. Halloran: Biomaterials, 23 (2002), p. 1283
[3] Jintao Tian and Jiemo Tian: Journal of Materials Science, 36 (2001), p. 3061
[4] B. Flautre, M. Descamps, C. Delecourt, M.C. Blary and P. Hardouin: Journal of Materials Science: Materials in Medicine, 12 (2001), p. 679
[5] J.X. Lu, B. Flautre, K. Anselme and P. Hardouin: Journal of Materials Science: Materials in medicine, 10 (1999), p. 111
[6] J.H. Kuhne, R. Bartl, B. Frish, C. Hanmer, V. Jansson and M. Zimmer: Acta Orthop. Scand., 65 (1994), p. 246
[7] P.S. Eggli, W. Muller and R.K. Schenk: Clinical Orthopaedics and Related Research, 232 (1988), p. 127
[8] J.D. Santos, J.C. Knowles, R.L. Reis, F.J. Monteiro, and G.W. Hasting: Biomaterials, 15 (1994), p.5